Functionalized carbon nitride materials boost non-sacrificial photocatalytic H_2O_2 production

Feb. 8th, 2021

Kyushu Institute of Technology

Graduate School of Engineering

Major: Engineering; Graduate School of Engineering

Zhenyuan Teng

Contents

d

Part 1

Introduction

1.1 Background

H_2O_2, a highly efficient and environmental-friendly oxidant, has been recognized as one of the 100 most important chemicals all over the world [1, 2]. The content of active oxygen (47.1% w/w) in H_2O_2 is the highest among all chemicals with merits of no toxic side products. In this case, H_2O_2 has been widely applied in the areas of disinfection and sterilization [3, 4], organic synthesis[5] and wastewater treatment [6]. Recently, H_2O_2 has also been found to work as both oxidant and reductant in an one-compartment fuel cell [7]. The results showed that the theoretical output potential of such an H_2O_2 fuel cell was 1.09 V, which is comparable to that of conventional hydrogen (H_2) fuel cell (1.23 V) [7-9]. Compared to H_2, H_2O_2 showed a promising prospect as a water soluble solar fuel (60wt% H_2O_2, 3.0 MJL^{-1}, higher energy density than compressed H_2 gas, 35 MPa, 2.8 MJL^{-1}) [8]. Compared to H_2, H_2O_2 is fully soluble in water and easily transportable which pave it as an ideal energy carrier alternative to H_2. The anthraquinone (AQ) method for H_2O_2 production is the dominate process in industry (more than 95% of the total production, Figure 1-1) [10]. The AQ process includes four steps: i) hydrogenation of anthraquinone (AQ) in an organic solvent by using Ni or Pd catalyst; ii) oxidation of hydrogenizes anthraquinone (HAQ) in air or oxygen-enriched environment with the aid of catalysts; iii) extraction of H_2O_2 and recycling HAQ to AQ; iv) purification and concentration of H_2O_2. The multistep hydrogenation and oxidation reactions require high energy input. Additionally, the AQ process is not environmentally benign because large amount of wastewater, exhaust gas and solid waste are generated [10, 11]. What's more, H_2O_2 is generally produced at high concentrations (as high as 70 wt.%) in order to reduce transport costs, since the anthraquinone processes are typically implemented centrally to maintain a high efficiency. However, only dilute H_2O_2 solutions are needed (typically 2–5 wt.%) for many applications [1, 12].

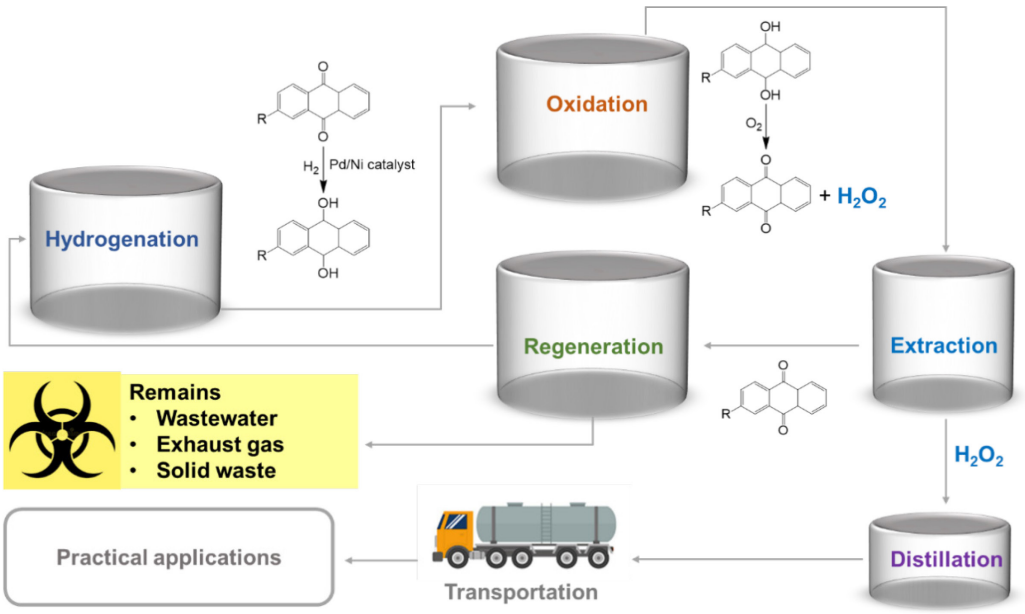

Figure 1-1. Schematic of the anthraquinone oxidation (AQ) process.

Therefore, many efforts have been devoted to developing new methods for H_2O_2 production, which can be operated under more moderate reaction conditions and do not generate waste [11]. One alternative route is the direct synthesis from H_2 and O_2 in the presence of Pd or bimetallic Au-Pd catalysts according to the simple reaction of $H_2 + O_2 = H_2O_2$. The typical reaction conditions mainly contain H_2/O_2 mixture feed gas, supported noble metal catalysts, acidic methanol solvent, nearly 0 °C reaction temperature, atmospheric or positive pressure and gas liquid-solid three-phase reaction [13, 14]. But unfortunately, the ratio of hydrogen to oxygen in the process needed to be precisely controlled because the H_2/O_2 mixtures are explosive over a wide range of concentrations although some diluents can be added into H_2/O_2 mixtures to mitigate the risk of explosions such as nitrogen, carbon dioxide, and argon [13, 14]. As a result, this process has not yet been scaled up to industrial applications. In this regard, a green and safe H_2O_2 production process is highly desired. Most recently, H_2O_2 production by a photocatalytic reaction process has been received increasing attention, which would be a meaningful breakthrough in H_2O_2 chemistry. Compared to the AQ method and direct synthesis process, the photocatalytic approach does not use dangerous H_2 and it only needs earth-abundant water and O_2 as raw materials, renewable sunlight as energy supply and some semiconductors as photocatalyst. Moreover, there is no pollutant emission in the overall

process, which makes it a safe and green method to produce H_2O_2.

In the last decades, many kinds of semiconductors has been prepared for photocatalytic H_2O_2 production, such as metal oxides, metal sulfides, metal organic compounds and carbon-based materials [15]. Among these photocatalysts, graphite-like carbon nitride (g-C_3N_4), also named as polymetric carbon nitride (PCN), as an analog of graphite and metal-free polymer n-type semiconductor, possesses a stacked two-dimensional (2D) structure of tri-s-triazine connected via tertiary amines. Because of its unique electrical, optical, structural and physiochemical properties, g-C_3N_4 has been recognized as a new class of cost-efficient multifunctional materials for electronic, catalytic and energy applications. Prof. Shiraishi firstly found pristine g-C_3N_4 showed some photocatalytic activity for H_2O_2 production with addition of ethanol as an electron donor in 2014 [16]. Generally, the structure of photocatalyst defines its properties, and the properties of the photocatalyst determine the performance. In this case, it is of great urgent to reveal the desired properties of g-C_3N_4 based photocatalyst for H_2O_2 production, thus leading to a comprehensive understanding of photocatalyst from rational structure design to satisfied performance.

In the introduction part, we firstly describe the fundamental principles of photocatalytic H_2O_2 production. Then, three most important issues for improving the H_2O_2 generation were proposed and summarized based on the band diagram and physiochemical properties of pristine g-C_3N_4. Combining the fundamental principles with the preparation strategies and possible influencing factors in liquid-phase photocatalytic systems, the research purpose of our research and the outline of the thesis has been presented.

1.2 Principles of photocatalytic H_2O_2 generation

In last decades, photocatalysis technique received enormous attention and has applied to various research areas, such as water splitting for H_2 and O_2 production [18], CO_2 reduction [19], degradation of pollutants [20], organic synthesis [21] and H_2O_2 production [15], due to solar energy is renewable and sustainable. Typically, reactions on photocatalyst materials includes three main steps (Figure 1-2) [22]. Firstly, photocatalyst

absorb photons with energy higher than its band gap. The electrons in valence band (VB) are excited to the conduction band (CB), leaving the holes in the VB. As a result, the negative-electron (e^-) and positive-hole (h^+) pairs are created in this step. Secondly, the photo-induced e^- and h^+ separate and migrate to the photocatalyst surface. Thirdly, the charge carriers react with the chemical species on the surface of photocatalyst. Meanwhile, the photo-induced e^- and h^+ also recombine with each other without participating in any chemical reactions.

Table 1-1. Standard electrode potentials for aqueous ORR half-reactions.

No.	Half-reactions	E^0 (V vs. SHE)	E^0 (V vs. RHE)
1	$O_2(g) + 4H^+ + 4e^- \leftrightarrow 2H_2O$	1.229	1.229
2	$O_2(g) + 2H^+ + 2e^- \leftrightarrow H_2O_2$	0.695	0.695
3	$H_2O_2 + 2H^+ + 2e^- \leftrightarrow 2H_2O$	1.763	1.763
4	$O_2(g) + 2H_2O + 4e^- \leftrightarrow 4OH^-$	0.401	1.229
5	$O_2 + H_2O + 2e^- \leftrightarrow HO_2^- + OH^-$	–0.065	0.764
6	$HO_2^- + H_2O + 2e^- \leftrightarrow 3OH^-$	0.867	1.696
7	$O_2(g) + e^- \leftrightarrow O_2^{\bullet-}$	–0.33	–0.33
8	$O_2(g) + H^+ + e^- \leftrightarrow HO_2^\bullet$	−0.05	–0.05
9	$HO_2^\bullet + e^- \leftrightarrow HO_2^-$	0.76	0.76
10	$HO_2^\bullet + H^+ + e^- \leftrightarrow H_2O_2$	1.44	1.44
11	$H_2O_2 + H^+ + e^- \leftrightarrow H_2O + \bullet OH$	0.793	0.793
12	$OH^\bullet + e^- \leftrightarrow OH^-$	1.89	2.72

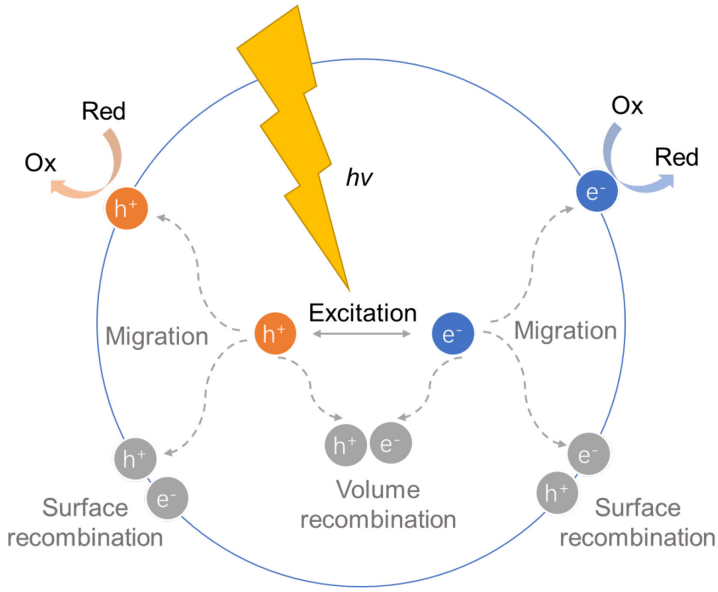

Figure 1-2. Photoexcitation and charge decay pathway in photocatalyst.

As for the photocatalytic production of H_2O_2, it is also governed by the basic photocatalytic reaction principle. At present, it is accepted that H_2O_2 can be generated through either water oxidation reaction (WOR) or oxygen reduction reactions (ORR) [23] as shown in Figure 1-3. The light-driven $2e^-$ WOR pathway (eq. 3, Table 1-1) is difficult to be achieved because of the uphill thermodynamics (1.76 V vs. SHE), i.e. the as-synthesized H_2O_2 will decompose at this highly oxidative potential because H_2O_2 is an excellent hole scavenger [24]. In case of ORR pathway, the H_2O_2 can be produced by either sequential two-step single-electron indirect reduction ($O_2 \rightarrow \bullet O_2^- \rightarrow H_2O_2$) or a one-step two-electron direct reduction ($O_2 \rightarrow H_2O_2$) route. For the h^+ in the VB, the most favorable reaction route is to oxidize H_2O into O_2 and H^+ via a $4e^-$ pathway (eq. 1). The eq. 7 to eq. 10 in Table 1-1 displays the H_2O_2 generation via the sequential two-step single-electron indirect reduction pathway. Firstly, the superoxide radicals ($\bullet O_2^-$) is formed by a one-electron reduction of O_2 (eq. 7), which further react with H^+ to produce $HO_2\bullet$ radicals (eq. 8). Then, the $HO_2\bullet$ radicals can readily undergo another one-electron reduction (eq. 9) to produce HO_2^- anions. Finally, the HO_2^- would react with H^+ to generate H_2O_2. The eq. 7 demonstrates the one-step two-electron direct reduction for the H_2O_2 production. In this process, the O_2 would directly react with two H^+ to form H_2O_2 product via the two-electron photoreduction. It is worth noting that the back reaction of WOR via a $4e^-$ pathway is the

ORR process via $4e^-$ pathway (eq. 1), which could also be a competitive reaction for H_2O_2 production via ORR. The most ideal situation is that the photocatalytic production of H_2O_2 is generated from H_2O and O_2 via $4e^-$ WOR and $2e^-$ ORR, which is an uphill reaction with a standard Gibbs free energy change (ΔG_0) of 117 kJ mol^{-1}.

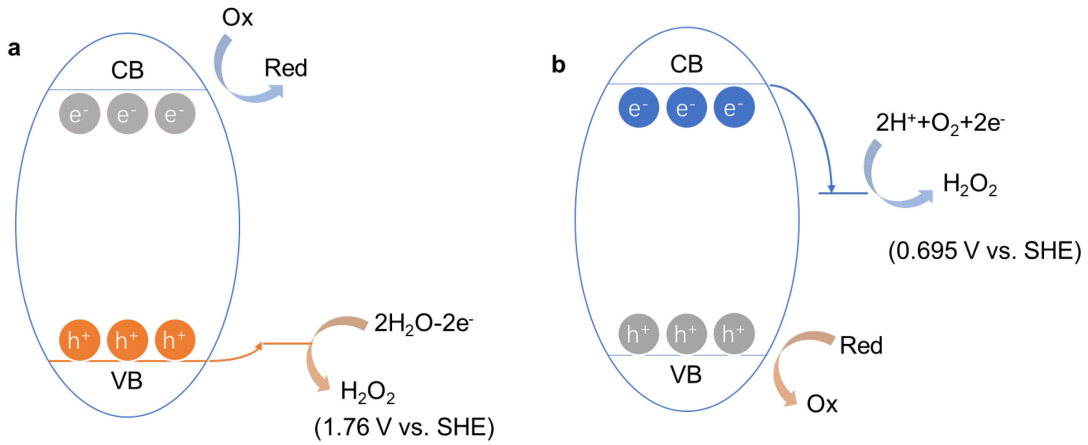

Figure 1-3. Schematic diagram for photocatalytic H_2O_2 production. (a) Photocatalytic H_2O_2 production via water oxidation reaction. (b) Photocatalytic H_2O_2 production via oxygen reduction.

1.3 Desired physicochemical properties of polymetric carbon nitride for photocatalytic H_2O_2 production

Since Wang and his coworkers first discovered the photocatalytic activities of g-C_3N_4 on H_2 and O_2 evolution in 2009 [25], g-C_3N_4-based photocatalysts have attracted boosting interest worldwide. The band gap of g-C_3N_4 is ~2.7 eV, corresponding to an optical wavelength of ~460 nm, which makes it a potential visible-light-active photocatalyst [26]. In addition, g-C_3N_4 possesses the photocatalytic ability for both water reduction and oxidation due to its appropriate band structure. In principle, g-C_3N_4 could be a promising photocatalyst candidate for H_2O_2 production [15] because its CB position (-1.3 V vs. NHE) is suitably located to facilitate O_2 reduction (0.28 V vs. RHE, pH=7) via $2e^-$ pathway while the VB potential (1.4 V vs. NHE) is lower than that of metal oxides which can effectively prevent the oxidative decomposition of H_2O_2 (Figure 1-4). Additionally, the conjugated heptazine ring in the PCN matrix can provide active sites for $2e^-$ ORR [16, 27], which is similar with the catalytic properties of graphene for $2e^-$ ORR [28, 29]. As such, g-C_3N_4 promptly becomes a star material in the field of photocatalysis H_2O_2 production.

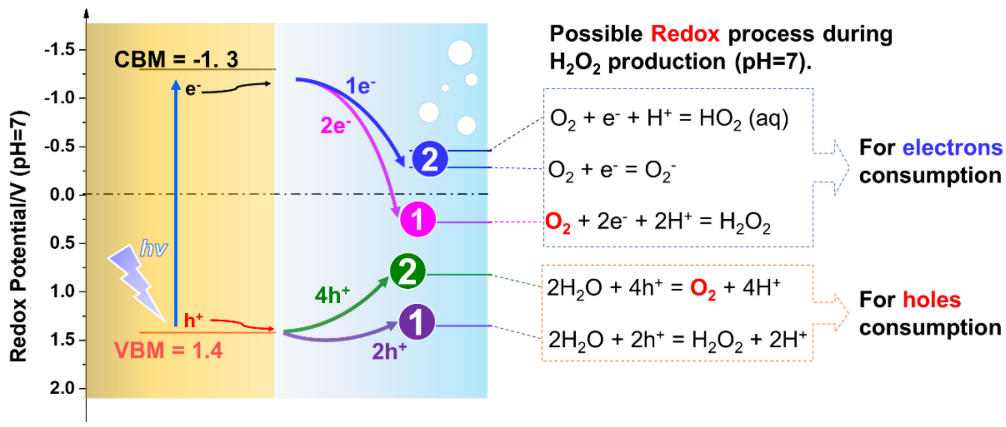

Figure 1-4. Band diagrams of g-C_3N_4 and the summary of potentials for redox reactions during the H_2O_2 production by using O_2 and/or H_2O.

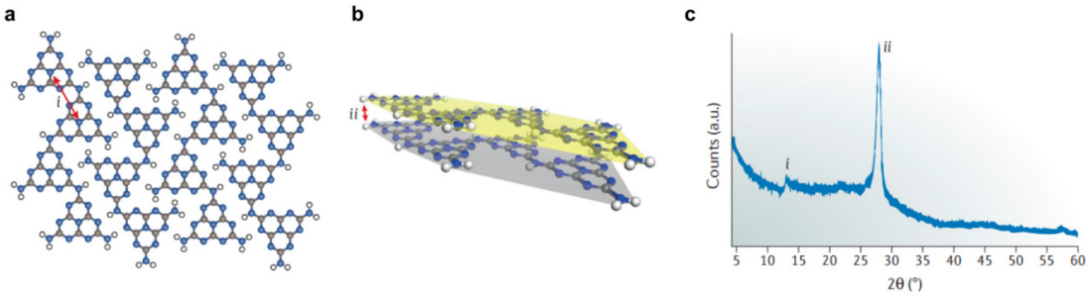

Figure 1-5. Possible interaction of hydrogen bond between melons. The possible features characteristic in-plane repeats between heptazine (C_6N_7) units (indicated with *i* in panels a and c) and a π–π stacking motif of the very same heptazines on top of each other (indicated with *ii* in panels b and c) in the matrix of PCN [30].

However, the photocatalytic H_2O_2 production activity of the g-C_3N_4 is still restricted by low efficiency. One crucial factor is the instinct difference between inorganic and organic semiconductors. In case of traditional crystalline inorganic semiconductors, they have high concentrations of mobile carriers ($N_{D,\ A}$) with low effective masses (m^* e^-, h^+), large dielectric constant (ε_r) and low exciton binding energy (E_{xBE}) [31]. These properties of inorganic photocatalysts usually result in high charge-carrier mobilities. As a result, the exciton binding energy (E_{xBE}) is usually low (~10 meV) in inorganic systems and, therefore, charge separation is relatively easy. Additionally, charge transport in the conduction band (CB) and valence band (VB) of inorganic systems has long ranges (dopant states defining the Fermi level (E_F) are close to the band edges). Therefore, tuning of defects and doping to increase the concentration of free charge carriers can be used to adjust bulk charge-

transfer properties, enabling long-range conductivity. This long-range conductivity of crystalline inorganic semiconductors results in a band-like transport for excitons via generation, separation and transferring to the surface, thus leading to a low charge recombination. On the contrary, the E_{xBE} of organic photocatalysts are extremely high, which can be rationalized by considering localized electronic states, akin to spatially separated HOMO and LUMO orbitals in the molecular, rather than dispersed valence and conduction bands, with low ε_r [31]. The strong interaction of the exciton with the molecular backbone often manifests polaronic transport, and the low ε_r prevents charge screening, leading to strong binding of e^- and h^+. As a result, in organic polymeric photocatalysts, such as carbon nitride, CTFs and COFs, charge transport mainly occurs through hopping rather than by band-like transport. Compared with the band like transfer, hopping usually result in high charge recombination rate and low charge separation efficiency, which leading to a low photocatalytic activity.

Besides the instinct properties of organic semiconductors, there are some other factors restricting the photocatalytic efficiency of PCN for H_2O_2 production. Firstly, the crystallinity of pristine g-C_3N_4 synthesized by thermal polymerization is significantly decreased because of the inevitably introduced defects [8, 26]. This means that the inner-plane structure of g-C_3N_4 is not completely composed by covalent bonds, i. e., the interaction of hydrogen bond between melons ($[C_6N_9H_3]_n$) are not the same as graphene (Figure 1-5). As a result, the charge separation and charge migration are significantly hindered during the after the excitation, which result in high charge recombination rate of PCN. Secondly, the large band gap (2.7 eV) and small absorption of visible light (K.M. absorbance usually less than 2, λ = 420 nm) result in the insufficient visible-light harvesting, i. e. only can short-wavelength of visible light participate in the photocatalytic reaction. Thirdly, although the side on adsorption of molecule oxygen on the π-conjugated heptazine ring enable g-C_3N_4 with some selectivity for $2e^-$ ORR, the stepwise 1 e^- to 1 e^- ORR reaction can hardly prevented since signals of superoxide radicals can still be detected during the photocatalytic reactions with electron spin resonance during the photocatalytic reactions [32]. In this case, reaction sites with higher selectivity for $2e^-$ ORR has to be constructed

for improving overall activity. To overcome these drawbacks, many protocols such as tuning morphologies, defect engineering, loading co-catalysts, copolymerization of semiconductors, doping elementals as well as hybridization, has been developed. Each of these functionalization strategies overcome one or two drawbacks by changing the following properties of pristine PCN: i) suppressing the charge recombination; ii) narrowing the bandgap or/and promoting light absorbance; iii) introducing the active sites for selective $2e^-$ ORR (Figure 1-6). Based on the improved physicochemical properties, the functionalization strategies for activity improvement of photocatalytic H_2O_2 production can also be divided in to three parts, which provide a comprehensive understanding from material preparation to physicochemical properties, thus revealing the insight relationships among the structure, properties and performance.

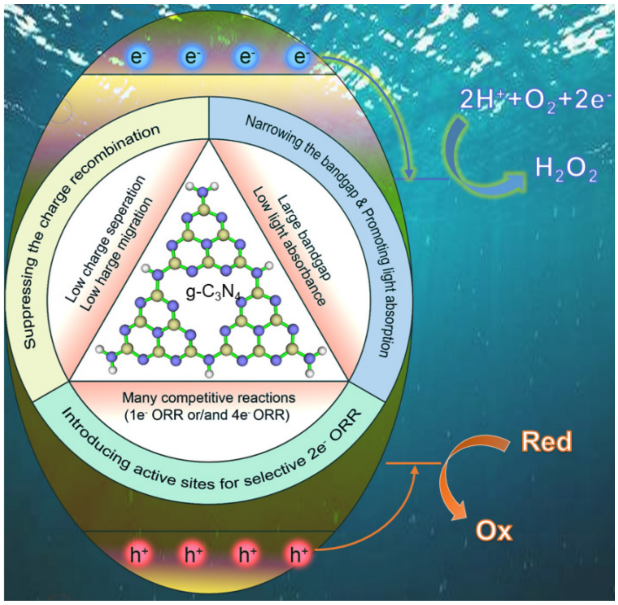

Figure 1-6. Solutions for overcoming the disadvantages of pristine g-C_3N_4 by manipulating physicochemical properties via $2e^-$ ORR.

1.3.1 Suppressing the charge recombination

1.3.1.1 Hybridization

(1) Hybridization with carbon-based materials

Carbonaceous nanomaterials have the distinctive properties of sp^2 hybridized carbon bonds with unusual physicochemical properties at the nanoscale, which generally exhibit excellent chemical, mechanical and electrical properties [28, 29, 33]. In photocatalysis field, carbonaceous nanomaterials are often acted as electron transfer materials and photosensitizer, which could broaden the adsorption edge and improve the migration efficiency of photo-induced electrons [34-37]. When carbonaceous nanomaterials are immobilized onto g-C_3N_4 photocatalyst, they can accept and transport the photoinduced electrons from the CB level of g-C_3N_4 and increase the activity of reduction reaction, thus leading an improved photocatalytic performance.

As typical carbonaceous nanomaterials, carbon nanotubes (CNTs) with the π-conjugative structure are capable of accepting, transporting and storing electrons [38]. Thus, g-C_3N_4-CNTs formed by incorporating CNTs into g-C_3N_4 can enhance photocatalytic activity. Zhao and co-workers utilized an amination reaction process to introduce CNTs in g-C_3N_4 nanosheets to form a hybrid catalyst of g-C_3N_4/CNTs, in which CNTs was covalent combined with g-C_3N_4 (Figure 1-7a) [39]. The TEM image (Figure 1-7b) confirmed that tube-like CNTs and g-C_3N_4 were effectively combined together after the covalent combination. The CNTs covalent combined with g-C_3N_4 promoted the electron generation via heightening the reducing ability and helpfully shifted CB level to enhance the single-electron reduction of O_2 to $\cdot O_2^-$ [39]. As shown in Figure 7c, the photocurrent of g-C_3N_4/CNTs significantly increased compared with the pristine PCN. Another case is that Shiraishi and co-works also employed reduced grapheme oxide (rGO) to incorporate with the g-C_3N_4/PDI catalyst for further activity improvement (Figure 1-7d,e), which benefited from the two-dimensional single-carbon monolayer nature of rGO (g-C_3N_4/PDI/$rGO_{0.05}$) with high charge carrier mobility, high photochemical and thermal stability [40]. As shown in Figure 3a, the photocurrent density of g-C_3N_4/PDI/$rGO_{0.05}$ is much larger than that of g-C_3N_4/PDI, where the rGO itself shows almost no response [40]. This indicates that the CB e^- transfer from the photoexcited g-C_3N_4/PDI to rGO indeed enhances charge separation

as observed for related semiconductor/rGO systems. It is worth noting that forming tight junctions between the g-C_3N_4 based photocatalyst and carbon based material is extremely important for forming electron transfer pathways since the photocurrent intensity of the physical mixture of g-C_3N_4/PDI and rGO significantly is 20% smaller than that of g-C_3N_4/PDI [40].

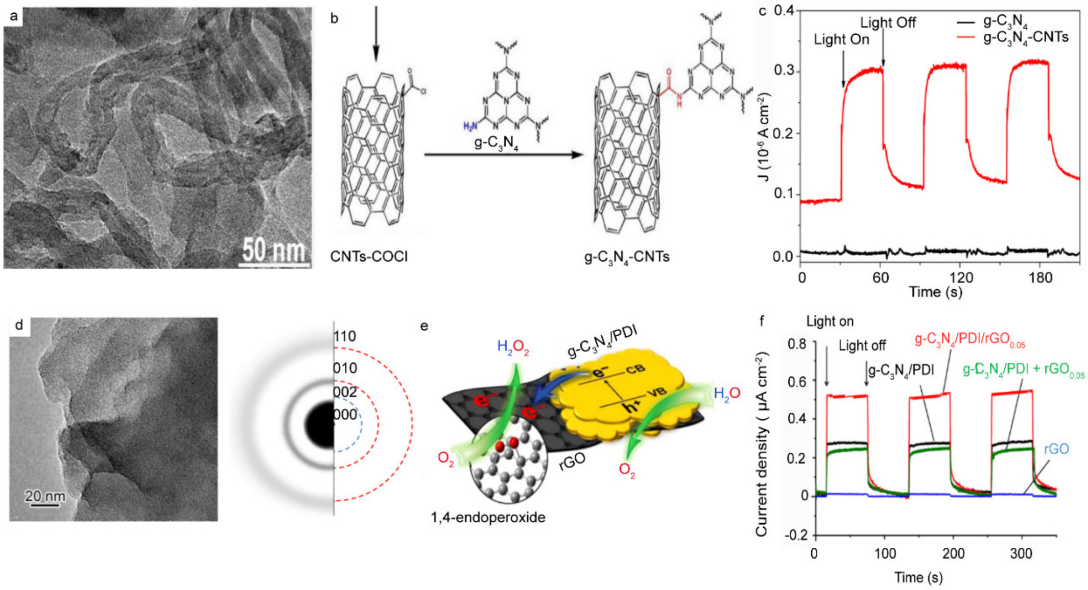

Figure 1-7. Hybridization with carbon-based material for improved charge separation. (a) A TEM image of g-C_3N_4-CNTs [39]. (b) Preparation process of g-C_3N_4-CNTs [39]. (c) Photocurrent response of g-C_3N_4-CNTs or g-C_3N_4-loaded electrodes under light at a bias of 0.25 V vs. SCE (λ ≥ 400 nm) [39]. (d) A TEM image of g-C_3N_4/PDI/$rGO_{0.05}$ and its SAED pattern (inverse contrast) with indexed graphite pattern [40]. (e) Schematic illustration of the proposed mechanism for photocatalytic H_2O_2 production on g-C_3N_4/PDI/rGO [40]. (f) Photocurrent response of the g-C_3N_4/PDI/$rGO_{0.05}$ and other g-C_3N_4 based catalysts measured on FTO in 0.1 M Na_2SO_4 solution under visible light (λ > 420 nm) at a bias of 0.5 V (vs Ag/AgCl) [40].

(2) Hybridization with metal and metal compounds

Fabrication of metal compounds to form a Schottky barrier between metal-based semiconductors and PCN material has been proved to be an efficient strategy for improving the photocatalytic efficiency for several reactions [26, 41]. The nature of the formation of Schottky barriers in PCN/Metal compounds is due to the differences between the charge potentials of metal compounds and the PCN under the light irradiation [42]. The electrons tend to migrate to the semiconductor that have more positive potential, while holes tend to migrate to the ones with negative potentials [22]. Although the overall redox potentials of

the photocatalyst is decreased, the charge separation of electron-hole pairs were significantly improved, thus leading to a significantly improved charge separation (Figure 1-8a). However, there are very few literatures for promoting the photocatalytic efficiency for H_2O_2 production by construction of heterojunctions based on PCN/Metal compounds. The reason may be attributed to the following two reasons. On the one hand, the potential of the conduction band minimum (1.3 V vs. SHE) of PCN is relatively more negative than that of common metal compounds (Figure 1-4). In this case, the photoelectrons tend to accumulate on the metal oxides. Thus, the potential of the metal compounds determines the reduction potential of the heterojunction materials. As shown in Figure 8b, the photocatalytic reduction potential of TiO_2, Cu_2O, CdS and ZnS can hardly facilitate the $2e^-$ ORR because the kinetically favored $1e^-$ ORR to form $\cdot O_2^-$, thus resulting in a stepwise ORR to generate H_2O_2. For other metal compound semiconductors, although the $1e^-$ ORR can be prevented because of the positively shifted CBM. However, the potential differences between the redox potential of O_2, $2H^+/H_2O_2$ and CBM of Fe_2O_3, $CuWO_4$, SnO_2, WO_3, etc. is quite small, which may lead to a poor thermodynamic driving force for $2e^-$ ORR. On the other hand, metal compounds is that they subsequently decompose the formed H_2O_2 by disproportionation or photoreaction on the surface. For instance, the formed H_2O_2 on TiO_2 is converted to the peroxy species (Ti−OOH) via the reaction with surface Ti−OH groups and decomposed by the reduction with e^- (Ti−OOH + H^+ +e^- → Ti−OH + OH^-) [43]. Therefore, forming the heterojunctions by contact PCN with one metal compound may be an unacceptable strategy unless unique electron transfer pathway between PCN and metal compounds is formed, such as Z-scheme catalysts, so that reduction will occur on the surface of PCN [44].

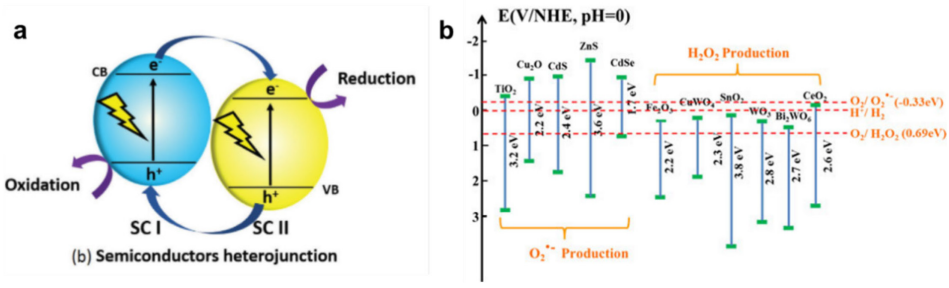

Figure 1-8. Schematic diagram of (a) the semiconductors heterojunctions and (b) Band diagram of common metal based photocatalyst [45].

Loading active noble metal nanoparticles (NPs) on photocatalyst is one of the effective approaches to improve the photocatalytic H_2O_2 production activity by promoting the charge separation [46, 47]. One study was reported by Chang *et al.* and they adopted a carbon-layer-stabilized method to load Au nanoparticles onto the C_3N_4 matrix [48]. The H_2O_2 yield of the fabricated Au/g-C_3N_4 photocatalyst increased 2.3 times compared of the pristine g-C_3N_4 [49]. In the other study, Zuo and coworkers observed similar improvement of Au/C_3N_4 photocatalyst on H_2O_2 production [49]. The authors also compared the effect of different cocatalysts (Au, Ag, Pd, and Pt) on g-C_3N_4 for H_2O_2 production in this study [48]. The results showed that Au Nps loaded g-C_3N_4 exhibited the best performance for H_2O_2 production [49]. The enhancing H_2O_2 production was attributed to the efficient separation of charge carriers between the finely dispersed Au NPs and g-C_3N_4 [49]. The function of Au Np on PCN for charge separation is quite similar to that of carbon materials. The Au Nps can improve the carrier mobility of photoelectrons so that the charge recombination could be suppressed.

(3) Hybridization with metal-free semiconductors and molecules

Organic semiconductors have advantages of low cost, easy fabrication and mechanical flexibility [50]. Particularly, organic photocatalysts are able to address the weaknesses of their inorganic counterparts, such as heavy metal with perceptive toxicity and limited concentration of active sites. In recent years, other organic semiconductors were also employed as photocatalysts, such as triazine [51] and aromatic diimides [27, 39, 52-54]. Aromatic diimides possess high electron mobility and stability, which are an important class of n-type organic semiconductors and have incorporated with g-C_3N_4 for photocatalytic H_2O_2 production.

Shiraishi's group incorporated several aromatic diimide (pyromellitic diimide [27, 52], PDI, biphenyl diimide [54], BDI, and mellitic triimide [53], MTI) into the g-C_3N_4 network by a facile thermal condensation (Figure 9a). In pure water with O_2, all of g-C_3N_4/PDI, g-C_3N_4/BDI and g-C_3N_4/MTI catalysts successfully produced millimolar levels of H_2O_2 [27, 39, 52-54]. The photocurrent showed significantly improvement after the co-polymerization

of aromatic diimindes. It should be noted that the introducing of more C=O groups significantly improved the photocurrent (Figure 9b) [53]. The C=O groups in these aromatic diimindes may accumulate negative charges and then increase the thickness of the space-charge region, which might facilitate the separation efficiency of photo-generated electron-hole pairs [4].

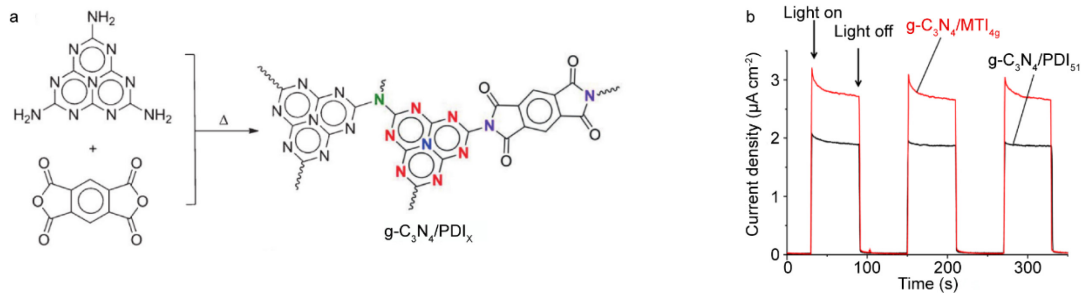

Figure 1-9. Hybridization with electron-deficient organic semiconductors for improved charge separation. (a) Synthesis scheme of g-C_3N_4 hybridized by aromatic diimide using g-C_3N_4/PDI_x as an example [27]. (b) The Photocurrent response of g-C_3N_4/MTI_{49} and g-C_3N_4/PDI_{51} in 0.1 M Na_2SO_4 (bias: 0.5 V vs Ag/AgCl) [52].

In case of incorporation with semiconductors, Shiraishi and co-workers has combined PCN/PDI with boron nitride (BN) to separate holes since BN have a relatively negative VBM (Figure 1-10a) [52]. In the system of g-C_3N_4-PDI-$BN_{0.2}$-rGO, the photocurrent increased about 20% [52], indicating the significantly charge separation (Figure 1-10b). It is worth noting that the oxygen evolution of the g-C_3N_4-PDI-$BN_{0.2}$-rGO increased over 15% compared with that of g-C_3N_4-PDI-$BN_{0.2}$-rGO (Figure 1-10c) [52], further confirming that the charge separation introduced by BN separated photogenerated holes. Yang *et al.* assembled perylene imides (PI) on g-C_3N_4 nanosheets to construct an all-solid-state Z-scheme heterojunction [56]. The hybrid g-C_3N_4/PI photocatalyst with Z-scheme configuration promoted the spatial separation of charge carriers, in which the photoinduced electrons in PI recombined with holes in g-C_3N_4, while the remained holes and electrons were left on PI and g-C_3N_4, respectively. As a result, more electrons from the CB of g-C_3N_4 part reduced O_2 to produce more H_2O_2 while the holes of g-C_3N_4/PI oxidized OH^- to $\cdot OH$ [56], which also subsequently reacted to produce H_2O_2. The shift of H_2O_2 generation from single-channel to two-channel, leading to a significant improvement in photocatalytic

production H_2O_2.

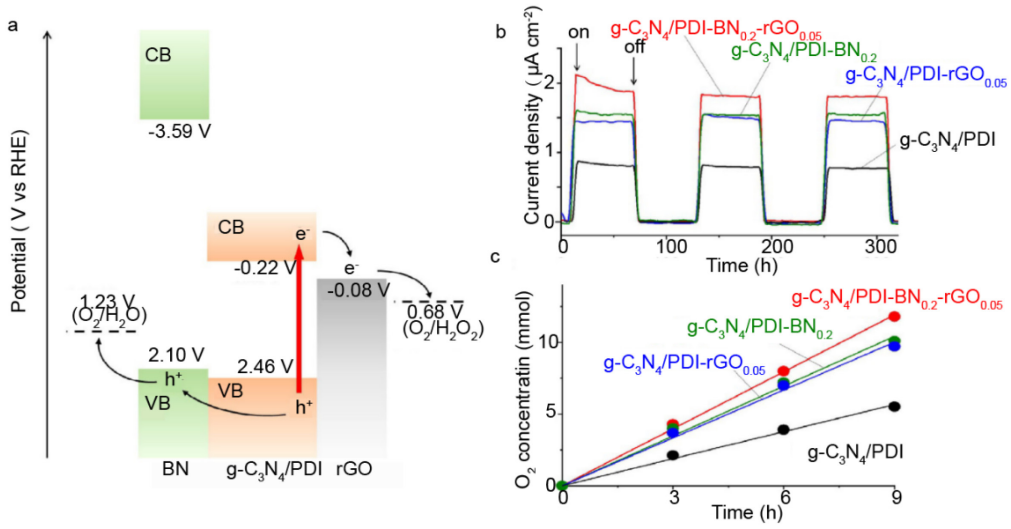

Figure 1-10. Hybridization with borne nitrides for improved charge separation. (a) Electronic band structures of g-C_3N_4/PDI, rGO, and BN. (b) Photocurrent of the catalysts on FTO under λ>420 nm irradiation at a bias of 0.5 V(vs. Ag/AgCl) in 0.1M Na_2SO_4. (c) Time-dependent change in the amounts of O_2 formed during photoreaction in an $AgNO_3$ as an electrolyte. Reaction conditions: catalyst (50 mg), 10 mm $AgNO_3$ solution (30 mL), Ar (1 atm), λ>420 nm (Xe lamp, intensity at 420-500nm: 43 Wm^{-2}), temperature (298 K).

1.3.1.2 Doping

(1) metal and non-metal doping

Doping has also been considered as a process of introducing additional elements and impurities into g-C_3N_4 framework to tune the optical, electronic and other physical properties [57]. In case of charge separation, one of the most efficient strategy is to incorporate of alkaline metal ions. Several works has used alkaline metal ions to functionalize PCN, leading to a promoted the charge separation for organic synthesis [58], HER [59], carbon dioxide reduction [60], nitrogen fixation [61] can all be facilitated by using alkaline metal ions incorporated PCN (Figure 11a). In case of $2e^-$ ORR, Qu *et al.* reported a co-doping of K^+ and Na^+ into g-C_3N_4 lattice by a molten salt method. The alkali metal ions doping increased visible-light absorption, promoted separation of electron-hole pairs to alter the H_2O_2 production way from “single channel pathway” to “two channel pathway”. The PL intensity of alkali metal ion incorporated PCN significantly decreased, indicating the incorporation of ions significantly decreased. The optimal doped photocatalyst displayed an outstanding H_2O_2 production of 4.6 mmol L^{-1}, being 9 times higher than that

of pure g-C_3N_4.

In regard to metal and non-metal co-doping in g-C_3N_4, Moon and coworkers reported an *in situ* incorporation of potassium (K), phosphorus (P), and oxygen (O) elements into a g-C_3N_4 matrix through solid-state thermal polymerization of melamine in the presence of dibasic potassium phosphate (KPD, K_2HPO_4) [62]. The radiative recombination of KPD was significantly suppressed, according to the significantly decreased PL intensity (Figure 1-11b). The heteroelements on the g-C_3N_4 matrix increased the lifetime of the transient species to a picosecond range and promoted the interfacial electron transfer to dioxygen and suppressed the decomposition of *in situ* generated H_2O_2. Consequently, the rate of H_2O_2 formation on K-P-O doped g-C_3N_4 was markedly enhanced in the O_2-saturated suspension in comparison to that of pure g-C_3N_4 [62]. In another related study, Zhang *et al.* reported a halogen (Br or Cl) doped g-C_3N_4 nanorods via saturated NH_4Br or NH_4Cl solution- hydrothermal post-treatment [63]. The introduction of heteroatoms into the π-conjugated g-C_3N_4 effectively accelerated the charge carriers transfer rate [63]. Kim *et al.* studied the co-doping of metal (K) and nonmetal ions (P and F) into the g-C_3N_4 framework [64]. This co-doped g-C_3N_4 also significantly promoted the charge separation. Under visible light irradiation, the co-doped g-C_3N_4 exhibited higher activity photocatalytic production of H_2O_2 compared to that of bare g-C_3N_4 (Figure 1-11d).

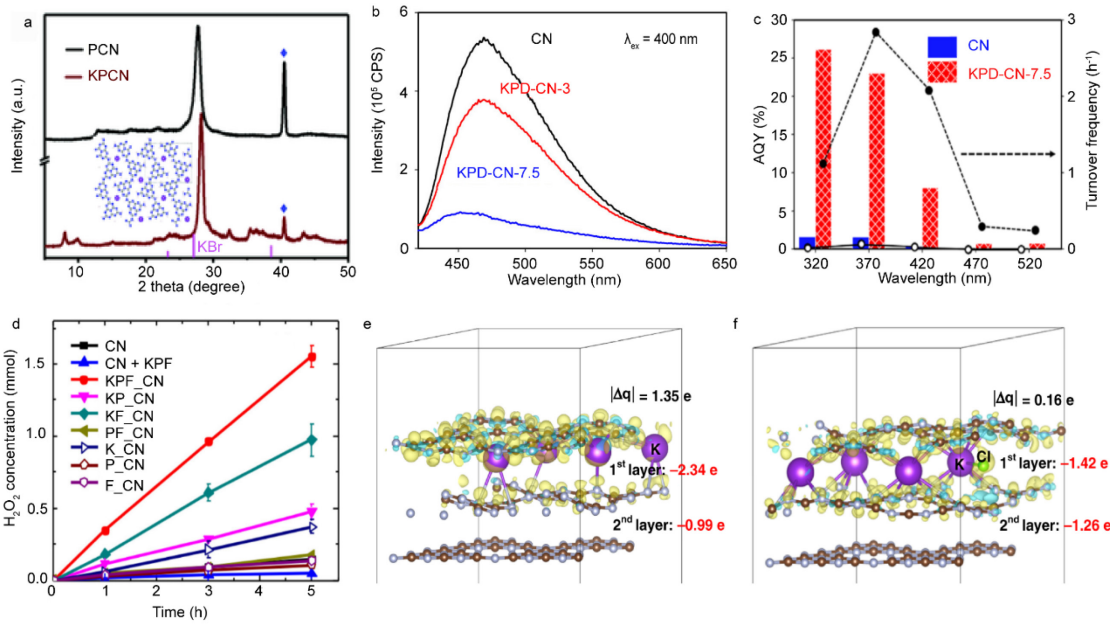

Figure 1-11. Metal and/or non-metal doping for improving the charge separation. (a) XRD patterns of pristine PCN and K^+ incorporated PCN [58]. (b) PL emission spectra (λ = 400 nm) and (b) PL excitation spectra at 470 nm of bare carbon nitride (CN), KPD-CN-3, and KPD-CN-7.5 [62]. (c) Apparent quantum yield (AQY, left axis) and turnover frequency (right axis) of bare CN and KPD-CN-7.5 for H_2O_2 production with monochromatic light irradiation [62]. (d) Time profiles of photocatalytic H_2O_2 generation using CN samples modified with various dopants and a control sample of the physical mixture of CN and KPF_6 (CN + KPF) [64]. The experimental conditions were 0.5 g L^{-1} photocatalyst, 10 vol% ethanol, pH 3, continuously purged with O_2 and polychromatic light through a long pass filter (k > 420 nm) [64]. Charge distribution Charge distribution of (e) K-GCN, (f) KCl-GCN obtained from density functional theory (DFT) calculations [65].

Zhang et. al used density functional theory (DFT) calculation also to reveal how the incorporated alkaline ions changes the charge distribution over different atoms [65]. Their calculation results confirmed that the electron-rich nitride pots in the three-fold N-bridge linking triazine units are liable to capture and confine the alkali cations of K^+ in the adjacent layers through the ion-dipole interaction [65]. The K-incorporated GCN structure with weak interlayer bridging made a relatively large number of electrons accumulated on the first layer (–2.34 e of layer charge) than on the second one (–0.99 e of layer charge) (Figure 1-11e), whereas the Cl-doping in GCN did not induce such localization of electrons between the layers [65]. As a result, the K-GCN exhibited a high value of the charge difference between the adjacent layers (|Δq| = 1.35 e) while that on Cl-GCN (|Δq| = 0.06 e) is insignificant. The presence of doped K atoms induces the anisotropic electron density

distribution, which is preferably accumulated on the first layer but the additional doping of Cl atoms makes the electron distribution more balanced between the layers (Figure 1-11f) [65]. In other words, when both K and Cl are co-present in the carbon nitride structure, the K-induced electron density polarization can be counterbalanced by Cl to lower $|\Delta q|$ (0.16 e) significantly [65]. This implies that the charge transfers between the layers in KCl-doped carbon nitride are more facilitated than those in pristine GCN, which may provide an explanation for its higher photocatalytic activity.

Non-metal doping of PCN also can manipulate the electronic configuration of PCN with significantly improve charge separation [66-69]. Zhu's research group developed an oxygen-enriched g-C_3N_4 (OCNs) photocatalyst which achieved enhanced H_2O_2 production [70]. Experimental results showed that compared to g-C_3N_4, the OCN samples achieved significantly enhanced H_2O_2 production efficiency in pure water without a sacrificial agent under visible light irradiation. The photocurrent measurement, ESI and PL spectra all proved that charge separation efficiency were significantly promoted after the O element were introduced to the PCN matrix.

(2) Doping with polyoxometalates and its derives

Polyoxometalates (POMs) are commonly made up of cations and polyanion clusters with structural diversity, in which the oxometal polyhedra of MO_x (M = W, Mo, V, Nb, Ta; x = 5, 6) are the basic construction units [71]. When the POMs irradiated by abundant light energy, it is excited and there is a charge transfer from O^{2-} to M^{n+} (n = 5, 6), leading to the formation of a hole center (O^-) and trapped electron center ($M^{(n-1)+}$) pair. In this case, the photo-excited POMs can serve as both electron donors and electron acceptors for improving the charge separation or/and serving as co-catalysts [71]. Zhao and coworkers prepared a series of POM clusters modified g-C_3N_4 for efficient photocatalytic H_2O_2 evolution by thermal condemnation method (Figure 1-12a) [72-74]. For instance, the amounts of formed H_2O_2 by the g-C_3N_4/PW_{11} reached 3.5 μmol within 60 min while the catalytic performance of pure 3DOM g-C_3N_4 was only 1.3 μmol [72]. This research group also employed other POM clusters, such as $[SiW_{11}O_{39}]^{8-}$ (SiW_{11}), $(NH_4)_3PW_{12}O_{40}$ (NH_4-

PW_{12}) and $(NH_4)_8Co_2W_{12}O_{42}$ (NH_4-Co_2W_{12}), to covalently combine with g-C_3N_4 [73]. All of these clusters significantly improved the charge separation of pristine PCN. As shown in Figure 1-12f, the photo-current densities of the g-C_3N_4-based catalysts decrease in the following order: g-C_3N_4-CoWO (0.57 μA cm^{-2}) > g-C_3N_4-WO (0.33 μA cm^{-2}) > g-C_3N_4-Co (0.13 μA·cm^{-2}) > g-C_3N_4 (0.05 μA cm^{-2}) [73]. The diameters of Nyquist semicircle obtained from the photoelectrochemical impedance spectroscopy (EIS) for the g-C_3N_4-based catalysts increase in the following order: g-C_3N_4-CoWO < g-C_3N_4-WO < g-C_3N_4-Co < g-C_3N_4 (Figure 1-12g) [73]. The above results reveal that the incorporation of CoWO into g-C_3N_4 framework can enhance the charge separation of g-C_3N_4-CoWO [73]. The action spectra measurement revealed that the band excitation result in the generation of H_2O_2 in both g-C_3N_4 and g-C_3N_4-CoWO systems [72-74], indicating that the function of POM incorporation may be as same as ion doping since POM clusters are all well dispersed in the PCN matrix (Figure 1-12b-e). The charge separation and charge transfer may be significantly improved because the in well-defined band gap of POM and separated positive and negative centers. The inner-panel charge transfer and the charge transfer between the layers may be significantly promoted by the introduction of highly dispersed POM clusters.

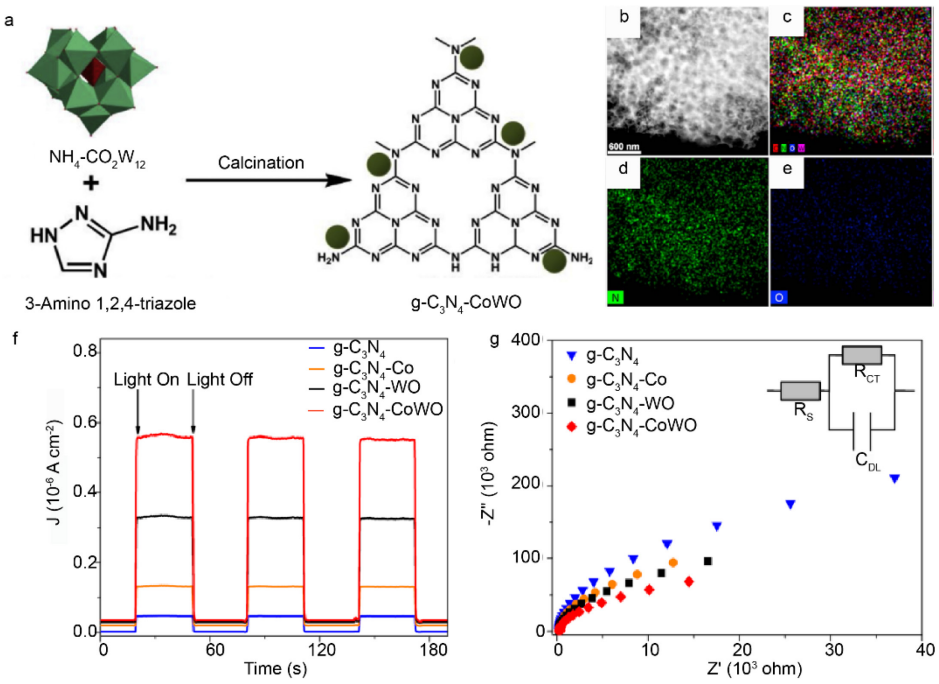

Figure 1-12. Doping with polyoxometalates and its derives for improved charge

separation. (a) Systematic diagram for incorporation of *polyoxometalates and its derives (g*-C_3N_4-CoWO is an example.). STEM images (b) and corresponding elemental mappings of 3DOM g-C_3N_4-PW_{11}. (c) Photocurrent response of catalysts-loaded electrodes under light at a bias of 0.25 V vs. SCE (λ ≥ 420 nm). (d) EIS Nyquist plots of the catalysts under visible light (λ ≥ 420 nm) at a bias of 5 mV vs. SCE in the frequency range of 10 mHz to 100 kHz.

1.3.1.3 Defect engineering

It is widely accepted that the high crystallinity of photocatalysts is beneficial for photocatalytic reaction while defects are often considered as charger combination sites. However, more recently, this viewpoint has been reconsidered and it has been verified that defects could benefit photocatalytic reactions as well if they are well controlled [75, 76]. Many research works showed that the introduced defects not only served as active sites for reactant molecules but also altered the electronic configurations, i. e., the defects possess more trapping sites, which could suppress the charge recombination. The defects in/on g-C_3N_4 photocatalysts are often formed by introducing carbon [32, 77] and nitrogen vacancies [78-81], in altering the optical and electronic properties towards promoted H_2O_2 production. For instance, Li et al. reported the creation of carbon vacancies in g-C_3N_4 through thermal annealing in an oxygen-deficient environment (Ar flow) [32]. As shown in Figure 1-13a-b, the formation of carbon vacancies in g-C_3N_4 (Cv-g-C_3N_4) was accompanied by the appearance of amino groups [32]. Under visible light irradiation [32], the H_2O_2 yield of Cv-g-C_3N_4 was much higher than that of pure g-C_3N_4 [32]. Such enhanced photocatalytic activity was first ascribed to the improved separation efficiency of photogenerated carriers as well as altering the H_2O_2 production pathway from a two-step indirect reaction to a one-step direct reaction, thus accelerating the H_2O_2 production.

Similar to carbon vacancy, nitrogen vacancy in g-C_3N_4 can boost the photocatalytic H_2O_2 production. Zhu and coworkers reported the creation of nitrogen vacancies in g-C_3N_4 through a reduction treatment under N_2 atmosphere, which was followed by a formation of functional group C≡N. Under visible light irradiation, the g-C_3N_4 with nitrogen vacancies presented an improved photocatalytic generation of H_2O_2 compared to the pristine g-C_3N_4. A maximum H_2O_2 yield of 170 μmol L^{-1} h^{-1} was achieved from pure water under ambient atmosphere without organic electron donors [81]. Other examples are that Li *et al.* [78] and

Qu et. al [79] demonstrated that nitrogen-vacancy could be created in g-C_3N_4 photocatalyst by a dielectric barrier discharge (DBD) plasma treatment. Their results showed that the H_2O_2 evolution can be improved at most 10 times compared with that of pristine PCN [78]. In another related study, Shi *et al.* employed a hydrazine-based photoreduction method to create holey defective C_3N_4 photocatalysts with nitrogen vacancies (Figure 1-13c). Interestingly, the as-prepared photocatalysts had the advantages of both morphological tuning and defect control. The holey defective C_3N_4 with abundant holes endowed more exposed catalytic active sites and rapid charge carriers from the bulk to surface, which is confirmed by PL measurements (Figure 1-13d). The introduced nitrogen vacancies narrowed the intrinsic bandgap and the formation of defect states within bandgap expended the visible-light absorption range and suppressed the electron-hole recombination (Figure 1-13e). As a result, the holey defective g-C_3N_4 photocatalysts showed much higher photocatalytic activity for visible-light-driven H_2O_2 production compared to pristine bulk g-C_3N_4.

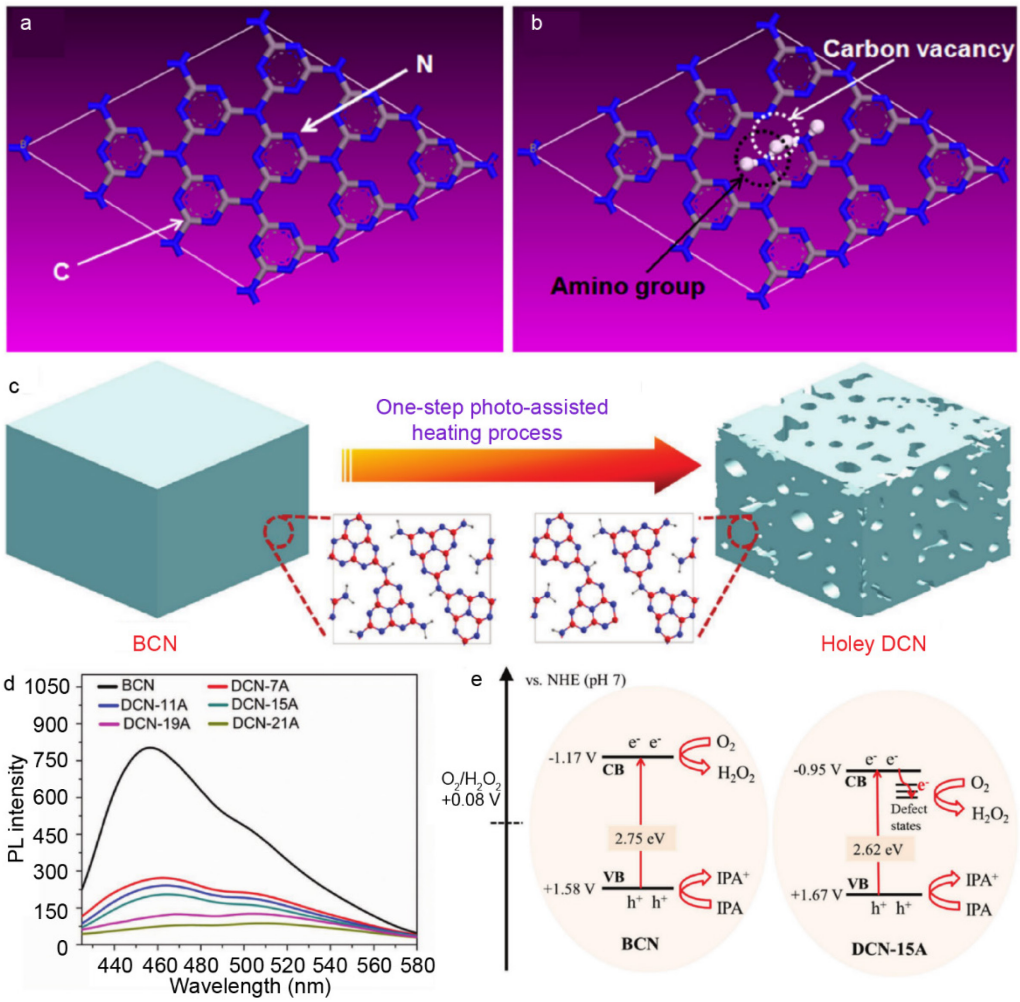

Figure 1-13. Defect engineering for promoting charge separation. (a) Schematic of g-C_3N_4; (b) carbon vacancy and amino group in g-C_3N_4. (c) Illustration of the preparation process of holey DCN, and the insets are their simulated structure (H, C, and N atoms are represented by the gray, red, and blue balls). (d) PL spectra of BCN and DCN samples. (e) Schematic of mechanisms underlying the photoexcited dynamics involved in photocatalytic H_2O_2 evolution over BCN and DCN-15A.

In summary, the functionalization strategies of doping and defect engineering for improving the charge separation for PCN based material used for $2e^-$ ORR process are quite similar to the functional strategies for other reactions, such as HER, COR, and ORR. However, the hybridization of PCN-based material, especially hybridization with electron-deficient semiconductors, enables PCN based photocatalyst with unique electronic properties for improving the charge separation. We believe that if the co-polymerization strategies to introduce other electron-deficient groups with higher charge separation efficiency could be able to generate π-conjugated and π-stacked donor–acceptor

couples [82] in PCN matrix, leading to a higher efficiency for photocatalytic H_2O_2 synthesis.

1.3.2 Improving the light harvesting

Although pristine PCN can use visible light for photocatalytic reaction, the large band gap (2.7 eV) and in sufficient light absorption result in the insufficient visible-light harvesting for further efficiency improvement [26]. In this case, improving the light absorbance of photocatalyst and narrowing the band gap are two practical strategies for H_2O_2 production.

Copolymerization of PCN with other organic molecules/semiconductors, such as triazine, barbituric acid and aromatic diimides cannot only improve the light absorbance of photocatalyst and narrowing the bandgap. As mentioned in Section 3.1.2, Shiraishi and co-workers has prepared a series of aromatic diimides hybridized PCN with significantly narrowed band gap form 2.7 eV of pristine PCN to 2.4 eV of PCN/PDI [27, 53, 54]. The light absorbance of the aromatic diimides hybridized PCN improved about ~20% at λ=400 nm, indicating the improved light absorption.

Doping of the alkaline metal ions can also expand the light absorption to a small extent (0.1 eV~0.3 eV) combined with the significantly light absorbance (50%) can be significantly improved. Alkaline metal and non-metal doping also proved to efficient strategies for improving the light absorbance [62, 64, 83]. Choi and co-workers found that the light absorption ability of CN samples was gradually improved with increasing KPF_6 content, even though KPF_6 alone did not exhibit any light absorption. This might be ascribed to alteration in the electronic states of bare CN and generation of unexpected defect sites. A very recent work using K and S co-doped PCN with functionalization of -OH group (AKMT) also showed significant improvement in both light absorption and narrowing the bandgap [83]. The light absorption edge expanded from ~450 nm of pristine PCN to ~520 nm of AKMT [83]. With the addition of sacrificial regent, AKMT exhibited an apparent quantum yield (AQY) 76% and 40% at 480 nm and 500 nm for H_2O_2 production, respectively (Figure 1e). By comparison, pristine PCN exhibited negligible activities at the same wavelengths.

Defect engineering also can slightly improve the light absorption. Li et. al [32] and Zhu et. al [81] reported that the UV-vis absorption spectra of g-C_3N_4 and carbon vacancy

functionalized g-C_3N_4 a red shift compared in absorption edges compared with that of pristine ones. Nitrogen vacancies also significantly improves the light absorption [78-80]. Ye and co-workers investigated optical properties of bulk PCN (BCN) and all N-defected CN samples (DCN), as measured by UV–vis absorption spectra [80]. The absorption edges of the photothermally treated g-C_3N_4 samples display ~40 nm redshifts in comparison with the pristine bulk sample [80]. Consistent with these absorption results, the color of the powders suffers a matching variation from yellow to brown as the current output increases. They also revealed that defect states can accommodate the electrons photoexcited from the valence band (VB) of BCN, which greatly contribute to the absorption of photons with energies smaller than the bandgap, promoting to more light harvesting [80].

Compared with the co-polymerization of electron-deficient semiconductor and metal/non-metal doping, the influence of defect engineering is relatively small because defect states usually lies on just below the CBM. In this case, the extent of the narrowing the bandgap by introducing defects is limited. The co-polymerization of electron-deficient semiconductors seems to be the most promising functionalization strategy for both improving the light absorbance and expand the absorption edge.

1.3.3 Introducing the active sites for selective $2e^-$ ORR

Introduction of active sites with specific physicochemical properties can significantly promote both selectivity and activities [84]. In this case, summarizing the strategies for promoting both amount and quality (both activity and selectivity) of active sites for efficient $2e^-$ ORR reaction by based on the PCN materials. To give a systematic review for this topic, three dominate strategies for introducing active sites for photocatalytic H_2O_2 production are presents as follows.

1.3.3.1 Increasing the surface area

The PCN prepared by thermal polymerization method is usually quite small (<15 m^2 g^{-1}) [85]. As previously mentioned, the conjugated heptazine ring in the PCN matrix can provide active sites for $2e^-$ ORR [16]. A plausible strategies for promoting the surface area of PCN so that the active sites can be significantly exposed to the liquid phrase so that the

$2e^-$ ORR can be further improved [69, 86, 87]. However, there is still some conflict for whether increasing the specific surface area of PCN is able to promote overall $2e^-$ ORR rate. Shiraishi and co-workers investigated the photocatalytic production of hydrogen peroxide (H_2O_2) from ethanol (EtOH) and molecular oxygen (O_2) with mesoporous graphitic carbon nitride (GCN) catalysts with different surface areas prepared by silica-templated thermal polymerization of cyanamide (Figure 1-14a) [88]. On these catalysts, the photo formed positive holes oxidize EtOH and the conduction band electrons localized at the 1,4-positions of the melem units promote two-electron reduction of O_2 (H_2O_2 formation). The GCN catalysts with 56 and 160 $m^2\ g^{-1}$ surface areas exhibit higher activity for H_2O_2 production than the catalyst prepared without silica template (surface area: 10 $m^2\ g^{-1}$) [88]. However, the GCN with the largest surface area (228 $m^2\ g^{-1}$) showed significant decreased activity and selectivity for H_2O_2 formation (Figure 1-14b) [88]. The mesoporous GCN with larger surface areas inherently contain a larger number of primary amine moieties at the surface of mesopores [88]. These defects behave as the active sites for $4e^-$ reduction of O_2, thus decreasing the H_2O_2 selectivity (Figure 1-14c) [88]. Furthermore, these defects also behave as the active sites for photocatalytic decomposition of the formed H_2O_2. Results from density function theory (DFT) confirmed that the (i) a large distribution of LUMO electrons onto the primary amine moieties and (ii) the decrease in H_2O_2 selectivity with an increase in the amount of primary amine moiety strongly suggest that the primary amine moieties on the surface of mesopores behave as the active sites for four-electron reduction (Figure 15d-e) [88]. Therefore, it is rational to predict that the GCN catalysts with relatively large surface area but with a small number of surface defects can promote relatively efficient H_2O_2 formation.

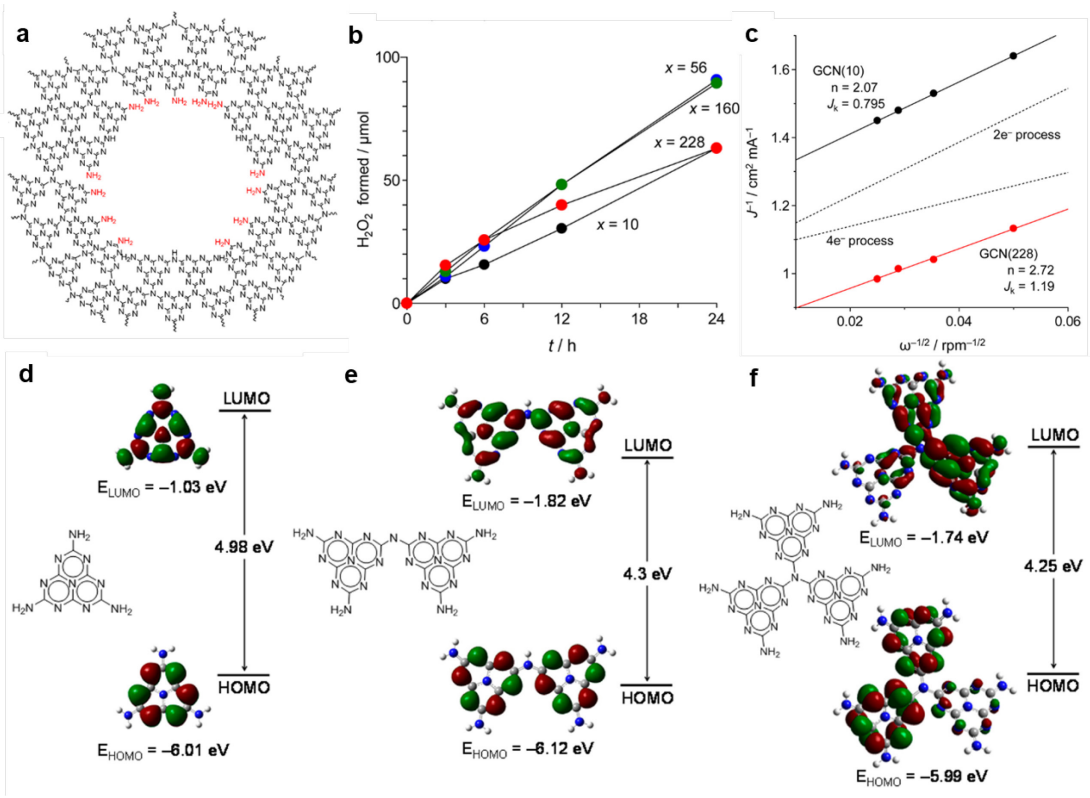

Figure 1-14. Effect of surface area and surface ammonia groups on H_2O_2 production. (a) Different N atoms of PCN [88]. (b) Time-dependent change in the amounts of H_2O_2 during photoreaction on the respective GCN(x) catalysts [88]. (c) Koutecky−Levich plots (at -0.6 V vs. Ag/AgCl). Interfacial plots of main orbitals for (d) single, (e) double, and (f) triple melem-conjugated models, calculated at the DFT level (B3LYP/631G(d)) [88].

1.3.3.2 Copolymerization with electron deficient semiconductors

Copolymerization with electron deficient semiconductors such as PDI, BDI and MTI has been also proved to be one of the most efficient strategies for promoting the selectivity of the photocatalyst [27, 53, 54]. First principle calculations based on the density functional theory (DFT) were performed to clarify the effect of PDI unit on the electronic structure of g-C_3N_4 with simple melem and melem-PDI models (Figure 1-15a) [27]. Their main electronic transitions ($S_0 \rightarrow S_1$) are HOMO→LUMO and HOMO→LUMO+2, respectively. The electrons on both HOMO and LUMO+2 of the melem-PDI model are located mainly at the melem unit with partial distribution to the PDI units [27]. This is reflected by the high electron affinity of PDI unit. The electrons on HOMO are located at the N2 and N6 positions of the melem unit, and those on LUMO+2 are at the C1 and N4 units [27]. The Raman spectra of g-C_3N_4 and g-C_3N_4/PDI confirmed that the side-on adsorption of O_2 were

significantly promoted on the surface of g-C_3N_4/PDI (Figure 1-15b), indicating the crucial role of co-polymerization of electron deficient semiconductors.

1.3.3.3 Doping/Heteroatom incorporation

Incorporation of specific transition metal species in PCN matrix can both improve the charge separation and introduce active sites for ORR [89]. Hu and co-workers fabricated hollow copper doped g-C_3N_4 microspheres through template assisted method. The copper-doped g-C_3N_4 photocatalyst showed much higher H_2O_2 production ability (up to 4.8 mmol·L^{-1}) than bare g-C_3N_4 (0.45 mmol·L^{-1}). DFT simulation further showed that the Cu(I)-N active sites could act not only as chemical adsorption sites to activate molecular O_2 but also as an electron transfer bridge to promote electron transfer from the catalyst to the adsorbed O_2 molecules (Figure 1-15c) [89]. Zhu and co-workers proposed oxygen-enriched carbon nitride polymer (OCN) models, which were proven to more easily produce 1,4-endoperoxide species and have a high selectivity for molecular oxygen reduction to H_2O_2 [70]. According to theoretical calculations, the OCNs had high selectivity for molecular oxygen reduction to H_2O_2 by the accompanied C-O-C group [70]. Choi and co-workers also investigated the electrons on the conjugated rings of S-doped CN can be donated to the antibonding π* orbital of adsorbed $*O_2$ (with −0.40 |e|) through the strong electron pushing effect between oxygen and carbon (1.87 Å, Figure 1-15d), which weakens the O−O bond (1.29 Å) (vs. free O_2 (1.23 Å)) and facilitates subsequent protonation in ORR kinetics [83]. The chemisorption of O_2 on the CN plane should be a prerequisite for highly selective ORR and the introduction of S dopants in the melon unit creates polarized active sites on which O_2 is preferably attracted [83].

1.3.3.4 Cocatalyst loading

Co-catalyst loading is an traditional strategy for introducing the active sites for specific reactions [22]. For instance, pristine PCN show quite low efficiency in photocatalytic hydrogen production, and the loading of the platinum species on the PCN usually significantly improve the HER performance [18]. The reason for loading co-catalyst to boost the photocatalytic reactions usually due to the decreased overpotential of the reactions on the co-catalyst surface compared with that on the pristine photocatalysts [46, 47, 90]. AQ

species could enhances the selectivity of O_2 reduction to H_2O_2, following the mechanism widely exploited in current industrial H_2O_2 production process [91, 92]. Kim and co-workers prepared several AQ modified PCN with significantly improved selectivity for $2e^-$ ORR (Figure 1-15d) [91]. Loading AQ cocatalyst onto ultrathin C_3N_4 improved H_2O_2 production selectivity, resulting in a 1.9-fold enhancement in H_2O_2 production [92]. Several works loaded Au nanoparticles onto the C_3N_4 matrix all showed significantly improve $2e^-$ ORR efficiency [48, 49]. This phenomenon may be attributed to the co-catalytic effects of Au surface on the photocatalytic $2e^-$ ORR, which has been already proved by investigating other photocatalyst and photocathodes.

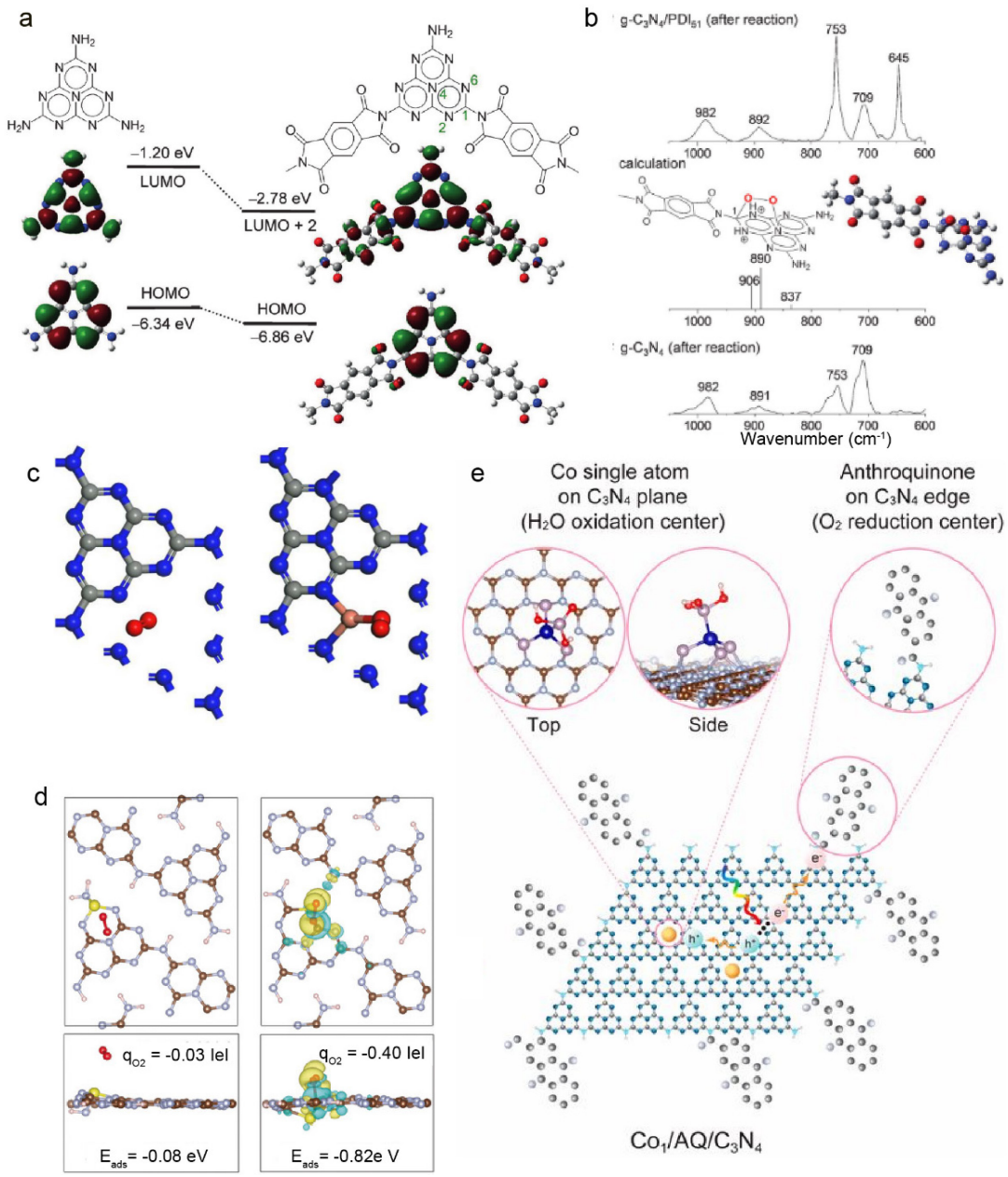

Figure 1-15. Typical strategies for introducing active sites for efficient 2e⁻ ORR. (a) Energy diagrams and interfacial plots of main orbitals for melem (left) and melem-PDI (right) models calculated at the DFT level (B3LYP/6-31g(d)). (b) Raman spectra for (up) fresh g-C_3N_4-PDI_{51} recovered after photoreaction, (middle) Calculated shift for the melem-PDI model and (down) g-C_3N_4 recovered after photoreaction (12 h) in a 2-PrOH solution with O_2. (c) The optimal O_2 adsorption models on GCN (left) and Cu(2)-SCN (right). (d) Top and side views of the structure with different charge densities for O_2 adsorption on C1 site substitution (left), and N2 site substitution (right). E_{ads} and q^{O2} represent the total adsorption energy of O_2 and the accumulated electron charge on O_2, respectively. The yellow and blue colors represent the electron accumulation and depletion at an isosurface value of 0.002 Å e^{-3}. The brown, gray, and yellow colors represent carbon, nitrogen, and sulfur, respectively. (f) Spatial separation of Co single atom (as oxidation center) and AQ (as reduction center) cocatalysts by anchoring them in the center (i.e., pyridinic N) and on

the edge (i.e., primary/secondary amine N) of 2D ultrathin C_3N_4, respectively [92].

In summary, there are two fundamental strategies for introducing active sites for the improved $2e^-$ ORR of PCN-based photocatalyst. One is to manipulate the electronic configurations of the functionalized PCN catalyst so that the selectivity and activity of π-conjugated heptazine ring for boosting H_2O_2 production could be significantly promoted. Similar strategies could be also found in some other carbon based materials for promoting the selective H_2O_2 production. However, the nature of this sort active sites is the side-on adsorption of oxygen [88], which might result in un-expected splitting of O-O, thus leading to the possible $4e^-$ ORR process and a limited selectivity for $2e^-$ ORR [93, 94]. The other one is to introduce active sites beyond the π-conjugated heptazine ring for selective $2e^-$ ORR. Up to now, only few co-catalyst is developed for selective ORR (Section 3.3.4). Further development of $2e^-$ ORR sites beyond the π-conjugated heptazine rings may overcome the disadvantage of side-on O_2 adsorption and shed light on the further improvement for H_2O_2 production.

1.4 Other influence factors for boosting photocatalytic efficiency for H_2O_2 production

1.4.1 Adding electron donors or not

The sacrificial regents are commonly used to consume the photogenerated electrons or holes so that one half of reaction could be significantly boosted [95]. In case of g-C_3N_4 based photocatalysts, most of the researchers used electron donors so that the reduction reactions could be maximized during in a certain photocatalytic system since the electron donor hindered the photogenerated electron from recombining with holes [96, 97]. Up to data, g-C_3N_4 has shown promising prospect in catalysing several photochemical reductions reactions with the electron donors, such as HER, NRR, CRR and ORR [98]. The reason may as follows: CBM of pristine PCN (-1.3 V) is quite negative, significantly larger the redox potential of HER, NRR, CRR and $2e^-$ ORR (0.695 V vs. SHE) [96]. Combined with the merits that the side-on O_2 adsorption on the melem units (forming 1-4 endoperoxide species) as an acceptable $2e^-$ reduction sites, PCN satisfied thermodynamic potential for H_2O_2 production via $2e^-$ ORR with the existence of alcohols. However, green and sustainable process for photocatalytic H_2O_2 synthesis requires the use of earth-

abundant water in place of alcohol, i. e., the water oxidation reaction instead of alcohol oxidation should occur for hole consumption. H_2O_2 can therefore be synthesized from water and O_2 sunlight irradiation with 100% atom efficiency.

There are several literatures systematically discussed the mechanisms for the photoreduction reactions by using g-C_3N_4 [96]. Since the functions of electron donors has been clarified in these works, we shall focus on the crucial properties and functionalization strategies for achieving the H_2O_2 production with water and oxygen. Typically, the oxygen evolution reaction (OER) from is a $4e^-$ reaction usually need to overcome the large overpotential. In this case, VBMs of photocatalysts for OER usually have quite positive potentials ($VBM_{TiO2\text{-}rutile}$ ~2.9 V vs. SHE, VBM_{BiVO4}~ 2.53 V) [23, 46]. As shown in Figure 1-16a, pristine PCN is, however, unsuccessful for H_2O_2 from water to oxygen because the top of the valence band (VB) lies at approximately 1.4 V, which show insufficient thermodynamic driving force for OER via water oxidation (ca. 0.8 V versus RHE, pH 7) [27]. To overcome this obstacle, band engineering and co-catalyst are two effective strategies.

The bandgap position of PCN can be easily manipulated by functionalization. Shiraishi and co-works successfully manipulate the band positions of PCN-based photocatalyst by copolymerized melamine with electron-deficient aromatic diimide [16, 27, 40, 53, 54]. The valence band of as-prepared co-polymerized PCN is about 1.8~2.4 V (vs. NHE). Taking g-C_3N_4/PDI as an example, the time-dependent change in the amounts of H_2O_2 formed on the respective catalysts revealed the significant roles of band engineering (Figure 1-16b). Pristine g-C_3N_4 (VBM = 1.40 V vs. NHE) scarcely produces H_2O_2, and g-C_3N_4/BDI51 (VBM = 1.86 V vs. NHE) produces 31 μmol H_2O_2 after the photocatalytic reaction for 48 h [54]. g-C_3N_4/BDI50 (VBM = 1.83 V vs. NHE) shows even higher: the amount of H_2O_2 formed is 41 μmol (1.4 mM). The rates of H_2O_2 formation on both catalysts are almost constant; the catalysts stably produce H_2O_2 without loss of activity and scarcely decompose the H_2O_2 formed in this concentration range [54]. With the addition of electron acceptors, O_2 can be detected by GC, which further confirmed that the water oxidation to generate oxygen consumed the generated holes during the photocatalytic reactions [54]. The activity of the g-C_3N_4/PDI-rGO photocatalyst could be further improved by introducing boron nitride (BN)

due to spatial separation of e^- and h^+ onto rGO and BN, respectively (Figure 1-10a) [52]. Additionally, preparation of POWs incorporated semiconductors with ideal electronic configurations and band positions also played similar roles for boosting the OER, which successfully achieved the H_2O_2 production via ORR and WOR (Figure 17c) [38, 72-74].

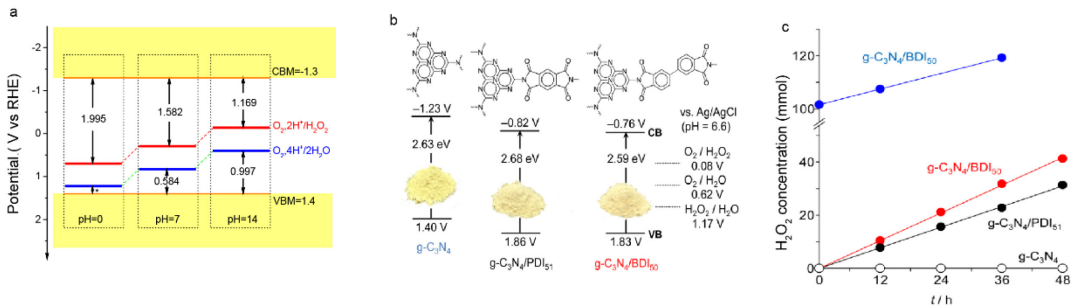

Figure 1-16. Typical strategies for preparation of g-C_3N_4 based catalyst for photocatalytic H_2O_2 production with water and O_2. (a) The real hydrogen electrode potential of $2e^-$ ORR and $4e^-$ WOR compared with the band diagram of PCN. (b) Electronic band structures of pristine PCN and g-C_3N_4/BDI_x. (c) Change in the amounts of H_2O_2 formed during photoreaction with respective catalysts. The irradiance at 420−500 nm is 27.3 W m^{-2}. Blue points show the results of photoreaction with water containing ca. 100 μmol of H_2O_2.

The other strategies for improving the OER activity of PCN is loading co-catalyst or OERs. More recently, Chu and co-workers has prepared single-atom dispersed Co as co-catalyst for water oxidation [92]. The X-ray absorption fine-structure spectroscopy (FT-EXAFS) showed that the oxidation state of the Co single atoms coordinated by P atoms is close to +2 [91]. Loading Co single atoms significantly enhanced C_3N_4 for water oxidation ($2H_2O \rightarrow O_2+4H^++4e^-$), as indicated by an 8.4-fold enhancement on 4-h O_2 evolution. The P-coordinated Co are all close to +2 both show high photocatalytic OER activities, indicating that the unique electronic configuration of Co(II)-P may provide active sites for OER during the solar H_2O_2 synthesis [92]. It is worthy to noting that the VBM of this single-atom dispersed Co dispersed PCN (~1.4 V vs. SHE) [92], quite close to that of PCN, is significantly more nagetive compared with that of metal oxides (>2.3 V vs. SHE). Thus, the Co(II)-P single atomic sites may significantly boosted the kinetics process of water oxidation.

In summary, accelerating the photocatalytic oxygen evolution reaction by using PCN-

based photocatalyst is the most crucial challenge for achieving photocatalytic H_2O_2 production with water and O_2. Band engineering and loading co-catalyst for OER may respectively improve the oxidation potential and promote the kinetics for $4e^-$ OER.

1.4.2 pH value of solution

The light-driven $2e^-$ WOR pathway is difficult to be achieved because of the uphill thermodynamics (1.76 V vs. NHE), i.e. the as-synthesized H_2O_2 will decompose at this highly oxidative potential because H_2O_2 could work also as a hole scavenger [98]. Therefore, the discussion on the pH value for $2e^-$ ORR pathway are of great importance. To data, substantial efforts has been devoted to the $2e^-$ ORR concept have aimed at high-yield production of H_2O_2 in basic, neutral, and acidic media [28, 29, 99]. The acid dissociation constant of H_2O_2 ($H_2O_2 \leftrightarrow H^+ + HO_2^-$, $K_a = \frac{[H^+][HO_2^-]}{[H_2O_2]}$, p$K_a$ = 11.7) suggests that the main form of H_2O_2 would be HO_2^- in alkaline water solution (pH > 11.7). Alkaline H_2O_2 are widely used in the pulp bleaching industry. However, the production of H_2O_2 in basic media has several limitations: (1) H_2O_2 is less stable and can self-decompose in alkaline condition (especially at pH > 9), thus it needs to be consumed timely [100]; (2) H_2O_2 is more widely used in natural or acidic media with stronger oxidation ability than in alkaline solution. For instance, Fenton's reagent that is widely used in effluent treatment and organic synthesis has a favorable pH range of 2.5–3.5 [101]. Therefore, improving H_2O_2 production in acidic or neutral media by photocatalysts has attracted great industrial attention. Over the past years, although various g-C_3N_4 catalysts have been developed for H_2O_2 production via the $2e^-$ ORR process (Figure 1-17a) [27], very few work has discussed the optimized pH conditions.

Kim and co-workers found that the photocatalytic activity was higher at lower pH because the production of H_2O_2 needs protons (Figure 18b) with the existence of electron donor. Comparing the photocatalytic activities between pH 3 and 1, it is noted that the activity of bare CN was more sensitively affected by pH than that of KPF_CN [64]. When pH 3 was lowered to pH 1, the production of H_2O_2 was enhanced more than 4 times with bare CN but only 1.1 times with KPF_CN [64]. This is probably because the proton conduction within the CN framework is much more facilitated in KPF_CN. The presence of

PF_6^- anions in the KPF_CN structure might enhance proton conduction through electrostatic interaction [64]. The higher charge carrier density in KPF_CN should be a favorable condition for facilitated proton conduction as well. The higher proton conductivity within the KPF_CN framework should favor the production of H_2O_2, particularly when the reaction between O_2 and protons occurs within the interlayer space. In this case, the overall production of H_2O_2 should be much less affected by pH. Although there is only few works discussed the influence of pH on the generated amount of H_2O_2, the pH value did play an essential role during the photosynthesis process. We believe that systematic investigations of the pH influence on the amount of H_2O_2, surface properties and electronic configurations should be investigated to reveal the mechanism of ORR and WOR during the photosynthesis of H_2O_2.

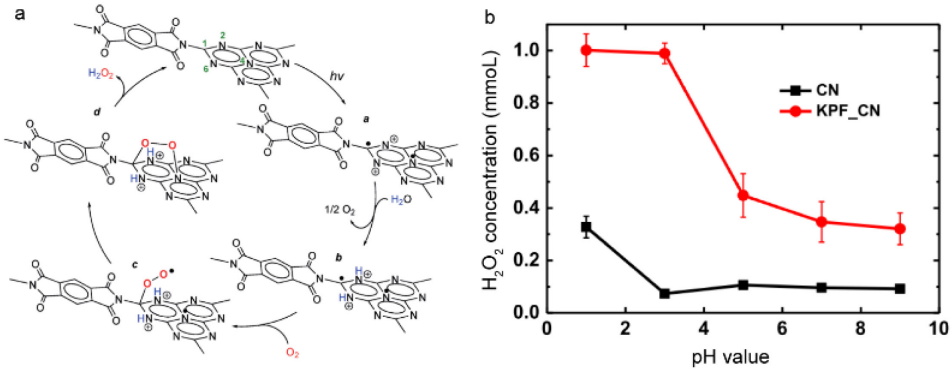

Figure 1-17. Influence of pH values during the H_2O_2 production by using PCN based photocatalyst. (a) Schematic diagram of the function of protons during the H_2O_2 production. (b) H_2O_2 production in the irradiated suspension of bare CN and KPF_CN_15 at different pHs.

1.5 Summary

Photocatalytic H_2O_2 production by using PCN based material has showed a promising prospective in environmental and energy-related realms. However, the current PCN based still suffer from the relatively low H_2O_2 yield, which are far from the requirements of industrially practical applications. The lower response to sunlight, high recombination rate of photogenerated species, low selectivity of two-electron reduction O_2 over $1e^-$ or $4e^-$ reduction of O_2. Improving the charge separation, transfer and migration, promoting the light absorption and introducing the active sites for $2e^-$ ORR to suppress the side reaction

are three attractive strategies for boosting the activities. Followed by these strategies, the most representative functionalization method is summarized based on the most desired properties for improving the photocatalytic activities for H_2O_2 production. Additionally, other influence factors for improving the H_2O_2 are also reviewed, such as adding of electron donors and pH value of the solution.

1.6 Research purpose

(1) Improving the light harvesting and charge separation, transfer and migration properties of PCN based material so that the ORR efficiency on melem units could be significantly boosted. With the co-catalyst (OER) loading, the half reaction of the H_2O_2 production for hole consuming could be accelerated, thus leading to a further improved H_2O_2 production.

(2) Seeking the other appropriate ORR sites beyond melem based on the time-dependent density function theory. Although melem sites could be serve as side-on adsorption sites for $2e^-$ ORR reaction, the configuration of side-on adsorption show some activities for 4 e^- ORR activities. The charge separation properties of the active sites in PCN skeleton could give a primary guideline for seeking the new efficient ORR sites for H_2O_2 production.

(3) Preparing the most efficient single-atom catalyst based on the theoretical guideline. After exploring the mechanism of the photocatalytic H_2O_2 production of the as-prepared single-atom photocatalyst, the principle relationships between experimental activity and simulated properties could be clarified.

References

[1] C.W. Jones, Applications of hydrogen peroxide and derivatives, Royal Society of Chemistry, (1999). ISSN: 978-0-85404-536-5.

[2] L. Pesterfield, The 100 most important chemical compounds: A reference guide (by Richard L. Myers), J Chem Educ, 86 (2009) 1182. https://doi.org/10.1021/ed086p1182.

[3] G. McDonnell, The use of hydrogen peroxide for disinfection and sterilization applications, PATAI'S Chemistry of Functional Groups, (2014) 1-34. https://doi.org/10.1002/9780470682531.pat0885.

[4] Z. Teng, N. Yang, H. Lv, S. Wang, M. Hu, C. Wang, D. Wang, G. Wang, Edge-functionalized g-C_3N_4 nanosheets as a highly efficient metal-free photocatalyst for safe drinking water, Chem, 5 (2019) 664-680. https://doi.org/10.1016/j.chempr.2018.12.009.

[5] W. Zhan, L. Ji, Z.-m. Ge, X. Wang, R.-t. Li, A continuous-flow synthesis of primary amides from hydrolysis of nitriles using hydrogen peroxide as oxidant, Tetrahedron, 74 (2018) 1527-1532. https://doi.org/10.1016/j.tet.2018.02.017.
[6] M.-h. Zhang, H. Dong, L. Zhao, D.-x. Wang, D. Meng, A review on Fenton process for organic wastewater treatment based on optimization perspective, Sci. Total Environ., 670 (2019) 110-121. https://doi.org/10.1016/j.scitotenv.2019.03.180.
[7] S.A. Mousavi Shaegh, N.-T. Nguyen, S.M. Mousavi Ehteshami, S.H. Chan, A membraneless hydrogen peroxide fuel cell using Prussian Blue as cathode material, Energy Environ. Sci., 5 (2012) 8225-8228. http://doi.org/10.1039/C2EE21806B.
[8] D. Kim, K.K. Sakimoto, D. Hong, P. Yang, Artificial photosynthesis for sustainable fuel and chemical production, Angew. Chem. Int. Ed., 54 (2015) 3259-3266. https://doi.org/10.1002/anie.201409116.
[9] Yusuke Yamada, Masaki Yoneda, S. Fukuzumi, A robust one-compartment fuel cell with a polynuclear cyanide complex as a cathode for utilizing H_2O_2 as a sustainable fuel at ambient conditions, Chem. Eur. J, 19 (2013) 11733 – 11741. https://doi.org/10.1002/chem.201300783.
[10] J.M. Campos-Martin, G. Blanco-Brieva, J.L.G. Fierro, Hydrogen peroxide synthesis: An outlook beyond the anthraquinone process, Angew. Chem. Int. Ed., 45 (2006) 6962-6984. https://doi.org/10.1002/anie.200503779.
[11] Y. Yi, L. Wang, G. Li, H. Guo, A review on research progress in the direct synthesis of hydrogen peroxide from hydrogen and oxygen: Noble-metal catalytic method, fuel-cell method and plasma method, Catal. Sci. Technol., 6 (2016) 1593-1610. http://dx.doi.org/10.1039/C5CY01567G.
[12] H. Miao, Z. Teng, S. Wang, L. Xu, C. Wang, H. Chong, Recent advances in the disinfection of water using nanoscale antimicrobial materials, Adv. Mater. Technol., 4 (2019) 1800213. https://doi.org/10.1002/admt.201800213.
[13] C. Xia, Y. Xia, P. Zhu, L. Fan, H. Wang, Direct electrosynthesis of pure aqueous H_2O_2 solutions up to 20% by weight using a solid electrolyte, Science, 366 (2019) 226. https://doi.org/10.1126/science.aay1844.
[14] S.J. Freakley, Q. He, J.H. Harrhy, L. Lu, D.A. Crole, D.J. Morgan, E.N. Ntainjua, J.K. Edwards, A.F. Carley, A.Y. Borisevich, C.J. Kiely, G.J. Hutchings, Palladium-tin catalysts for the direct synthesis of H_2O_2 with high selectivity, Science, 351 (2016) 965. https://doi.org/10.1126/science.aad5705.
[15] H. Hou, X. Zeng, X. Zhang, Production of hydrogen peroxide by photocatalytic processes: A critical review of recent advances, Angew. Chem. Int. Ed., n/a (2019). https://doi.org/10.1002/anie.201911609.
[16] Y. Shiraishi, S. Kanazawa, Y. Sugano, D. Tsukamoto, H. Sakamoto, S. Ichikawa, T. Hirai, Highly selective production of hydrogen peroxide on graphitic carbon nitride (g-C_3N_4) photocatalyst activated by visible light, ACS Catal., 4 (2014) 774-780. https://doi.org/10.1021/cs401208c.
[17] A. Torres-Pinto, M.J. Sampaio, C.G. Silva, J.L. Faria, A. M. T. Silva, Recent strategies for hydrogen peroxide production by metal-free carbon nitride photocatalysts, Catalysts, 9 (2019). http://doi.org/10.3390/catal9120990.
[18] Q. Wang, K. Domen, Particulate photocatalysts for light-driven water splitting:

Mechanisms, challenges, and design strategies, Chem. Rev., 120 (2020) 919-985. https://doi.org/10.1021/acs.chemrev.9b00201.
[19] A. Dhakshinamoorthy, S. Navalon, A. Corma, H. Garcia, Photocatalytic CO_2 reduction by TiO_2 and related titanium containing solids, Energy Environ. Sci., 5 (2012) 9217-9233. https://doi.org/10.1039/C2EE21948D.
[20] W.S. Koe, J.W. Lee, W.C. Chong, Y.L. Pang, L.C. Sim, An overview of photocatalytic degradation: Photocatalysts, mechanisms, and development of photocatalytic membrane, Environ. Sci. Pollut. Res., 27 (2020) 2522-2565. https://doi.org/10.1007/s11356-019-07193-5.
[21] D. Friedmann, A. Hakki, H. Kim, W. Choi, D. Bahnemann, Heterogeneous photocatalytic organic synthesis: State-of-the-art and future perspectives, Green Chem., 18 (2016) 5391-5411. https://doi.org/10.1039/C6GC01582D.
[22] Yoshio Nosaka, A. Nosaka, Introduction to photocatalysis: From basic science to applications, Royal Society of Chemistry, (2016). ISSN: 978-1-78262-320-5.
[23] W. Fan, B. Zhang, X. Wang, W. Ma, D. Li, Z. Wang, M. Dupuis, J. Shi, S. Liao, C. Li, Efficient hydrogen peroxide synthesis by metal-free polyterthiophene via photoelectrocatalytic dioxygen reduction, Energy Environ. Sci., 13 (2020) 238-245. https://doi.org/10.1039/C9EE02247C.
[24] X. Shi, S. Siahrostami, G.-L. Li, Y. Zhang, P. Chakthranont, F. Studt, T.F. Jaramillo, X. Zheng, J.K. Nørskov, Understanding activity trends in electrochemical water oxidation to form hydrogen peroxide, Nat. Commun., 8 (2017) 701. https://doi.org/10.1038/s41467-017-00585-6.
[25] X. Wang, K. Maeda, A. Thomas, K. Takanabe, G. Xin, J.M. Carlsson, K. Domen, M. Antonietti, A metal-free polymeric photocatalyst for hydrogen production from water under visible light, Nat. Mater., 8 (2009) 76-80. https://doi.org/10.1038/nmat2317.
[26] W.-J. Ong, L.-L. Tan, Y.H. Ng, S.-T. Yong, S.-P. Chai, Graphitic carbon nitride (g-C_3N_4)-based photocatalysts for artificial photosynthesis and environmental remediation: Are we a step closer to achieving sustainability?, Chem. Rev., 116 (2016) 7159-7329. https://doi.org/10.1021/acs.chemrev.6b00075.
[27] Y. Shiraishi, S. Kanazawa, Y. Kofuji, H. Sakamoto, S. Ichikawa, S. Tanaka, T. Hirai, Sunlight-driven hydrogen peroxide production from water and molecular oxygen by metal-free photocatalysts, Angew. Chem. Int. Ed., 53 (2014) 13454-13459. https://doi.org/10.1002/anie.201407938.
[28] H.W. Kim, M.B. Ross, N. Kornienko, L. Zhang, J. Guo, P. Yang, B.D. McCloskey, Efficient hydrogen peroxide generation using reduced graphene oxide-based oxygen reduction electrocatalysts, Nat. Catal., 1 (2018) 282-290. https://doi.org/10.1038/s41929-018-0044-2.
[29] Z. Lu, G. Chen, S. Siahrostami, Z. Chen, K. Liu, J. Xie, L. Liao, T. Wu, D. Lin, Y. Liu, T.F. Jaramillo, J.K. Nørskov, Y. Cui, High-efficiency oxygen reduction to hydrogen peroxide catalysed by oxidized carbon materials, Nat. Catal., 1 (2018) 156-162. https://doi.org/10.1038/s41929-017-0017-x.
[30] F.K. Kessler, Y. Zheng, D. Schwarz, C. Merschjann, W. Schnick, X. Wang, M.J. Bojdys, Functional carbon nitride materials — design strategies for electrochemical devices, Nat. Rev. Mater., 2 (2017) 17030. https://doi.org/10.1038/natrevmats.2017.30.

[31] Banerjee, T., Podjaski, F., Kröger, J. et al. Polymer photocatalysts for solar-to-chemical energy conversion. Nat Rev Mater, (2020). https://doi.org/10.1038/s41578-020-00254-z.
[32] S. Li, G. Dong, R. Hailili, L. Yang, Y. Li, F. Wang, Y. Zeng, C. Wang, Effective photocatalytic H_2O_2 production under visible light irradiation at g-C_3N_4 modulated by carbon vacancies, Appl. Catal. B, 190 (2016) 26-35. https://doi.org/10.1016/j.apcatb.2016.03.004.
[33] S. Yang, A. Verdaguer-Casadevall, L. Arnarson, L. Silvioli, V. Čolić, R. Frydendal, J. Rossmeisl, I. Chorkendorff, I.E.L. Stephens, Toward the decentralized electrochemical production of H_2O_2: A focus on the catalysis, ACS Catalysis, 8 (2018) 4064-4081. https://doi.org/10.1021/acscatal.8b00217.
[34] G.-h. Moon, W. Kim, A.D. Bokare, N.-e. Sung, W. Choi, Solar production of H_2O_2 on reduced graphene oxide–TiO_2 hybrid photocatalysts consisting of earth-abundant elements only, Energ Environ Sci, 7 (2014) 4023-4028. https://doi/org/10.1039/C4EE02757D.
[35] S. Thakur, T. Kshetri, N.H. Kim, J.H. Lee, Sunlight-driven sustainable production of hydrogen peroxide using a CdS–graphene hybrid photocatalyst, J Catal, 345 (2017) 78-86. https://doi.org/10.1016/j.jcat.2016.10.028.
[36] X. Zeng, Z. Wang, N. Meng, D.T. McCarthy, A. Deletic, J.-h. Pan, X. Zhang, Highly dispersed TiO_2 nanocrystals and carbon dots on reduced graphene oxide: Ternary nanocomposites for accelerated photocatalytic water disinfection, Appl. Catal. B, 202 (2017) 33-41. https://doi.org/10.1016/j.apcatb.2016.09.014.
[37] L. Zheng, J. Zhang, Y.H. Hu, M. Long, Enhanced photocatalytic production of H_2O_2 by nafion coatings on S,N-codoped graphene-quantum-dots-modified TiO_2, J. Phys. Chem. C, 123 (2019) 13693-13701. https://doi.org/10.1021/acs.jpcc.9b02311.
[38] D. Tasis, N. Tagmatarchis, A. Bianco, M. Prato, Chemistry of carbon nanotubes, Chem. Rev., 106 (2006) 1105-1136. https://doi.org/10.1021/cr050569o.
[39] S. Zhao, T. Guo, X. Li, T. Xu, B. Yang, X. Zhao, Carbon nanotubes covalent combined with graphitic carbon nitride for photocatalytic hydrogen peroxide production under visible light, Applied Catalysis B: Environmental, 224 (2018) 725-732. https://doi.org/10.1016/j.apcatb.2017.11.005.
[40] Y. Kofuji, Y. Isobe, Y. Shiraishi, H. Sakamoto, S. Tanaka, S. Ichikawa, T. Hirai, Carbon nitride–aromatic diimide–graphene nanohybrids: Metal-free photocatalysts for solar-to-hydrogen peroxide energy conversion with 0.2% efficiency, J. Am. Chem. Soc., 138 (2016) 10019-10025. https://doi.org/10.1021/jacs.6b05806.
[41] I.F. Teixeira, E.C.M. Barbosa, S.C.E. Tsang, P.H.C. Camargo, Carbon nitrides and metal nanoparticles: From controlled synthesis to design principles for improved photocatalysis, Chem. Soc. Rev., 47 (2018) 7783-7817. https://doi.org/10.1039/C8CS00479J.
[42] Z. Zhang, J.T. Yates, Band bending in semiconductors: Chemical and physical consequences at surfaces and interfaces, Chem. Rev., 112 (2012) 5520-5551. https://doi.org/10.1021/cr3000626.
[43] X. Li, C. Chen, J. Zhao, Mechanism of photodecomposition of H_2O_2 on TiO_2 surfaces under visible light irradiation, Langmuir, 17 (2001) 4118-4122. https://doi.org/10.1021/la010035s.
[44] S. Wang, Z. Teng, Y. Xu, M. Yuan, Y. Zhong, S. Liu, C. Wang, G. Wang, T. Ohno, Defect

as the essential factor in engineering carbon-nitride-based visible-light-driven Z-scheme photocatalyst, Appl. Catal. B, 260 (2020) 118145. https://doi.org/10.1016/j.apcatb.2019.118145.
[45] Q. Li, Research progress on highly efficient visible-light-activated photocatalysts with post-illumination photocatalytic "memory" effect, Institute of Metal Research Chinese Academy of Sciences, (2009). URL: http://english.imr.cas.cn/research/researchprogress/201603/t20160304_160260.html.
[46] H. Hirakawa, S. Shiota, Y. Shiraishi, H. Sakamoto, S. Ichikawa, T. Hirai, Au nanoparticles supported on $BiVO_4$: Effective inorganic photocatalysts for H_2O_2 production from water and O_2 under visible light, ACS Catal., 6 (2016) 4976-4982. https://doi.org/10.1021/acscatal.6b01187.
[47] D. Tsukamoto, A. Shiro, Y. Shiraishi, Y. Sugano, S. Ichikawa, S. Tanaka, T. Hirai, Photocatalytic H_2O_2 production from ethanol/O_2 system using TiO_2 loaded with Au–Ag bimetallic alloy nanoparticles, ACS Catal., 2 (2012) 599-603. https://doi.org/10.1021/acscatal.5b00408.
[48] X. Chang, J. Yang, D. Han, B. Zhang, X. Xiang, J. He, Enhancing light-driven production of hydrogen peroxide by anchoring Au onto C_3N_4 catalysts, Catalysts, 8 (2018). http://doi.org/10.3390/catal8040147.
[49] G. Zuo, S. Liu, L. Wang, H. Song, P. Zong, W. Hou, B. Li, Z. Guo, X. Meng, Y. Du, T. Wang, V.A.L. Roy, Finely dispersed Au nanoparticles on graphitic carbon nitride as highly active photocatalyst for hydrogen peroxide production, Catal Commun, 123 (2019) 69-72. https://doi.org/10.1016/j.catcom.2019.02.011.
[50] D.D.L. Chung, Carbon materials: Science and applications, MRS Bull., 44 (2019) 661-662. https://doi.org/10.1557/mrs.2019.196.
[51] X. Jiang, P. Wang, J. Zhao, 2D covalent triazine framework: A new class of organic photocatalyst for water splitting, J. Mater. Chem., 3 (2015) 7750-7758. https://doi.org/10.1039/C4TA03438D.
[52] Y. Kofuji, Y. Isobe, Y. Shiraishi, H. Sakamoto, S. Ichikawa, S. Tanaka, T. Hirai, Hydrogen peroxide production on a carbon nitride–boron nitride-reduced graphene oxide hybrid photocatalyst under visible light, ChemCatChem, 10 (2018) 2070-2077. https://doi.org/10.1002/cctc.201701683.
[53] Y. Kofuji, S. Ohkita, Y. Shiraishi, H. Sakamoto, S. Ichikawa, S. Tanaka, T. Hirai, Mellitic triimide-doped carbon nitride as sunlight-driven photocatalysts for hydrogen peroxide production, ACS Sustain. Chem. Eng., 5 (2017) 6478-6485. https://doi.org/10.1021/acssuschemeng.7b00575.
[54] Y. Kofuji, S. Ohkita, Y. Shiraishi, H. Sakamoto, S. Tanaka, S. Ichikawa, T. Hirai, Graphitic carbon nitride doped with biphenyl diimide: Efficient photocatalyst for hydrogen peroxide production from water and molecular oxygen by sunlight, ACS Catal., 6 (2016) 7021-7029. https://doi.org/10.1021/acscatal.6b02367.
[55] Z. Teng, W. Cai, S. Liu, C. Wang, Q. Zhang, S. Chenliang, T. Ohno, Bandgap engineering of polymetric carbon nitride copolymerized by 2,5,8-triamino-tri-s-triazine (melem) and barbituric acid for efficient nonsacrificial photocatalytic H_2O_2 production, Appl. Catal. B, 271 (2020) 118917. https://doi.org/10.1016/j.apcatb.2020.118917.
[56] L. Yang, G. Dong, D.L. Jacobs, Y. Wang, L. Zang, C. Wang, Two-channel

photocatalytic production of H_2O_2 over g-C_3N_4 nanosheets modified with perylene imides, J Catal., 352 (2017) 274-281. https://doi.org/10.1016/j.jcat.2017.05.010.
[57] X. Liu, R. Ma, L. Zhuang, B. Hu, J. Chen, X. Liu, X. Wang, Recent developments of doped g-C_3N_4 photocatalysts for the degradation of organic pollutants, Crit. Rev. Environ. Sci. Technol., (2020) 1-40. https://doi.org/10.1080/10643389.2020.1734433.
[58] C. Qiu, Y. Xu, X. Fan, D. Xu, R. Tandiana, X. Ling, Y. Jiang, C. Liu, L. Yu, W. Chen, C. Su, Highly crystalline K-intercalated polymeric carbon nitride for visible-light photocatalytic alkenes and alkynes deuterations, Adv. Sci., 6 (2018) 1801403-1801403. https://pubmed.ncbi.nlm.nih.gov/30643725.
[59] S. Sun, J. Li, J. Cui, X. Gou, Q. Yang, Y. Jiang, S. Liang, Z. Yang, Simultaneously engineering K-doping and exfoliation into graphitic carbon nitride (g-C_3N_4) for enhanced photocatalytic hydrogen production, Int. J. Hydrog. Energy, 44 (2019) 778-787. https://doi.org/10.1016/j.ijhydene.2018.11.019.
[60] S. Wang, J. Zhan, K. Chen, A. Ali, L. Zeng, H. Zhao, W. Hu, L. Zhu, X. Xu, Potassium-doped g-C_3N_4 achieving efficient visible-light-driven CO_2 Reduction, ACS Sustain. Chem. Eng., 8 (2020) 8214-8222. https://doi.org/10.1021/acssuschemeng.0c01151.
[61] X. Li, X. Sun, L. Zhang, S. Sun, W. Wang, Efficient photocatalytic fixation of N_2 by KOH-treated g-C_3N_4, J. Mater. Chem., 6 (2018) 3005-3011. https://doi.org/10.1039/C7TA09762J.
[62] G.-h. Moon, M. Fujitsuka, S. Kim, T. Majima, X. Wang, W. Choi, Eco-friendly photochemical production of H_2O_2 through O_2 reduction over carbon nitride frameworks incorporated with multiple heteroelements, ACS Catal., 7 (2017) 2886-2895. https://doi.org/10.1021/acscatal.6b03334.
[63] J. Chunlong Zhang, LinMa, YangLv, FeiWang, Xiaoxin Zhang, XingzhouYuan, Shaozheng Hu, Synthesis of halogen doped graphite carbon nitride nanorods with outstanding photocatalytic H_2O_2 production ability via saturated $NH4_X$ (X = Cl, Br) solution-hydrothermal post-treatmen, Diam. Relat. Mater., 87 (2018) 215-222. https://doi.org/10.1016/j.diamond.2018.06.013.
[64] S. Kim, G.-h. Moon, H. Kim, Y. Mun, P. Zhang, J. Lee, W. Choi, Selective charge transfer to dioxygen on KPF_6-modified carbon nitride for photocatalytic synthesis of H_2O_2 under visible light, J Catal, 357 (2018) 51-58. https://doi.org/10.1016/j.jcat.2017.10.002.
[65] P. Zhang, D. Sun, A. Cho, S. Weon, S. Lee, J. Lee, J.W. Han, D.-P. Kim, W. Choi, Modified carbon nitride nanozyme as bifunctional glucose oxidase-peroxidase for metal-free bioinspired cascade photocatalysis, Nat. Commun., 10 (2019) 940. https://doi.org/10.1038/s41467-019-08731-y.
[66] F. Wei, Y. Liu, H. Zhao, X. Ren, J. Liu, T. Hasan, L. Chen, Y. Li, B.-L. Su, Oxygen self-doped g-C_3N_4 with tunable electronic band structure for unprecedentedly enhanced photocatalytic performance, Nanoscale, 10 (2018) 4515-4522. https://doi.org/10.1039/C7NR09660G.
[67] K. Wang, Q. Li, B. Liu, B. Cheng, W. Ho, J. Yu, Sulfur-doped g-C_3N_4 with enhanced photocatalytic CO_2-reduction performance, Appl. Catal. B, 176-177 (2015) 44-52. https://doi.org/10.1016/j.apcatb.2015.03.045.
[68] M. Bellardita, E.I. García-López, G. Marcì, I. Krivtsov, J.R. García, L. Palmisano, Selective photocatalytic oxidation of aromatic alcohols in water by using P-doped g-C_3N_4,

Appl. Catal. B, 220 (2018) 222-233. https://doi.org/10.1016/j.apcatb.2017.08.033.
[69] M.A. Mohamed, M.F. M. Zain, L. Jeffery Minggu, M.B. Kassim, N.A. Saidina Amin, W.N. W. Salleh, M.N.I. Salehmin, M.F. Md Nasir, Z.A. Mohd Hir, Constructing bio-templated 3D porous microtubular C-doped g-C_3N_4 with tunable band structure and enhanced charge carrier separation, Appl. Catal. B, 236 (2018) 265-279. https://doi.org/10.1016/j.apcatb.2018.05.037.
[70] Z. Wei, M. Liu, Z. Zhang, W. Yao, H. Tan, Y. Zhu, Efficient visible-light-driven selective oxygen reduction to hydrogen peroxide by oxygen-enriched graphitic carbon nitride polymers, Energ Environ Sci, 11 (2018) 2581-2589. https://doi.org/10.1039/C8EE01316K.
[71] X.-B. Han, Y.-G. Li, Z.-M. Zhang, H.-Q. Tan, Y. Lu, E.-B. Wang, Polyoxometalate-based nickel clusters as visible light-driven water oxidation catalysts, J. Am. Chem. Soc., 137 (2015) 5486-5493. https://doi.org/10.1021/jacs.5b01329.
[72] S. Zhao, X. Zhao, H. Zhang, J. Li, Y. Zhu, Covalent combination of polyoxometalate and graphitic carbon nitride for light-driven hydrogen peroxide production, Nano Energy, 35 (2017) 405-414. https://doi.org/10.1016/j.nanoen.2017.04.017.
[73] S. Zhao, X. Zhao, Insights into the role of singlet oxygen in the photocatalytic hydrogen peroxide production over polyoxometalates-derived metal oxides incorporated into graphitic carbon nitride framework, Appl. Catal. B, 250 (2019) 408-418. https://doi.org/10.1016/j.apcatb.2019.02.031.
[74] S. Zhao, X. Zhao, S. Ouyang, Y. Zhu, Polyoxometalates covalently combined with graphitic carbon nitride for photocatalytic hydrogen peroxide production, Catal. Sci. Technol., 8 (2018) 1686-1695. http://dx.doi.org/10.1039/C8CY00043C.
[75] Z. Pei, L. Ding, J. Hu, S. Weng, Z. Zheng, M. Huang, P. Liu, Defect and its dominance in ZnO films: A new insight into the role of defect over photocatalytic activity, Appl. Catal. B, 142-143 (2013) 736-743. https://doi.org/10.1016/j.apcatb.2013.05.055.
[76] J. Xiong, J. Di, J. Xia, W. Zhu, H. Li, Surface defect engineering in 2D nanomaterials for photocatalysis, Adv. Funct. Mater., 28 (2018) 1801983. https://doi.org/10.1002/adfm.201801983.
[77] J. Goclon, K. Winkler, Computational insight into the mechanism of O_2 to H_2O_2 reduction on amino-groups-containing g-C_3N_4, Appl. Surf. Sci., 462 (2018) 134-141. https://doi.org/10.1016/j.apsusc.2018.08.070.
[78] X. Li, J. Zhang, F. Zhou, H. Zhang, J. Bai, Y. Wang, H. Wang, Preparation of N-vacancy-doped g-C_3N_4 with outstanding photocatalytic H_2O_2 production ability by dielectric barrier discharge plasma treatment, Chinese J. Catal., 39 (2018) 1090-1098. https://doi.org/10.1016/S1872-2067(18)63046-3.
[79] X. Qu, S. Hu, P. Li, Z. Li, H. Wang, H. Ma, W. Li, The effect of embedding N vacancies into g-C_3N_4 on the photocatalytic H_2O_2 production ability via H_2 plasma treatment, Diam. Relat. Mater., 86 (2018) 159-166. https://doi.org/10.1016/j.diamond.2018.04.027.
[80] L. Shi, L. Yang, W. Zhou, Y. Liu, L. Yin, X. Hai, H. Song, J. Ye, Photoassisted construction of holey defective g-C_3N_4 photocatalysts for efficient visible-light-driven H_2O_2 production, Small, 14 (2018) 1703142. https://doi.org/10.1002/smll.201703142.
[81] Z. Zhu, H. Pan, M. Murugananthan, J. Gong, Y. Zhang, Visible light-driven photocatalytically active g-C_3N_4 material for enhanced generation of H_2O_2, Appl. Catal. B, 232 (2018) 19-25. https://doi.org/10.1016/j.apcatb.2018.03.035.

[82] Y. Shiraishi, T. Takii, T. Hagi, S. Mori, Y. Kofuji, Y. Kitagawa, S. Tanaka, S. Ichikawa, T. Hirai, Resorcinol–formaldehyde resins as metal-free semiconductor photocatalysts for solar-to-hydrogen peroxide energy conversion, Nat. Mater., 18 (2019) 985-993. https://doi.org/10.1038/s41563-019-0398-0.
[83] P. Zhang, Y. Tong, Y. Liu, J.J.M. Vequizo, H. Sun, C. Yang, A. Yamakata, F. Fan, W. Lin, X. Wang, W. Choi, Heteroatom dopants promote two-electron O_2 reduction for photocatalytic production of H_2O_2 on polymeric carbon nitride, Angew. Chem. Int. Ed., n/a (2020). https://doi.org/10.1002/anie.202006747.
[84] Y. Bo, C. Gao, Y. Xiong, Recent advances in engineering active sites for photocatalytic CO_2 reduction, Nanoscale, 12 (2020) 12196-12209. https://doi.org/10.1039/D0NR02596H.
[85] Z. Teng, H. Lv, C. Wang, H. Xue, H. Pang, G. Wang, Bandgap engineering of ultrathin graphene-like carbon nitride nanosheets with controllable oxygenous functionalization, Carbon, 113 (2017) 63-75. https://doi.org/10.1016/j.carbon.2016.11.030.
[86] H. Ou, P. Yang, L. Lin, M. Anpo, X. Wang, Carbon nitride aerogels for the photoredox conversion of water, Angew. Chem. Int. Ed., 56 (2017) 10905-10910. https://doi.org/10.1002/anie.201705926.
[87] G. Liao, Y. Gong, L. Zhang, H. Gao, G.-J. Yang, B. Fang, Semiconductor polymeric graphitic carbon nitride photocatalysts: The “holy grail” for the photocatalytic hydrogen evolution reaction under visible light, Energy Environ. Sci., 12 (2019) 2080-2147. http://dx.doi.org/10.1039/C9EE00717B.
[88] Y. Shiraishi, Y. Kofuji, H. Sakamoto, S. Tanaka, S. Ichikawa, T. Hirai, Effects of surface defects on photocatalytic H_2O_2 production by mesoporous graphitic carbon nitride under visible light irradiation, ACS Catal., 5 (2015) 3058-3066. https://doi.org/10.1021/acscatal.5b00408.
[89] S. Hu, X. Qu, P. Li, F. Wang, Q. Li, L. Song, Y. Zhao, X. Kang, Photocatalytic oxygen reduction to hydrogen peroxide over copper doped graphitic carbon nitride hollow microsphere: The effect of Cu(I)-N active sites, Chem. Eng. Sci., 334 (2018) 410-418. https://doi.org/10.1016/j.cej.2017.10.016.
[90] Y. Peng, L. Wang, Y. Liu, H. Chen, J. Lei, J. Zhang, Visible-light-driven photocatalytic H_2O_2 production on g-C_3N_4 loaded with CoP as a noble metal free cocatalyst, Chem. Eur. J., 2017 (2017) 4797-4802. https://doi.org/10.1002/ejic.201700930.
[91] H.-i. Kim, Y. Choi, S. Hu, W. Choi, J.-H. Kim, Photocatalytic hydrogen peroxide production by anthraquinone-augmented polymeric carbon nitride, Appl. Catal. B, 229 (2018) 121-129. https://doi.org/10.1016/j.apcatb.2018.01.060.
[92] C. Chu, Q. Zhu, Z. Pan, S. Gupta, D. Huang, Y. Du, S. Weon, Y. Wu, C. Muhich, E. Stavitski, K. Domen, J.-H. Kim, Spatially separating redox centers on 2D carbon nitride with cobalt single atom for photocatalytic H_2O_2 production, Proc. Natl. Acad. Sci. U.S.A., 117 (2020) 6376. https://doi.org/10.1073/pnas.1913403117.
[93] S. Siahrostami, A. Verdaguer-Casadevall, M. Karamad, D. Deiana, P. Malacrida, B. Wickman, M. Escudero-Escribano, E.A. Paoli, R. Frydendal, T.W. Hansen, I. Chorkendorff, I.E.L. Stephens, J. Rossmeisl, Enabling direct H_2O_2 production through rational electrocatalyst design, Nat. Mater., 12 (2013) 1137-1143. https://doi.org/10.1038/nmat3795.
[94] A. Verdaguer-Casadevall, D. Deiana, M. Karamad, S. Siahrostami, P. Malacrida, T.W.

Hansen, J. Rossmeisl, I. Chorkendorff, I.E.L. Stephens, Trends in the electrochemical synthesis of H_2O_2: Enhancing activity and selectivity by electrocatalytic site engineering, Nano Lett., 14 (2014) 1603-1608. https://doi.org/10.1021/nl500037x.
[95] J. Schneider, D.W. Bahnemann, Undesired role of sacrificial reagents in photocatalysis, J. Phys. Chem. Lett., 4 (2013) 3479-3483. https://doi.org/10.1021/jz4018199.
[96] Y. Wang, A. Vogel, M. Sachs, R.S. Sprick, L. Wilbraham, S.J.A. Moniz, R. Godin, M.A. Zwijnenburg, J.R. Durrant, A.I. Cooper, J. Tang, Current understanding and challenges of solar-driven hydrogen generation using polymeric photocatalysts, Nat. Energy, 4 (2019) 746-760. https://doi.org/10.1038/s41560-019-0456-5.
[97] M. Wang, S. Shen, L. Li, Z. Tang, J. Yang, Effects of sacrificial reagents on photocatalytic hydrogen evolution over different photocatalysts, J. Mater. Sci., 52 (2017) 5155-5164. https://doi/org/10.1007/s10853-017-0752-z.
[98] K. Fuku, K. Sayama, Efficient oxidative hydrogen peroxide production and accumulation in photoelectrochemical water splitting using a tungsten trioxide/bismuth vanadate photoanode, Chem. Commun., 52 (2016) 5406-5409. https://doi.org/10.1039/C6CC01605G.
[99] D. Iglesias, A. Giuliani, M. Melchionna, S. Marchesan, A. Criado, L. Nasi, M. Bevilacqua, C. Tavagnacco, F. Vizza, M. Prato, P. Fornasiero, N-doped graphitized carbon nanohorns as a forefront electrocatalyst in highly selective O_2 Reduction to H_2O_2, Chem, 4 (2018) 106-123. https://doi.org/10.1016/j.chempr.2017.10.013.
[100] Z. Qiang, J.-H. Chang, C.P. Huang, Electrochemical generation of hydrogen peroxide from dissolved oxygen in acidic solutions, Water Res., 36 (2002) 85-94. https://doi.org/10.1016/S0043-1354(01)00235-4.
[101] W.G. Kuo, Decolorizing dye wastewater with Fenton's reagent, Water Res., 26 (1992) 881-886. https://doi.org/10.1016/0043-1354(92)90192-7.

PART 2

Bandgap engineering of polymetric carbon nitride copolymerized by 2,5,8-triamino-tri-s-triazine (melem) and barbituric acid for efficient nonsacrificial photocatalytic H_2O_2 production

2.1 Introduction

H_2O_2 is recognized as an industrially important green oxidant [1-4] and a promising future solar fuel (60wt% H_2O_2, 3.0 MJL^{-1}, higher energy density than that of compressed H_2 gas, 35 MPa, 2.8 MJL^{-1}) [5]. H_2O_2 is commonly generated by the reaction of anthraquinone with O_2. The as-obtained anthrahydroquinone was reduced to re-generate anthraquinone with H_2 on Pd-based catalysts [6]. As an alternative to this complicated energy-consuming process, direct synthesis of H_2O_2 with H_2 and O_2 has been achieved by utilizing Pd-based catalysts has been proposed [7,8]. By using this strategy, H_2O_2 is quantitatively generated, but the mixture of H_2/O_2 is naturally explosive. Processes for photocatalytic production of H_2O_2 on semiconductor materials have emerged as promising safe, environment-friendly, and energy-saving processes [9-19]. One of the most promising processes for photocatalytic H_2O_2 production is via water and O_2 (eq. 1) with an ideal atom efficiency up to 100% [15-18]. Both reduction of O_2 (eq. 2) via two electron transfer pathways and efficient water oxidation (eq. 3) are required for the photocatalyst to achieve this process.

$$2H_2O+O_2 \rightarrow 2H_2O_2 \quad (1)$$

$$O_2+2H^++2e^- \rightarrow H_2O_2 \text{ (0.695 V vs. NHE)} \quad (2)$$

$$2H_2O+4h^+ \rightarrow O_2+4H^+ \text{ (1.23 V vs. NHE)} \quad (3)$$

$$H^++O_2+e^- \rightarrow \bullet OOH \text{ (-0.046 V vs. NHE)} \quad (4)$$

$$O_2+e^- \rightarrow \bullet O_2^- \text{ (-0.284 V vs. NHE)} \quad (5)$$

Metal oxides and polymeric carbon nitrides (PCNs) based semiconductors have been widely studied for achieving photocatalytic H_2O_2 production since the band structures of metal oxides and PCNs are capable of catalyzing both of the reactions shown in eq. 2 and eq. 3. However, the selectivity of metal oxides for photocatalytic H_2O_2 production is quite low because 1-electron reduction of O_2 (superoxide (hydrogen peroxide radical formation (•OOH), eq. 4; $\bullet O_2^-$) radical formation, eq 5) usually dominates, thus suppressing 2-electron reduction [20-25]. PCNs, which has been recognized as a promising metal-free photocatalyst under visible-light irradiation [26-27], can promote selective photoreduction of O_2 and produces H_2O_2 via the formation of 1-4 endoperoxide on 2,5,8-triamino-tri-s-

triazine (melem) units by a rapid stepwise reaction via 1-e^- pathway [16-18]. However, most of the PCN-based materials produce a large amount of H_2O_2 only with the existence of electron donors [11-14, 19] since it seems that the holes captured in the valence band maximum (VBM) of PCN (around 1.4~1.6 V vs. standard hydrogen electrode, SHE) seems not positive enough to overcome the large potential for water oxidation (c.a. > 0.8 V). To overcome this obstacle, Shiraishi and co-workers proved that the co-polymerization of light adsorption units with C=O could significantly shift the band position of PCN to the positive side, leading to an enhanced photocatalytic activity for oxygen evolution reaction (OER) [15-17]. However, the reason of the band shift was not clarified at the electronic energy level, and the large bandgap width of PCN (~2.7 eV), even with co-polymerization of BDI [15, 17] or PDI [16], limits the ratio of the visible light that can be used, resulting in limited solar to chemical conversion (SCC) efficiency (~ 0.2%) [18].

Co-polymerization of barbituric acid (BA), which also contains a large amount of C=O groups, has been used for narrowing the bandgap of PCN, a process that was firstly reported by Zhang et al. [27-30]. The light adsorption range of PCN samples obtained by co-polymerization of nitrogen-rich precursors and BA was significantly expanded [27-30]. However, the conduction band minimum (CBM) and VBM shift to the opposite side, leading to suppressed photo-redox activity [27]. One possibility is that in the previously reported mechanisms, BA molecules are directly incorporated into the classical carbon nitride condensation scheme via an S_N2 nucleophilic substitution reaction (Scheme 1A) [27]. In that scheme, the quaternary carbon atoms of BA molecules were nucleophilically attacked by the amino groups of dicyandiamide, and then the oxygen groups are removed from the PCN matrix [27]. To keep the C=O groups in the PCN matrix, the S_N2 nucleophilic substitution has to be suppressed during the co-polymerization. Typically, this nucleophilic addition would be suppressed if the molecular weights of nucleophilic regents are increased, i. e., the steric hindrance effect could be improved (Scheme 1B). As a result, the deamination selectivity could be enhanced. Thus, C=O groups could remain during the thermal polymerization if precursors with large molecular weights are used. Melem (Scheme 1C), as an intermediate product during the thermal polymerization of PCN with a

large molecule weight [32], could serve as an ideal co-polymerization precursor for co-polymerization with BA. The molecular weight of melem (218.1) is more than 2-times larger than that of dicyandiamide (84.1), leading to a large steric effect that can suppress the S_N2 nucleophilic substitution. Therefore, co-polymerization of melem and BA (Scheme 1C) enabled the introduction of C=O groups into the PCN matrix, leading to an improved photocatalytic water oxidation activity with promoted light usage of the PCN-based photocatalyst.

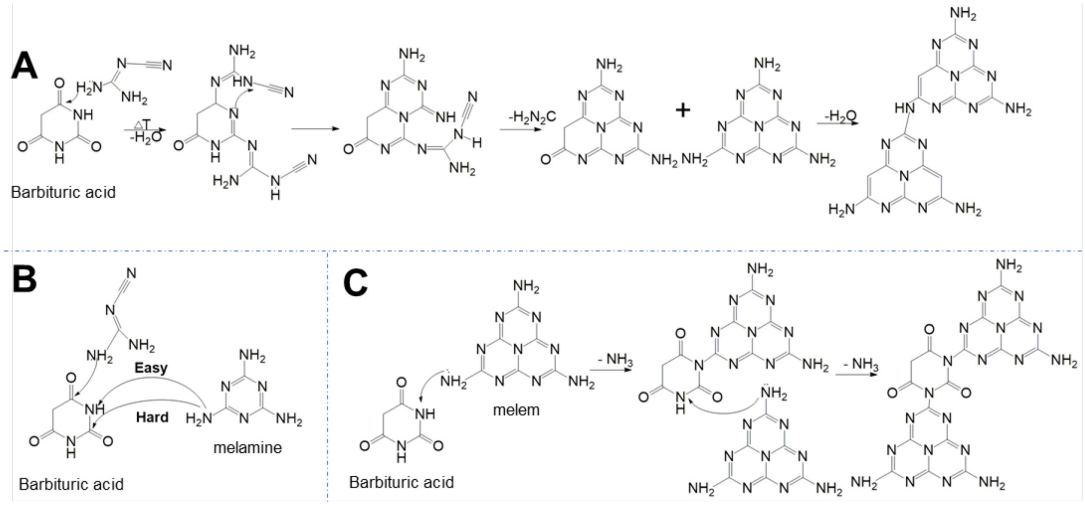

Scheme 2-1. Thermal polymerization of different nitrogen rich precursors with barbituric acid. Precursors with (A) small molecular weights and (B) large molecular weights. (C) Polymerization process with barbituric acid and melem as precursors.

Herein, we engineered the band positions of polymetric carbon nitride prepared by using barbituric acid and melem as precursors (denoted as PCNBA). The C=O groups were maintained in the as-prepared PCN matrix, and the band positions of the as-prepared PCNBA shifted positively with a sufficient oxidation potential (up to 1.85 V vs. SHE) for water oxidation. The narrowed bandgap width ranging from 2.77 eV to 2.18 eV also significantly expanded the adsorption range of solar light. Furthermore, the reason of the band shift caused by the co-polymerization of barbituric acid was clarified at the electronic level by combining the results of XPS measurements and density functional theory (DFT) simulations. With the optimized co-polymerization and loading of $Na_2CoP_2O_7$ as an OER co-catalyst [33], the PCNBAs showed a high apparent quantum yield (ΦAQY) of 8.0% and SCC efficiency of 0.30% for photocatalytic H_2O_2 production with only H_2O and O_2.

Moreover, the co-relationships between the charge separation and the photocatalytic activities for H_2O_2 production were clarified for the first time. This work provides a primary guideline and a practical approach for designing materials with an appropriate band structure to achieve optimized performance for photocatalytic H_2O_2 production.

2.2 Experimental details

2.2.1 Preparation of photocatalyst

Unless otherwise stated, the purities of all reagents for preparation of photocatalysts preparation and for photoelectrochemical measurements were above analytical grade. Melem was prepared by calcination of melamine at 420 °C in N_2 for 4 h. [32] The polymetric carbon nitride with barbituric acid co-polymerization (PCNBA) was prepared as follows: 3 g melem with a certain amount of barbituric acid (SIGMA-ALDRICH, Co., Ltd.) was ball-milled in the presence of ethanol for 2 h (400 rpm). Then the mixture was drying in a vacuum oven at 60 °C for 4 h. The as-obtained white powder was calcinated in a furnace at 560 °C in air for 4h with an increasing temperature rate of 2 °C. The bulk material was obtained when the furnace was cooled down to room temperature. The adding amounts of barbituric acid (BA) added were 0.01 g, 0.05 g, 0.1 g, 0.2 g and 0.5 g. These samples were named PCNBA0.01, PCNBA0.05, PCNBA0.1, PCNBA0.2 and PCNBA0.5, respectively.

$Na_2CoP_2O_7$ was prepared by following previous reports. Na_2CO_3 (1. 06 g, Wako Pure Chemical Industries, Ltd.), $CoNO_3{\cdot}6H_2O$ (2.91 g, Wako Pure Chemical Industries, Ltd.) and $(NH_4)_2HPO_4$ (2.64 g, Wako Pure Chemical Industries, Ltd.) were ball-milled with acetone for 1 h. Then the purple mixture was dried in a vacuum oven for 8 h at 25 °C. The purple powder was calcined at 600 °C for 16 h. After cooling down to the room temperature, blue bulk material was obtained [34].

The loading of $Na_2CoP_2O_7$ onto the PCNBA was conducted using a simple ball milling method. Specifically, the 0.2 g of PCNBA samples with a certain amount of $Na_2CoP_2O_7$ (0.002 g, 0.005 g, 0.01 g and 0.02 g) was ball-milled for 15 min. The as-prepared samples were named PCNBAxCo1%, PCNBAxCo2.5%, PCNBAxCo5% and PCNBAxCo10%, respectively.

2.2.2 Measurements of photocatalytic activities

Each catalyst (50 mg) was added to pure water (30 mL) within a borosilicate glass bottle (φ 45 mm; capacity, 50 mL), and the bottle was sealed with a rubber septum cap. The catalyst was dispersed well by ultrasonication for 15 min, and O_2 was bubbled through the solution for 30 min. The bottle was immersed in a temperature-controlled air bath at 298 ± 0.5 K with wind flowing and was photo-irradiated at λ > 420 nm using a 500 W Xe lamp (PXE-500, USHIO Inc.) with magnetic stirring. Water oxidation with $AgNO_3$ as a sacrificial electron acceptor was performed with a catalyst (100 mg) in a buffered La_2O_3 (30 mg) solution (30 mL, pH 8−9) with $AgNO_3$ (10 mM) under an Ar atmosphere (1 atm). The amount of H_2O_2 was determined by a colorimetric method using PACKTEST (WAK-H_2O_2, KYORITSU CHEMICAL-CHECK Lab., Corp.) equipped with a digital PACKTEST spectrometer (ED723, GL Sciences Inc.).

2.2.3 Action spectrum analysis.

Photocatalytic reactions were carried out in pure water (30 mL) with catalysts (50 mg) with or without the addition of et-OH as an electron donor reagent. After ultrasonication and O_2 bubbling, the bottle was photoirradiated photoirradiated by a Xeon lamp for 6 h with magnetic stirring. The incident light was monochromated by band-pass glass filters (Asahi Techno Glass Co.), where the full-width at half-maximum of the lights was 11−16 nm. The numbers of photons that entered into the reaction vessel was determined with a 3684 optical power meter (HIOKI E.E. CORPORATION).

2.2.4 Determination of SCC efficiency.

Solar to chemical conversion (SCC) efficiency was determined by photoreactions with a PEC-L01 solar simulator (Peccell Technologies, Inc.). Photoreactions were performed in pure water (100 mL) with catalysts (each 500 mg) under O_2 (1 atm) in a borosilicate glass bottle, with λ > 420 nm cutoff filter was used to avoid subsequent decomposition of the formed H_2O_2 by absorbing UV light [18]. The irradiance of the solar simulator was adjusted to the AM1.5 global spectrum.[15] The SCC efficiency was calculated by the following equation:

$$SCC(\%) = \frac{\Delta G_{H_2O_2} \times n_{H_2O_2}}{t_{ir} \times S_{ir} \times I_{AM}} \times 100\%.$$

In the equation, $\Delta G_{H_2O_2}$ is the free energy for H_2O_2 generation (117 kJ mol^{-1}). $n_{H_2O_2}$ is the amount of H_2O_2 generated, and t_{ir} is the irradiation time (s). The overall irradiation intensity (I_{AM}) of the AM1.5 global spectrum (300−2500 nm) is 1000 W m^{-2}, and the irradiation area (S_{ir}) is 0.628 × 10^{-4} m^2 [15].

2.2.5 Instruments

High-resolution transmission electron microscopy (HRTEM), high-angle annular dark field scanning transmission electron microscopy (HAADF-STEM), selected area electron diffraction (SAED) and energy-dispersive X-ray spectroscopy (EDS) were performed using a Tecnai G2 F30 S-Twin electron microscope with an accelerating voltage of 300 kV. The crystalline phases were characterized by using a powder X−ray diffraction (XRD) instrument (MiniFlex II, Rigaku Co.) with CuKα (λ=1.5418 Å) radiation (cathode voltage: 30 kV, current: 15 mA). Absorption properties of powder samples were determined by using the diffuse reflection method with a UV/VIS/NIR spectrometer (UV-2600, Shimadzu Co.) attached to an integral sphere at room temperature. X−ray photoelectron spectroscopy (XPS) measurements were performed by using a Kratos AXIS Nova spectrometer (Shimazu Co.) with a monochromatic Al Kα X−ray source. The binding energy was calibrated by taking the carbon (C) 1s peak of contaminant carbon as a reference at 284.6 eV. Valence band X-ray photoelectron spectroscopy (VBXPS) was performed on an ESCALAB 250Xi (Thermo Scientific, USA). Electron spin resonance (ESR) signals of spin-trapped paramagnetic species with 5,5-diemthyl-1-pyrroline N-oxide (DMPO, methanol solution) were recorded with an A300-10/12 spectrometer.

2.2.6 Photoelectrochemical characterizations

Photoelectrochemical (PEC) characterizations were conducted using a conventional three-electrode potentiostat setup connected to an Electrochemical Analyzer (Model 604D, CH Instruments, Inc.). The Fluoride-doped tin oxide (FTO) glass of 1 cm × 2 cm in size was covered with a photocatalyst that was fabricated by first mixing a catalyst (100 mg) with ethyl cellulose binder (10 mg) in ethanol for one hour and then depositing the final viscous mixture by a doctor blade method and drying at room temperature and further drying at 40 °C overnight in a vacuum oven. The area of the photocatalytic coating was

controlled to be 1 cm^2 by the doctor blade method. The PEC reactor consisted of FTO glass covered by a PCN sample, coiled Pt wires and a saturated Ag/AgCl/KCl (saturated) electrode as working, counter, and reference electrodes, respectively. The photocurrent derived from photo-generated charge carriers on photocatalysts was collected on a Pt working electrode (at 0.8 V vs. SHE (0.6 V vs. Ag/AgCl)) in phosphate buffer solutions. The solutions were saturated with O_2 by bubbling O_2 for 15 min (0.5 L/min) [1, 2]. Electrochemical impedance spectroscopy (EIS) analysis was performed at a DC voltage of -0.6 V *vs*. Ag/AgCl, an AC voltage amplitude of 50 mV, and a frequency ranging from 100 kHz to 0.01 Hz. For Mott-Schottky measurements, similar strategies were performed on FTO glass (1.5 cm × 3 cm) by the same doctor blade method.

Rotating disk electrode (RDE) measurements were performed on a computer-controlled CHI760 advanced electrochemical system with a conventional three-electrode cell. An Ag/AgCl electrode and a Pt wire electrode were used as the reference and counter electrodes, respectively. The working electrode was prepared as follows. A catalyst (20 mg) was dispersed in water (5 mL) by ultrasonication. The slurry (20 μL) was put onto a Pt disk electrode and dried at room temperature. The electrode surface was coated with a Nafion solution (1 wt %, 20 μL) and dried in air. Linear-sweep voltammograms were obtained in an O_2-saturated 0.1 M KOH solution (pH 13) with a scan rate of 10 mV s^{-1} at different rotating speeds (400, 625, 900, 1225, 1600 and 2025 rpm). After each scan, O_2 was bubbled for 5 min to re-saturate O_2. The average number of electrons (n) involved in the overall O_2 reduction was determined by the slopes of Koutecky−Levich plots with the following equation:

$$j^{-1} = j_k^{-1} + B^{-1}\omega^{-1/2}$$
$$B = 0.2nFv^{-1/6}CD^{2/3}$$

where j is the measured current density at a constant potential, j_k is the kinetic current density, and ω is the electrode rotating speed (rpm),. F is the Faraday constant (96 485 C mol^{-1}), v is the kinetic viscosity of water (0.01 cm^2 s^{-1}), C is the bulk concentration of O_2 in solution (1.3 × 10^{-6} mol cm^{-3}), and D is the diffusion coefficient of O_2 (2.7 × 10^{-5} cm^2 s^{-1}).

2.2.7 Calculation details

2.2.7.1 Optimization and DOS calculations

Melem_4 and Melem_4 inserted with one or two barbituric acid units (Melem_4BA1 and Melem_4BA1) were fabricated to represent the elementary units of PCN and PCN with co-polymerization of BA motifs with low and high concentration of BA motifs, respectively. The optimization and frequency were conducted via density functional theory (DFT) in the Gaussian 09 program S2, which was carried out by utilizing wb97xd/6-311 G(d) level of theory. The schematic diagram of optimized models and Cartesian coordinates of optimized models were presented as Figure 2-1, Table 2-1, Table 2-2 and Table 2-3.

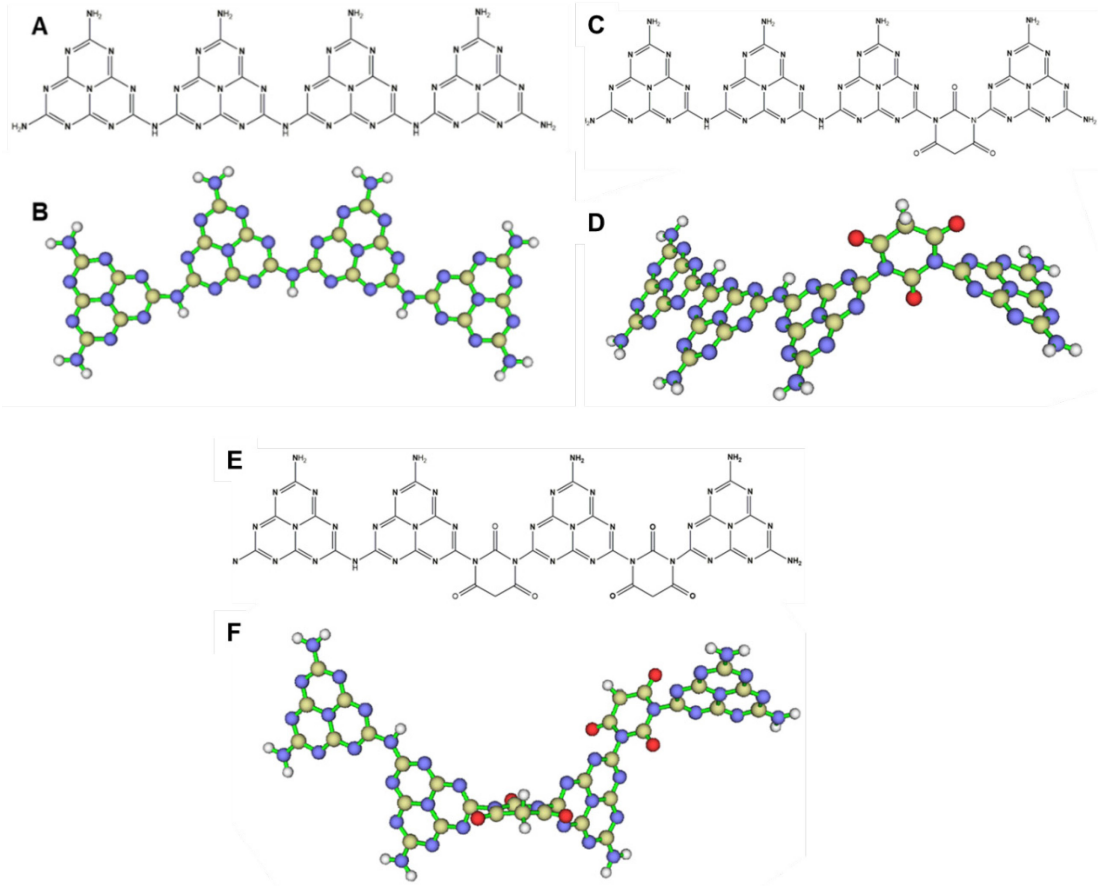

Figure 2-1. (A) Molecular formula and (B) optimized molecular structure of Melem4. (C) Molecular formula and (D) optimized structure of Melem_4BA1. (E) Molecular formula and (F) the optimized molecular structure of Melem_4BA2.

Table 2-1. Cartesian coordinates of optimized melem_4.

	axis	X	y	z		axis	x	y	z
1	(C)	5.041609	4.292458	-0.57829	39	(C)	-22.3562	-7.06309	-0.37043
2	(C)	2.380353	0.976598	-0.64064	40	(C)	-22.7178	-2.88552	0.470012
3	(C)	6.532443	-0.04384	-0.52697	41	(C)	-22.6956	1.314807	1.266471
4	(C)	10.76053	-0.67068	-0.34387	42	(C)	-18.8554	-0.39218	0.49994
5	(C)	9.54875	3.406043	-0.41757	43	(N)	-12.6058	-2.45257	-0.55286
6	(C)	7.990211	7.382262	-0.51137	44	(N)	-16.1952	-4.70447	-0.61486
7	(N)	10.00677	5.850099	-0.42376	45	(N)	-19.8386	-7.07863	-0.66035
8	(N)	4.16172	-0.82109	-0.6078	46	(N)	-23.8451	-5.09092	0.178901
9	(N)	2.678301	3.453631	-0.64513	47	(N)	-20.0809	-2.7225	0.196449
10	(N)	5.541923	6.727479	-0.58522	48	(N)	-16.3608	-0.26651	0.246927
11	(N)	8.430152	-1.66016	-0.45461	49	(N)	-24.0174	-0.82589	1.013805
12	(N)	11.41765	1.737174	-0.32969	50	(N)	-20.189	1.634858	1.036541
13	(N)	7.04018	2.552021	-0.50289	51	(N)	-24.0268	3.394686	1.816879
14	(C)	-2.38321	0.985196	-0.53987	52	(N)	-23.5195	-9.29093	-0.66533
15	(C)	-6.54334	-0.00817	-0.52654	53	(H)	-22.4919	-10.8287	-1.08371
16	(C)	-5.01558	4.289201	-0.05278	54	(H)	-25.4033	-9.39037	-0.47445
17	(C)	-9.52997	3.426625	0.016452	55	(H)	-11.9082	-4.1995	-0.86928
18	(C)	-10.7764	-0.61736	-0.41306	56	(H)	-23.1231	5.04934	2.021068
19	(C)	-7.93662	7.369731	0.419419	57	(H)	-25.9096	3.272707	2.006223
20	(N)	-11.4133	1.775628	-0.10067	58	(C)	18.8728	-0.38406	0.165183
21	(N)	-2.65982	3.445113	-0.22752	59	(C)	15.17025	-2.46117	-0.0438
22	(N)	-8.45471	-1.60525	-0.64737	60	(C)	18.62336	-4.96561	0.31015
23	(N)	-7.02914	2.569699	-0.18788	61	(C)	22.28099	-7.13859	0.687916
24	(N)	-4.17983	-0.78953	-0.71021	62	(C)	22.70943	-2.88534	0.565196
25	(N)	-9.96645	5.855768	0.320158	63	(C)	22.75289	1.386612	0.405851
26	(N)	-5.49436	6.70922	0.253589	64	(N)	24.04584	-0.77819	0.592965
27	(N)	-0.00583	-0.05246	-0.69939	65	(N)	16.13765	-4.79205	0.106876
28	(N)	-8.40188	9.834917	0.724047	66	(N)	16.37247	-0.27659	-0.03299
29	(N)	8.47743	9.861925	-0.52492	67	(N)	20.2426	1.689133	0.193339
30	(H)	7.036391	11.09339	-0.58931	68	(N)	19.75543	-7.1769	0.480613
31	(H)	10.27787	10.45611	-0.4728	69	(N)	23.80592	-5.11844	0.737684
32	(N)	12.57366	-2.5237	-0.22995	70	(N)	20.06608	-2.7436	0.347718
33	(H)	11.85679	-4.29142	-0.23251	71	(N)	24.12132	3.514447	0.433508
34	(H)	-10.1968	10.43315	0.856983	72	(H)	23.23992	5.187795	0.294964
35	(H)	-6.95013	11.0524	0.80984	73	(H)	26.00832	3.406608	0.585338
36	(H)	-0.01196	-1.95707	-0.80595	74	(N)	23.41313	-9.39453	0.867585
37	(C)	-15.1955	-2.40573	-0.28657	75	(H)	22.35825	-10.97	0.838699
38	(C)	-18.6763	-4.89516	-0.37456	76	(H)	25.3009	-9.47908	1.023935

Table 2-2. Cartesian coordinates of optimized Melem_4BA1.

	x	y	z		x	y	z		x	y	z
1C	2.596855	-6.447426	-0.317725	**39N**	-20.716774	7.658172	2.350287	**79N**	14.482482	0.715631	2.856915
2C	4.505529	-2.874404	1.814553	**40N**	-24.787556	6.648652	0.584802	**80N**	10.872286	-1.799772	3.540619
3C	8.68256	-3.029027	2.496819	**41N**	-21.30075	3.963289	-0.051777	**81C**	12.313171	-0.382383	1.851626
4C	7.107069	-6.427566	0.513057	**42N**	-17.86464	1.213016	-0.751455	**82O**	11.729455	-0.141292	-0.325307
5C	5.163829	-9.664817	-1.471585	**43N**	-25.293465	3.026955	-1.76916	**83C**	15.305288	0.593142	5.348827
6N	7.30853	-8.649496	-0.565686	**44N**	-21.748838	0.254933	-2.449992	**84O**	17.258937	1.548081	6.001022
7N	2.275963	-1.795495	1.95626	**45N**	-25.63216	-0.578343	-4.081367	**85C**	11.359015	-2.188706	6.093202
8N	0.365534	-5.315188	-0.149565	**46N**	-24.137149	10.192416	2.923488	**86O**	10.054725	-3.554915	7.352911
9N	2.833646	-8.673478	-1.397112	**47H**	-23.014911	11.328496	3.946077	**87H**	12.807047	0.678065	8.45395
10N	6.564594	-1.754668	2.739851	**48H**	-25.970383	10.599993	2.661171				
11N	9.117478	-5.250251	1.478737	**49H**	-13.16928	3.862567	1.977572				
12N	4.74469	-5.244874	0.675183	**50H**	-24.880268	-2.154879	-4.819886				
13C	-8.338544	-0.768506	0.618481	**51H**	-27.461512	-0.148729	-4.335708				
14C	-7.327351	-4.924024	-1.037758	**52C**	16.911473	5.853341	-0.671628				
15C	-11.668271	-3.417522	-1.08508	**53C**	16.033296	2.106718	1.103472				
16C	-12.430121	0.470768	0.463025	**54C**	19.239965	2.015643	-1.664434				
17C	-10.556463	-7.271303	-2.556286	**55C**	22.422875	2.312157	-4.489451				
18N	-13.330742	-1.612328	-0.576836	**56C**	20.355749	5.973215	-3.698242				
19N	-4.91136	-4.531079	-0.47922	**57C**	18.070742	9.439989	-2.669307				
20N	-10.033381	0.992167	1.10457	**58N**	19.949089	8.413415	-4.013984				
21N	-9.108334	-3.034205	-0.507748	**59N**	17.766359	0.755952	-0.04869				
22N	-5.922192	-0.438628	1.163698	**60N**	15.491554	4.52226	0.935021				
23N	-12.377819	-5.566811	-2.115655	**61N**	16.534885	8.278443	-1.009289				
24N	-8.075308	-7.053619	-2.074955	**62N**	21.044486	0.868176	-2.915393				
25N	-11.297557	-9.448609	-3.601566	**63N**	22.165506	4.78636	-4.938163				
26N	5.38397	-11.924886	-2.570958	**64N**	18.828019	4.607071	-2.004091				
27H	3.840499	-12.767614	-3.282873	**65N**	17.663526	11.909739	-3.005537				
28H	7.090453	-12.746644	-2.679852	**66H**	16.270676	12.763183	-2.041309				
29H	-13.133019	-9.711176	-4.00155	**67H**	18.750441	12.878465	-4.221082				
30H	-10.008521	-10.790653	-3.968602	**68N**	24.262898	1.124316	-5.747895				
31C	-16.559691	2.838846	0.615956	**69H**	24.528377	-0.73383	-5.474201				
32C	-19.755964	5.5831	1.366032	**70H**	25.355902	2.105921	-6.947536				
33C	-23.177356	8.080902	1.912327	**71C**	-4.363192	-2.338733	0.573206				
34C	-23.861932	4.562955	-0.420945	**72C**	0.323137	-3.086358	0.966312				
35C	-24.170853	0.966016	-2.710647	**73N**	-1.90106	-1.784021	1.222264				
36C	-20.289623	1.754444	-1.110088	**74H**	-1.700193	-0.080965	2.059082				
37N	-14.024266	2.428629	1.055059	**75C**	13.567629	-0.747577	7.162106				
38N	-17.348373	4.986532	1.688852	**76H**	14.690431	-2.0271	8.324175				

Table 2-3. Cartesian coordinates of optimized Melem_4BA2

	x	y	z		x	y	z		x	y	z
1C	-9.754698	-6.52919	0.802821	**39N**	15.747897	5.219379	0.962055	**77H**	-1.088415	-7.15561	8.941122
2C	-9.695141	-2.115309	2.07261	**40N**	18.081402	6.788366	4.288743	**78N**	0.392447	-5.430601	3.203475
3C	-13.129869	0.248461	1.133013	**41N**	22.570634	6.069039	4.459626	**79N**	-3.992882	-5.092362	3.888268
4C	-13.331651	-3.813375	-0.12695	**42N**	20.134824	4.495275	1.08784	**80O**	-2.293493	-4.517915	-0.016429
5C	-13.220795	-7.937779	-1.245712	**43N**	17.773924	2.882115	-2.318707	**81O**	3.087191	-6.412094	6.373778
6N	-14.471059	-5.735665	-1.216442	**44N**	24.527297	3.822998	1.289558	**82O**	-5.693172	-5.819609	7.745844
7N	-7.392087	-2.4652	3.039505	**45N**	22.073076	2.193662	-2.178356	**83H**	-0.910533	-3.874163	8.578441
8N	-7.461504	-6.805104	1.818026	**46N**	26.317266	1.592359	-1.917905	**84C**	12.130965	1.418279	-1.830694
9N	-10.920404	-8.426291	-0.283482	**47N**	20.498842	8.268485	7.51542	**85C**	12.723895	5.49945	-4.091842
10N	-10.815643	0.092741	2.179136	**48H**	18.907052	8.989039	8.253904	**86C**	10.140563	5.193825	-5.250427
11N	-14.421738	-1.559686	0.001081	**49H**	22.169018	8.478573	8.389471	**87C**	8.817051	2.697295	-4.928278
12N	-10.91623	-4.153855	0.92021	**50H**	26.188755	0.645603	-3.556621	**88H**	10.264168	5.623339	-7.261754
13C	5.464908	-3.172164	-0.496734	**51H**	27.986065	1.820758	-1.0459	**89O**	12.879522	-0.093111	-0.316758
14C	4.789248	-7.628858	-1.338877	**52C**	-20.218227	3.469931	-1.186411	**90O**	6.939564	2.13281	-6.071661
15C	8.077032	-5.3596	-3.565203	**53C**	-16.371288	3.698701	0.601849	**91O**	14.065529	7.274801	-4.536807
16C	8.549701	-1.243033	-2.656241	**54C**	-18.551923	7.378198	0.555132	**92N**	13.452231	3.616021	-2.408525
17C	7.328874	-9.512639	-4.205981	**55C**	-21.015556	10.858844	0.322454	**93N**	9.874452	1.073701	-3.149681
18N	9.300209	-3.193149	-3.98684	**56C**	-22.730631	7.315269	-1.347686	**94H**	8.919295	6.64569	-4.424125
19N	2.901463	-7.603375	0.336439	**57C**	-24.122988	3.588765	-2.913978				
20N	6.743009	-1.065627	-0.948209	**58N**	-24.549841	6.043873	-2.48852				
21N	6.106788	-5.376204	-1.794257	**59N**	-16.46313	6.153188	1.186441				
22N	3.584186	-3.225931	1.157913	**60N**	-18.095592	2.29824	-0.52615				
23N	8.677889	-7.437528	-4.771362	**61N**	-22.054209	2.24192	-2.320643				
24N	5.415784	-9.698046	-2.546659	**62N**	-18.82703	9.801821	1.045591				
25N	7.957102	-11.621991	-5.42905	**63N**	-22.968238	9.744839	-0.840566				
26N	-14.392708	-9.875592	-2.357751	**64N**	-20.4967	6.05209	-0.661196				
27H	-13.536203	-11.566754	-2.431934	**65N**	-25.975093	2.312274	-4.069916				
28H	-16.115032	-9.614419	-3.10918	**66H**	-25.745201	0.464415	-4.429355				
29N	-14.109697	2.631552	1.35107	**67H**	-27.567764	3.218119	-4.558717				
30H	-12.942026	3.864464	2.221298	**68N**	-21.275623	13.323848	0.826014				
31H	9.374133	-11.582611	-6.690939	**69H**	-19.866743	14.250131	1.693934				
32H	7.005389	-13.225469	-5.07579	**70H**	-22.873965	14.213085	0.325477				
33C	15.849566	3.926439	-1.152407	**71C**	2.446494	-5.426656	1.427908				
34C	17.949457	5.535601	2.156644	**72C**	-6.47738	-4.762865	2.827167				
35C	20.388043	6.992053	5.339441	**73C**	-1.993751	-4.968546	2.184399				
36C	22.475089	4.804345	2.312476	**74C**	-3.833478	-5.565168	6.471588				
37C	24.231327	2.577535	-0.889878	**75C**	0.972974	-5.904964	5.724147				
38C	20.015041	3.153569	-1.189557	**76C**	-1.197573	-5.645462	7.545465				

2.2.7.2 Details of Partial Density of States

For analysis of the density of states (DOS), Multiwfn Ver. 3.6 (released on May 21, 2019) [3] were used to calculate the total DOS (TDOS) and partial DOS (PDOS) analysis. Two kinds of PDOS calculations were conducted: one is States of N 2p, O 2p and C 2p and the other is the states of fragments of BA units and melem units.

Melem_4

The PDOS of Melem_4 was conducted by the definition of C 2p and N 2p states. The C 2p state contains the atoms from No. 1-6, 14-19, 37-42 and 58-63, and the N 2p states contains the atoms from No. 7-13, 20-29, 32, 43-52, 64-71 and 74.

Melem_4BA1

The PDOS of Melem_4BA1 was conducted by two kinds of fragment definition. One is the state of C 2p, N 2p or O 2p. The C 2p state contains the atoms form No. 1-5,13-17, 31-36, 52-57, 71-72, 75, 79, 81 and 83. The N 2p state contains the atoms form No. 6-12, 18-26, 37-46, 58-65, 68, 73 and 77-78. The O 2p state contains the atoms form No. 80, 82 and 84.

The PDOS was also defined by the molecule fragments, i. e., the melem fragments or the BA fragments, were shown as follows. The states of melem fragments contains the atoms from No. 1-26, 31-46, 52-65, 68, 71-73, and the states of BA fragments contains the atoms from No. 75, 77-84. A schematic diagram of the definition of fragments is shown in Figure 2-2A.

Melem_4BA2

The PDOS of Melem_4BA1 was conducted by two kinds of fragment definition. One is the state of C 2p, N 2p or O 2p. The C 2p state contains the atoms from No. 1-5, 13-17, 33-38, 52-57, 71-76 and 84-87. The N 2p states contains the atoms from No. 6-12, 18-26, 29, 39-47, 58-65, 68, 78-79 and 92-93. The O 2p contains the atoms from No. 80-82 and 89-91.

The PDOS was also defined by the molecule fragments, i. e., the melem fragments and two BA fragments. The state of melem fragments contains the atoms from No. 1-26, 29, 33-47, 52-65, 68 and 71-72. The state of BA1 fragments contains the atoms from No.

73-76 and 78-82. The state of BA1 fragments contains the atoms from No. 84-87 and 89-93. A schematic diagram of the definitions of fragments is shown in Figure 2-2B.

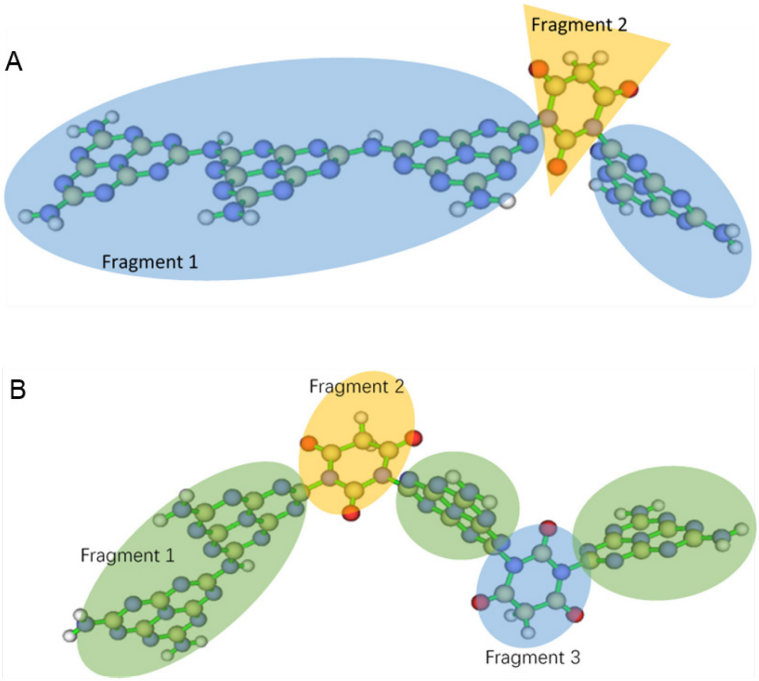

Figure 2-2. Schematic diagram of the definition of fragments. (A) Melem_4BA1: Fragment 1 is the melem fragment; Fragment 2 is the BA fragment. (B) Melem_4BA2: Fragment 1 is the melem fragment; Fragment 2 is the BA1 fragment; Fragment 3 is the BA2 fragment.

2.2.8 Preparation of alkali metal incorporated with PCN

Alkalized GCN (ACN) was synthesized by similar procedure to GCN, but the proper amount (10 mmol) of potassium chloride or sodium chloride was mixed with melamine and grounded together before calcination process. The as-prepared mixture was put into porcelain cup with a cap and calcined at 550 °C for 4 h with a ramping rate of 2.2 °C min^{-1}. After heating, the resulting product was gently grounded and treated under ultrasonication for 3 h as an aqueous solution (1 g L^{-1}) [4].

2.3 Results and discussion

2.3.1 Characterization of PCNBA

Successful synthesis of PCNBA from melem with copolymerization of barbituric acid was confirmed by XRD, TEM, SAED, EDS-mapping, and FT-IR absorption and XPS spectral analyses (Figure 2-3). XRD measurements were first used to investigate the crystallinity changes after co-polymerization of PCN when the amount of BA added was increased from 0.01 g to 0.5 g (Figure 2-3A). The two characterization diffraction peaks at

13.1° and 27.4° did not show any obvious shift, indicating that the interplanar spacing did not change [27, 31]. Additionally, the peaks at 13.0° assigned to the c-axis remained almost constant, whereas the intensity of the interlayer (002) peak at 27.4° clearly decreased. These results might be due to the disturbance of the graphitic structure by inserting BA motifs in the layered structure. Selected area electronic diffraction patterns of PCNBA (inserted in Figure 2-3B) also revealed that the crystalline structure of PCN did not change after the addition of the motifs. Therefore, the crystalline structure of the PCN matrix after BA co-polymerization almost remained constant compared with the pristine ones [35].

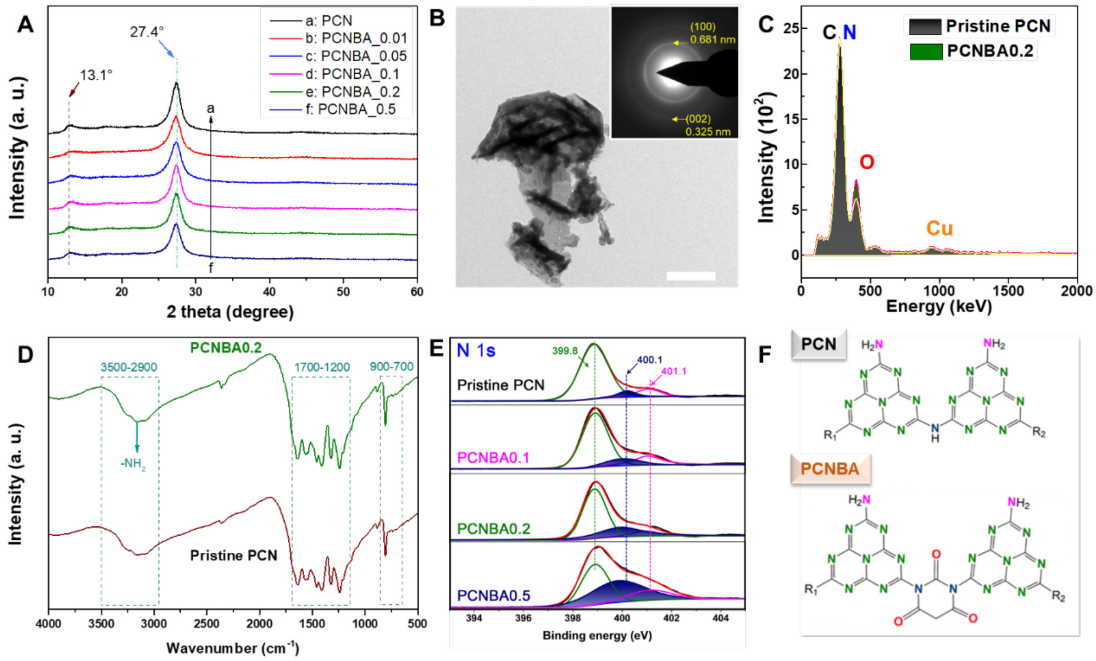

Figure 2-3. Thermal polymerization of different nitrogen rich precursors with barbituric acid. Precursors with (A) small molecular weights and (B) large molecular weights. (C) Polymerization process with barbituric acid and melem as precursors.

To investigate the elemental distribution differences between pristine PCN and PCNBA, scanning TEM-energy-dispersive X-ray spectroscopy (STEM-EDS) mappings were conducted. PCNBA0.2 was selected as a representative example of all PCNBA samples due to its optimum motif addition concentration. As shown in Figure 2-4 and Figure 2-3B, the morphologies of pristine PCN and PCNBA0.2 are quite similar, whereas the oxygen content of PCNBA0.2 is slightly increased (Figure 2-3C). It was also found that after copolymerization with BA, the oxygen homogenously distributed in the PCN matrix. To further investigate the functional groups of PCNBA0.2 after co-polymerization, Fourier

transform infrared (FT-IR) spectroscopy was performed. The FTIR spectra (Figure 1D) exhibited all of the characteristic stretch modes of aromatic CN heterocycles and the breathing mode of heptazine units at 1200-1700 cm^{-1} and 700-900 cm^{-1}, respectively [31, 35]. Additionally, the broad peaks between 2900 cm^{-1} and 3500 cm^{-1} could be assigned to hydroxyl (-OH) stretching (the adsorption water) and N-H stretching (PCNBA skeleton), indicating that the NH and/or NH_2 groups exist in the PCN matrix [31, 35]. Although PCNBA0.2 showed fundamental groups similar to those of the pristine PCN, the oxygen groups could hardly be identified by FTIR since due to overlap of heptazine breathing (1200-1700 cm^{-1}) and carbonyl stretching (1700 cm^{-1}) [35, 36].

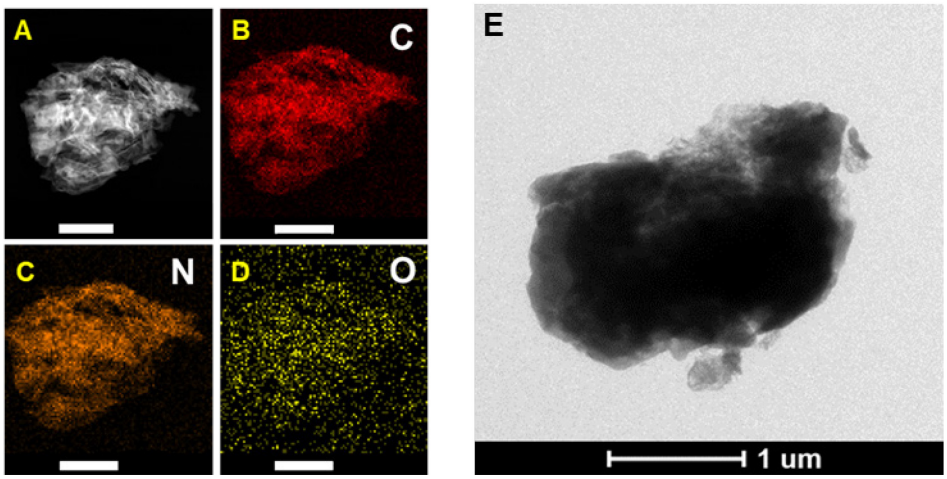

Figure 2-4. HAADF STEM images combined with EDX measurements and TEM images of PCNBA samples. (A) HAADF STEM image of PCNBA0.2. EDX mapping image of (B) C, (C) N and (D) O. (E) TEM image of pristine polymetric carbon nitride (PCN).

To further investigate the chemical composition and chemical states in as-prepared samples, XPS measurements were conducted. The survey spectra and C 1s high resolution spectra of pristine PCN revealed that only C and N elements exist (Figure 2-5 and 2-6), with a very small amount of O element that was due to the H_2O adsorption (Figure 2-7A, 532.5 eV). In the case of PCNBA, the O 1s peak gradually increased with the increasing addition of BA motifs, and a newly deconvoluted peak at 531.8 eV could be assigned to the existence of C=O groups in the PCN matrix (Figure 2-5 and 2-7B-7D) [35]. In the case of the C 1s high-resolution XPS spectra (Figure 2-6), the peak at 287.9 eV was assigned to N-C-N coordination, and the other deconvoluted peak at 284.6 eV was due to

sp^2 C-C bonds resulting from the carbon-adsorption contamination [31, 35, 37]. When BA was used in the co-polymerization, there was a newly deconvoluted peak at 288.7 eV that was assigned to the C=O coordination, which supports the results of O 1s spectra. In the high-resolution XPS spectrum of N 1s (Figure 2-3E), the three deconvoluted peaks observed at 401.1 eV, 400.1 eV and 398.8 eV were assigned to amino groups C-N-H, tertiary nitrogen groups, and sp^2 C-N-C bonds, respectively [35, 37]. Furthermore, the greater number of the BA units used in the co-polymerization was, the higher was the intensity of the peak at 400.1 eV. This result can be attributed to the co-polymerization nature of melem and BA (Figure 2-3F). When BA units were inserted into the melon molecules, the number of tertiary nitrogen groups of PCN-BA would increase accordingly. Further evidence is that the intensities of deconvoluted peaks at 284.6 eV (C-C) and 533.1 eV (O=C) gradually increased when the concentration of motifs (BA units) increased, indicating the existence of BA in the PCN matrix. Therefore, these results collectively indicated the well-preserved structure of PCN as well as the successful construction of BA units with the existence of C=O-based covalent networks through this copolymerization synthesis.

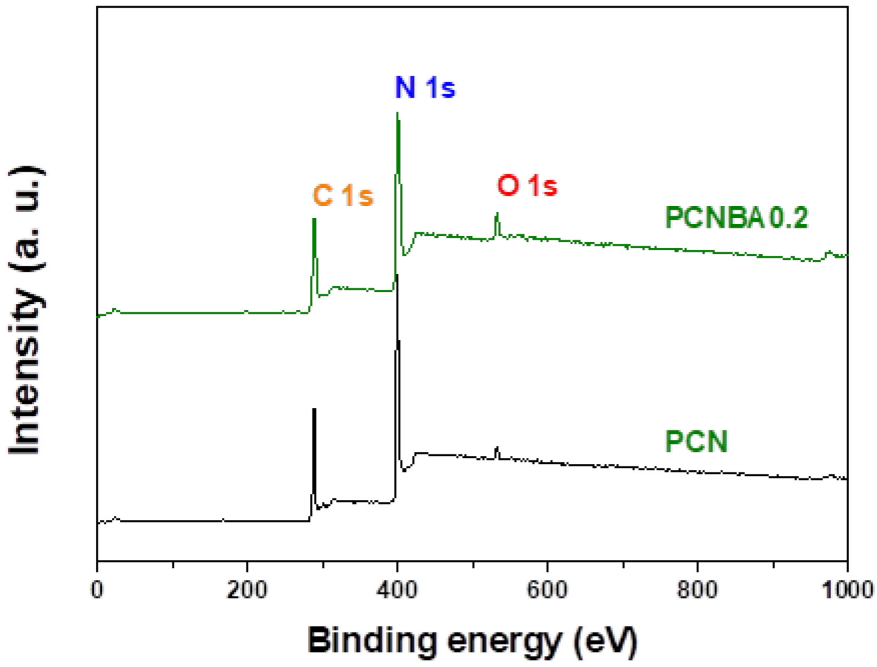

Figure 2-5. XPS survey spectra of PCN and PCNBA0.2.

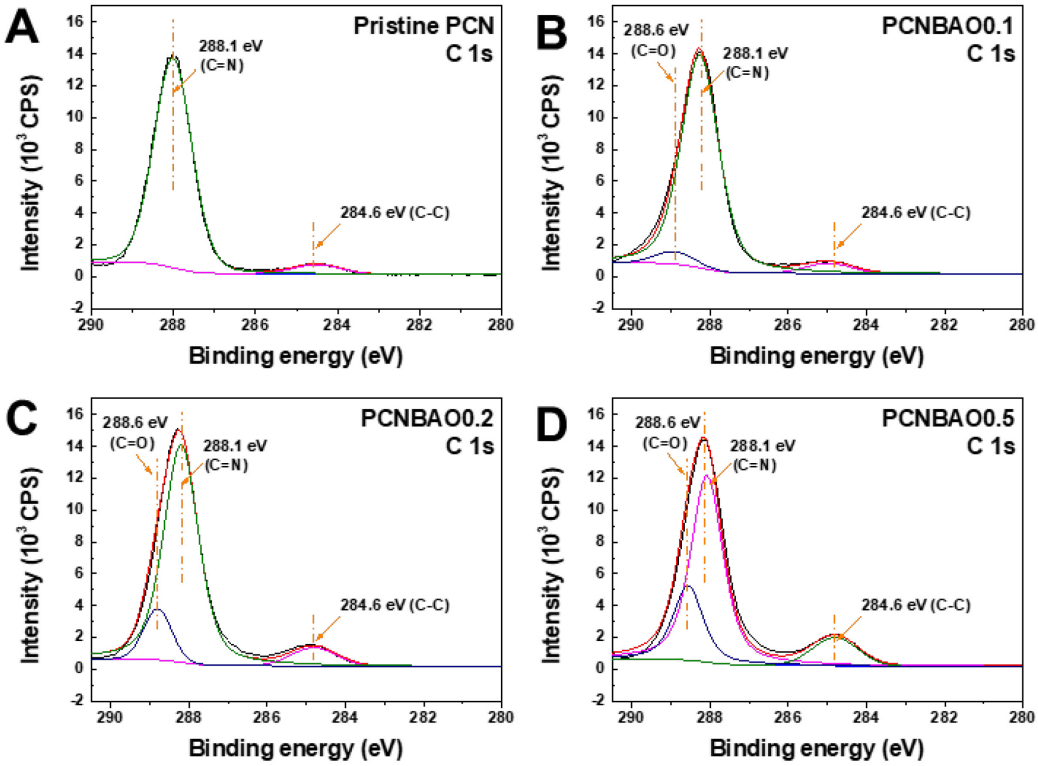

Figure 2-6. High resolution C 1s of (**A**) pristine PCN, (**B**) PCNBA0.1, (**C**) PCNBA0.2 and (**D**) PCNBA0.5.

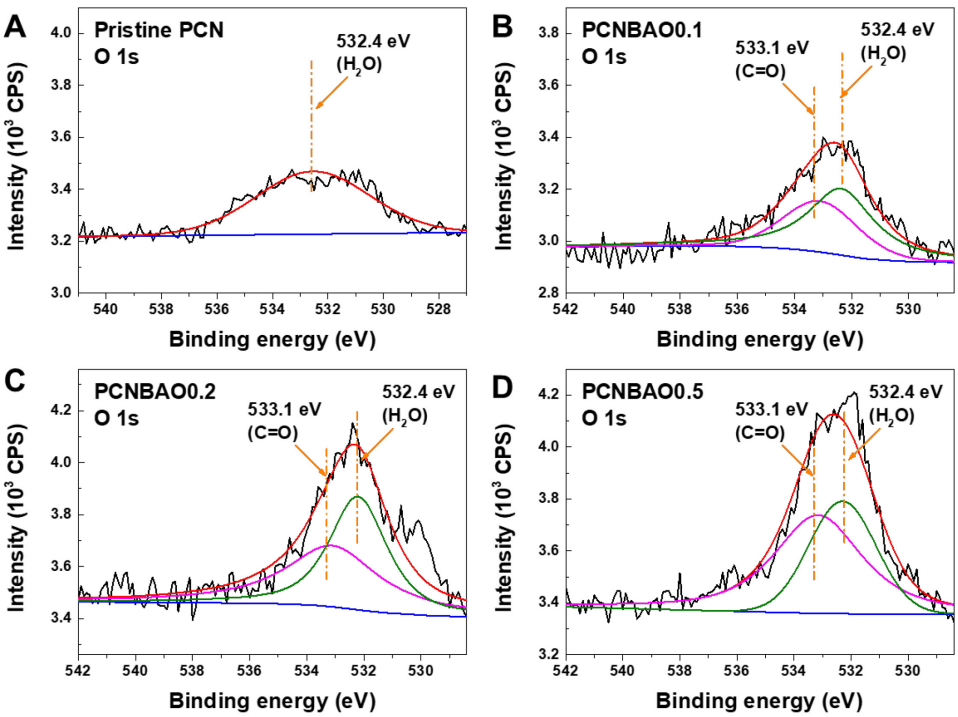

Figure 2-7. High resolution O 1s of (**A**) pristine PCN, (**B**) PCNBA0.1, (**C**) PCNBA0.2 and (**D**) PCNBA0.5.

The morphologies of bare PCN and PCNBA were investigated by TEM and BET measurements. As shown in Figure 2-4 and Figure 2-3B, both pristine PCN and PCNBA0.2 showed a bulky morphology. The surface area of PCNBA0.2 (2 m^2g^{-1}) was only slightly smaller than that of pristine PCN (3 m^2g^{-1}), which was also supported that the bulk morphology of the PCNBA0.2. The pore size and pore volume of the PCNBA0.2 decreased slightly when BA units were introduced to the PCN matrix. Since the holes formed in bulk PCN material are attributed to the secondary particle piled pores, the slight decrease of PCNBA0.2 may be attributed the smaller particle size of PCNBA0.2 compared with that of pristine PCN. As shown in Figure 2-8D, PCNBA prepared with BA and melem showed a macroscopic deep orange color, rather than the pale yellow of pristine PCN, providing the success in the improved visible-light absorption [31, 35]. To determine the precise band positions of PCNBAs, UV-vis, Mott-Schottky measurements and valence band XPS were conducted to investigate the bandgap width, CBM and VBM, respectively.

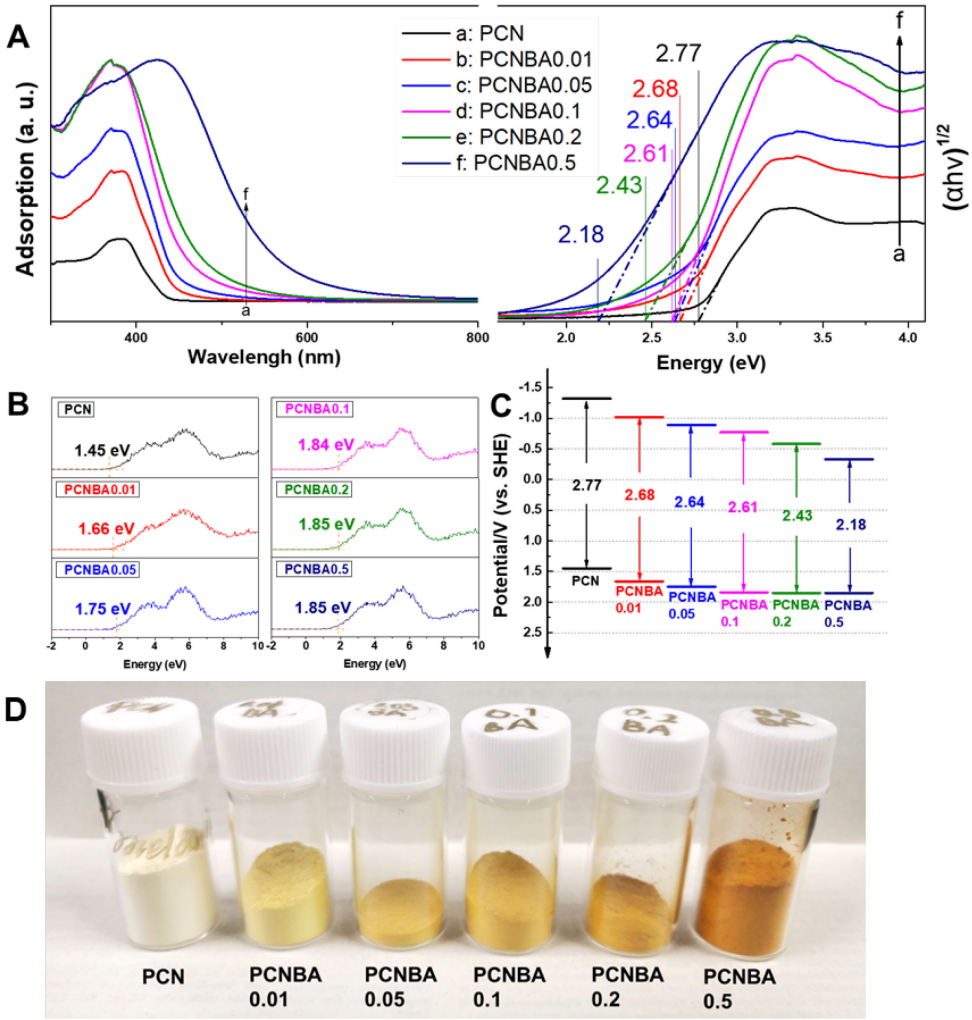

Figure 2-8. Band positions and photographs of PCN and PCNBA samples. (**A**) UV-vis spectra of PCN and PCNBA samples: absorbance spectra on the left and Tauc-plots on the right. (**B**) Valence band XPS of PCN and PCNBA samples. (**C**) Band diagrams of PCN and as-prepared PCNBA samples. (**D**) Digital photographs of pristine PCN and PCNBA samples.

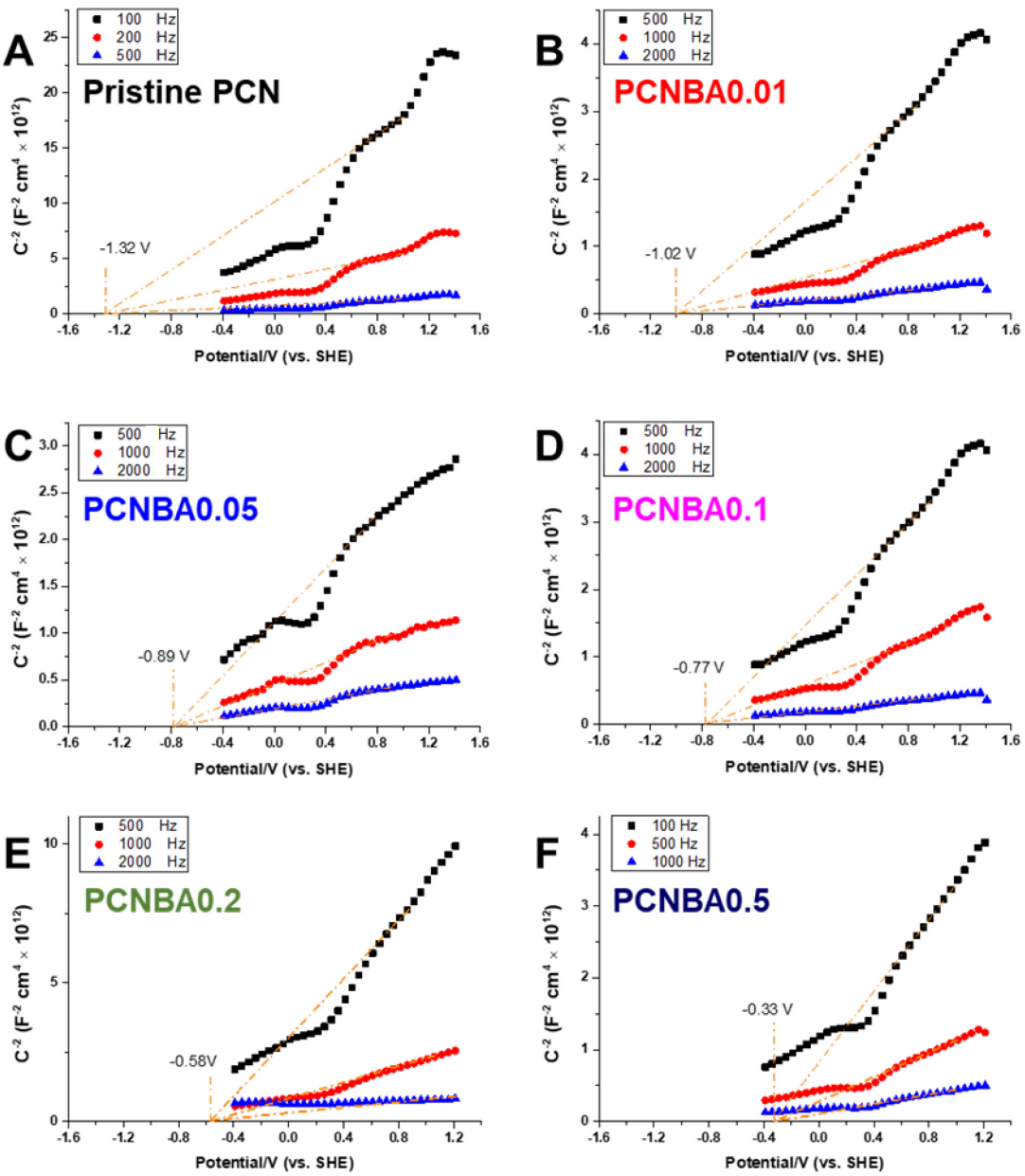

Figure 2-9. Mott-Schottky plots of PCN and PCNBA samples. (**A**) Pristine PCN samples. (**B-F**) PCNBA samples.

As shown in Figure 2-8A, the light adsorption (<450 nm) of PCNBAs significantly increased, possibly due to the changes in electronic states [13]. With increased addition of BA motifs, the adsorption of long-wave visible light gradually increased, resulting in the narrowing of bandgap width from 2.77 eV to 2.18 eV. Mott-Schottky plots revealed that the CBM of PCNBA samples gradually became more positive from -1.33 eV for pristine PCN to -0.33 eV for PCNBA0.5 (Figure 2-9). VB-XPS results also showed that the VBM of PCNBA gradually became positive from 1.45 eV to 1.85 eV (Figure 2-8B). By summarizing

these results for band positions, we can draw band position diagrams of pristine PCN and PCNBA samples, as shown in Figure 2-8C. Generally, an ideal photocatalyst for H_2O_2 production from dissolved O_2 and water usually has two crucial properties: one is reducing O_2 to effectively produce H_2O_2 (eq. 2) and the other is sufficient oxidization potential for overcoming the large overpotential of water oxidation (eq. 3). Since the melem units in the PCN matrix can form 1,4-endoperoxides for efficient H_2O_2 production, the bottleneck of improving photocatalytic H_2O_2 production by PCN from water and O_2 is to overcome the insufficient oxidation potential (VBM_{PCN}=1.45 eV vs. a standard hydrogen electrode, SHE) for water oxidation. Compared with other samples, PCNBA0.1, PCNBA0.2 and PCNBA 0.5 eV all had positive VBMs at 1.85 eV (vs. SHE), indicating that water oxidation might occur on these catalysts, thus leading to an effective H_2O_2 production from O_2 and water.

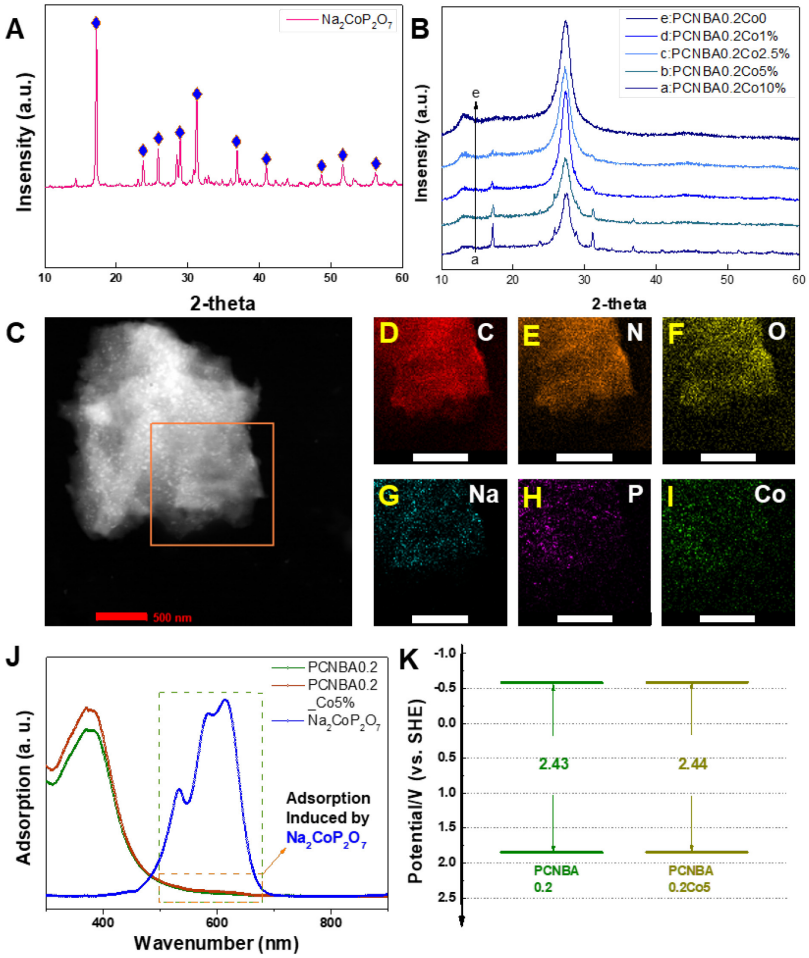

Figure 2-10. Characterization of co-catalyst-loaded PCNBA. (**A**) XRD patterns of $Na_2CoP_2O_7$. (**B**) XRD patterns of PCNBA loaded with $Na_2CoP_2O_7$ (PCNBAO0.2Co5%). (**C**) HAADF of PCNBA0.2Co5%. STEM EDS mapping images of (**D**) Carbon, (**E**) Nitrogen, (**F**)

Oxygen, (**G**) Sodium, (**H**) Phosphorus and (**I**) Cobalt. (**J**) UV-vis absorbance spectra of pure $Na_2CoP_2O_7$ and PCNBAO0.2Co5%. (**K**) Band diagrams of $Na_2CoP_2O_7$ and PCNBAO0.2Co5%.

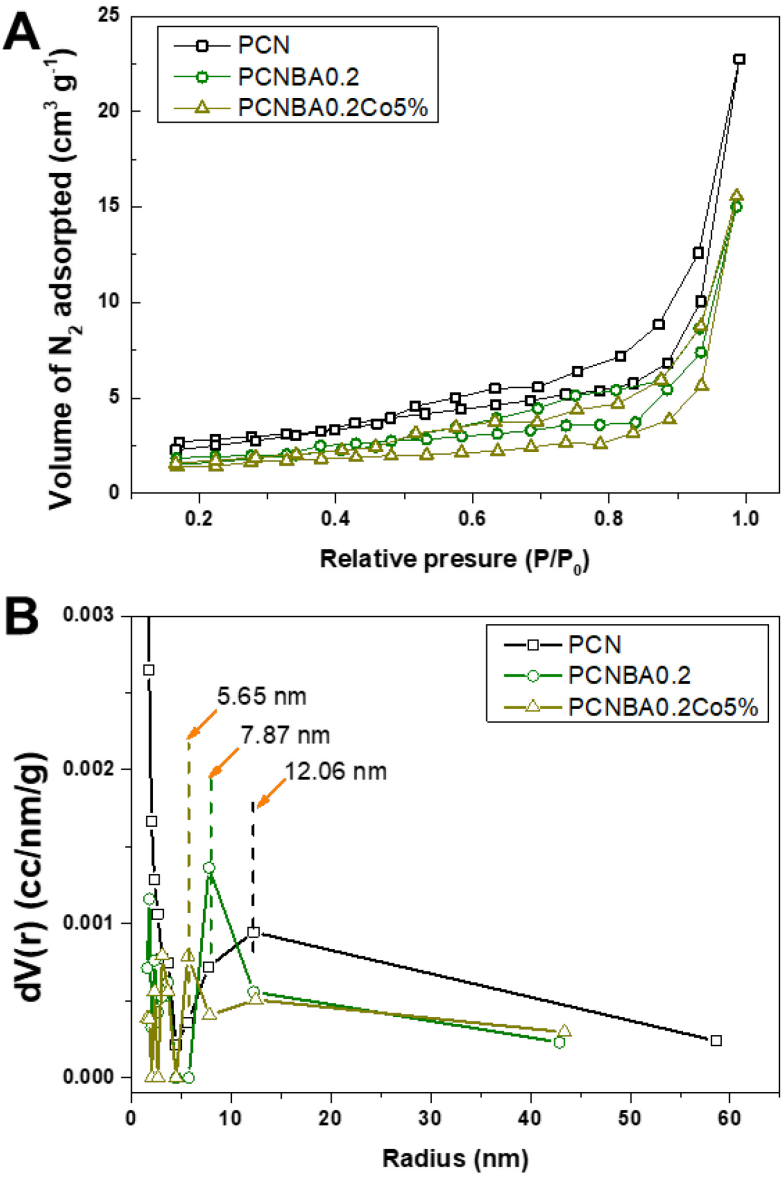

Figure 2-11. Brunauer-Emmett-Teller (BET) surface area analysis of PCN, PCNBA0.2 and PCNBA0.5. (**A**) Dynamic adsorption curves of as-prepared PCN samples. (**B**) Pore size and pole volume distribution of o as-prepared PCN samples.

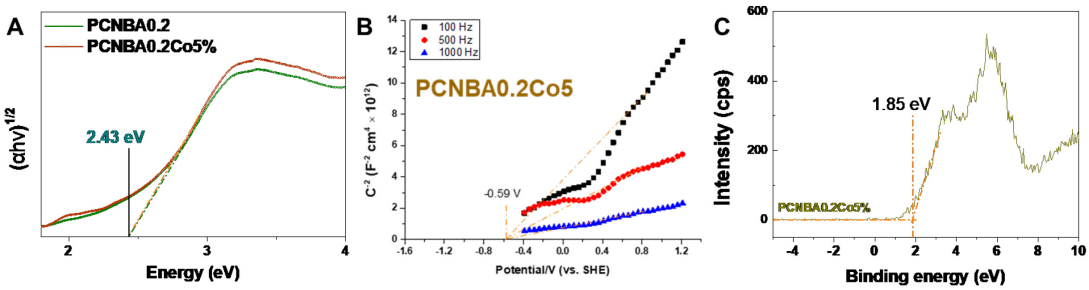

Figure 2-12. Band diagram measurement for PCNBA0.2Co5. (A) UV-Vis absorption spectra of PCNBA0.2 and PCNBA0.2Co5% with Tauc conversion. (B) Mott-Schottky plots of PCNBA0.2Co5%. (C) VB-XPS of PCNBA0.2Co5%.

To further improve the overall H_2O_2 production by PCNBA from water and O_2, loading a co-catalyst for water oxidation is an effective strategy since the VBM of PCNBA is still more negative than those of traditional photocatalysts for water oxidation such as TiO_2 [38], Ta_2O_5 [39], WO_3 [40, 41], $BiVO_4$ [42]. Therefore, $Na_2CoP_2O_7$, one of the most efficient co-catalysts for water oxidation, was prepared for enhancing the water oxidation [33]. X-ray diffraction (XRD) patterns of the synthesized $Na_2CoP_2O_7$ matched excellently with those in previous reports without impurities [33, 34, 44]. After loading $Na_2CoP_2O_7$ on PCNBA0.2 by a facile ball milling method, the characterization peak of PCN at diffraction angles of 13.1° and 27.4° still existed, indicating that the crystalline structure was well maintained. Additionally, the peak intensities of $Na_2CoP_2O_7$ diffractions gradually increased with an increase in the loading amount, indicating that $Na_2CoP_2O_7$ also maintained the same structure after the ball milling. To investigate the distribution properties of $Na_2CoP_2O_7$, high-angle annular dark field (HAADF) STEM combined with energy-dispersive X-ray spectroscopy (STEM-EDS) mappings were conducted. As shown in Figure 2-10C, some bright particles were dispersed well on the large bulk material, and the average particle size was ~20 nm. EDS mapping showed that the elemental components of the large bulk material contain high concentrations of carbon, nitrogen and oxygen, which is consistent with the mapping image of PCNBA0.2. As shown in Figure 2-10G-I, the elemental compositions of bright particles in Figure 2-10C are Na, P and Co, indicating that these particles are $Na_2CoP_2O_7$. Therefore, the proposed ball milling strategy could effectively disperse $Na_2CoP_2O_7$ onto PCNBA samples. The surface area of PCNBA0.2Co5% (2 m^2g^-

^{1}) is almost as same as that of pristine PCNBA0.2 (2 m^2g^{-1}), indicating that loading of the co-catalyst did not significantly change the morphology of PCNBA0.2 (Figure 2-10C). Additionally, pore size and pore volume were further decreased after the co-catalyst loading, indicating that the loaded $Na_2CoP_2O_7$ particle has filled pores piled by secondary particles (Figure 2-12). The BET analysis further supported the TEM and STEM-EDS mapping results, demonstrating the successful loading of co-catalyst. UV-vis was conducted to determine the effect of $Na_2CoP_2O_7$ loading on the light absorption properties of PCNBA since $Na_2CoP_2O_7$ could naturally absorb orange light (Figure 2-10J, blue line.). The UV-vis spectrum of PCNBA loaded with $Na_2CoP_2O_7$ (mass ratio of 5%) is almost as same as that of PCNBA0.2 except for a small absorption band that appeared between 550 nm and 650 nm. This small adsorption band may be due to the light absorption introduced by $Na_2CoP_2O_7$. Tauc-plots (Figure 2-12A), Mott-Schottky plots (Figure 2-12B) and VB-XPS measurements (Figure 2-12B) also confirmed that the band positions did not change after $Na_2CoP_2O_7$ loading. Therefore, uniformly dispersed $Na_2CoP_2O_7$ particles on PCNBA0.2 could serve as a co-catalyst to further improve the photocatalytic water oxidation, leading to an improved H_2O_2 production.

2.3.2. Photocatalytic activities of PCNBA and PCNBACo for H_2O_2 production

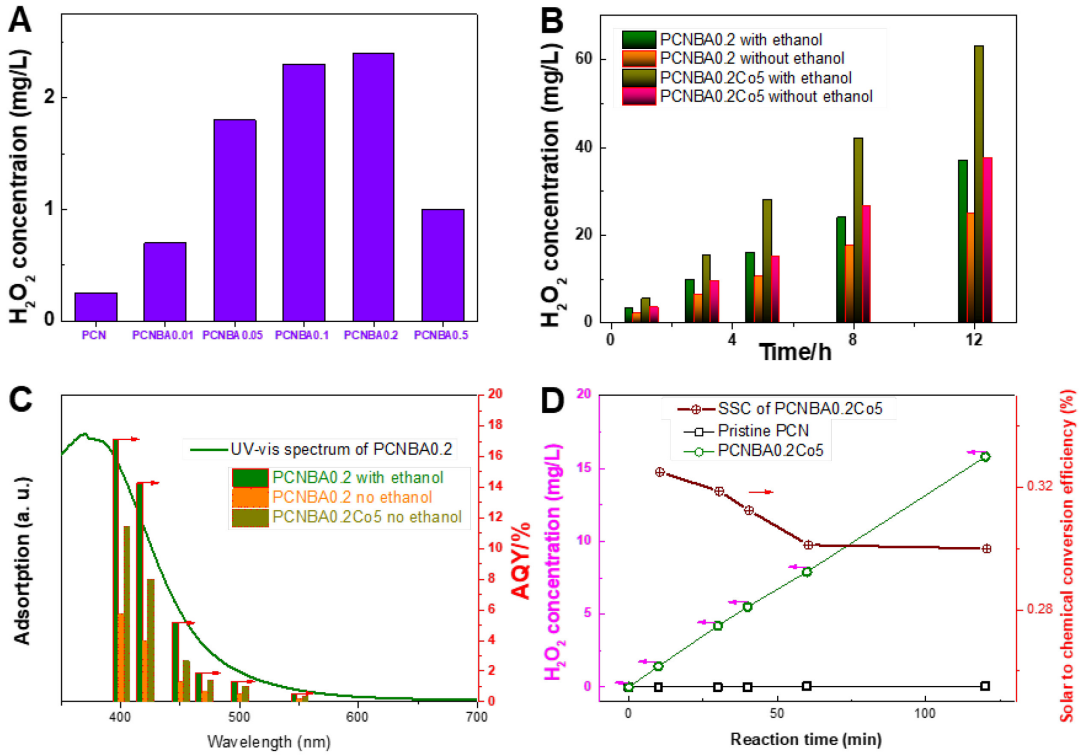

Figure 2-13. Photochemical properties of PCNBAs and PCNBA0.2Co5%. Photoluminescence spectra of (**A**) PCN and PCNBA samples and (**B**) PCNBA0.2Co5% under 365 nm excitation. (**C**) Photocurrents of electrodes prepared by PCN, PCNBA0.2 and PCNBA0.5 (line a: pristine PCN; line b: PCNBA0.2; line c: PCNBA0.2Co0.5%). (**D**) EIS of electrodes prepared by PCN, PCNBA0.2 and PCNBA0.5 illuminated under visible light irradiation.

Since the inefficient water oxidation of PCN (VBM ranging from 1.4 eV-1.6 eV vs. SHE), most of photocatalytic production of H_2O_2 based on PCN system were investigated by utilizing electron donors. The band position of PCNBA samples is positively shifted (Figure 2-10K), i.e., the photocatalytic water oxidation ability should be improved. Therefore, the condition of photocatalytic H_2O_2 production must be investigated with and without the addition of electron donors (ethanol). First, the optimized BA unit concentration was investigated, as shown in Figure 2-13A. The activity of pure PCN for H_2O_2 production is quite low, whereas the PCN samples with BA motifs all exhibited markedly increased activities. Among the various PCN samples modified with BA, the activity of PCNBA0.2 was the highest which is the 9.6-fold compared with that of PCN counterpart. It should be noted that PCNBA0.5 produced less than half the amount H_2O_2 compared with PCNBA0.2,

which may be attributed to the positive shift of CBM (-0.33 V vs. SHE). Since O_2 reduction to generate H_2O_2 is a multi-electron transfer reaction, the overpotentials of multi-electron transfer reactions are non-negligible. For instance, hydrogen evolution reactions usually need >0.4 V without loading Ni or Pt as HER cocatalysts. The relatively positive CBM of PCNBA0.5 may not provide sufficient potentials for efficient O_2 reduction via two-electron pathways.

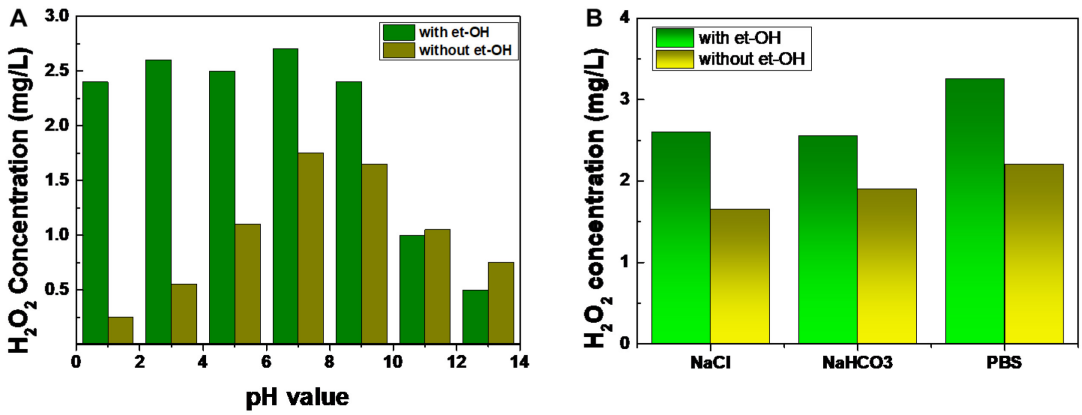

Figure 2-14. Optimization of experimental parameters. (A) Optimization of pH condition for H_2O_2 production when PCNBA0.2 was used as a photocatalyst. (B) Effects of ion on H_2O_2 production when PCNBA0.2 was used as a photocatalyst.

The optimal pH conditions were investigated by measuring photocatalytic H_2O_2 production by utilizing PCNBA0.2 (Figure 2-14A). When ethanol was introduced into the system, the amount of H_2O_2 remained almost constant when the pH value was increased from 1 to 9 and then decreased drastically. This result indicates that the lowest $[H^+]$ is 10^{-9} mol L^{-1} for the O_2 reduction to H_2O_2 production. When no sacrificial agent was added into the system, the amount of H_2O_2 rapidly increased before the pH value reaches 7 and then gradually decreased, indicating that a low concentration of OH^- also restricts the generation of O_2 from water [11, 44]. Therefore, the optimal pH condition for H_2O_2 production from O_2 and water is 7-9. The optimal solution was also investigated, as shown in Figure 2-14B. A photocatalyst in phosphate buffer solution (PBS) showed the highest activity for H_2O_2 production with or without the existence of ethanol. This is thought to be because phosphate ions can serve as a stabilizer for H_2O_2 under light irradiation [11]. The pH value of the phosphate buffer ranges from 5.5 to 8.5, which is also consistent with the optimal

pH condition for H_2O_2 production. Figure 2-13B shows the time-dependent change of the amounts of H_2O_2 produced. The generation rates of H_2O_2 on PCNBA0.2 and PCNBA0.2Co5% kept almost constant even after long-term reaction, indicating that the catalyst could continuously produces H_2O_2 with good stability. Figure 2-13C shows the action spectrum on PCNBA0.2 and PCNBA0.2Co5% determined by light irradiation for H_2O_2 production. Compared with the absorption spectra of the catalyst, the ΦAQYs agree well, which shows that the production of H_2O_2 is attributed to the bandgap excitation of PCNBA0.2. ΦAQYs at 420 nm of PCNBA0.2 and PCNBA0.2Co5% were determined to be 4.0% and 8.0%, respectively, much which are higher than that (6.1%) of g-C_3N_4/PDI/rGO0.05 [15], one of the most efficient PCN-based photocatalysts for nonsacrificial H_2O_2 production. Additionally, the action adsorption edge extend form 450 nm for g-C_3N_4/PDI/rGO0.05 to 550 nm for PCNBA0.2 and PCNBA0.2Co5%, indicating that the band engineering with BA units significantly promoted the photon usage. The ΦAQY of PCNBA0.2Co5% was almost two-times larger than that of PCNBA0.2, and no H_2O_2 was produced by the excitation between 550 nm and 650 nm, indicating that the excitation introduced by $Na_2CoP_2O_7$ does not produce H_2O_2, i. e. $Na_2CoP_2O_7$ plays a role as a co-catalyst during photocatalytic H_2O_2 production. The SCC efficiency for H_2O_2 production on PCNBA0.2Co5% was measured by AM1.5G solar simulator (1 sun irradiation) to be 0.30% (see Experimental Section) and was almost constant even after the photoirradiation for 2 h. As shown in Figure 2-15, the adsorption band at 600-900 cm^{-1} and 1200-1700 cm^{-1} scarcely changed after the 5 run, indicating the functional groups of PCNBA0.2 kept almost constant after the reaction. The XRD of the samples obtained after 5 circles showed similar diffraction patterns as the raw sample, indicating that the crystallinity of PCNBA0.2 and $Na_2CoP_2O_7$ rarely changed during the photocatalytic H_2O_2 production. The intensities of the diffractions contributed by $Na_2CoP_2O_7$ showed a slight decrease. This slight decrease may be due to the loaded co-catalyst slightly detached during the long-time stirring during the H_2O_2 production. After 5 cycles of measurements, the efficiency was still maintained at 90% (Figure 2-15C), indicating the good stability of the catalyst. The SCC efficiency of PCNBA0.2Co5% is comparable to the highest levels obtained by PCN-based

photocatalysts (Figure 2-13D), suggesting that band engineering combined with co-catalyst loading has great potential for the development of highly efficient photocatalysts with improved activity for nonsacrifical H_2O_2 production. This strategy would also inspire other artificial photosynthesis, such as overall water splitting, N_2 fixation, etc. [15-18, 45].

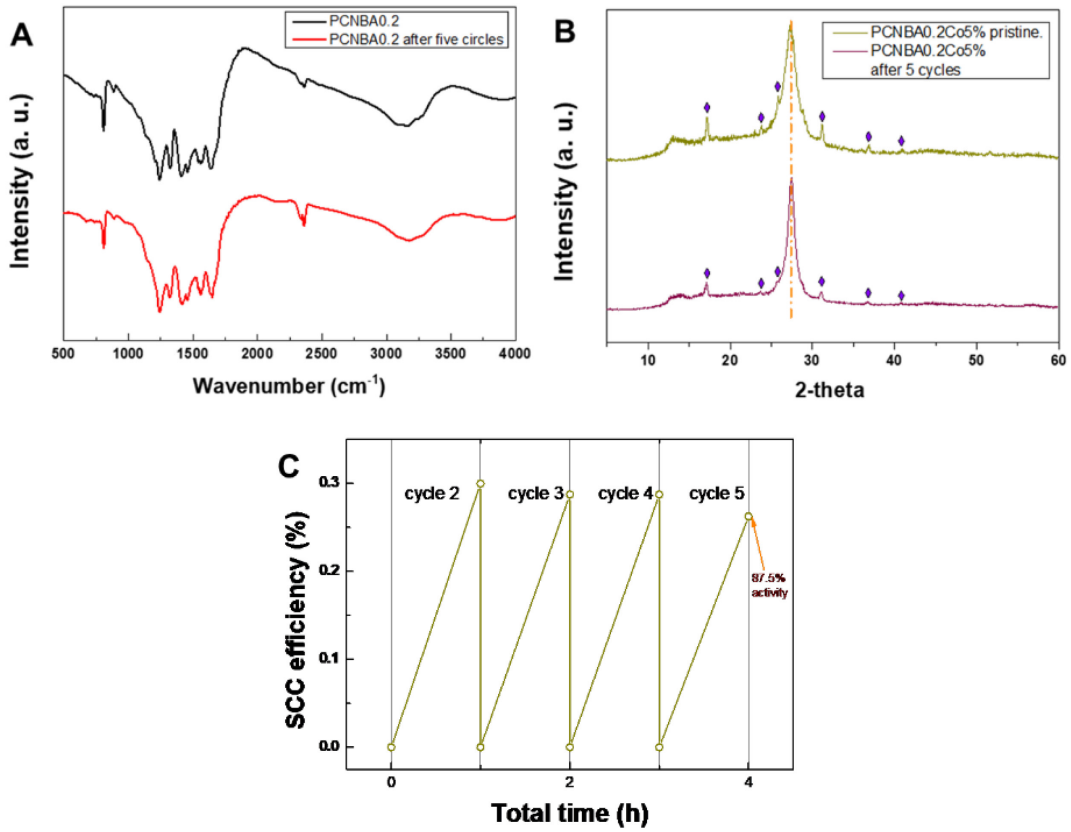

Figure 2-15. Stability investigation. (**A**) FT-IR measurements of PCNBA0.2 before and after 5 run. (**B**) XRD patterns of PCNBA0.2Co5% before (upper) and after (lower) 5 cycles of photocatalytic measurements. (**C**) Photostability of PCNBA0.2Co5% for H_2O_2 production after 5 reaction cycles.

2.3.3 Mechanism of photocatalytic H_2O_2 production

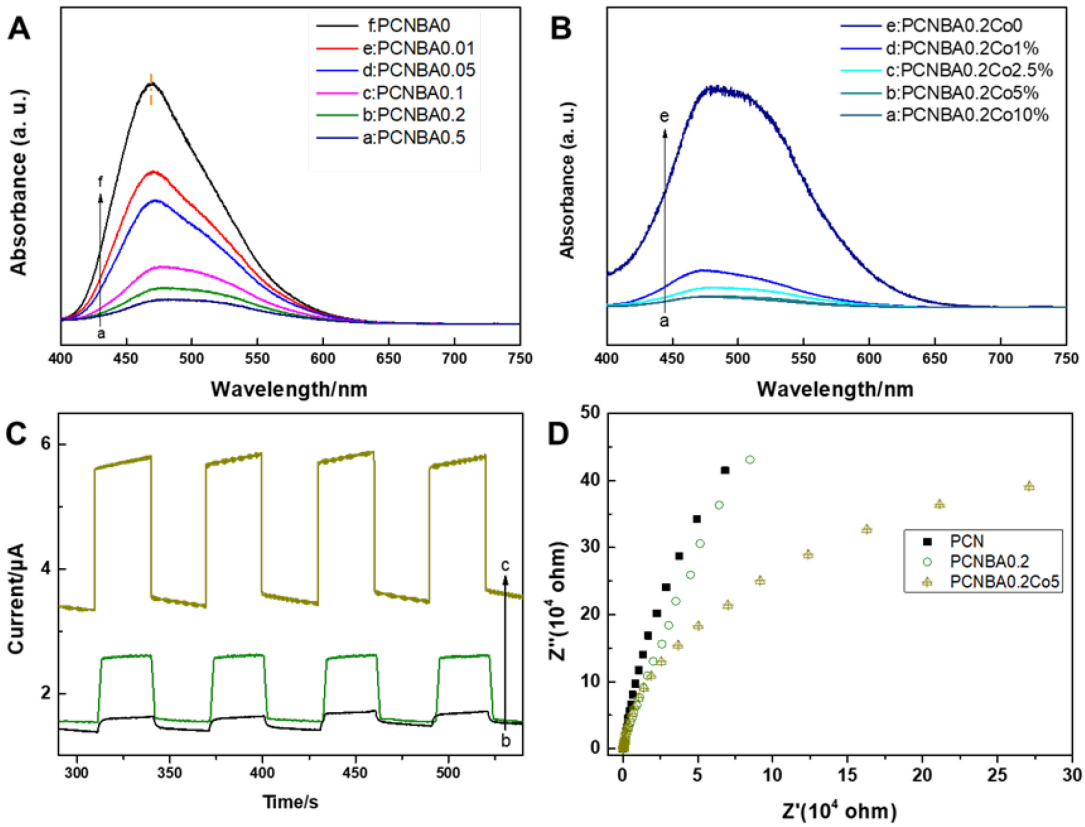

Figure 2-16. Photochemical properties of PCNBAs and PCNBA0.2Co5%. Photoluminescence spectra of (**A**) PCN and PCNBA samples and (**B**) PCNBA0.2Co5% under 365 nm excitation. (**C**) Photocurrents of electrodes prepared by PCN, PCNBA0.2 and PCNBA0.5 (line a: pristine PCN; line b: PCNBA0.2; line c: PCNBA0.2Co0.5%). (**D**) EIS of electrodes prepared by PCN, PCNBA0.2 and PCNBA0.5 illuminated under visible light irradiation.

As shown in the photoluminescence (PL) spectra (Figure 2-16A), there was a redshift toward a longer wavelength with an increase in the modified content of BA together with a notable decrease in intensity, being consistent with previous reports [31, 35]. Additionally, loading of $Na_2CoP_2O_7$ did not change the emission wavelength, whereas PL intensity significantly decreased with increase in the loading amount of $Na_2CoP_2O_7$, indicating that the co-catalyst also improves the charge separation of PCNBA samples (Figure 2-16B). Photocurrent (I_{ph}) measurements of the samples showed a significant increase in I_{ph} of PCNBA0.2 compared to that of pristine PCN (Figure 2-16C), indicating enhanced efficiency of the charge separation. With loading of $Na_2CoP_2O_7$, I_{ph} was further enhanced, indicating that the co-catalyst loading also significantly suppressed recombination, leading to an

improved charge transference. Moreover, the diameter of semicircle (PCNBA0.2Co5%) was the smallest in Nyquist plots measurements by the A. C. electrochemical impedance spectra (EIS) (Figure 2-16D), indicating that PCNBA0.2Co5% showed the best charge transfer. Therefore, co-polymerization of BA units and loading of a co-catalyst significantly suppressed charge recombination and promoted charge transfer of the PCNBA, leading to an enhanced photocatalytic H_2O_2 production.

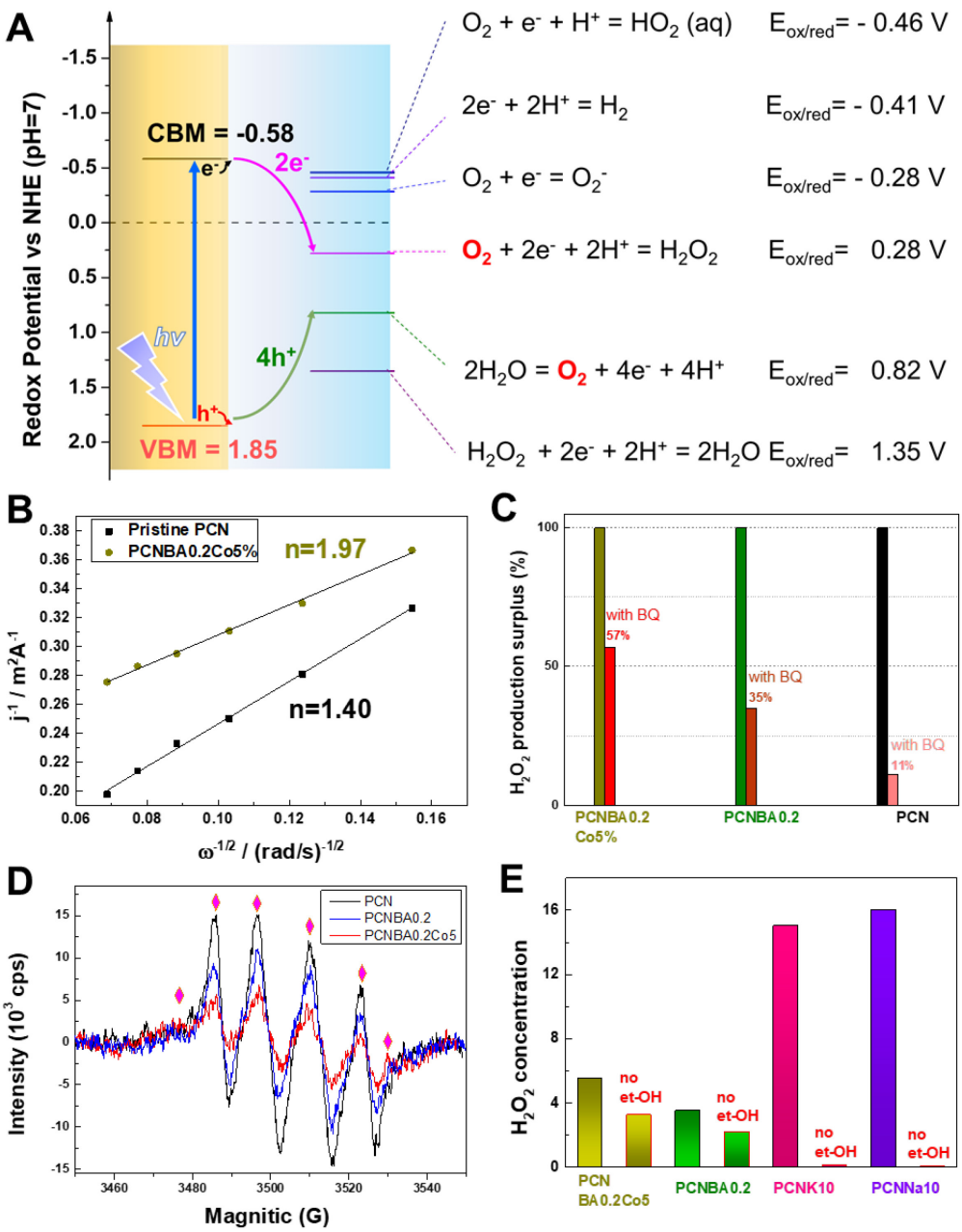

Figure 2-17. Mechanism of PCNBA0.2 with co-catalyst loading. (A) Possible photo-redox reactions during photocatalytic H_2O_2 production with PCNBA0.2. (B) H_2O_2 production with or without 1 mM BQ in the systems of PCN, PCNBA0.2 and PCNBA0.2Co5%. (C) ESR

spectra of PCN, PCNBA0.2 and PCNBA0.2Co5% in methanol solution using 5,5-diemthyl-1-pyrroline N-oxide as a radical trapper. (D) Koutecky−Levich plots of data obtained by RDE measurements in a buffered pH 7 solution with O_2 at −0.6 V (vs Ag/AgCl). (E) Comparison of the activities of PCNBAs and alkali metal-incorporated PCNs for H_2O_2 production.

The possible photo-redox reactions in the PCNBA0.2 system are summarized in Figure 2-17A. An ORR reaction via the one-electron transfer pathway is a competitive reaction for H_2O_2 generation at the reduction side. Water oxidation via the 4-electron pathway to generate O_2 and water oxidation via the 2-electron pathway to generate H_2O_2 are competitive reactions at the oxidation side as follows:

$$O_2 + 2e^- + 2H^+ \rightarrow H_2O_2 \text{ +0.28 V vs. RHE (pH=7)} \quad (6)$$

$$2H_2O - 2e^- \rightarrow H_2O_2 + 2H^+ \text{ +1.35 V vs. RHE (pH=7)} \quad (7)$$

The CBM and VBM of PCNBA0.2 are -0.58 V and 1.85 V, respectively, indicating that both eq. 6 and eq. 7 are thermodynamically possible [46]. Ag^+ was added into the system as an electron acceptor to improve charge separation, resulting in acceleration of the photocatalytic oxidation reactions. As shown in Figure 2-18A, O_2 was steadily generated when Ag^+ was added, whereas H_2O_2 was hardly detected in the photocatalytic system of either PCNBA0.2 or PCNBA0.2Co5%. These results proved that H_2O_2 production does not originate from the photocatalytic water oxidation reactions. It should be noted that the activities of PCN samples for photocatalytic oxygen evolution reactions (OERs) were significantly increased after the band engineering and were further increased by the loading of $Na_2CoP_2O_7$. These results revealed that the more positive VBM of PCNBA promotes the OER activity and that $Na_2CoP_2O_7$ behaves as a co-catalyst for water oxidation. The accelerated OER may further increase the overall reaction rate for photocatalytic H_2O_2 production from water and oxygen.

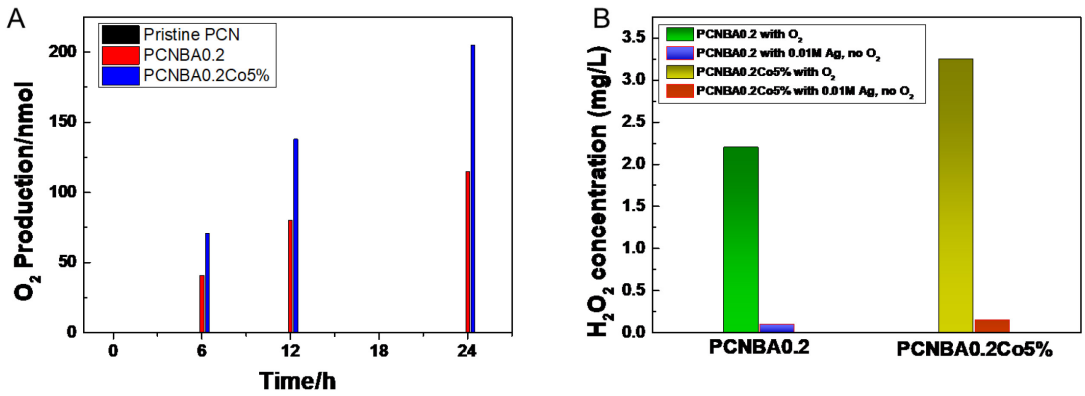

Figure 2-18. Oxygen evolution reaction (OER) measurements. (A) OER activity compared with PCN and PCNBA0.2Co5%. (B) Photocatalytic H_2O_2 production by PCNBA0.2 and PCNBA0.2Co5% with an electron acceptor (O_2) or (Ag^+).

Since H_2O_2 can be generated via a one-step, two-electron transfer reaction or via a stepwise one-electron transfer reaction (Figure 2-17A), rotating disk electrode (RDE) analysis were conducted to investigate the properties of the electron transfer to O_2 on PCN samples. The number of electrons (n) transferred to O_2 were estimated by the results obtained from the slope value of Koutecky–Levich plots (Figure 2-17B and 2-19). The estimated "n" value was 1.4 for pristine PCN, indicating that one-electron reduction dominates in the photocatalytic O_2 reduction. In the case of PCNBA0.2Co5%, the estimated "n" value was close to 2, indicating that O_2 molecules were reduced via an apparent two-electron transfer reaction. To get the insight of the intermediate products during photocatalytic H_2O_2 production, sacrificial reagents for quenching of active species quenching were added into the system. As shown in Figure 2-17C, with the addition of a $\cdot O_2^-$ scavenger, p-benzoquinone (BQ. 1 mM), the H_2O_2 production significantly decreased in all PCN photocatalytic systems, indicating that $\cdot O_2^-$ is a crucial intermediate during photocatalytic H_2O_2 production. This result supports the previous theory that the H_2O_2 production catalyzed by a PCN-based photocatalyst is a rapid step-wise one-electron to one-electron reaction [12-19], which was first proposed by Prof. Shiraishi and co-workers. The magnitude of decrease in H_2O_2 production with the addition of BQ followed the sequence of PCN, PCNBA0.2 and PCNBA0.2Co5%, indicating less lifetime of $\cdot O_2^-$ in PCNBA0.2 systems [47], i. e., the generated $\cdot O_2^-$ may rapidly be further reduced to form 1,4-endoperoxide. In the case of pristine PCN, the generated $\cdot O_2^-$ may hardly be reduced

to form 1,4-endoperoxide, resulting in the accumulation of $\cdot O_2^-$.

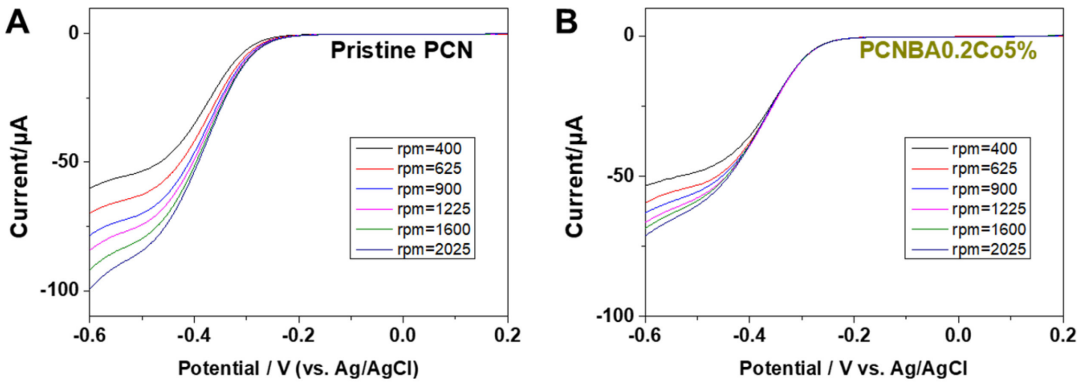

Figure 2-19. RDE measurements. (**A**) Pristine PCN and (**B**) PCNBA0.2Co5%-modified electrodes in aqueous solutions with saturated O_2. The pH value of the solution is 13.

ESR analysis also confirmed the results of scavenger quenching experiments (Figure 2-17D). When methanol was used as a solvent and electron donor, 6 characterization peaks of DMPO-$\cdot O_2^-$ were observed in the spectrum of PCN, indicating that the superoxide radical is an intermediate product during photocatalytic H_2O_2 production [37]. The peak intensity of DMPO-$\cdot O_2^-$ in the PCNBA0.2 system slightly decreased, and the intensity significantly decreased in the PCNBA0.2Co5% system. The rapid reduction of $\cdot O_2^-$ in the photocatalytic system of PCNBA0.2Co5% could be attributed to the promoted charge separation. The improved charge separation results in a high density of photoelectrons trapped in the CB, which could accelerate further reduction of $\cdot O_2^-$ to form 1,4-endoperoxide (Scheme 2) [16], rather than to remain as $\cdot O_2^-$ in the case of pristine PCN. Therefore, the apparent electron transfer number was calculated to be 2 in the PCNBA0.2Co5% system, which significantly promoted the H_2O_2 production.

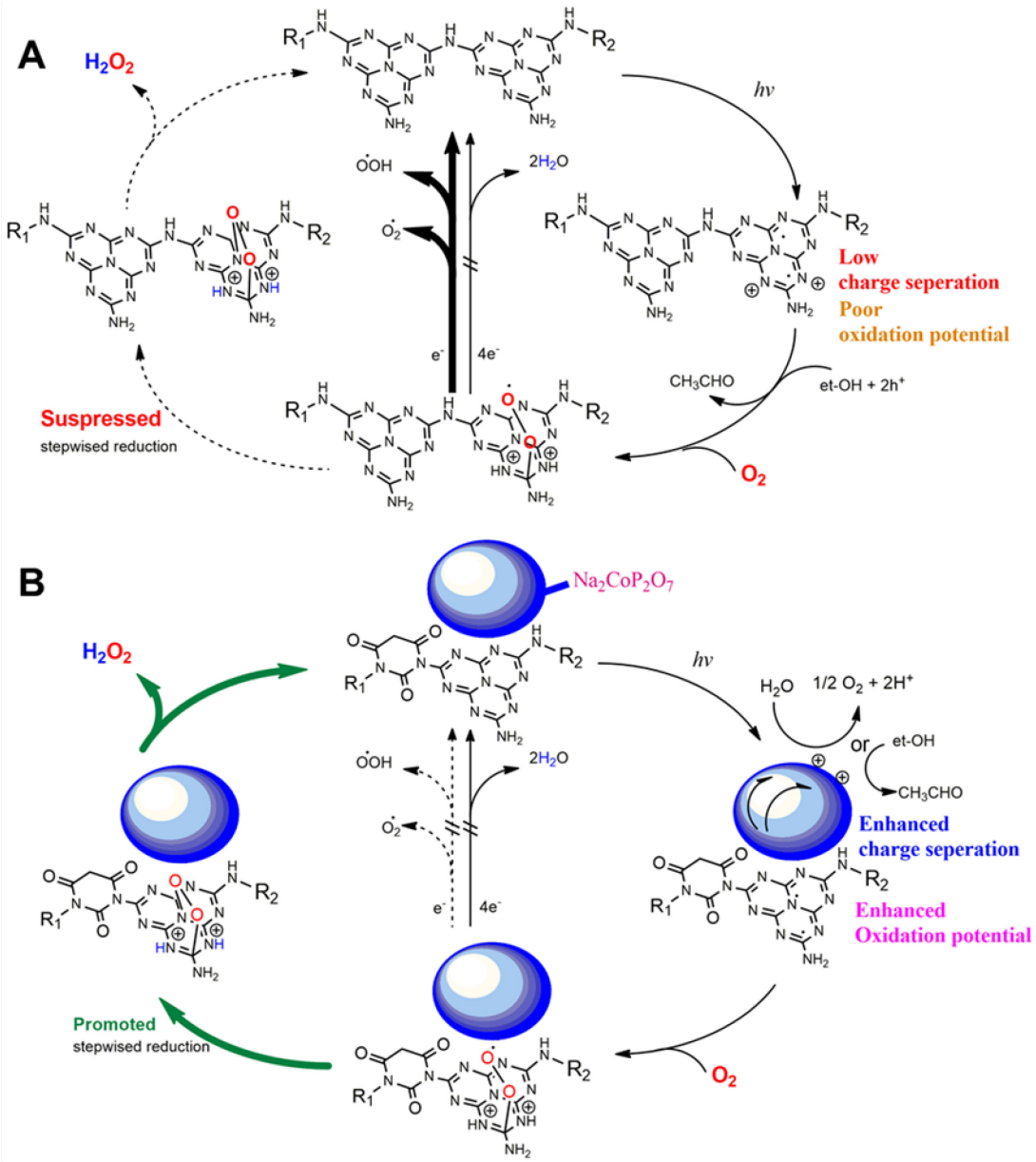

Scheme 2-2. Possible reaction route of oxygen evolution reactions using (**A**) pristine PCN or (**B**) PCNBA0.2Co5% as photocatalysts.

Alkali metal incorporated with a PCN framework has been reported to significantly promote the production of H_2O_2 with the existence of electron donors [11, 12, 14]. As shown in Figure 2-17E, PCN samples incorporated with alkali metal ions (PCNK10 and PCNNa10) showed almost triple activity improvement compared with the activity of PCNBA0.2Co5% with the addition of ethanol as an electron donor. On the other hand, PCNK10 and PCNNa10 showed no improvement of H_2O_2 production without the addition of sacrificial reagents. The inferior performance of PCNK10 and PCNNa10 may be due to the constant

VBM of PCNs incorporated alkali metals ions [12, 49]. The shallow VBM of PCNK10 could not overcome the large potential of water oxidation (>0.8 V). This result revealed the crucial role of band-engineering for improving photocatalytic H_2O_2 production using water and oxygen (Scheme 2-2).

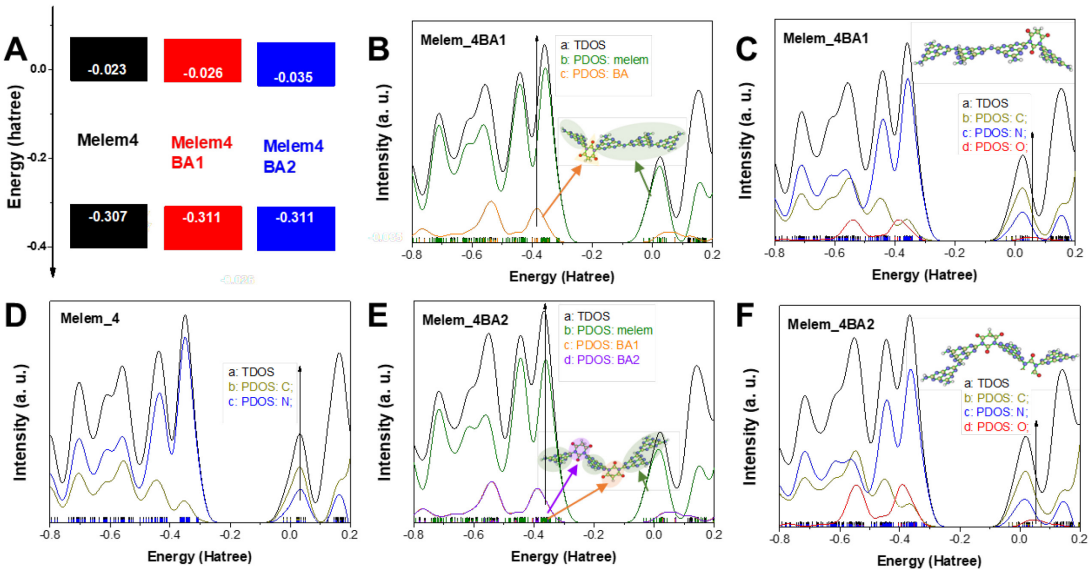

Figure 2-20. Computer simulation of density of states (DOS) with different co-polymerizations of BA motifs. (**A**) Calculated HOMO and LUMO of Melem_4 model (representing PCN), Melem_4BA1 (representing PCNBA with a low motif concentration) and Melem_4BA2 (representing PCNBA with a high motif concentration). Partial DOS and total DOS of the simulated (**D**) Melem_4, (**B**, **E**) Melem_4BA1 and (**C**, **F**) Melem_4BA2.

To elucidate the insight of the band engineering introduced by the BA motif, density function theory calculations combined with analysis of the density of states was conducted by inserting one or two BA units (i. e., Melem_4BA1 and Melem_4BA2) into the melon molecules. A model composed of 4 melem units was also constructed to present melon molecules (Melem_4). The calculation results showed that the value of E_g was 7.73 eV. It was larger than the value obtained from the DRS discussed above (2.77 eV), which was due to the limited model size and the known limitation of DFT [49, 50]. In this case, this work discussed the changing tendency of calculated E_g and the band positions based on the experimental results, which could validate the band engineering induced by BA motifs. As shown in Figure 2-20A, E_g of Melem_4BA2 narrowed after modification with BA motifs compared with E_g of Melem_4. The calculated CBM and VBM of Melem_4BA1 and Melem_4BA2 also showed an obvious positive shift compared with those of Melem_4. The

calculated potential of the bandgap width and the shift in band positions showed the same tendency as that in experimental results, indicating that the BA motifs inserted in the melon matrix result in induction of a positive shift of VBMs.

To further investigate the electronic properties of the PCNBA samples, the total DOS and partial DOS of Melem_4, Melem_4BA1 and Melem_4BA2 were obtained, as shown in Figures 2-20B-F [51]. For Melem_4, representing pristine PCNs, the partial DOS showed that its valence band (VB) and conduction band (CB) consist of N 2p and C 2p states, respectively. For Melem_4BA1 and Melem_4BA2, their CBs also consist of N 2p and C 2p states, whereas O 2p state did not appear in composition states of the CBM. However, the VB of Melem_4BA2 is mainly composed of N 2p, C 2p and O 2p states. Since the electronic potential of O 2p is much more positive than that of N 2p and C 2p, as shown in Figure 2-20C and 7F, N 2p, C 2p and O 2p states of Melem_4BA1 and Melem_4BA2 formed more positive VBM compared with the VBMs consisting with only N 2p and C 2p states (Melem_4). The partial DOS of molecular fragments also indicates that the inserted BA fragments result in the positive shift of band positions (Figure 2-20B and 2-20E). Therefore, we could draw a conclusion that the band engineering induced by BA motifs is due to the O 2p states introduced by BA units. The co-polymerization of nitrogen-rich precursors and oxygen-rich motifs has been theoretically proved for the first time to result in a more positive band position, thus providing a new approach for designing efficient photocatalytic systems for nonsacrificial H_2O_2 production.

2.4 Conclusion

In summary, the band positions of polymetric carbon nitride can be rationally designed by using melem and barbituric acid as precursors for efficient photocatalytic H_2O_2 production. The C=O groups incorporated in the PCN matrix formed a positive valence band with sufficient potential (1.85 eV vs. SHE) for overcoming the large overpotential of water oxidation (c.a.>0.8 V). The light absorption edge also expanded from 450 to 550 nm, indicating the promoted light harvesting. With the further loading of $Na_2CoP_2O_7$ as an OER co-catalyst, the PCNBAs showed a record-high apparent quantum yield of 8.0% and a SCC of 0.30% for photocatalytic H_2O_2 production with only H_2O and O_2. The co-

polymerization of BA and melem, as well as the loading of $Na_2CoP_2O_7$ significantly improved the charge separation. Analysis by DFT calculation combined with DOS showed that the positive shift of the band position is due to the O 2p states introduced by the co-polymerization of BA units. Co-polymerization of oxygen-rich motifs has been proven for the first time to be an effective approach for developing catalytic systems for enhanced H_2O_2 production in the aspect of electronic energy level. Therefore, this work provides not only a primary guideline for designing an appropriate band structure but also a practical approach to achieve the optimized performance for photocatalytic H_2O_2 production with a PCN-based material.

Reference

[1] K.P. Bryliakov, Catalytic asymmetric oxygenations with the environmentally benign oxidants H_2O_2 and O_2, Chem. Rev. 117 (2017) 11406-11459. https://doi.org/10.1021/acs.chemrev.7b00167.

[2] M. Nakano, I. Uchiyama, H. Takamatsu, Method for cleaning semiconductor wafers, US Patent (1995) US5626681A.

[3] T. Kitano, Etching solution and etching method for semiconductors, US Patent (1993) US5419808A.

[4] E. Neyens, J. Baeyens, A review of classic Fenton's peroxidation as an advanced oxidation technique, J. Hazard. Mater. 98 (2003) 33-50. https://doi.org/10.1016/S0304-3894(02)00282-0.

[5] S.A.M. Shaegh, N.-T. Nguyen, S.M.M. Ehteshamiab, S.H. Chan, A membraneless hydrogen peroxidefuel cell using Prussian Blue as cathode material, Energy Environ. Sci. 5 (2012) 8225-8228. https://doi.org/10.1039/C2EE21806B.

[6] F. Sandelin, P. Oinas, T. Salmi, J. Paloniemi, H. Haario, Kinetics of the recovery of active anthraquinones, Ind. Eng.Chem. Res. 45 (2006) 986-992. https://doi.org/10.1021/ie050593s.

[7] J.K. Edwards, B.E. Solsona, P. Landon, A.F. Carley, A. Herzing, C.J. Kiely, G.J. Hutchings, Direct synthesis of hydrogen peroxide from H_2 and O_2 using TiO_2-supported Au–Pd catalysts, J. Catal. 236 (2005) 69-79. https://doi.org/10.1016/j.jcat.2005.09.015.

[8] J.C. Pritchard, Q. He, E.N. Ntainjua, M. Piccinini, J.K. Edwards, A.A. Herzing, A.F. Carley, J.A. Moulijn, C.J. Kiely, G.J. Hutchings, The effect of catalystpreparation method on the performance of supported Au–Pd catalysts for the direct synthesis of hydrogen peroxide, Green Chem. 12 (2010) 915-921. https://doi.org/10.1039/B924472G.

[9] K. Fuku, K. Sayama, Efficient oxidative hydrogen peroxide production and accumulation in photoelectrochemical water splitting using a tungsten trioxide/bismuth vanadate photoanode, Chem. Commun. 52 (2016) 5406-5409.

https://doi.org/10.1039/C6CC01605G.
[10] K. Fuku, Y. Miyase, Y. Miseki, T. Funaki, T. Gunji, K. Sayama, Photoelectrochemical hydrogen peroxide production from water on a $WO_3/BiVO_4$ photoanode and from O_2 on an au cathode without external bias, Chem. Asian J. 12 (2017) 1111-1119. https://doi.org/10.1002/asia.201700292.
[11] P. Zhang, D. Sun, A. Cho, S. Weon, S. Lee, J. Lee, J. W. Han, D.-P. Kim, W. Choi, Modified carbon nitride nanozyme as bifunctional glucose oxidase-peroxidase for metal-free bioinspired cascade photocatalysis, Nat. Comm. (2019). https://doi.org/10.1038/s41467-019-08731-y.
[12] G. Moon, M. Fujitsuka, S. Kim, T. Majima, X. Wang, W. Choi, Photochemical production of H_2O_2 through O_2 reduction over carbon nitride frameworks incorporated with multiple heteroelements, ACS Catal. 7 (2017) 2886-2895. https://doi.org/10.1021/acscatal.6b03334.
[13] S. Kim, G. Moon, H. Kim, Y. Mun, P. Zhang, J. Lee, W. Choi, Selective charge transfer to dioxygen on KPF_6-modified carbon nitride for photocatalytic synthesis of H_2O_2 under visible light, J. Catal. 357 (2018) 51-58. https://doi.org/10.1016/j.jcat.2017.10.002.
[14] H. Kim, Y. Choi, S. Hu, W. Choi, J.-H. Kim, Photocatalytic hydrogen peroxide production by anthraquinone-augmented polymeric carbon nitride, APPL CATAL B-ENVIRON. 229, (2018) 121-129. https://doi.org/10.1016/j.apcatb.2018.01.060.
[15] Y. Kofuji, Y. Isobe, Y. Shiraishi, H. Sakamoto, S. Tanaka, S. Ichikawa, T. Hirai, Carbon nitride–aromatic diimide–graphene nanohybrids: Metal-free photocatalysts for solar-to-hydrogen peroxide energy conversion with 0.2% efficiency, J. Am. Chem. Soc. 138 (2016) 10019-10025. https://doi.org/10.1021/jacs.6b05806.
[16] Y. Shiraishi, S. Kanazawa, Y. Kofuji, H. Sakamoto, S. Ichikawa, S. Tanaka, T. Hirai, Sunlight-driven hydrogen peroxide production from water and molecular oxygen by metal-free photocatalysts, Angew. Chem. 126 (2014) 13672 -13677. https://doi.org/10.1002/anie.201407938.
[17] Y. Kofuji, S. Ohkita, Y. Shiraishi, H. Sakamoto, S. Tanaka, S. Ichikawa, T. Hirai, Graphitic carbon nitride doped with biphenyl diimide: Efficient photocatalyst for hydrogen peroxide production from water and molecular oxygen by sunlight, ACS Catal. 6 (2016) 7021-7029. https://doi.org/10.1021/acscatal.6b02367.
[18] Y. Shiraishi, T. Takii, T. Hagi, S. Mori, Y. Kofuji, Y. Kitagawa, S. Tanaka, S. Ichikawa, T. Hirai, Resorcinol–formaldehyde resins as metal-free semiconductor photocatalysts for solar-to-hydrogen peroxide energy conversion, Nat. Mater. 18, (2019) 985-993. https://doi.org/10.1038/s41563-019-0398-0.
[19] Z. Wei, M. Liu, Z. Zhang, W. Yao, H. Tanban, Y. Zhu, Efficient visible-light-driven selective oxygen reduction to hydrogen peroxide by oxygen-enriched graphitic carbon nitride polymer, Energy Environ. Sci. 11 (2018) 2581-2589. https://doi.org/10.1039/C8EE01316K.
[20] M. Teranishi, S. Naya, H. Tada, Temperature- and pH-dependence of hydrogen peroxide formation from molecular oxygen by gold nanoparticle-loaded titanium(IV) oxide photocatalyst, J. Phys. Chem. C 120 (2016) 1083-1088. https://doi.org/10.1021/acs.jpcc.5b10626.
[21] D. Tsukamoto, A. Shiro, Y. Shiraishi, Y. Sugano, S. Ichikawa, S. Tanaka, T. Hirai,

Photocatalytic H_2O_2 production from ethanol/O_2 system using TiO_2 loaded with Au–Ag bimetallic alloy nanoparticles, ACS Catal. 2 (2012) 599-603. https://doi.org/10.1021/cs2006873.

[22] Y. Shiraishi, S. Kanazawa, D. Tsukamoto, A. Shiro, Y. Sugano, T. Hirai, Selective hydrogen peroxide formation by titanium dioxide photocatalysis with benzylic alcohols and molecular oxygen in water, ACS Catal. 3 (2013) 2222−2227. https://doi.org/10.1021/cs400511q.

[23] N. Kaynan, B.A. Berke, O. Hazut, R. Yerushalmi, Sustainable photocatalytic production of hydrogen peroxide from water and molecular oxygen, J. Mater. Chem. A 2 (2014) 13822−13826. https://doi.org/10.1039/c4ta03004d.

[24] G.-H. Moon, W. Kim, A.D. Bokare, N.-E. Sung, W. Choi, Solar production of H_2O_2 on reduced graphene oxide-TiO_2 hybrid photocatalysts consisting of earth-abundant elements only, Energy Environ. Sci. 7 (2014) 4023−4028. https://doi.org/10.1039/C4EE02757D.

[25] H.-I. Kim, O. S. Kwon, S. Kim, W. Choi, J.-H. Kim, Solar production of H_2O_2 on reduced graphene oxide-TiO_2 hybrid photocatalysts consisting of earth-abundant elements only, Energy Environ. Sci. 9 (2016) 1063-1073. https://doi.org/10.1039/C4EE02757D.

[26] X. Wang, K. Maeda, A. Thomas, K. Takanabe, G. Xin, J. M. Carlsson, K. Domen, M. Antonietti, A metal-free polymeric photocatalyst for hydrogen production from water under visible light, Nat. Mater. 8 (2009) 76−80. https://doi.org/10.1038/nmat2317.

[27] J. Zhang, X. Chen, K. Takanabe, K. Maeda, K. Domen, J. D. Epping, X. Fu, M. Antonietti, X. Wang, Synthesis of a carbon nitride structure for visible-light catalysis by copolymerization, Angew. Chem. Int. Ed. 49 (2010) 441-444. https://doi.org/10.1002/anie.200903886.

[28] J. Zhang, G. Zhang, X. Chen, S. Lin, L. Möhlmann, G. Dołęga, G. Lipner, M. Antonietti, S. Blechert, X. Wang, Co-monomer control of carbon nitride semiconductors to optimize hydrogen evolution with visible light, Angew. Chem. Int. Ed. 51 (2012) 3183-3187. https://doi.org/10.1002/anie.201106656.

[29] J. Zhang, M. Zhang, R.Q. Sun, X. Wang, A facile band alignment of polymeric carbon nitride semiconductors to construct isotype heterojunctions, Angew. Chem. 124 (2012) 10292-10296. https://doi.org/10.1002/anie.201205333.

[30] M. Zhang, X. Wang, Two dimensional conjugated polymers with enhanced optical absorption and charge separation for photocatalytic hydrogen evolution, Ener. Environ. Sci. 7 (2014) 1902-1906. https://doi.org/10.1039/C3EE44189J.

[31] J. Qin, S. Wang, H. Ren, Y. Hou, X. Wang, Photocatalytic reduction of CO_2 by graphitic carbon nitride polymers derived from urea and barbituric acid, APPL CATAL B-ENVIRON. 179 (2015) 1-8. https://doi.org/10.1016/j.apcatb.2015.05.005.

[32] B. Jürgens, E. Irran, J. Senker, P. Kroll, H. Müller, W. Schnick, Melem (2,5,8-triamino-tri-s-triazine), an important intermediate during condensation of melamine rings to graphitic carbon nitride: Synthesis, structure determination by X-ray powder diffractometry, solid-state NMR, and theoretical studies, J. Am. Chem. Soc. 125 (2003) 10288-10300. https://doi.org/10.1021/ja0357689.

[33] H. Kim, J. Park, I. Park, K. Jin, S. E. Jerng, S. H. Kim, K. T. Nam, K. Kang, Coordination tuning of cobalt phosphates towards efficient water oxidation catalyst, Nat. Commun 6

(2015) 8253. https://doi.org/10.1038/ncomms9253.
[34] F. Erragh, A. Boukhari, B. Elouadi, E. M. Holt, Disodium zinc pyrophosphate and disodium (europium) zinc pyrophosphate, J. Crystallogr. Spectrosc. Res. 21 (1991) 321-326. https://doi.org/10.1107/S0108270198006246.
[35] Z. Teng, H. Lv, C. Wang, H. Xue, H. Pang, G. Wang, Bandgap engineering of ultrathin graphene-like carbon nitride nanosheets with controllable oxygenous functionalization, CARBON 113 (2017) 63-75. https://doi.org/10.1016/j.carbon.2016.11.030.
[36] J.D. Figueroa-Villar, S.C.G. de Oliveira, Synthesis and mechanism of formation of oxadeazaflavines by microwave thermal cyclization of ortho-halobenzylidene barbiturates, J. Braz. Chem. Soc. 22 (2011) 2101-2107. http://dx.doi.org/10.1590/S0103-50532011001100012.
[37] Z. Teng, N. Yang, H. Lv, S. Wang, Ma. Hu, C. Wang, D. Wang, G. Wang, Edge-functionalized g-C_3N_4 nanosheets as a highly efficient metal-free photocatalyst for safe drinking water, Chem 5 (2019) 664–680. https://doi.org/10.1016/j.chempr.2018.12.009.
[38] H. Hirakawa, M. Hashimoto, Y. Shiraishi, T. Hirai, Photocatalytic conversion of nitrogen to ammonia with water on surface oxygen vacancies of titanium dioxide, J. Am. Chem. Soc., 139 (2017) 10929-10936. https://doi.org/10.1021/jacs.7b06634.
[39] H. Sakamoto, T. Ohara, N. Yasumoto, Y. Shiraishi, S. Ichikawa, S. Tanaka, T. Hirai, Hot-electron-induced highly efficient O_2 activation by Pt nanoparticles supported on Ta_2O_5 driven by visible light, J. Am. Chem. Soc., 137 (2015) 9324-9332. https://doi.org/10.1021/jacs.5b04062.
[40] H. Wang, T. Lindgren, J. He, A. Hagfeldt, S.-E. Lindquist, Photolelectrochemistry of nanostructured WO_3 thin film electrodes for water oxidation: Mechanism of electron transport, J. Phys. Chem. B 104 (2000) 5686-5696. https://doi.org/10.1021/jp0002751.
[41] Q. Mi, Y. Ping, Y. Li, B. Cao, B.S. Brunschwig, P.G. Khalifah, G.A. Galli, H.B. Gray, N.S. Lewis, Thermally stable N_2-intercalated WO_3 photoanodes for water oxidation, J. Am. Chem. Soc. 134 (2012) 18318-18324. https://doi.org/10.1021/ja3067622.
[42] T.W. Kim, K.-S. Choi, Nanoporous $BiVO_4$ photoanodes with dual-layer oxygen evolution catalysts for solar water splitting, Science 343 (2014) 990-994. https://doi.org/10.1126/science.1246913.
[43] H. Kim, S. Lee, Y.-U. Park, H. Kim, J. Kim, S. Jeon, K. Kang, Neutron and X-ray diffraction study of pyrophosphate-based $Li_{2-x}MP_2O_7$ (M = Fe, Co) for lithium rechargeable battery electrodes, Chem. Mater. 23 (2011) 3930-3937. https://doi.org/10.1021/cm201305z.
[44] Q. Wang, K. Domen, Particulate photocatalysts for light-driven water splitting: Mechanisms, challenges, and design strategies, Chem. Rev. (2019) https://doi.org/10.1021/acs.chemrev.9b00201.
[45] Y. Kofuji, Y. Isobe, Y. Shiraishi, H. Sakamoto, S. Ichikawa, S. Tanaka, T. Hirai, Hydrogen peroxide production on a carbon nitride-boron nitride-reduced graphene oxide hybrid photocatalyst under visible light, 10 (2018) 2070-2077. https://doi.org/10.1002/cctc.201701683.
[46] L. Chen, L. Wang, Y. Wan, Y. Zhang, Z. Qi, X. Wu, H. Xu, Acetylene and diacetylene functionalized covalent triazine frameworks as metal-free photocatalysts for hydrogen

peroxide production: A new two-electron water oxidation pathway, Adv. Mater. 2019, (2019) 1904433. https://doi.org/10.1002/adma.201904433.

[47] Y. Peng, L. Wang, Y. Liu, H. Chen, J. Lei, J. Zhang, Visible-light-driven photocatalytic H_2O_2 production on g-C_3N_4 loaded with CoP as a noble metal free cocatalyst, Eur. J. Inorg. Chem. 2017 (2017), 4797-4802. https://doi.org/10.1002/ejic.201700930.

[48] C. Qiu, Y. Xu, X. Fan, D. Xu, R. Tandiana, X. Ling, Y. Jiang, C. Liu, L. Yu, W. Chen, C. Su, Highly crystalline K-intercalated polymeric carbon nitride for visible-light photocatalytic alkenes and alkynes deuterations, Adv. Sci. 6 (2018) 1801403. https://doi.org/10.1002/advs.201801403.

[49] K. Wang, Q. Li, B. Liu, B. Cheng, W. Ho, J. Yu, Sulfur-doped g-C_3N_4 with enhanced photocatalytic CO_2-reduction performance, APPL CATAL B-ENVIRON. 176-177 (2015) 44-52. https://doi.org/10.1016/j.apcatb.2015.03.045.

[50] X.W. Li, J. Zhou, Q. Wang, Y. Kawazoe, P. Jena, Patterning graphitic C–N sheets into a kagome lattice for magnetic materials, J. Phys. Chem. Lett. 4 (2013) 259. https://doi.org/10.1021/jz3018804.

[51] T. Lu, F. Chen, Multiwfn: A multifunctional wavefunction analyzer, J. Comput. Chem., 33 (2012) 580-592. https://doi.org/10.1002/jcc.22885.

Part 3

Photoexcited single metal atom catalysts for heterogeneous photocatalytic H_2O_2 production: Pragmatic guidelines for predicting charge separation

3.1 Introduction

To achieve a high selectivity and rate for H_2O_2 production [1-9], it is necessary to boost the $2e^-$ oxygen reduction reaction (ORR) [10] (eq. 1) or $2e^-$ water oxidation reaction (WOR) (eq. 2) [11]. A photocatalytic $2e^-$ WOR pathway is quite difficult to achieve because the as-synthesized H_2O_2 will decompose at the high oxidative potential (1.76 V vs. NHE) [11, 12]. Alternatively, solar H_2O_2 can be obtained from an ORR via a $2e^-$ pathway [9, 10, 13-17]. Various photocatalysts such as inorganic ZnO, TiO_2, and CdS and organic graphitic carbon nitride (g-C_3N_4) have been found to be active for the artificial photosynthesis of H_2O_2 in a particulate system [10, 18-20]. Nevertheless, the activity achieved is limited to a low level due to (1) low selectivity for the $2e^-$ process and (2) the low charge separation of photocatalysts.

$$O_2+2H^++2e^-\rightarrow H_2O_2 \quad (0.695\ \text{V vs. NHE}) \tag{1}$$
$$2H_2O+2h^+\rightarrow H_2O_2+2H^+ \quad (1.76\ \text{V vs. NHE}) \tag{2}$$
$$O_2+4H^++4e^-\rightarrow 2H_2O \quad (1.23\ \text{V vs. NHE}) \tag{3}$$

Tuning metallic sites into catalytic centers can boost both the activity and selectivity of ORR [21]. $4e^-$ ORR and $2e^-$ ORR are two competitive reactions in electrochemical systems that strongly depend on the type of O_2 adsorption [21]. O_2 adsorption on a metal surface can be generally classified into three types (Scheme 1A): one end-on type (Pauling-type), two side-on types (Griffiths-type and Yeager-type) [21, 22]. Side-on adsorption of O_2 is used to split O-O bond, which may result high selectivity for $4e^-$ ORR, while the end-on O_2 adsorption can minimize the O-O bond breaking, leading to a suppressed $4e^-$ ORR (eq. 3) and thus a highly selective $2e^-$ ORR [23]. Both end-on and side-on types of O_2 molecular adsorption occur on the surfaces of metal particles, and thus the O-O bond splitting on the surface of metal particles is therefore difficult to prevent [21-23]. On the other hand, the adsorption of O_2 molecule on atomically isolated sites is usually end-on type (Scheme 1B), which therefore could reduce the possibility of O-O bond breaking [24-26]. For instance, supported single-atom catalysts (SACs) with Pt^{2+} [27, 28] and Co-N_4 [29, 30] centers can electrochemically reduce O_2 to H_2O_2 via a $2e^-$ ORR pathway with ultrahigh selectivity (>96%). Many theoretical investigations have also revealed the nature of ORR selectivity to predict favorable reaction pathways for $2e^-$ ORR using a computational hydrogen

electrode (CHE) model [31]. However, these SACs and the CHE models is difficult to be directly used in the case of photocatalytic systems since the charge separation properties are not the dominant factor to influence electrochemical activity but a crucial factor to affect the photocatalytic activity [32, 33]. For instance, transition metals (TMs) with the half-filled d electrons, i. e., Mn, Fe, Co, Ni and Cu, usually show high activities if these elements are used to construct efficient electrocatalysts [29, 30, 34], while these elements usually show low photocatalytic activities because of the charge recombination occurred at these metallic sites [35]. Main-group metals with a d^{10} electronic configuration can eliminate the formation of an intermediate band in the band structure and usually show good activities in many artificial photosynthesis systems [36]. A systematic investigation of electronic configuration and excitation properties of isolated main-group metal and TM sites could provide a comprehensive understanding between theoretical design to practical activities.

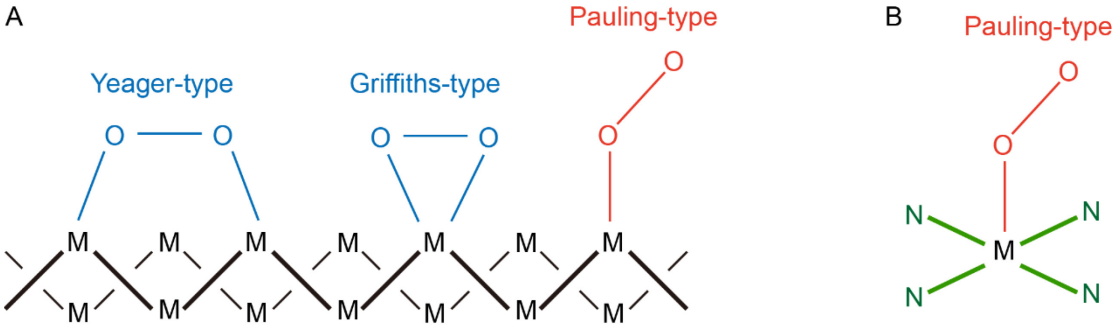

Scheme 1. Adsorption types of molecular oxygen on metallic surface. Molecular oxygen adsorption on the surface of (A) metal particles and (B) single atom catalyst.

To this end, a series of metal ion-incorporated single atom photocatalysts (M-SAPCs) was prepared by a facile wet-chemical method combined with the thermal condensation treatment by isolation of TM metals (Fe, Co, Ni) and main-group (In, Sn) sites with a nitrogen-rich polymeric carbon nitride skeleton. The chemical states of the metal element and the band positions of the catalyst were firstly investigated. Based on the experimental data, we then constructed and validated cluster models that can represent the electronic structure of as-prepared SAPCs. The nature of excited states (ES) was clarified in these models to obtain a comprehensive understanding of possible charge separation properties of M-SAPCs for the first time by employing the time-dependent density functional theory (TDDFT). Verified by the experimental results of photoluminescence (PL), light-driven

electrochemical impedance spectroscopy (EIS) and photocurrent response profiles, a theoretical guideline based on the validated electronic configuration and excitation properties has been established. This guideline provides a blueprint for the design of an efficient single-atom photocatalyst at atomic levels.

3.2 Experimental details

3.2.1 Preparation of single metallic atom photocatalysts

The purities of all reagents for preparation of photocatalysts and for photoelectrochemical measurements were above analytical grade unless otherwise stated. Pristine polymeric carbon nitride (PCN) was prepared by calcination of 4 g dicyandiamide at 560 °C in N_2 for 4 h. Typically, $FeCl_3 \cdot 6H_2O$ (Wako Pure Chemical Industries, Ltd.), $CoCl_2 \cdot 6H_2O$ (Wako Pure Chemical Industries, Ltd.), $NiCl_2 \cdot 6H_2O$ (Wako Pure Chemical Industries, Ltd.), $InCl_3 \cdot 4H_2O$ (Wako Pure Chemical Industries, Ltd.) and $SnCl_4 \cdot 5H_2O$ (SIGMA-ALDRICH, Co., Ltd.) were used as metallic sources for the formation of metal catalytic sites. First, 1 mmol metal chloride were dissolved into ethanol solution with sonification treatment for 60 min. Then, 4 g dicyandiamide was dispersed into solution by sonification for another 60 min. After that, the solution was removed by a vacuum evaporator, and the as-obtained powders were dried in a vacuum oven at 60 °C for 4 h. The metal ion-dispersed M-SAPCs were prepared by calcinating the obtained mixture at 560 °C in N_2 for 4 h (Figure 3-1A). The as-prepared M-SAPCs were named according to the incorporated metal species, i. e., Fe-SAPC, Co-SAPC, Ni-SAPC, In-SAPC and Sn-SAPC. The as-prepared sample were all washed in the 2% (v/v) HCl at 80 °C for 24 h to remove the unfixed metal species such as nanoparticles [29].

3.2.2 Material characterization

High-resolution transmission electron microscopy (HRTEM), high-angle annular dark field scanning transmission electron microscopy (HAADF-STEM) and energy-dispersive X-ray spectroscopy (EDS) were performed using a Titan Cubed Themis G2 300 electron microscope (Field Electron and Ion Company, USA) with an accelerating voltage of 300 kV. The crystalline phases were characterized by a powder X−ray diffraction (XRD) instrument (MiniFlex II, Rigaku Co.) with CuKα (λ = 1.5418 Å) radiation (cathode voltage: 30 kV, current: 15 mA). X−ray photoelectron spectroscopy (XPS) measurements were performed

using an ESCALAB 250Xi (Thermo Scientific, USA). The binding energy was calibrated by taking the carbon (C) 1s peak of adventitious carbon at 284.6 eV. UV-vis diffuse reflectance spectroscopy (UV-DRS) was performed using a UV/VIS/NIR spectrometer (UV-2600, Shimadzu Co.). Photoluminescence spectroscopy was acquired using a FP-8500 spectrofluorometer (JASCO Corporation, Japan).

3.2.3 Computational methods

To analyze the excited states of pristine PCN and PCN coordinated with single metal ions, the Gaussian09 program S2 within TDDFT was used [37]. All optimization and frequency simulations were carried out by utilizing wb97xd/6-311 G(d) level of theory for C, N and H elements and SDD for metal elements [9]. PCN synthesized by thermal polymerization usually contains several defects and shows a poor crystallinity with a short range order of the lattice [38, 39]. In this case, the single metal atom-dispersed catalysts are simulated using three cluster models, which the M atom is bound with the skeleton. The melem_3M represents a single metallic ion coordinated by non-defected PCN unit, i.e., *graphitic carbon nitride (g-C_3N_4) unit*. The melem_4MS and melem_4MC are used to simulate two possible geometry configurations of metal ions coordinated by a defected PCN unit, i. e., *melon unit*. Based on the influence of ionizable groups on the isoelectric points of carbon-based materials previously reported [40, 41], the incorporated metal ions show positive charges in nature. In this case, the charges for cluster models are set to be the same as the chemical states which are confirmed by XPS measurements. The stability of SACs is evaluated by calculating the formation energy [29], which is defined as:

$$E_{form} = E_{Melem\_xM} - E_{Melem\_x} - E_M,$$

where E_{Melem_xM}, E_{Melem_x}, and E_M represent the energies of metal ion coordinated by PCN, pristine PCN, and metallic ions.

Multiwfn Ver. 3.6 (released on May 21, 2019) was used for analysis of the excitation and charge transfer properties [42]. The charge transfer (CT) length in the Cassian coordinates (X/Y/Z) could be measured by the distance between the centroid of hole and electron in the corresponding directions (denoted as *D* index) [37, 42]. Furthermore, Coulomb attraction between hole and electron (exciton binding energy) was also computed

for estimation of charge recombination properties [43, 44].

Visualization of holes, electrons and transition density was also performed by Multiwfn: functions of *IOp(9/40=3)* were set during the vertical excitation based on TD-DFT calculation [42]. The electron distributions at these excited states were presented as heatmaps by using the combination of GaussView 5.0 and Multiwfn. The iso-surface of LUMO orbitals was presented by setting the isovalue to 0.05.

3.2.4 Activity measurements

Each catalyst (50 mg) was added to 10% ethanol solution (3 mL ethanol with 27 mL deionized water) in a borosilicate glass bottle (φ 45 mm; capacity, 50 mL), and the bottle was sealed with a rubber septum cap. The catalyst was dispersed well by ultrasonication for 15 min, and O_2 was bubbled through the solution for 30 min. The bottle was immersed in a temperature-controlled air bath at 298 ± 0.5 K with wind flowing and was photo-irradiated at λ > 420 nm using a 500 W Xe lamp (PXE-500, USHIO Inc.) with magnetic stirring. The amount of H_2O_2 was determined by a colorimetric method using PACKTEST (WAK-H_2O_2, KYORITSU CHEMICAL-CHECK Lab., Corp.) equipped with a digital PACKTEST spectrometer (ED723, GL Sciences Inc.).

3.2.5 Photoelectrochemical characterizations

Photoelectrochemical (PEC) characterizations were conducted using a conventional three-electrode potentiostat setup connected to an Electrochemical Analyzer (Model 604D, CH Instruments, Inc.). The Fluoride-doped tin oxide (FTO) glass of 1.5 cm × 3 cm in size was covered with photocatalyst, which was fabricated by first mixing catalyst (100 mg) with ethyl cellulose binder (10 mg) in ethanol for one hour and then depositing the final viscous mixture by a doctor blade method and drying at room temperature and further drying at 40 °C overnight in a vacuum oven. The area of the photocatalytic coating was controlled to be 2.25 cm^2 by the doctor blade method. The PEC reactor consisted of FTO glass covered by a PCN sample, coiled Pt wires and a saturated Ag/AgCl/KCl (saturated) electrode as working, counter, and reference electrodes, respectively. The photocurrent derived from photo-generated charge carriers on photocatalysts was collected on a Pt working electrode (at 0.8 V vs. SHE (0.6 V vs. Ag/AgCl)) in phosphate buffer solutions. The

solutions were saturated with O_2 by bubbling O_2 for 15 min (0.5 L min^{-1}). Electrochemical impedance spectroscopy (EIS) analysis was performed at a DC voltage of -0.6 V *vs.* Ag/AgCl, an AC voltage amplitude of 50 mV, and a frequency ranging from 100 kHz to 0.01 Hz. For Mott-Schottky measurements, similar strategies were performed on FTO glass (1.5 cm × 3 cm) by the same doctor blade method.

3.3 Results and discussion

3.3.1 Characterization of M-SAPCs

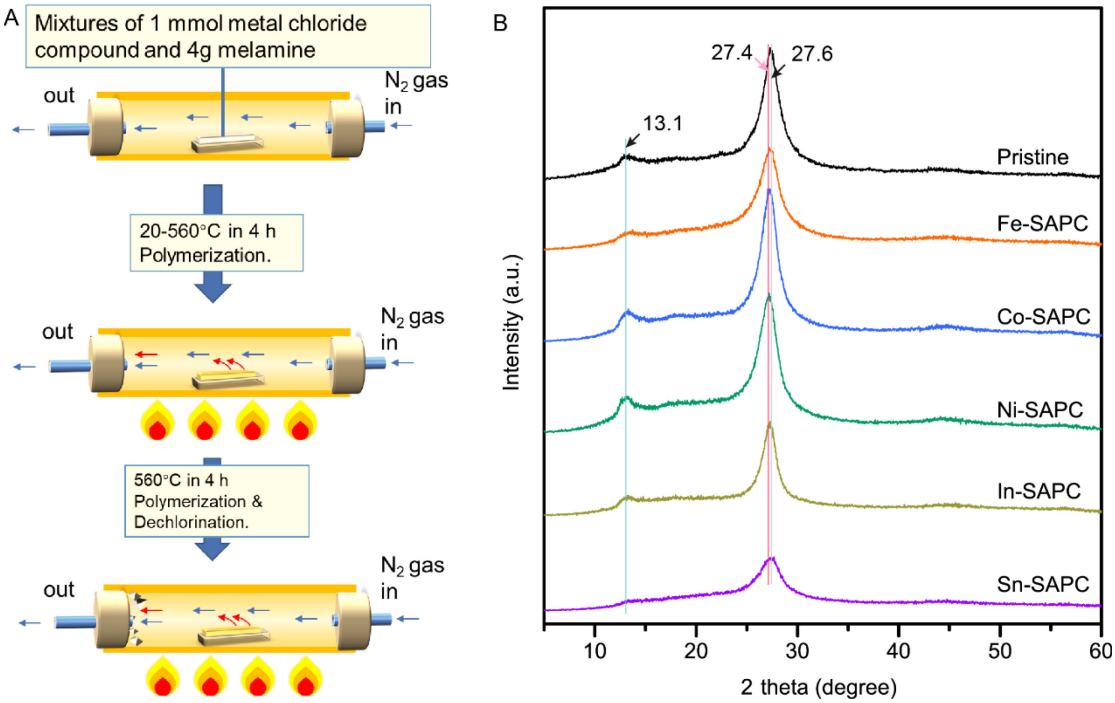

Figure 3-1. Synthesis and crystalline structure of M-SAPCs. (A) Thermal polymerization procedure of M-SAPCs by utilizing melamine and metal chloride compound as precursors. (B) XRD patterns of pristine PCN and M-SAPCs.

The crystalline structures of M-SAPCs were firstly investigated by XRD measurements (Figure 3-1B). XRD patterns of all M-SAPC samples showed two characterization peaks at about 27.4° and 13.1°, ascribing to the interlayer stacking {002} and the inner planar structure packing {100} of tri-s-triazine units, respectively. The slight shift in the diffraction pattern of the {002} lattice compared with the XRD pattern of pristine PCN (27.6°) can be attributed to the electrostatic repulsion between interlayers when positive ions were incorporated into the PCN matrix [9]. Although the peak intensities of the {002} lattice slightly changed after the introduction of heterometal ions, there was almost no change in the peak intensity of the {100} lattice, indicating that the incorporation of metal species has

almost no influence on the in-plane structure of tri-s-triazine [20].

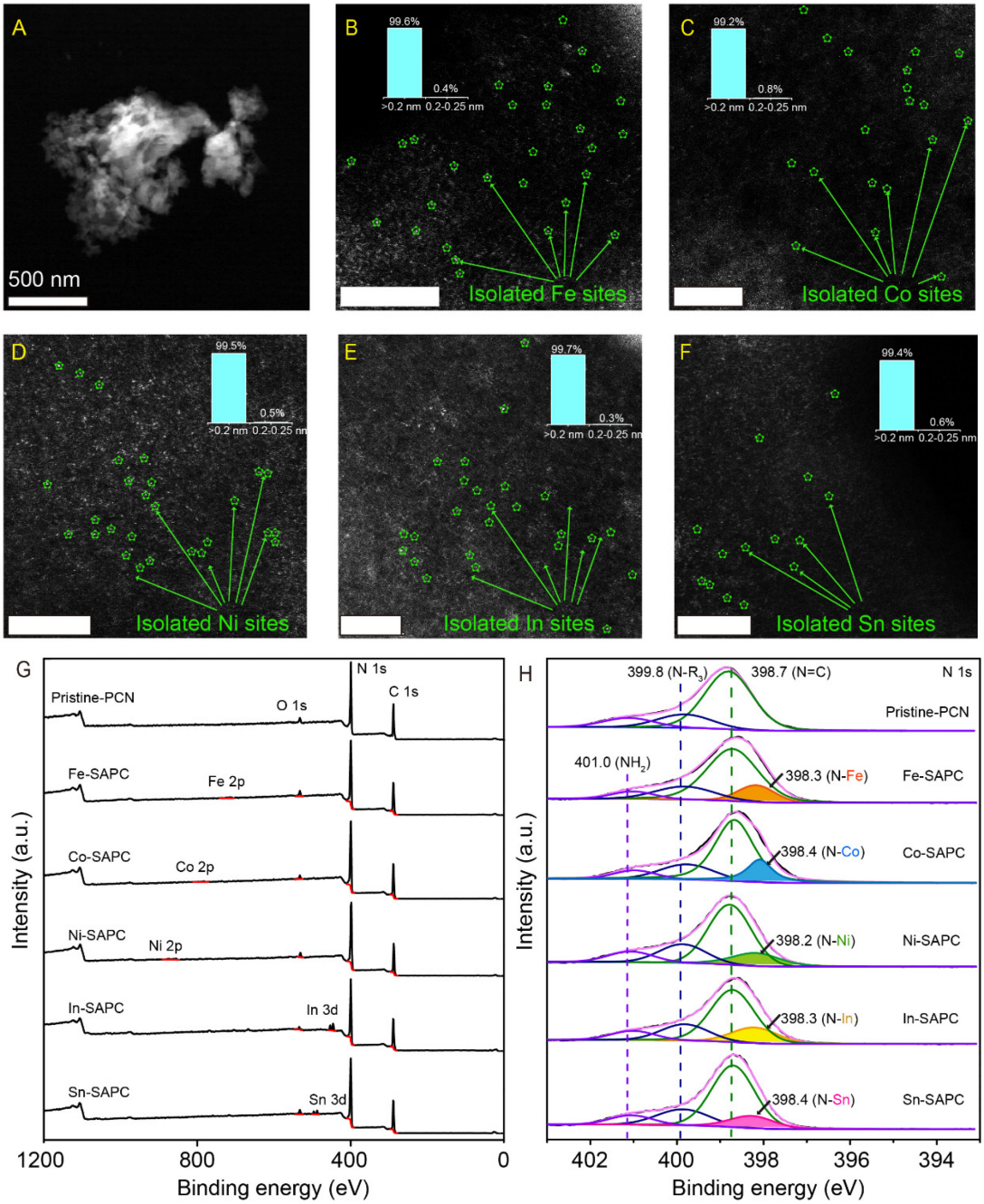

Figure 3-2. Characterization of M-SAPCs. (A) Low-magnification HAADF-STEM image of pristine PCN. High-magnification HAADF-STEM images of (B) Fe-SAPC, (C) Co-SAPC, (D) Ni-SAPC, (E) In-SAPC and (F) Sn-SAPC. Inset is the size distribution of the bright spots. (G) XPS-survey spectra of pristine PCN and M-SAPCs. (H) High-resolution XPS N 1s spectra of pristine PCN and M-SAPCs.

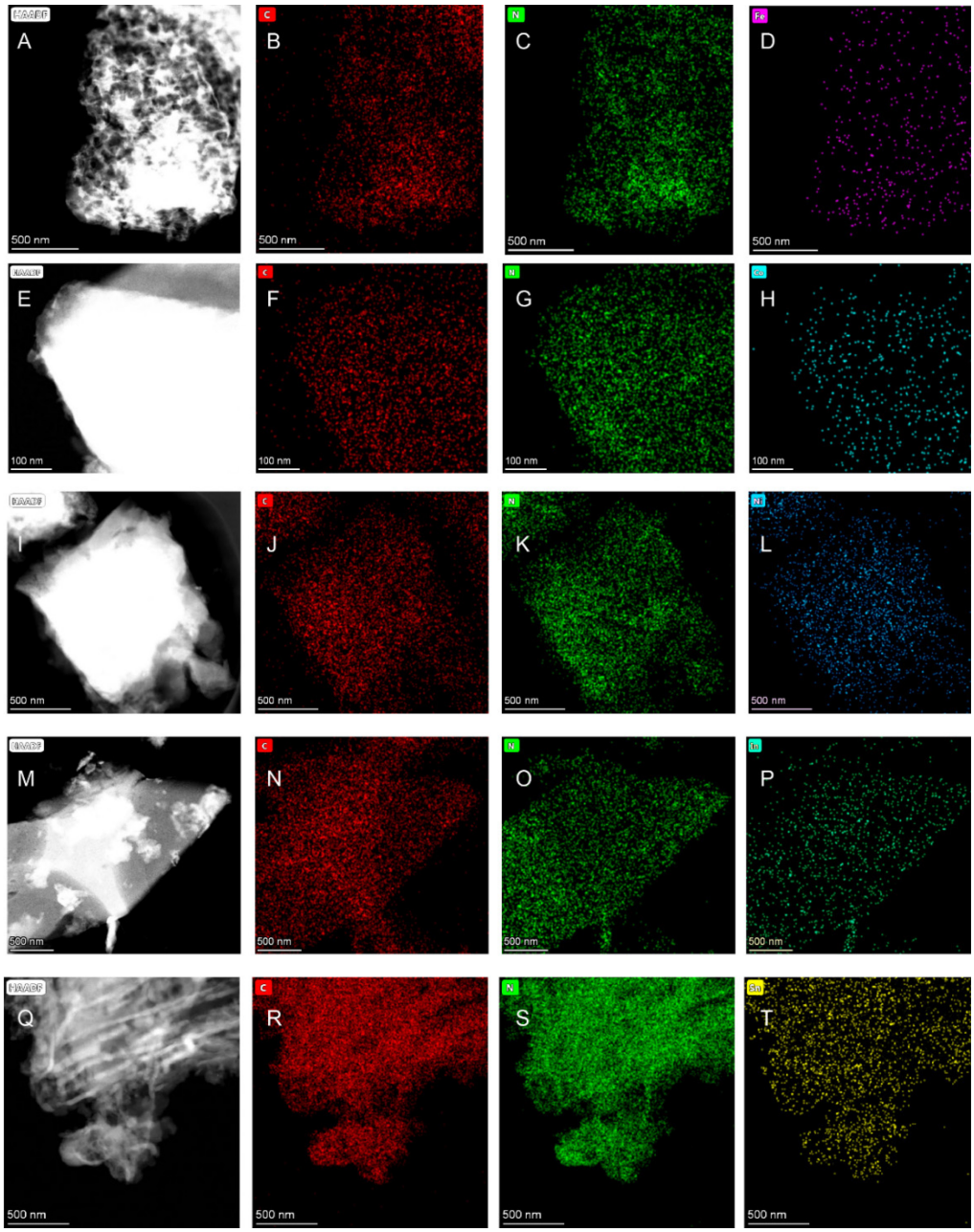

Figure 3-3. HAADF STEM images combined with EDX measurements of as-prepared samples. (A) HAADF STEM image of Fe-SAPC. EDX mapping image of (B) C, (C) N and (D) Fe in Fe-SAPC samples. (E) HAADF STEM image of Co-SAPC. EDX mapping image of (F) C, (G) N and (H) Co in Co-SAPC samples. (I) HAADF STEM image of Ni-SAPC. EDX mapping image of (J) C, (K) N and (L) Ni in Ni-SAPC samples. (M) HAADF STEM image of In-SAPC. EDX mapping image of (N) C, (O) N and (P) In in In-SAPC samples. (Q) HAADF STEM image of Sn-SAPC. EDX mapping image of (R) C, (S) N and (T) Sn in Sn-SAPC samples.

As a powerful tool for discerning individual heavy atoms, high-angle annular dark-field scanning transmission electron microscopy (HAADF-STEM) was used to further confirm the morphology and elemental distribution and configuration of metal species. The

morphologies of pristine PCN (Figure 3-2A) and all M-SAPCs were bulk materials with a homogeneous distribution of metal elements as shown in the HAADF-STEM mapping images with low magnification (Figure 3-3). After aberration-correction TEM measurement in high magnification, Figure 3-2B-F show that the bright spots with high density corresponding to metallic atoms are uniformly dispersed in the carbon nitride matrix. The size distribution inserted in Figure 3-2B-F reveals that the size of 99.6% of the metallic species is less than 0.2 nm, manifesting that incorporated metal exists exclusively as atomically dispersed single atoms [45]. The weight percentages of the metal species in the as-prepared M-SAPCs are all less than 1% (Table 3-1) with a similar amount of metal atom in a certain mass of catalyst (about 0.5~0.6 mmol per 1 g catalyst). Note that metal nanoparticles could remain on the surface of M-SAPC (taking In-SAPC as an example) if the as-prepared photocatalyst did not undergo the acid washing process (Figure 3-4).

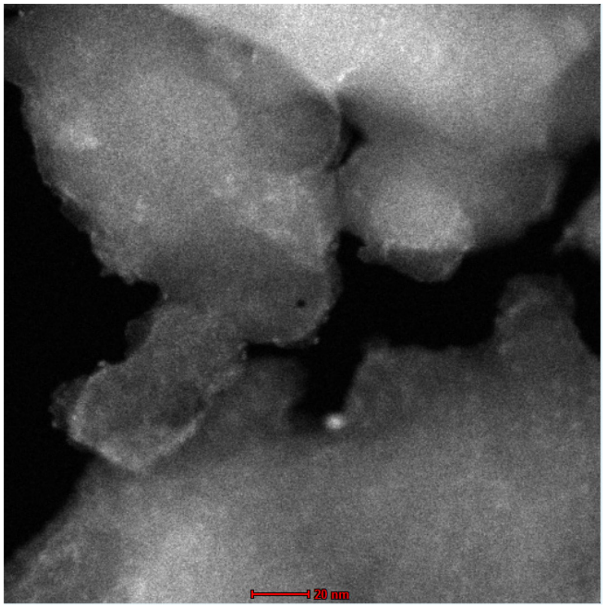

Figure 3-4. As-prepared In-SAPC before washing by 2% (v/v) HCl.

To further reveal the interaction between the isolated metallic sites and the PCN skeleton, chemical states of pristine PCN and M-SAPCs were investigated by XPS measurements. The ratio obtained by dividing the integration area of the C 1s peak by the integration area of N 1s was almost constant in the XPS survey spectra of pristine PCN and M-SAPC (Figure 3-2G), further indicating that incorporation of isolated metallic ion sites has almost no influence on the skeleton of PCN matrix. As shown in the high-

resolution C 1*s* spectra of pristine PCN and M-SAPC (Figure 3-5), the typical components around 288.1 eV and 284.6 eV (indexed as N–C=N and adventitious carbon, respectively) are almost the same, whereas no new peak appeared in C 1s spectra. These results revealed that the chemical state of surface carbon remained almost the same, indicating that the carbon atoms hardly interact with metallic ions. Three peaks at 401.0 eV, 399.8 eV and 398.7 eV can be assigned to $-NH_2$, tertiary nitrogen, and C=N-C bonds, respectively. It is notable that nitrogen peak (N 1s) appears around 398.3 eV in the spectra of M-SAPC, which could be assigned to the chemical composition of N-Metal (Figure 3-2H) [46]. High-resolution Cl 2p spectra (Figure 3-6) confirmed that all fluoride elements were completely removed, excluding the possibility of chemical states of M-Cl. The spectra of Fe 2p can be deconvoluted to six peaks at 728.0 eV, 724.0 eV, 722.0 eV, 715.2 eV, 711.2 eV and 709.2 eV (Figure S6A), which could be respectively assigned to the satellite peak of Fe $2p_{1/2}$, Fe^{3+}-N $2p_{1/2}$, Fe^{2+}-N $2p_{1/2}$, satellite peak of Fe $2p_{3/2}$, Fe^{3+}-N $2p_{3/2}$ and Fe^{2+}-N $2p_{3/2}$, which is close to the binding energy of Fe_2O_3 and FeO. These results revealed that that the chemical states of Fe is mixed with (II) and (III). Similarly, referring to the chemical states of CoO, NiO, In_2O_3 and SnO_2, the chemical states of atomically dispersed Co, Ni, In and Sn species in the as-prepared M-SAPC are close to (II), (II), (III) and (IV) (Figure 3-7B-E), respectively [46].

Table 3-1. Mass percentage of as-prepared SAPCs.

	Total mass (mg)	Concentration (mg L^{-1})	Volume (L)	Weight percentage (wt%)	amount per 1g catalyst (mmol)
In-SAPC	9.2	5.54	0.0100	0.602%	0.0524
Sn-SAPC	9.4	5.72	0.0100	0.609%	0.0513
Fe-SAPC	10.2	3.32	0.0100	0.325%	0.0583
Co-SAPC	10.1	3.57	0.0100	0.353%	0.0600
Ni-SAPC	10.4	3.84	0.0100	0.369%	0.0629

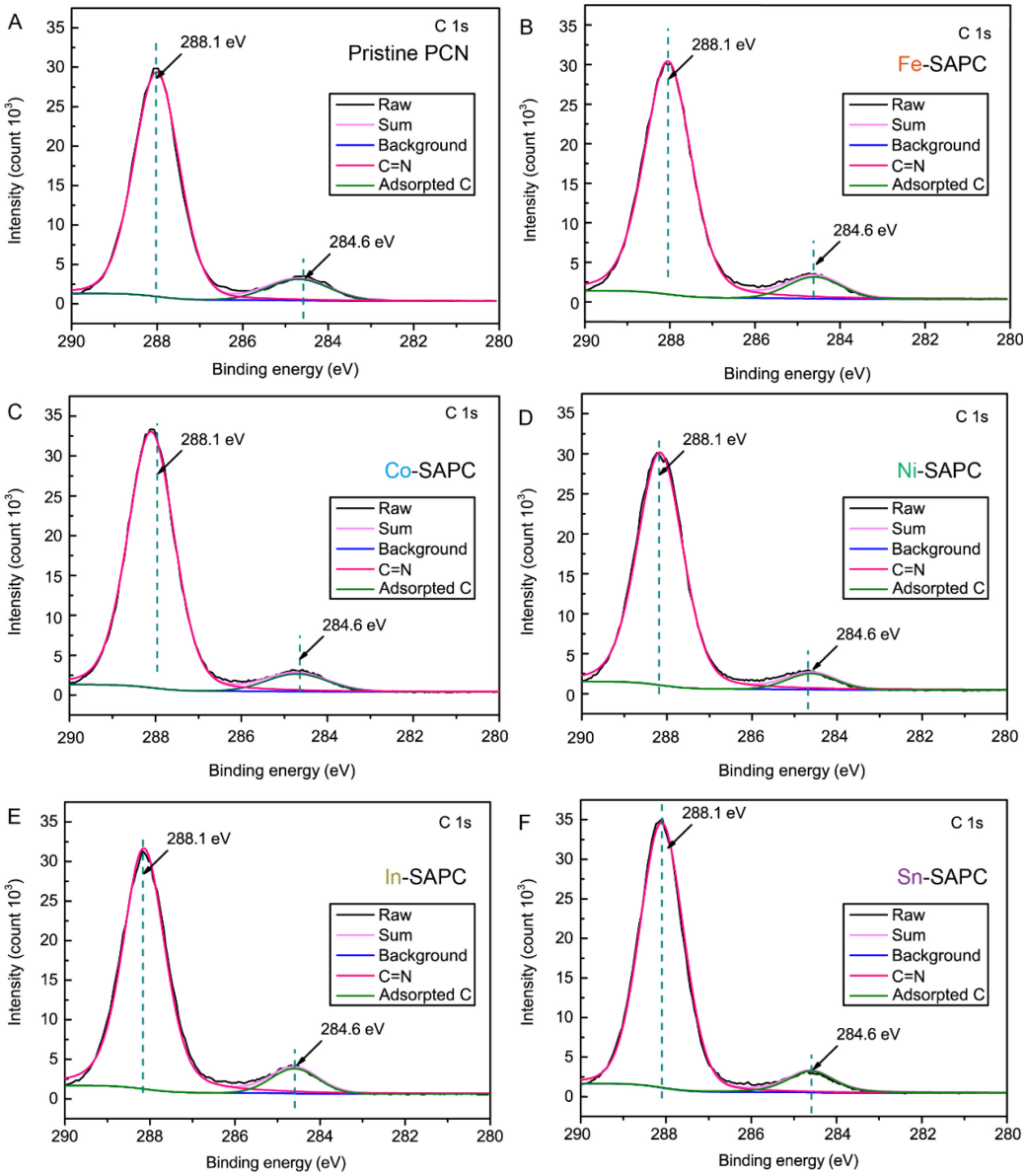

Figure 3-5. High resolution C 1s of (A) pristine PCN, (B) Fe-SAPC, (C) Co-SAPC, (D) Ni-SAPC, (E) In-SAPC and (F) Sn-SAPC.

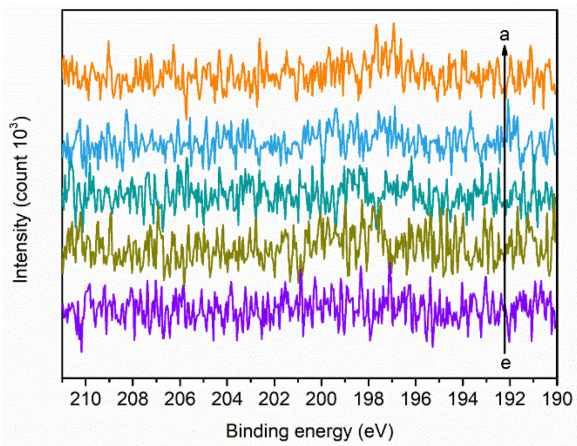

Figure 3-6. High resolution Cl 2p of as-prepared samples. Line a: Fe-SAPC; Line b: Co-SAPC; Line c: Ni-SAPC; Line d: In-SAPC; line e: Sn-SAPC.

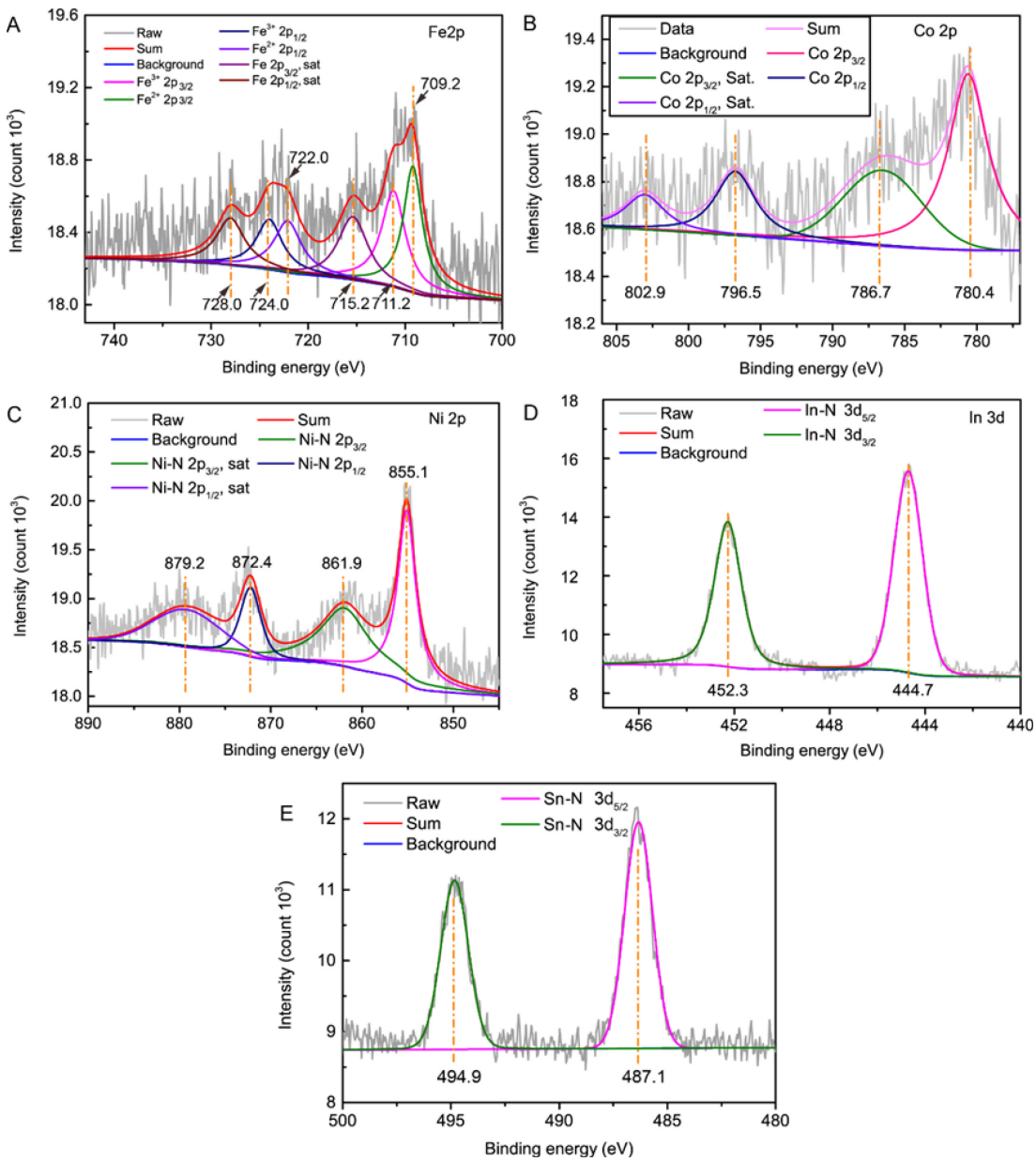

Figure 3-7. High resolution XPS spectra of metal elements obtained by as-prepared samples. (A) High resolution Fe 2p of Fe-SAPC. (B) High resolution Co 2p of Co-SAPC. (C) High resolution Ni 2p of Ni-SAPC. (D) High resolution In 3d of In-SAPC. (E) High resolution Sn 3d of Sn-SAPC.

To investigate the bandgap width, CBM and VBM of the as-prepared M-SAPC samples, UV-vis DRS, Mott-Schottky and VB-XPS measurements were respectively conducted. As shown in Figure 3-8A, the light absorption edge of pristine PCN (445 nm) is smaller than that of M-SAPCs (> 450 nm), indicating that the incorporation of metal ions narrowed the band gap. The band gap width followed a sequence of $E_{gIn\text{-}SAPC} > E_{gNi\text{-}SAPC} \approx E_{gCo\text{-}SAPC} > E_{gSn\text{-}SAPC} > E_{gFe\text{-}SAPC}$. The VBM of M-SAPCs remained almost constant to be 1.46 eV as

shown in the VB-XPS results (Figure 3-9). As shown in Mott-Schottky plots (Figure 3-10), the CBM of M-SAPC samples gradually became more positive from -1.28 eV for pristine PCN to -1.00 eV for M-SAPCs (Figure 3-11). Based on as-obtained bandgap width and band positions, band diagrams of M-SAPCs and pristine PCN can be presented as shown in Figure 3-8B. The introduction of isolated metal ions resulted in a more positive conduction band minimum, indicating that intermediate band may be introduced by single metallic sites. Being specific, the introduction of Fe^{2+} and Fe^{3+}, Co^{2+}, Ni^{2+}, In^{3+} and Sn^{4+} sites respectively shifted the CBM of the as-prepared catalyst for +0.28 eV, +0.21 eV, +0.19 eV, +0.09 eV and +0.24 eV. Based on the characterization details shown above, we can confirm that the metal ions were isolated by the nitrogen atoms of PCN skeleton with a little influence on the CBM. However, it is difficult to obtain the rigorous coordination status of isolated metal ions and N atoms since there are several possible structures of polymeric carbon nitrides prepared by thermal polymerization [38, 39]. In this case, a detailed theoretical simulation of M-SAPCs is necessary to reveal the comprehensive influences of isolated metal sites on the electronic configuration, thus leading to a further validation the structure of isolated metallic sites and a deep understanding of the changes in charge separation properties of M-SAPCs.

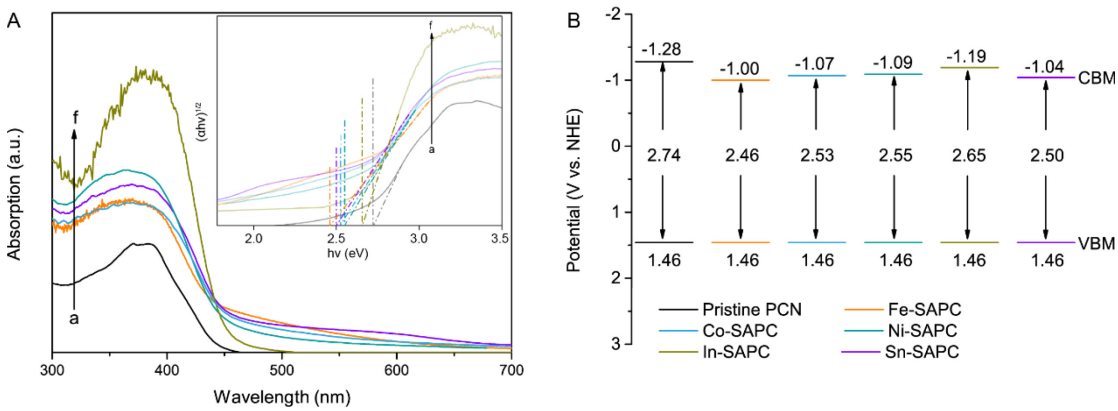

Figure 3-8. Optical absorption and band positions of pristine PCN and M-SAPC samples. (A) UV-vis spectra of pristine PCN and M-SAPC samples: absorbance spectra with inserted Tauc plots. Lines a-f: a: pristine PCN; b: Fe-SAPC; c: Co-SAPC; d: Ni-SAPC; e: In-SAPC; c: Sn-SAPC. (B) Band diagrams of PCN and as-prepared M-SAPC samples.

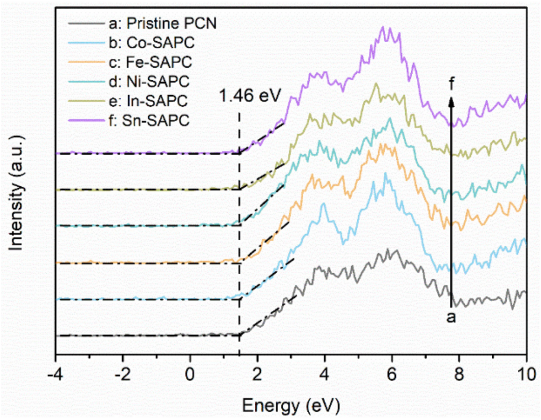

Figure 3-9. VBXPS of PCN and M-SAPCs samples.

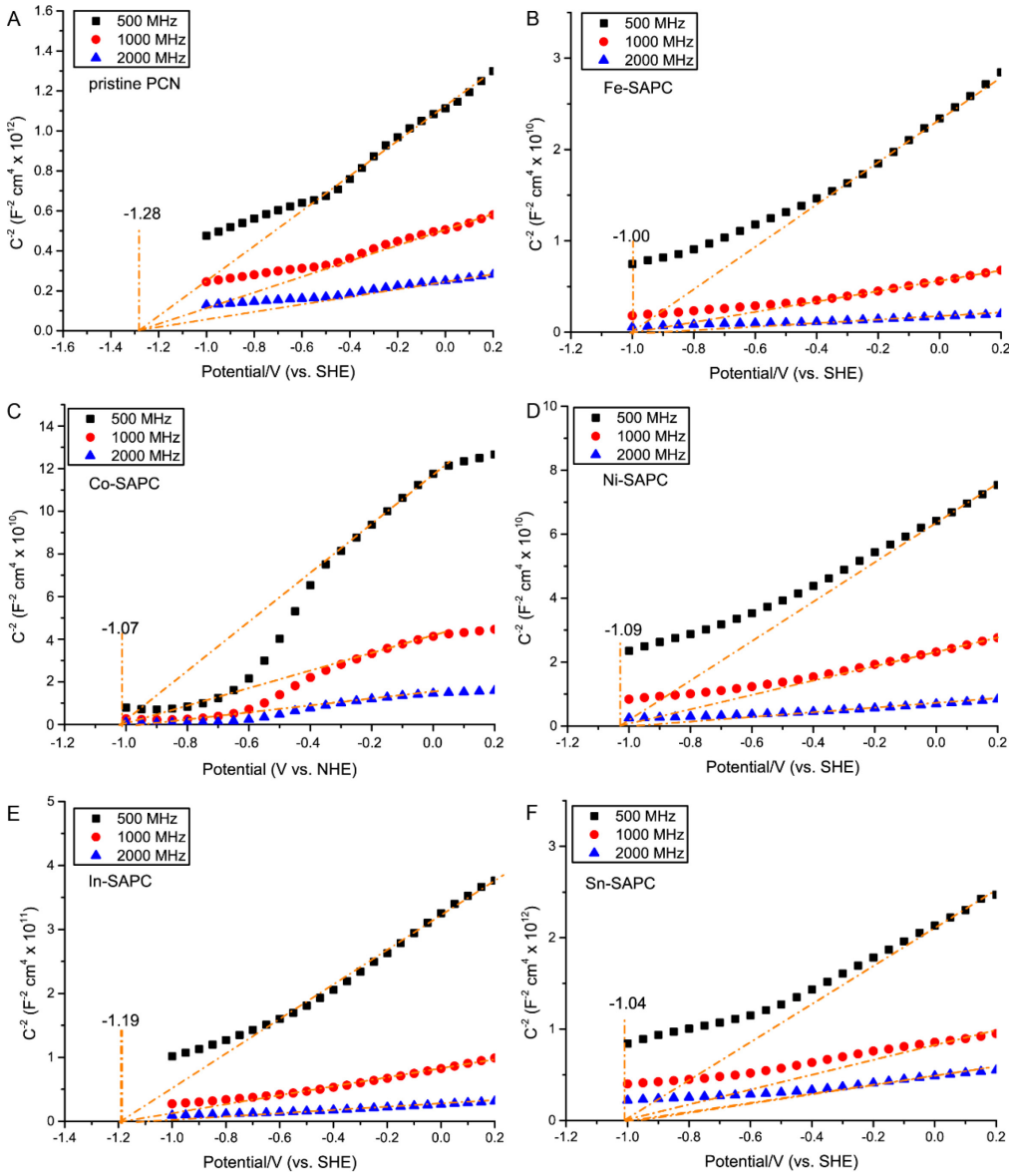

Figure 3-10. Mott-Schottky plots of PCN and M-SAPC samples. Mott-Schottky plots of (A) Pristine PCN, (B) Fe-SAPC, (C) Co-SAPC, (D) Ni-SAPC, (E) In-SAPC, and (F) Sn-SAPC.

3.3.2 Development and validation of cluster models

Transition metals such as Fe, Cu, Zn, and Ni, and so forth have been used to construct models of single catalytic sites [34]. Based on previous experimental and theoretical results [34, 39], the skeleton of PCN can formed pores filled with six nitrogen lone-pairs of electrons in 2D planes, which is favorable ion coordination [39]. Additionally, the PCN prepared by thermal polymerization at high temperature showed the existence of $-NH_2$ as revealed in deconvoluted peak at 401.0 eV (Figure 3-2H). Previous reports showed that the mass ratio of the H element in PCN prepared by a thermal polymerization strategy is above 1.0% or more, quite close to that of poly(aminoimino)heptazine, i.e., melon (the hydrogen content of melon is approximately 1.5wt%) [38]. These facts suggest that melon could also exist in the M-SAPC matrix.

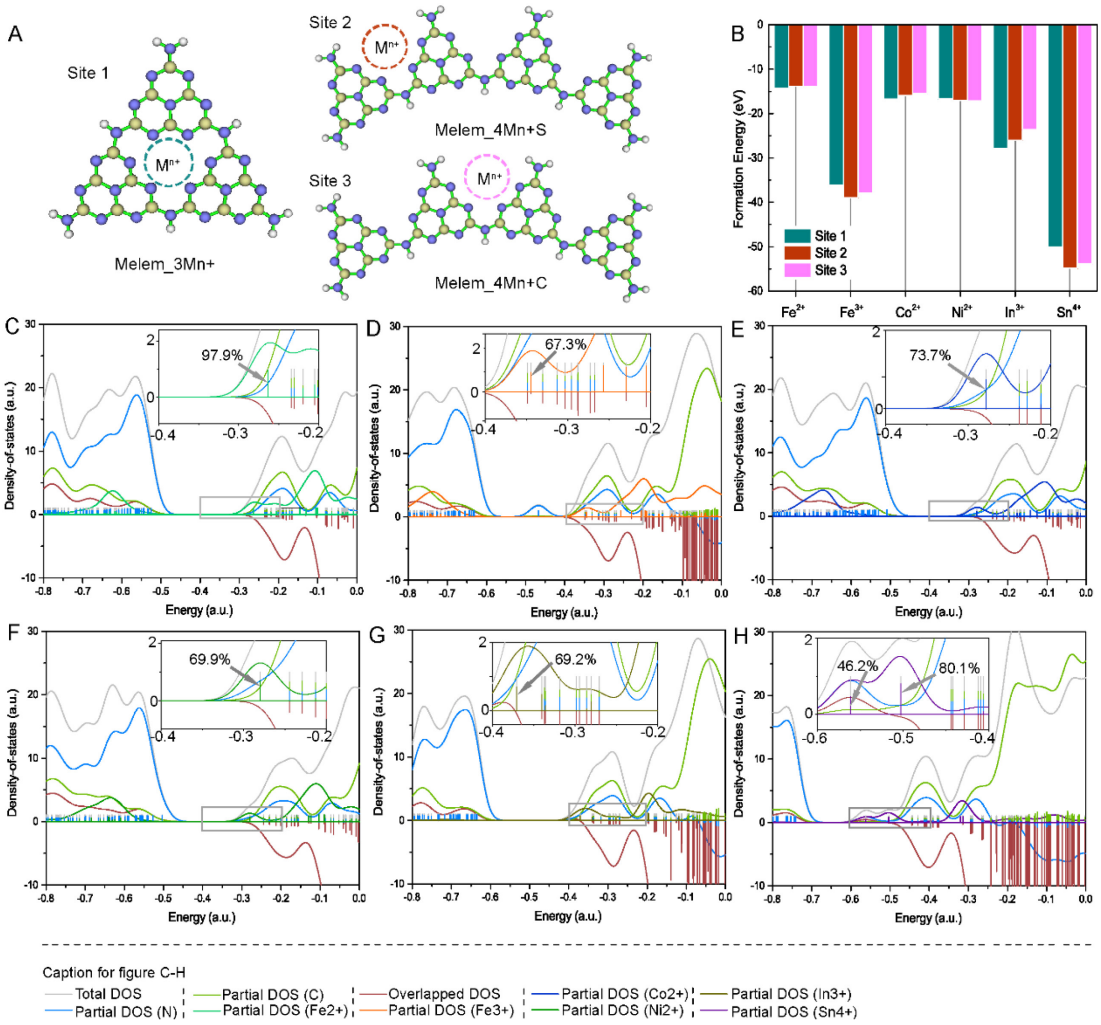

Figure 3-11. Stabilities and electronic configurations of cluster models. (A) Schematic diagram for two cluster models and three possible sites for coordination of metal ions. (B) Formation energies of various transition metals embedded in Melem_3 or Melem_4. Computed simulation of density of states (DOS) with different embedded (C) Fe^{2+}, (D) Fe^{3+}, (E) Co^{2+}, (F) Ni^{2+}, (G) In^{3+}, and (H) Sn^{4+} with the coordination of the large nitrogen pots in Melem_3. The insert figures are amplified the states (metal) that formed the orbitals those close to LUMO.

In this case, two cluster models of Melem_3 (Figure 3-11A, left; Figure 3-12A) and Melem_4 (Figure 3-11A, Right; Figure 3-12B) [47] were built to represent the non-defected g-C_3N_4 units and melon units in the material matrix, respectively. Metal ions are coordinated by N atoms of Melem_3 and Melem_4 form single atomic sites. Distinguished by the geometry position of the metal ions, three models that represent single-atom photocatalysts could be built as well. It should be noted that the introduction of cations usually results in localized charge sites in the PCN matrix. In this case, the charges and multiplicities of cluster models were set by referring to the chemical states of incorporated metals. Aiming to assess the stability of M-SAPCs, the formation energies of metal ions embedded in the Melem_3 and Melem_4 models were calculated. As shown in Figure 3-11B, all of the values of formation energy are negative, suggesting that the coordination of metal ions with nitrogen is thermodynamically favorable. These results indicate that both g-C_3N_4 units and melon units could stabilize metal ions by forming strong metal-nitrogen bonds.

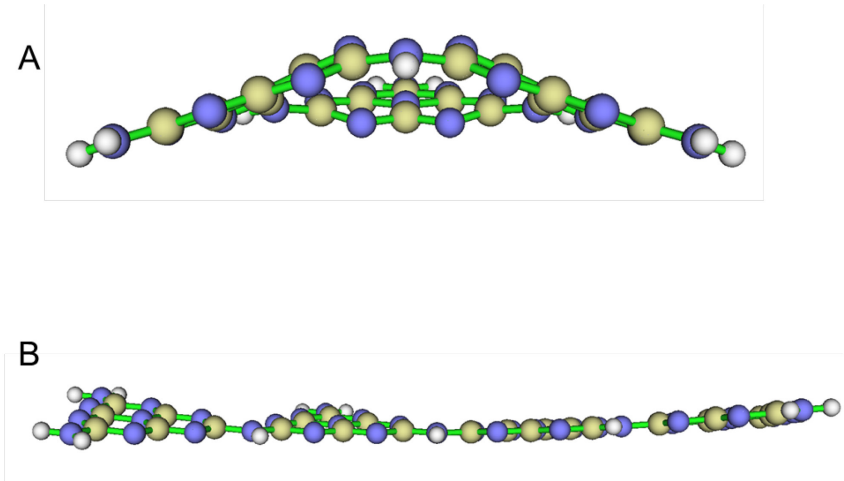

Figure 3-12. Side-view of the two different kinds of Melem_3 model.

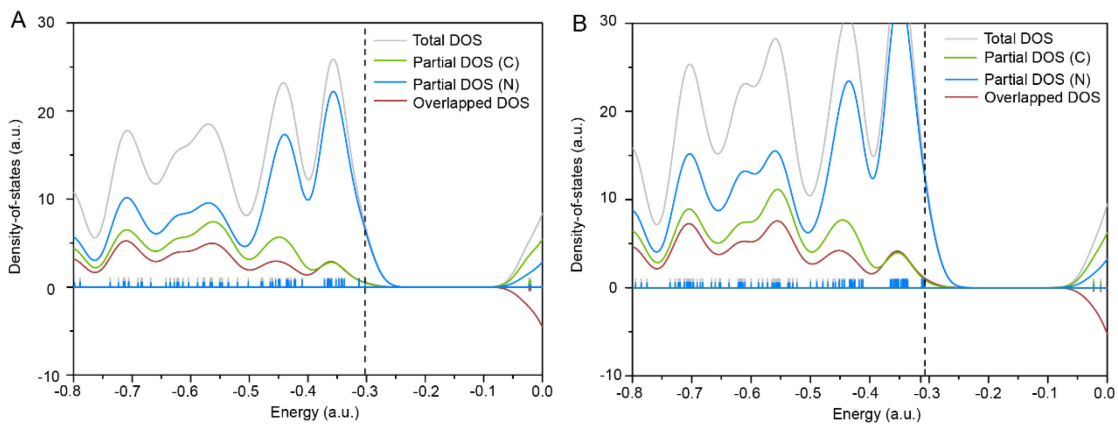

Figure 3-13. Electronic configuration of cluster models representing pristine PCN. Computed simulation of density of states (DOS) of (A) Melem_3 and (B) Melem_4. The unit of energy in these figures is Hartree.

The energy difference between the ionization potential (IP) and electron affinity (EA)

usually corresponds to the band gap of material. Thus, the band gap is equivalent to, at the material level, the molecular fundamental gap. In this case, the fundamental gap usually approximately corresponds to the HOMO–LUMO gap [48]. In this work, wb97xd—a function with large amounts of Hartree–Fock (HF) exchange—was used to simulate the charge transfer densities during the excitation. Previous works revealed that this function usually overestimates the HOMO-LUMO gap and excitation energies in the case of p-conjugated polymers. Additionally, p-conjugated molecules adjacent to the one carrying a charge do strongly polarize (about 2 eV) in the solid state [48]. Although the computed HOMO-LUMO gap is considerably larger than the experimentally measured band gap, the relative changing tendencies of HOMO-LUMO gaps can still reveal the influence of ion incorporation if the same function and basis are used. In this case, the energetic levels of HOMO and LUMO of Melem_3, Melem_4, Melem_3M, Melem_4MC, and Melem_4MS were symmetrically investigated (Table 3-2) to reveal the influence of metal ions on the electronic configurations combined with density of states analysis, thus to validate the clusters models by estimating the correlations with experimental results.

Table 3-2. Detailed HOMO-LUMO gaps cluster models for simulation of single atom catalyst.

Sample	Energy (eV)		Sample	Energy (eV)		Sample	Energy (eV)	
	HOMO	LUMO		HOMO	LUMO		HOMO	LUMO
Melem_3	-8.24	-0.62	Melem_4	-8.35	-0.62			
Melem_3Fe2+	-14.28	-7.18	Melem_4Fe2+S	-10.52	-7.89	Melem_4Fe2+C	-11.73	-7.70
Melem_3Fe3+	-17.17	-12.71	Melem_4Fe3+S	-13.85	-9.84	Melem_4Fe3+C	-12.54	-11.09
Melem_3Co2+	-13.84	-7.59	Melem_4Co2+S	-10.79	-8.75	Melem_4Co2+C	-11.19	-10.10
Melem_3Ni2+	-13.71	-7.61	Melem_4Ni2+S	-10.52	-7.69	Melem_4Ni2+C	-11.75	-7.49
Melem_3In3+	-17.28	-10.09	Melem_4In3+S	-13.48	-12.55	Melem_4In3+C	-17.81	-15.86
Melem_3Sn4+	-20.16	-15.29	Melem_4Sn4+S	-16.43	-14.08	Melem_4Sn4+C	-15.00	-14.33

Melem_3 and Melem_4 show similar HOMO and LUMO positions with similar HOMO-LUMO gaps of 7.61 eV and 7.73 eV, respectively, indicating that both the g-C_3N_4 units and melon units in the PCN matrix have similar electronic configurations. The N 2p states and C 2p states contribute to HOMO~HOMO-4 and LUMO~LUMO+4, respectively, indicating that N 2p states and C 2p states fundamentally compose the VB and CB of pristine PCN.

The introduction of metal ions into g-C_3N_4 units (Melem_3M) have almost no effect on the orbital composition of HOMO~HOMO-4, which is in accordance with the almost constant VBMs of M-SAPCs (Figure 3-9). The introducing the metal ions result in several intermediate energy levels which is 0.5 ~ 2 eV lower than the lowest energy level dominated by C 2p state (The amplified DOS curves of incorporated metals are inserted in the Figure 3-11C-H). Most of newly formed energetic levels compose LUMO levels, leading to narrowed HOMO-LUMO gaps (Figure 3-11C-H) compared with that of Melem_3 (Figure 3-13), which is in accordance with the experimental results (Figure 3-8B). On the other hand, the HOMO levels of Melem_4MS (Figure 3-14) and Melem_4MC (Figure 3-15) are significantly shifted after the introduction of metallic ions, due to the formations of new energetic levels composed by N 2p or M 3d states. Additionally, several intermediate energetic levels also appeared between the HOMO of Melem_4MS and that of Melem_4MC (These energy levels all formed LUMO of Melem_4M.), leading to a significantly narrowed HOMO-LUMO gap that is even smaller than the experimental band gap. The normalized LUMOs of Melem_3M, Melem_4MS and Melem_4MC (M being Co2+, Ni2+, In3+, and Sn4+) are summarized in Figure 3-16. The experimental CBMs of M-SAPCs and pristine PCN (black line) were also summarized for comparison. The changing tendency of LUMOs in the simulation results indicates that only the metal ions isolated by Melem_3 units (red line) show acceptable in accordance with M-SAPCs in terms of HOMO-LUMO positions for theoretical simulation and band positions for experimental results (The interrelationship between the HOMO-LUMO gap is explained in the beginning of this section). In this case, although the coordination of metal ions with melon units is thermodynamically acceptable, the band structures and electronic configurations show poor relationships with experimental band diagram. Therefore, cluster models of Melem_3M were utilized for simulating the influence of isolated metal sites on the excitation properties of M-SAPCs.

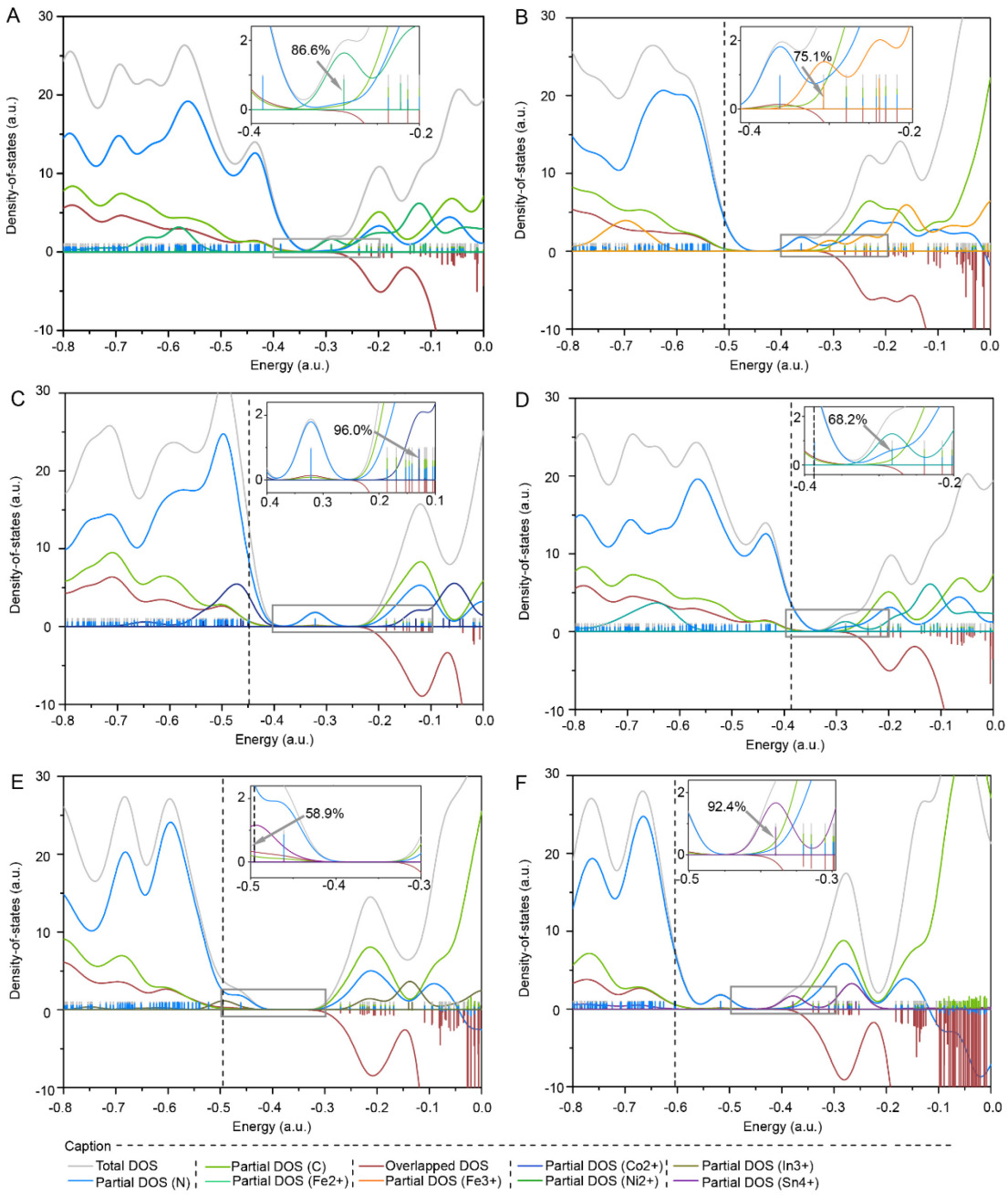

Figure 3-14. Electronic configuration of cluster models representing melon coordinated single metal atomic sites (site 2). Computed simulation of density of states (DOS) of (A) Melem_4Fe2+S, (B) Melem_4Fe3+S,(C) Melem_4Co2+S,(D) Melem_4Ni2+S,(E) Melem_4In3+S, and (F) Melem_4Sn4+S. The unit of energy in these figures is Hartree. The insert figures are amplified the states (metal) that formed the orbital close to HOMO or LUMO.

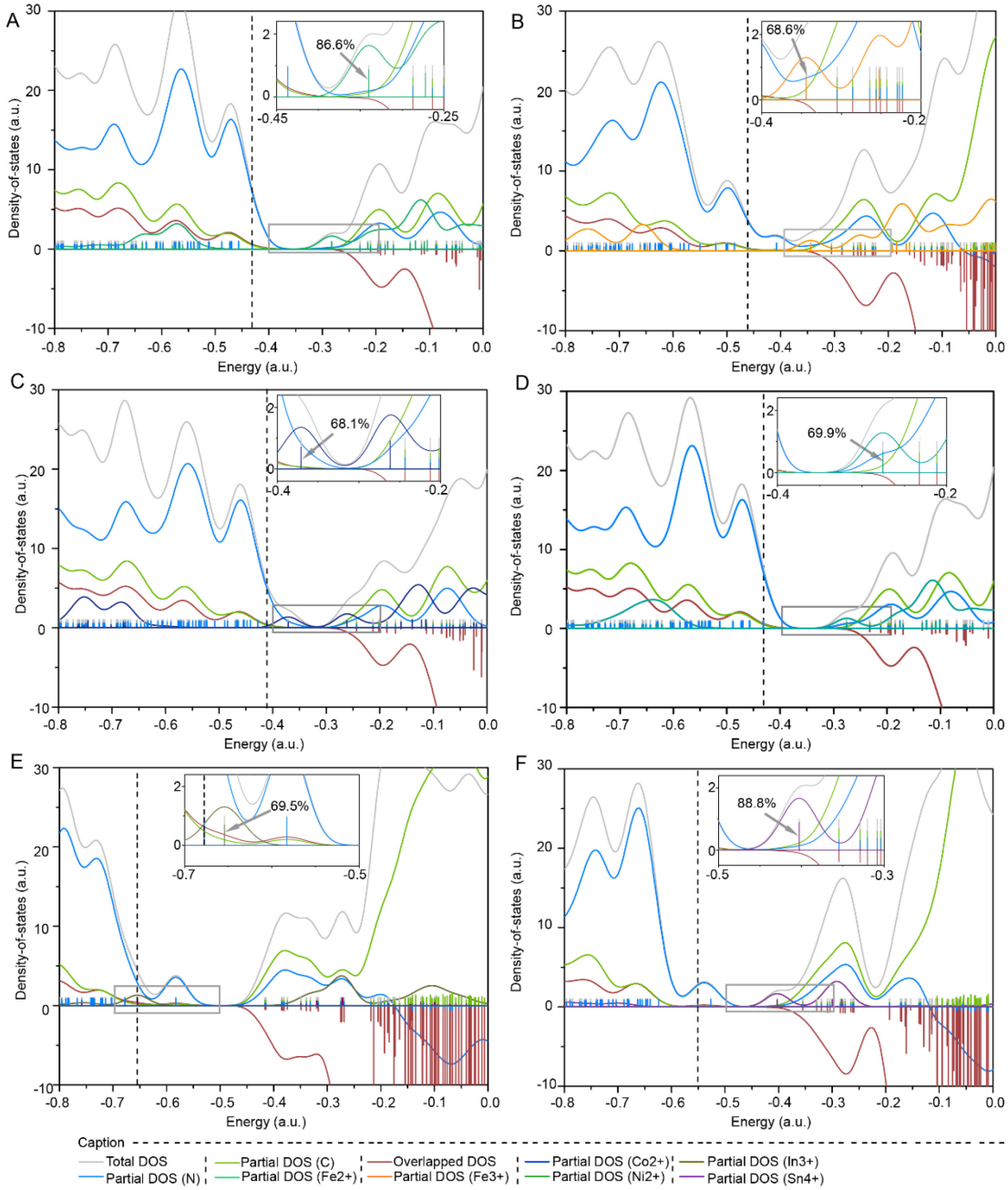

Figure 3-15. Electronic configuration of cluster models representing melon coordinated single metal atomic sites (site 3). Computed simulation of density of states (DOS) of (A) Melem_4Fe2+C, (B) Melem_4Fe3+C,(C) Melem_4Co2+C,(D) Melem_4Ni2+C,(E) Melem_4In3+C, and (F) Melem_4Sn4+C. The unit of energy in these figures is Hartree. The insert figures are amplified the states (metal) that formed the orbital close to HOMO or LUMO.

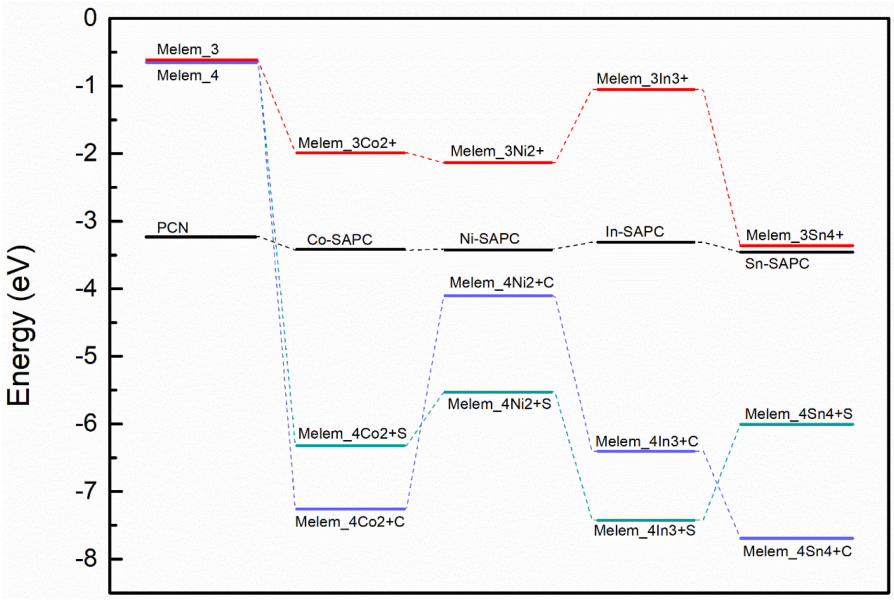

Figure 3-16. Comparison between the normalized E_{LUMO} and CBM measured by Mott-Schottky measurement. E_{LUMO} of Melem_3M is normalized by the difference between the E_{HOMO} and E_{LUMO} of Melem_3 and Melem_3M. E_{LUMO} of Melem_4M is normalized by the difference between the E_{HOMO} and E_{LUMO} of Melem_4 and Melem_4M. Detailed energy level data were presented in Table 3-2.

3.1 Molecular orbitals and transition densities

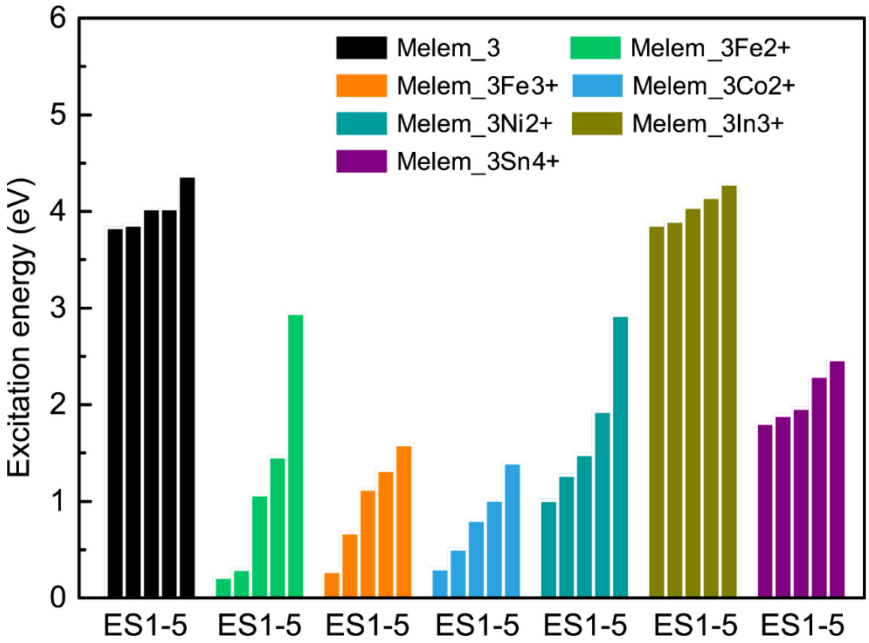

Figure 3-17. Vertical excitation energy of Melem_3 and Melem_3M. The energy difference form ground state (ES0, also can be named as S_0) and first five excited states (ES1-ES5, also can be named as S_1-S_5) were calculated.

Visible light irradiation is used for photocatalytic H_2O_2 since UV irradiation ($\lambda < 400$ nm) will drastically decompose H_2O_2 generated by $2e^-$ ORR [10, 49]. In case of PCN and its

derives, the adsorption edge is near 450~470 nm, i. e., the excitations with low energy play crucial roles in the visible light-driven H_2O_2 production [49]. In this case, the lowest-lying electronic transition computed by TDDFT usually represents the most possible excitations which can generate the electron hole pairs for photocatalytic $2e^-$ ORRs when using PCN and its derivatives [49]. In this work, the first 5 excited states (ES1-ES5, ES1 referring to the excited state 1 with the lowest excitation energy) of Melem_3 and Melem_3M were computed to investigate the most possible excitation properties and electronic transition properties [45]. The excitation energies of ES1 to ES5 are summarized in Figure 3-17. The computed optimal gap of Melem_3 is slightly larger than the experimental band gap, due to the fact that wb97xd contains a large amount of HF exchange. Therefore, the changing tendency of excitation energy was compared with the changing tendency of HOMO-LUMO gap, which is used to give an approximation for E_{fund}, leading to a primary understanding of the electron-hole pair binding energy (E_b, E_b is rigorously defined as: $E_b = E_{fund} – E_{opt,}$ in which E_{opt} is the energy difference between ES0 and ES1.) In this work, the approximated binding energy of electron-hole pairs (E_{abX}) in each excited state is defined as follows:

$$E_{abX} = E_{HOMO-LUMO} - E_{ecX}$$

where E_{abX} and E_{ecX} refer to the approximated binding energy of electron-hole pairs and the excitation energy of excited state No. X, respectively (Figure 3-18A). The E_{abX} values of Melem_3 and Melem_3M are shown as in Figure 3-18B. With the incorporation of Fe^{2+}, Fe^{3+}, Co^{2+} and Ni^{2+}, E_{abX} of Melem_3M significantly increased. On the other hand, Melem_3In3+ and Melem_3Sn4+ showed similar values of E_{abX}, which are both smaller than E_{abX} of Melem_3. These results indicate that the charge recombination may be suppressed by the introduction of In^{3+} and Sn^{4+} into g-C_3N_4 units, whereas the incorporation of Fe^{2+}, Fe^{3+}, Co^{2+}, and Ni^{2+} could result in a thermodynamically recombination tendency.

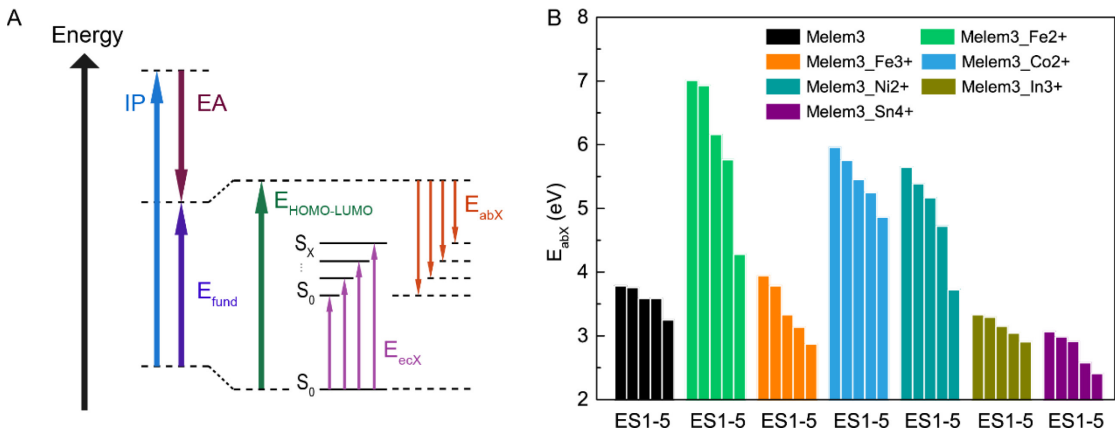

Figure 3-18. Approximate binding energies of Melem_3 and Melem_3M. (A) Illustration of gap energies in the molecular case: S_0 denotes the electronic ground state and S_X is the No. X excited state. The $S_X \rightarrow S_0$ energy difference then corresponds to the excitation energy E_{ecX}. The magnitude of the ionization potential is shown by the blue-colored vertical line and the magnitude of the electron affinity is shown by the wine-colored vertical line; the IP→EA difference represents (violet line) the fundamental gap, E_{fund}, which is usually smaller than the HOMO-LUMO gap, $E_{HOMO\text{-}LUMO}$. The approximate electron–hole pair binding energy, E_{abX}, is given by $E_{HOMO\text{-}LUMO}$ - E_{ecX}. (B) The computed approximate binding energies of Melem_3 and Melem_3M for the five lowest-lying excited states.

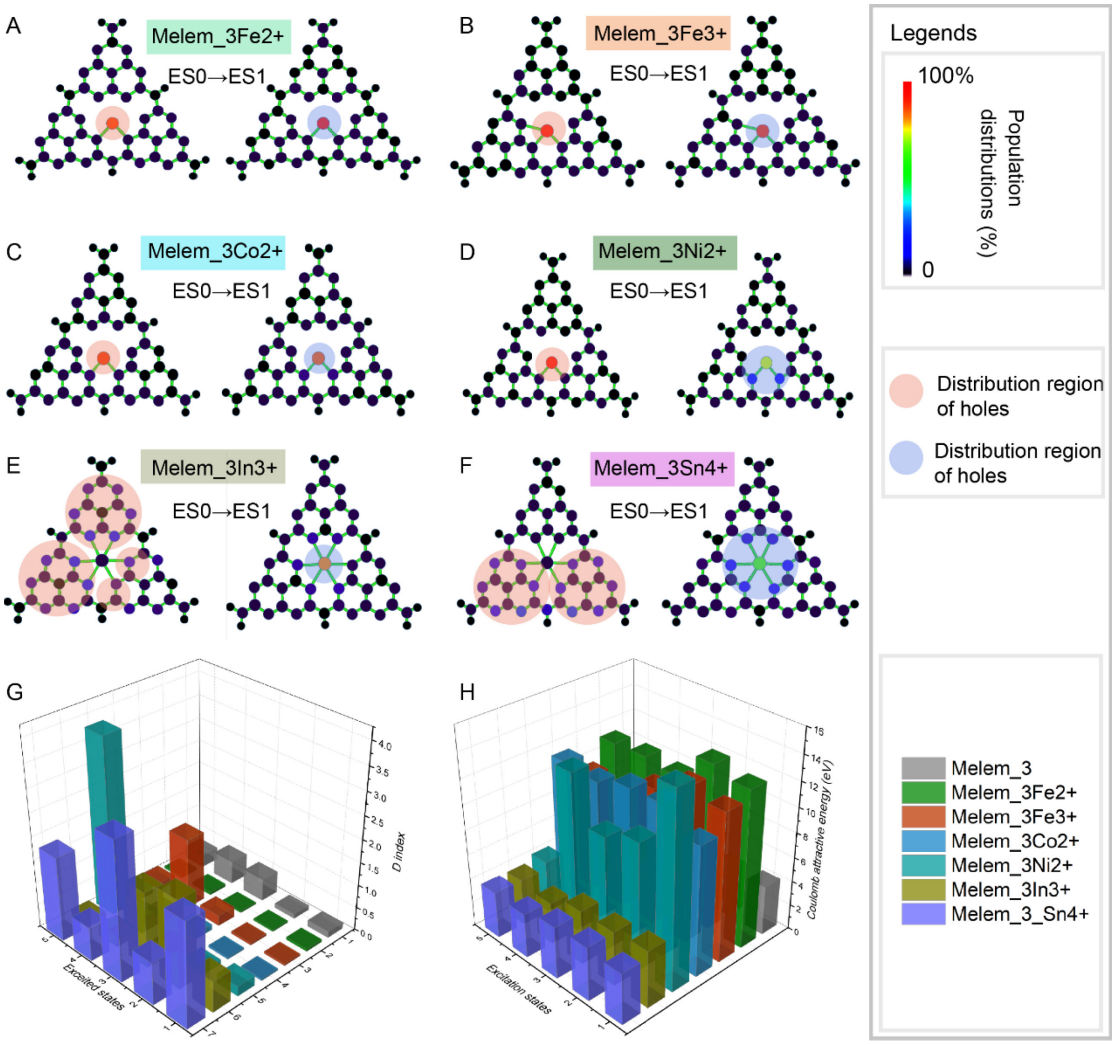

Figure 3-19. Transition densities of Melem_3M. Population of electron and hole distributions (vertical excitation at the excited state 1) and quantitative investigation of the charge separation. The color in the heatmap refers to the sum of MO contribution at each atom for simulated electrons and holes of (A) Melem_3Fe2+, (B) Melem_3Fe3+, (C) Melem_3Co2+, (B) Melem_3Ni2+, (E) Melem_3In3+, and (F) Melem_3Sn4+. The orange and blue shadows are accumulated regions of hole and electrons, respectively. (G) D index and (H) Coulomb attraction between hole and electron of Melem_3 and Melem_3M.

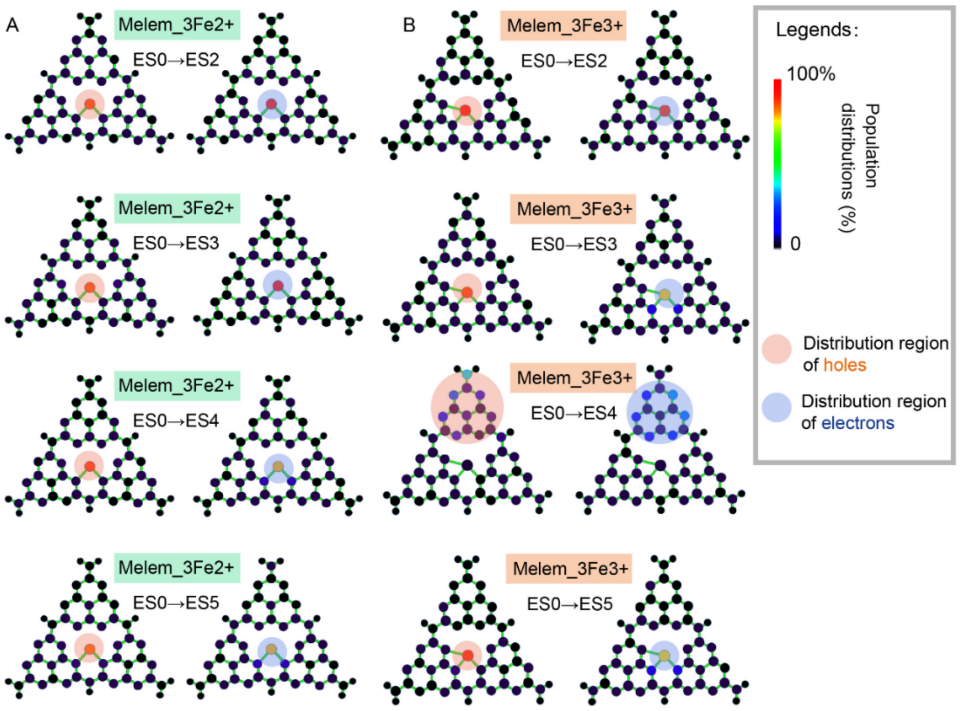

Figure 3-20. The population of electron and hole distribution of (A) Melem_3Fe2+ and (B) Melem_3Fe3+ obtained by TD-DFT (vertical excitation at excited states from 2 to 5). The color in the heatmap refers to the sum of MO contribution at each atom for simulated electrons and holes.

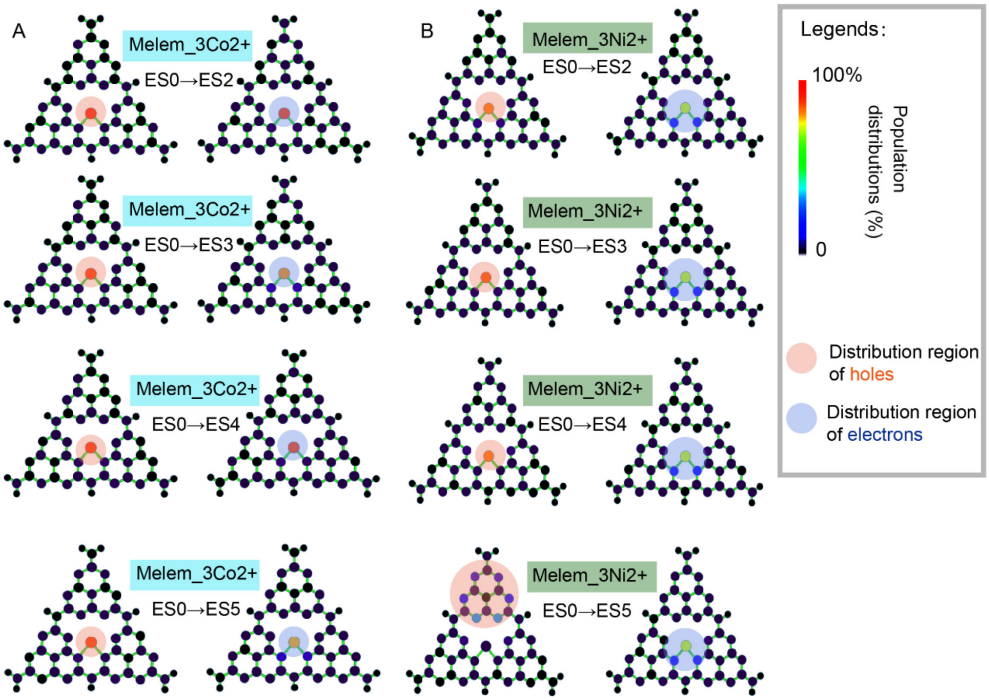

Figure 3-21. The population of electron and hole distribution of (A) Melem_3Co2+ and (B) Melem_3Ni2+ obtained by TD-DFT (vertical excitation at excited states from 2 to 5). The color in the heatmap refers to the sum of MO contribution at each atom for simulated electrons and holes.

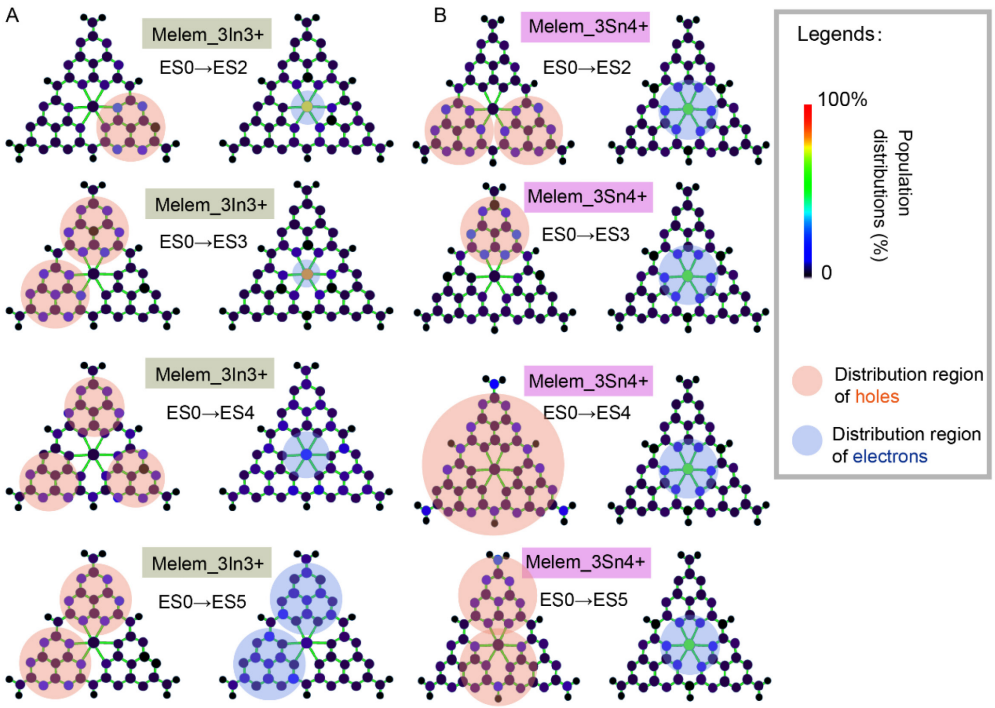

Figure 3-22. The population of electron and hole distribution of (A) Melem_3In3+ and (B) Melem_3Sn4+ obtained by TD-DFT (vertical excitation at excited states from 2 to 5). The color in the heatmap refers to the sum of MO contribution at each atom for simulated electrons and holes.

Table 3-3. TDDFT results for the five lowest-lying excited singlet state for melem_3M (M = In3+ and Sn4+): Molecule obtital contribution (MO contr.) and multiplicity (S**2).

	Melem_3In3+*					Melem_3Sn4+*				
States	MO contr. (Hole)		MO contr. (Electron)		S**2**	MO contr. (Hole)		MO contr. (Electron)		S**2
	MO 132	1.2%	MO 154	97.8%		MO 131	1.6%	MO 154	99.2%	
	MO 150	2.4%				MO 138	4.4%			
$S_0 \rightarrow S_1$	MO 153	49.9%			0	MO 150	21.0%			0
						MO 152	2.8%			
						MO 153	66.9%			
	MO 140	11.4%	MO 154	90.9%		MO 137	2.2%	MO 154	99.1%	
	MO 144	3.1%	MO 155	2.3%		MO 145	22.1%			
$S_0 \rightarrow S_2$	MO 149	11.0%	MO 156	1.5%	0	MO 147	13.2%			0
	MO 150	4.4%	MO 157	1.5%		MO 149	17.4%			
	MO 153	63.5%				MO 151	40.5%			
	MO 130	2.1%	MO 154	96.3%		MO 132	3.2%	MO 154	99.1%	
	MO 239	12.8%	MO 156	1.3%		MO 145	30.6%			
$S_0 \rightarrow S_3$	MO 148	11.9%			0	MO 147	26.2%			0
	MO 150	1.2%				MO 149	6.5%			
	MO 152	68.5%				MO 151	30.0%			
	MO 149	3.5%	MO 154	7.5%		MO 141	5.1%	MO 154	99.3%	
	MO 150	9.4%	MO 155	12.3%		MO 143	3.3%			
$S_0 \rightarrow S_4$	MO 151	5.6%	MO 156	30.7%	0	MO 150	3.4%			0
	MO 152	30.7%	MO 157	29.1%		MO 152	77.8%			
	MO 153	40.8%	MO 158	6.8%		MO 153	8.6%			
	MO 148	4.3%	MO 156	51.7%		MO 138	12.7%	MO 154	99.3%	
	MO 149	2.9%	MO 157	21.3%		MO 148	3.2%			
$S_0 \rightarrow S_5$	MO 150	31.3%	MO 158	4.4%	0	MO 150	44.0%			0
	MO 152	29.0%	MO 161	8.0%		MO 152	11.1%			
	MO 153	23.0%	MO 162	3.2%		MO 153	20.2%			

The HOMO and LUMO of Melem3_In3+ and Melem3_Sn4+* is MO160 and MO161, respectively.

S2=S(S+1); S is the spin quantum number of the as-prepared cluster model.

Table 3-4. TDDFT results for the five lowest-lying excited singlet state for melem_3TMs (TM = Fe2+, Fe3+, Co2+, Ni2+): Molecule orbital contribution (MO contr.) and multiplicity (S**2).

States	Melem_3Fe2+**					Melem_3Fe3+**					Melem_3Co2+***					Melem_3Ni2+***				
	MO (Hole)	contr.	MO (Electron)	contr.	S**2	MO (Hole)	contr.	MO (Electron)	contr.	S**2	MO (Hole)	contr.	MO (Electron)	contr.	S**2	MO (Hole)	contr.	MO (Electron)	contr.	S**2
	134	8.5%	161	91.5%		141B*	7.7%	161B	11.3%		134B	8.0%	162A*	11.2%		135	1.3%	162	99.5%	
	138	4.4%	163	1.0%		143B	4.3%	163B	18.4%		137B	12.6%	161B	51.0%		140	14.8%			
$S_0 \rightarrow S_1$	141	7.3%	164	1.4%	0	150B	7.9%	165B	17.0%	2.0	138B	6.1%	162B	24.9%	1.6	141	21.5%			0
	144	51.3%	165	1.8%		151B	47.2%	166B	10.7%		139B	20.0%	163B	7.4%		145	60.4%			
	158	9.3%	172	2.1%		152B	9.0%	170B	10.5%		144B	6.0%	171B	1.5%						
	132	8.5%	161	91.5%		141B	7.1%	163B	17.8%		134B	18.2%	161B	77.9%		133	20.6%	162	99.5%	
	137	9.1%	163	1.0%		143B	4.5%	164B	5.9%		138B	16.5%	162A	1.8%		134	13.3%			
$S_0 \rightarrow S_2$	139	36.8%	164	1.4%	0	150B	7.4%	165B	14.8%	2.0	140B	8.5%	162B	25.6%	1.4	138	11.2%			0
	147	10.0%	165	1.8%		151B	43.5%	166B	13.1%		143B	7.9%	163B	16.5%		146	30.9%			
	149	18.8%	172	2.1%		152B	11.5%	170B	18.3%		145B	13.5%	171B	1.9%		150	6.2%			
	135	8.7%	161	96.4%		140A	11.2%	163A	41.9%		133A	22.5%	162A	47.8%		126	3.3%	162	99.5%	
	139	6.9%	172	1.4%		142A	9.3%	164A	2.4%		134A	12.5%	163A	2.4%		130	2.3%			
$S_0 \rightarrow S_3$	142	32.0%			0	142B	7.2%	168B	42.3%	3.7	137B	4.5%	161B	25.6%	2.3	137	68.7%			0
	143	18.9%				147B	6.8%	169B	5.3%		139B	11.4%	162B	16.5%		139	7.3%			
	153	13.1%				152B	20.4%	170B	2.2%		140B	4.8%	163B	4.1%		153	11.9%			
	135	10.1%	164	40.4%		150A	1.7%	161A	97.5%		131B	47.1%	162A	1.5%		125	17.8%	162	99.2%	
	142	34.2%	165	51.2%		156A	60.4%				135B	5.0%	161B	70.8%		131	55.9%			
$S_0 \rightarrow S_4$	143	20.3%	167	6.7%	0	158A	19.0%			2.0	137B	4.7%	162B	16.0%	1.4	141	3.6%			0
	153	11.4%				159A	2.7%				139B	8.0%	163B	5.4%		154	3.2%			
	156	4.4%				160A	11.8%				145B	3.5%	171B	1.9%		155	6.9%			
	134	6.9%	161	3.9%		143A	26.8%	163A	58.2%		132A	12.0%	162A	39.8%		142	6.6%	162	99.8%	
	138	6.2%	164	40.0%		144A	11.3%	164A	3.3%		133A	10.8%	163A	1.9%		152	6.3%			
$S_0 \rightarrow S_5$	141	48.7%	165	48.6%	0	147A	7.9%	166B	2.4%	3.2	134A	5.0%	162B	43.4%	2.2	156	6.2%			0
	155	4.8%	167	6.1%		151A	7.2%	168B	23.1%		131B	34.7%	163B	12.4%		159	48.4%			
	158	13.9%				151B	17.2%	169B	2.6%		140B	4.7%				161	20.9%			

*A and B respectively refers to alpha and beta orbitals for cluster models with open-shell electronic configurations.

**The HOMO and LUMO of Melem3_Fe2+ and Melem3_Fe3+ is MO160 and MO161, respectively.

***The HOMO and LUMO of Melem3_Co2+ and Melem3_Ni2+ is MO161 and MO162, respectively.

The distribution heatmaps of photo-generated electrons and holes (electronic transition densities) of Melem_3M were further investigated to identify the excitation types and to predict the spatial charge separation of the M-SAPCs. As shown in Figure 3-20 and Figure 3-21, the distribution of electrons and holes at the first 5 ESs for Melem_3Fe2+, Fe3+, Co2+, and Ni2+ is extremely localized. Both the electrons and holes are distributed in a very small region just near the metal sites, indicating that typical localized transitions

occurred. On the other hand, the lowest energy transitions (ES1-ES5) in Melem_3In3+ and Melem_3Sn4+ are dominated by charge transfer excitations, which are mostly associated with In and Sn atoms (Figure 3-22). To quantitatively investigate the charge separation properties of Melem_3M, the D index (i. e., the distance between the two barycenters of electrons or holes) and the Coulomb attraction between holes and electrons (E_{Coulmb}, also called exciton binding energy) were further computed (Figure 3-19G-H). D index and E_{Coulmb} of melem_3 were also computed for comparison. As given in Figure 3-19G-H, the transition distance of electron-hole pairs in Melem_3In3+ and Melem_3In4+ drastically increased compared with that in Melem_3 and considerably larger than most of the D index values of Melem_3Fe2+, Fe3+, Co2+, and Ni2+. E_{Coulmb} values of Melem_3In3+ and Melem_3In4+ were almost same as that in Melem_3, while E_{Coulmb} values of Melem_3Fe2+, Fe3+, Co2+, and Ni2+ drastically increased. There results further verified the charge separation tendency revealed by E_{abX}, further suggesting that charge separation of atomically dispersed In and Sn sites can significantly facilitate charge separation and suppress charge recombination. Note that 60%~70% of the electronic densities are concentrated at In sites, while only 40%~50% of the electrons are accumulated at Sn sites. Thus, with the help of obvious differences among the E_{abX}, D index, and E_{Coulmb} values of Melem_3 and Melem_3M, the highly concentrated electrons in Melem_3In3+ and Melem_3Sn4+ predict a much higher charge separation efficiency of In-SAPC and Sn-SAPC than that of Fe-SAPC, Co-SAPC and Ni-SAPC.

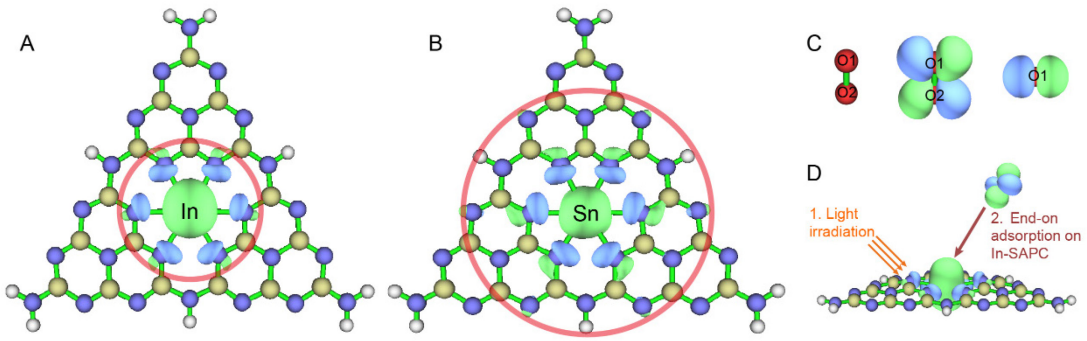

Figure 3-23. Visualization of the dominant contributing molecular orbitals and transition. Visualization of the LUMOs of (A) Melem_3In3+ and (B) Melem_3Sn4+. Red circles refer to the observable region of isosurface on Melem_3In3+ and Melem_3Sn4+. (C) Visualization of HOMO of O_2. (D) Schematic diagram of possible O_2 adsorption

configuration on the Melem_3In3+ surface after light irradiation.

To further determine the influence of metal atoms on photo-redox reactions, the contribution of molecular orbitals (MOs) to holes and electrons from ES1 to ES5 of Melem_3M were investigated (Tables 3-3 and 3-4). Several MOs with energetic levels equal to or lower than the HOMO all contribute to holes (ranging from 0% to ~60%), while the LUMO is dominants for electron in ES1-ES3 of Melem_3In3+ and in ES1-ES5 of Melem_3Sn4+ (> 90%). These observations suggest that the electronic configuration of LUMO can almost represent the photogenerated electronic configuration if the electrons are accumulated to the atomic sites. Thus, the iso-surface of LUMO of Melem_In3+ and Melem_3Sn4+ was plotted as shown in Figures 3-23A-B. If can be clearly seen that electrons are concentrated at the In and Sn sites. The photo-generated electrons tend to form a highly condensed region atomic sites of In and Sn. The iso-surface of LUMO also showed that the electrons tend to form a highly condensed region in In sites during the excitation. Furthermore, the iso-surface of Melem_3In3+ and Melem_3Sn4+ showed an ideal electronic configuration for the adsorption of electrophilic oxygen, indicating that the ORR reduction could be accelerated at In and Sn sites (Figures 3-23C-D).

3.3.3 Experimental charge separation properties and activity for H_2O_2 production

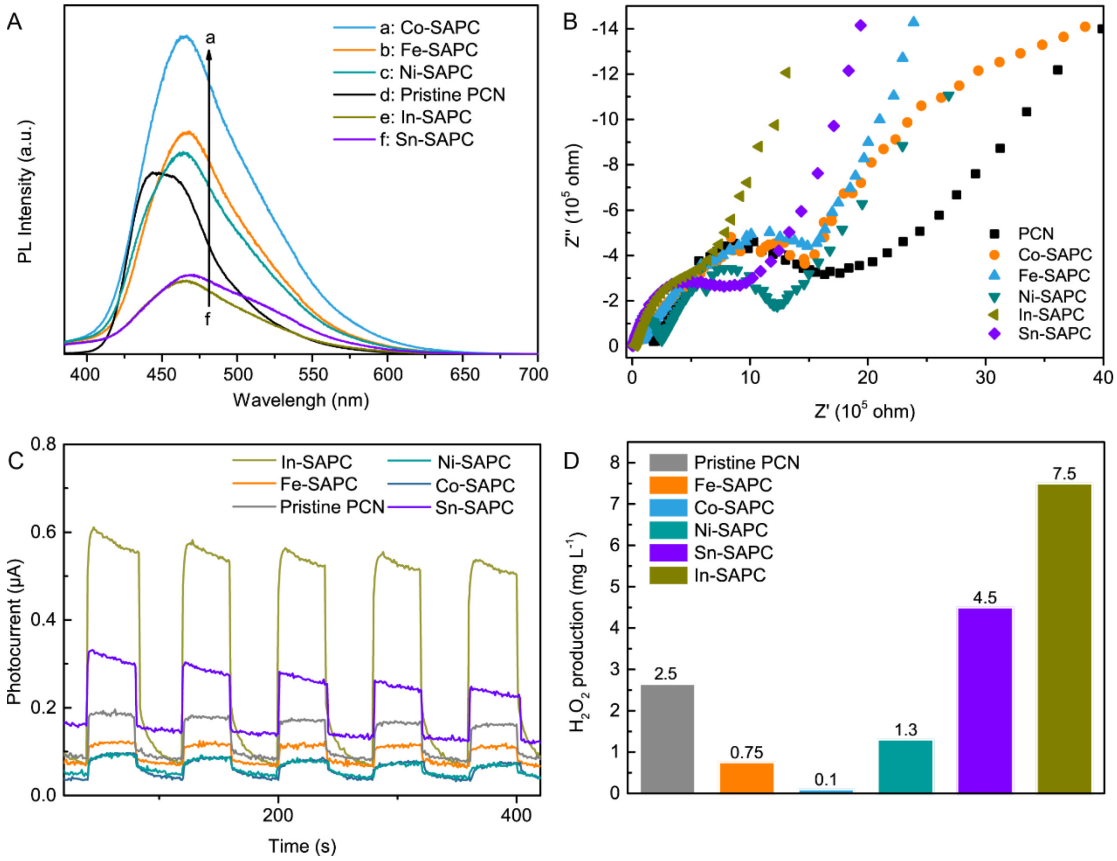

Figure 3-24. Photoexcitation properties and photocatalytic activities of pristine PCN and M-SAPCs. (A) Photoluminescence spectra of pristine PCN and M-SAPCs under 365 nm excitation. (B) EIS of electrodes prepared by PCN and M-SAPCs under visible light irradiation. (C) Photocurrents of electrodes prepared by pristine PCN and M-SAPCs. (D) Photocatalytic activities of pristine PCN and M-SAPCs for H_2O_2 production in 10% (v/v) ethanol aqueous solution.

To verify the theoretical prediction of charge separation efficiency obtained from the simulation of molecular orbitals and transition densities, the photochemical properties of as-prepared M-SAPCs were measured. As shown in the photoluminescence (PL) spectra (Figure 3-24A), the PL intensities of Sn-SAPC and In-SAPC were significantly decreased, indicating drastically suppressed charge recombination. On the other hand, the PL intensities of Fe-SAPC, Co-SAPC and Ni-SAPC all increased obviously, manifesting that the introduction of Fe, Co, and Ni ions into the PCN matrix facilitates charge recombination. The PL intensity ($I_{M\text{-}SAPC}$) of M-SAPC follows a sequence of $I_{Co} > I_{Fe} > I_{Ni} > I_{Sn} > I_{In}$, being in accordance with the E_{abx} ($E_{abCo} \approx E_{abNi} > E_{abSn} \approx E_{abIn}$) as shown in Figure 3-18. As shown in Nyquist plots, the diameter of the semicircle (In-SAPC) was the smallest (Figure 3-24B),

indicating that In-SAPC showed the best charge transfer. Moreover, photocurrent (I_{ph}) measurements of the samples showed a significant increase in I_{ph} of In-SAPC and Sn-SAPC (Figure 3-24C), indicating enhanced efficiency of charge separation. On the other hand, the incorporation of Fe, Co, and Ni ions weakened I_{ph}, indicating significantly promoted charge recombination. The photocatalytic activity for H_2O_2 production (λ > 420 nm) of pristine PCN and as-prepared M-SAPC samples were measured with 10% (v/v) ethanol as an electron donor. After 3 reproductive experiments (Figure 3-24D and Figure 3-25), In-SAPC and Sn-SAPC showed superior photocatalytic activity among all of the M-SAPC samples, while the atomically dispersed Fe, Co, and Ni sites all drastically decreased the photocatalytic activity compared with that of pristine PCN, which is consisted with both experimental and theoretical charge separation properties.

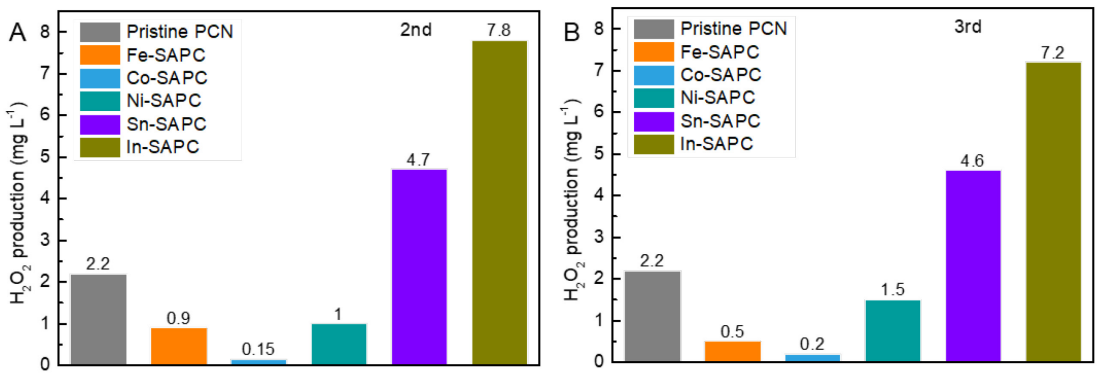

Figure 3-25. Reproductivity measurements of M-SAPCs. (A) The second experiment. (B) The third experiment.

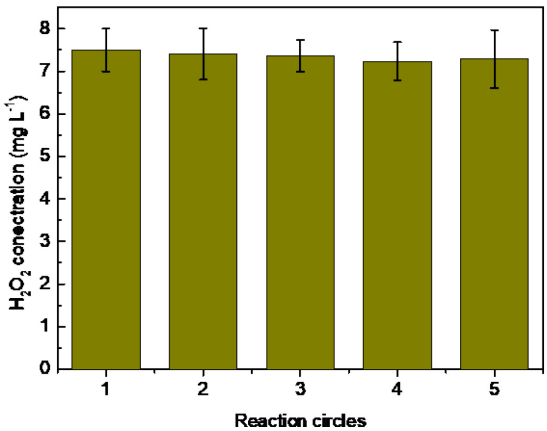

Figure 3-26. Stability of In-SAPC. Photocatalytic performance of **In-SAPC** for H_2O_2 production in 5 cycles (5 h) under visible light irradiation. After each circle, the fixed catalyst was washed by deionized water for at least 5 times.

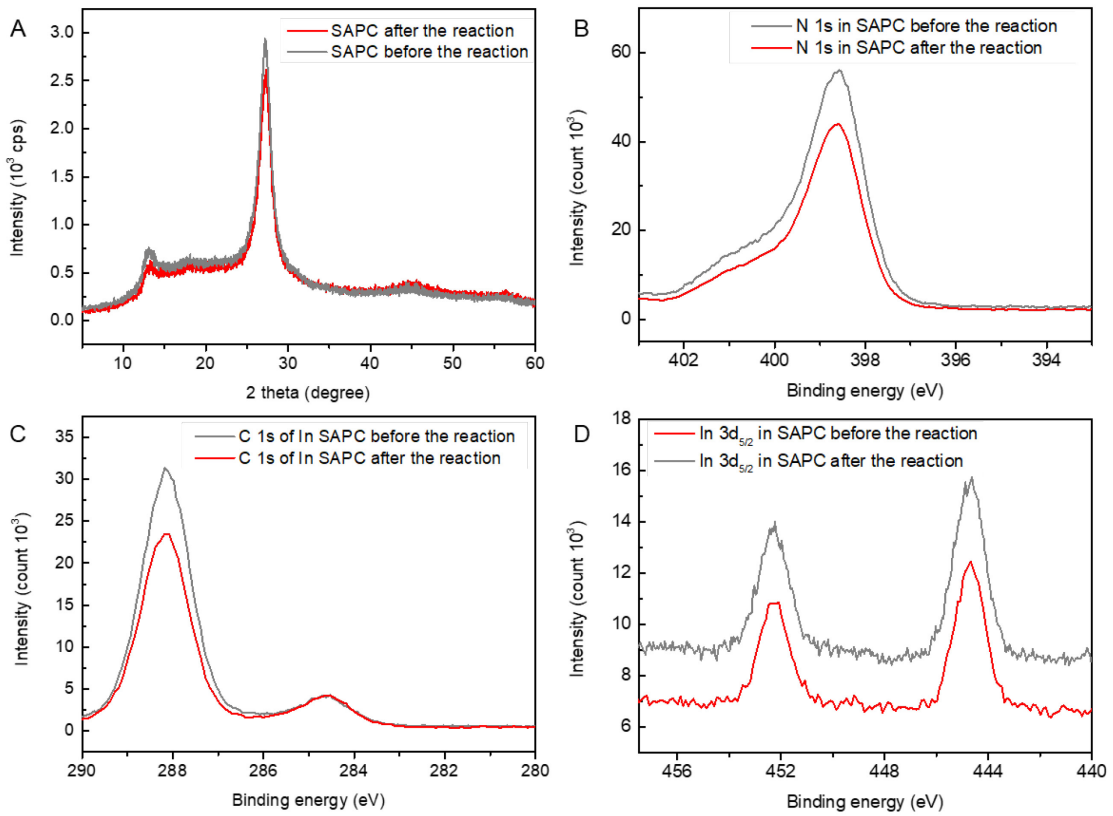

Figure 3-27. Photochemical stability of In-SAPC. XRD patterns of In-SAPC before and after photocatalytic H_2O_2 production for 5 cycles. N 1s, C 1s and In 3d XPS spectra of In-SAPC before and after continuous photocatalytic H_2O_2 production for 5 cycles. Each circle last 1h. After each reaction circle, the fixed catalyst was washed by deionized water for at least 5 times.

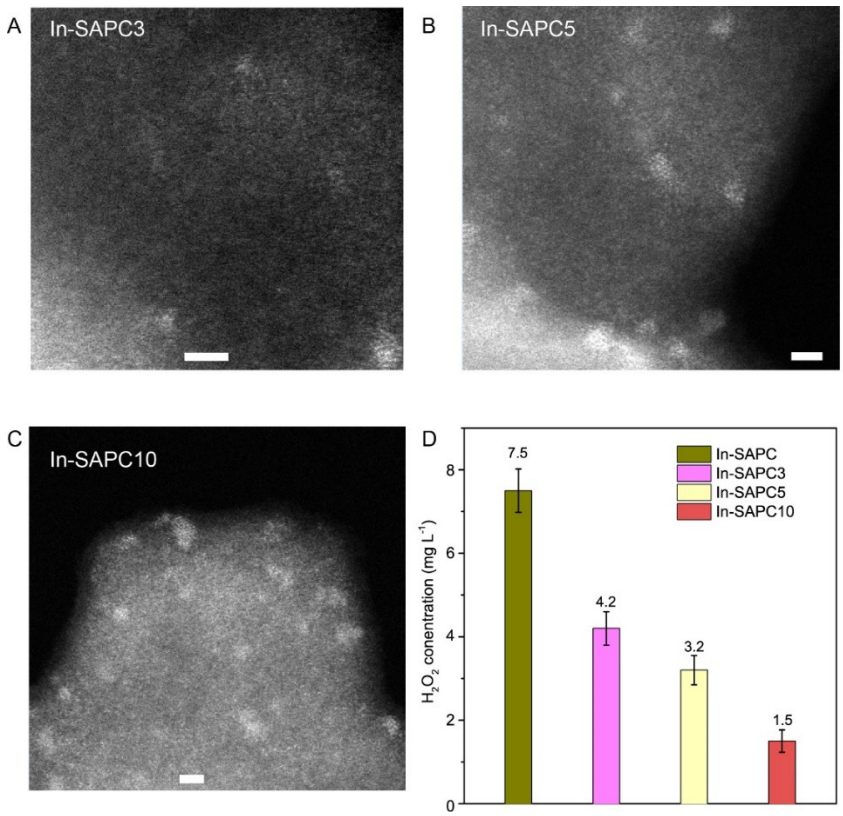

Figure 3-28. Photocatalytic H_2O_2 production by using metal nanoparticle loaded PCN. STEM-HAADF of (A) In-SAPC3, (B) In-SAPC5 and (C) In-SAPC10. The scale bar refers to 2 nm. (D) Comparison of photocatalytic activities for H_2O_2 production by using In-SAPC, In-SAPC3, In-SAPC5 and In-SAPC10. Irradiation condition: λ > 420 nm (Xe lamp, light intensity at 400−500 nm: 21.5 W m^{-2}), at 298 K. Irradiation time: 60 min.

The performance of the In-SAPC remained >90% after 5 repetitive photocatalytic reactions (Figure 3-26). After 5 reaction circles, the crystallinity of In-SAPC showed no obvious change (Figure 3-27A), and the chemical states of N, C and In kept almost constant (Figure 3-27B-D). These results indicate that the In-SAPC showed good stability during the photocatalytic activity. Note that the metal particle may also sever as co-catalyst during photocatalytic reactions. Thus, the activity of metal nanoparticle loaded PCN were also measured to investigate whether nanoparticle could contribute to photocatalytic H_2O_2 production. Since In-SAPC is the most efficient photocatalyst in this work, 3, 5, 10 mmol were mixed with melamine to prepare the In nanoparticle loaded PCN (Figure 3-28A-C). The photocatalytic H_2O_2 production significantly decreased (Figure 3-29D) with the addition of increasing amount of metal source ($InCl_3$). These results indicated that the remained In nanoparticles significantly suppressed the photocatalytic synthesis of

photocatalytic activity. From the results above, experimental charge separation properties of M-SAPC showed good accordance with the computed charge transfer profile of Melem_3M. The correlations among activity and experimental and theoretical charge separation properties also manifested the rationalities of the proposed model and methodology for estimating charge separation properties.

3.4 Conclusion

In summary, a series of metal ion-incorporated single-atom photocatalyst (M-SAPCs) was prepared by isolating TM metal (Fe, Co, Ni) and main-group (In, Sn) sites with pyridinic N atoms in PCN skeleton. The chemical state of atomically dispersed Fe is between (II) and (III), and the chemical states of Co, Ni, In and Sn species catalyst is close (II), (II), (III) and (IV), respectively. The simulation results revealed that the metal ions isolated by non-defected Melem_3 units are consistent with the practically prepared M-SAPC in terms of band structures and electronic configurations. E_{abX}, transition density distribution of elections and holes, D index and E_{Coulmb} revealed that the incorporation of atomically dispersed main-group metals (In (III) and Sn (IV)) significantly improved the charge separation efficiency. Additionally, the iso-surface of the dominant MO (electrons) in the models of Melem_3In3+ and Melem_3Sn4+ showed an ideal electronic configuration for the adsorption of electrophilic oxygen, indicating that the ORR reduction could be accelerated by In and Sn sites. Furthermore, the experimental charge separation properties of M-SAPCs showed good accordance with the computed charge transfer profile of Melem_3M. The correlations among activity and experimental and theoretical charge separation properties also showed the rationalities of the proposed model for estimating charge separation properties. Our work provides not only a theoretical guideline based on the validated electronic configuration and excitation properties but also a blueprint for the design of single-atom photocatalyst with a high charge separation profile at atomic levels. Combined with the traditional simulation strategies such as CHE models and transition states, a precise benchmark for predicting both activity and selectivity might be established for many artificial photo-synthesis systems in a very near future.

Reference

[1] K.P. Bryliakov, Catalytic asymmetric oxygenations with the environmentally benign oxidants H_2O_2 and O_2, Chem. Rev., 117 (2017) 11406-11459. https://doi.org/10.1021/acs.chemrev.7b00167.

[2] S.J. Freakley, Q. He, J.H. Harrhy, L. Lu, D.A. Crole, D.J. Morgan, E.N. Ntainjua, J.K. Edwards, A.F. Carley, A.Y. Borisevich, C.J. Kiely, G.J. Hutchings, Palladium-tin catalysts for the direct synthesis of H_2O_2 with high selectivity, Science, 351 (2016) 965-968. https://doi.org/10.1126/science.aad5705.

[3] H.B. Gray, Powering the planet with solar fuel, Nat. Chem., 1 (2009) 7-7. https://doi.org/10.1038/nchem.141.

[4] S.A. Mousavi Shaegh, N.-T. Nguyen, S.M. Mousavi Ehteshami, S.H. Chan, A membraneless hydrogen peroxide fuel cell using Prussian Blue as cathode material, Energy Environ. Sci., 5 (2012) 8225-8228. https://doi.org/10.1039/C2EE21806B.

[5] S. Yang, A. Verdaguer-Casadevall, L. Arnarson, L. Silvioli, V. Čolić, R. Frydendal, J. Rossmeisl, I. Chorkendorff, I.E.L. Stephens, Toward the decentralized electrochemical production of H_2O_2: A focus on the catalysis, ACS Catal., 8 (2018) 4064-4081. https://doi.org/10.1021/acscatal.8b00217.

[6] Y. Yi, L. Wang, G. Li, H. Guo, A review on research progress in the direct synthesis of hydrogen peroxide from hydrogen and oxygen: Noble-metal catalytic method, fuel-cell method and plasma method, Catal. Sci. Technol., 6 (2016) 1593-1610. https://doi.org/10.1039/C5CY01567G.

[7] H. Hou, X. Zeng, X. Zhang, Production of hydrogen peroxide by photocatalytic processes, Angew. Chem. Int. Ed., n/a (2019). https://doi.org/10.1002/anie.201911609.

[8] X. Shi, S. Siahrostami, G.-L. Li, Y. Zhang, P. Chakthranont, F. Studt, T.F. Jaramillo, X. Zheng, J.K. Nørskov, Understanding activity trends in electrochemical water oxidation to form hydrogen peroxide, Nat. Commun., 8 (2017) 701. https://doi.org/10.1038/s41467-017-00585-6.

[9] Z. Teng, W. Cai, S. Liu, C. Wang, Q. Zhang, C. Su, T. Ohno, Bandgap engineering of polymetric carbon nitride copolymerized by 2,5,8-triamino-tri-s-triazine (melem) and barbituric acid for efficient nonsacrificial photocatalytic H_2O_2 production, Appl. Catal. B: Environ., 271 (2020) 118917. https://doi.org/10.1016/j.apcatb.2020.118917.

[10] Y. Shiraishi, S. Kanazawa, Y. Kofuji, H. Sakamoto, S. Ichikawa, S. Tanaka, T. Hirai, Sunlight-driven hydrogen peroxide production from water and molecular oxygen by metal-free photocatalysts, Angew. Chem. Int. Ed., 53 (2014) 13454-13459. https://doi.org/10.1002/anie.201407938.

[11] K. Fuku, K. Sayama, Efficient oxidative hydrogen peroxide production and accumulation in photoelectrochemical water splitting using a tungsten trioxide/bismuth vanadate photoanode, Chem. Commun., 52 (2016) 5406-5409. https://doi.org/10.1039/C6CC01605G.

[12] J.H. Baek, T.M. Gill, H. Abroshan, S. Park, X. Shi, J. Nørskov, H.S. Jung, S. Siahrostami, X. Zheng, Selective and efficient Gd-doped $BiVO_4$ photoanode for two-electron water oxidation to H_2O_2, ACS Energy Lett., 4 (2019) 720-728. https://doi.org/10.1021/acsenergylett.9b00277.

[13] C. Chu, Q. Zhu, Z. Pan, S. Gupta, D. Huang, Y. Du, S. Weon, Y. Wu, C. Muhich, E.

Stavitski, K. Domen, J.-H. Kim, Spatially separating redox centers on 2D carbon nitride with cobalt single atom for photocatalytic H_2O_2 production, PNAS, 117 (2020) 6376-6382. https://doi.org/10.1073/pnas.1913403117.
[14] W. Fan, B. Zhang, X. Wang, W. Ma, D. Li, Z. Wang, M. Dupuis, J. Shi, S. Liao, C. Li, Efficient hydrogen peroxide synthesis by metal-free polyterthiophene via photoelectrocatalytic dioxygen reduction, Energy Environ. Sci., 13 (2020) 238-245. https://doi.org/10.1039/C9EE02247C.
[15] M. Jakešová, D.H. Apaydin, M. Sytnyk, K. Oppelt, W. Heiss, N.S. Sariciftci, E.D. Głowacki, Hydrogen-bonded organic semiconductors as stable photoelectrocatalysts for efficient hydrogen peroxide photosynthesis, Adv. Funct. Mater., 26 (2016) 5248-5254. https://doi.org/10.1002/adfm.201601946.
[16] Y. Shiraishi, T. Takii, T. Hagi, S. Mori, Y. Kofuji, Y. Kitagawa, S. Tanaka, S. Ichikawa, T. Hirai, Resorcinol–formaldehyde resins as metal-free semiconductor photocatalysts for solar-to-hydrogen peroxide energy conversion, Nat. Mater., 18 (2019) 985-993. https://doi.org/10.1038/s41563-019-0398-0.
[17] Z. Wei, M. Liu, Z. Zhang, W. Yao, H. Tan, Y. Zhu, Efficient visible-light-driven selective oxygen reduction to hydrogen peroxide by oxygen-enriched graphitic carbon nitride polymers, Energy Environ. Sci., 11 (2018) 2581-2589. https://doi.org/10.1039/C8EE01316K.
[18] M. Teranishi, S.-i. Naya, H. Tada, In situ liquid phase synthesis of hydrogen peroxide from molecular oxygen using gold nanoparticle-loaded titanium(IV) dioxide photocatalyst, J. Am. Chem. Soc., 132 (2010) 7850-7851. https://doi.org/10.1021/ja102651g.
[19] A.J. Hoffman, E.R. Carraway, M.R. Hoffmann, Photocatalytic production of H_2O_2 and organic peroxides on quantum-sized semiconductor colloids, Environ. Sci. Technol., 28 (1994) 776-785. https://doi.org/10.1021/es00054a006.
[20] H.-i. Kim, O.S. Kwon, S. Kim, W. Choi, J.-H. Kim, Harnessing low energy photons (635 nm) for the production of H_2O_2 using upconversion nanohybrid photocatalysts, Energy Environ. Sci., 9 (2016) 1063-1073. https://doi.org/10.1039/C5EE03115J.
[21] A. Kulkarni, S. Siahrostami, A. Patel, J.K. Nørskov, Understanding catalytic activity trends in the oxygen reduction reaction, Chem. Rev., 118 (2018) 2302-2312. https://doi.org/10.1021/acs.chemrev.7b00488.
[22] E. Watanabe, H. Ushiyama, K. Yamashita, Theoretical studies on the mechanism of oxygen reduction reaction on clean and O-substituted Ta_3N_5(100) surfaces, Catal. Sci. Technol., 5 (2015) 2769-2776. https://doi.org/10.1039/C5CY00088B.
[23] C. Chu, D. Huang, Q. Zhu, E. Stavitski, J.A. Spies, Z. Pan, J. Mao, H.L. Xin, C.A. Schmuttenmaer, S. Hu, J.-H. Kim, Electronic tuning of metal nanoparticles for highly efficient photocatalytic hydrogen peroxide production, ACS Catal., 9 (2019) 626-631. https://doi.org/10.1021/acscatal.8b03738.
[24] M.M. Montemore, M.A. Van Spronsen, R.J. Madix, C.M. Friend, O_2 activation by metal surfaces: Implications for bonding and reactivity on heterogeneous catalysts, Chem. Rev., 118 (2018) 2816-2862. https://doi.org/10.1021/acs.chemrev.7b00217.
[25] M.L. Pegis, C.F. Wise, D.J. Martin, J.M. Mayer, Oxygen reduction by homogeneous molecular catalysts and electrocatalysts, Chem. Rev., 118 (2018) 2340-2391. https://doi.org/10.1021/acs.chemrev.7b00542.

[26] A. Wang, J. Li, T. Zhang, Heterogeneous single-atom catalysis, Nat. Rev. Chem., 2 (2018) 65-81. https://doi.org/10.1038/s41570-018-0010-1.
[27] R. Shen, W. Chen, Q. Peng, S. Lu, L. Zheng, X. Cao, Y. Wang, W. Zhu, J. Zhang, Z. Zhuang, C. Chen, D. Wang, Y. Li, High-concentration single atomic Pt sites on hollow CuS_x for selective O_2 reduction to H_2O_2 in acid solution, Chem, 5 (2019) 2099-2110. https://doi.org/10.1016/j.chempr.2019.04.024.
[28] S. Yang, J. Kim, Y.J. Tak, A. Soon, H. Lee, Single-atom catalyst of platinum supported on titanium nitride for selective electrochemical reactions, Angew. Chem. Int. Ed., 55 (2016) 2058-2062. https://doi.org/10.1002/anie.201509241.
[29] J. Gao, H.b. Yang, X. Huang, S.-F. Hung, W. Cai, C. Jia, S. Miao, H.M. Chen, X. Yang, Y. Huang, T. Zhang, B. Liu, Enabling direct H_2O_2 production in acidic media through rational design of transition metal single atom catalyst, Chem, 6 (2020) 658-674. https://doi.org/10.1016/j.chempr.2019.12.008.
[30] E. Jung, H. Shin, B.-H. Lee, V. Efremov, S. Lee, H.S. Lee, J. Kim, W. Hooch Antink, S. Park, K.-S. Lee, S.-P. Cho, J.S. Yoo, Y.-E. Sung, T. Hyeon, Atomic-level tuning of Co–N–C catalyst for high-performance electrochemical H_2O_2 production, Nat. Mater., 19 (2020) 436-442. https://doi.org/10.1038/s41563-019-0571-5.
[31] J.K. Nørskov, J. Rossmeisl, A. Logadottir, L. Lindqvist, J.R. Kitchin, T. Bligaard, H. Jónsson, Origin of the overpotential for oxygen reduction at a fuel-cell cathode, J. Phys. Chem. B, 108 (2004) 17886-17892. https://doi.org/10.1021/jp047349j.
[32] T. Takata, K. Domen, Particulate photocatalysts for water splitting: Recent advances and future prospects, ACS Energy Lett., 4 (2019) 542-549. https://doi.org/10.1021/acsenergylett.8b02209.
[33] T. Takata, J. Jiang, Y. Sakata, M. Nakabayashi, N. Shibata, V. Nandal, K. Seki, T. Hisatomi, K. Domen, Photocatalytic water splitting with a quantum efficiency of almost unity, Nature, 581 (2020) 411-414. https://doi.org/10.1038/s41586-020-2278-9.
[34] X. Chen, H. Rui, DFT-based study of single transition metal atom doped g-C_3N_4 as alternative oxygen reduction reaction catalysts, Int. J. Hydrog. Energy, 44 (2019) 15409-15416. https://doi.org/10.1016/j.ijhydene.2019.04.057.
[35] Y. Nosaka, A. Nosaka, Introduction to photocatalysis: From basic science to applications, (2016) ISBN: 978-971-78262-78320-78265.
[36] Y. Inoue, Photocatalytic water splitting by RuO_2-loaded metal oxides and nitrides with d^0- and d^{10} -related electronic configurations, Energy Environ. Sci., 2 (2009) 364-386. https://doi.org/10.1039/B816677N.
[37] C. Adamo, D. Jacquemin, The calculations of excited-state properties with time-dependent density functional theory, Chem. Soc. Rev., 42 (2013) 845-856. https://doi.org/10.1039/C2CS35394F.
[38] F.K. Kessler, Y. Zheng, D. Schwarz, C. Merschjann, W. Schnick, X. Wang, M.J. Bojdys, Functional carbon nitride materials — design strategies for electrochemical devices, Nat. Rev. Mater., 2 (2017) 17030. https://doi.org/10.1038/natrevmats.2017.30.
[39] W.J. Ong, L.L. Tan, Y.H. Ng, S.T. Yong, S.P. Chai, Graphitic carbon nitride (g-C_3N_4)-based photocatalysts for artificial photosynthesis and environmental remediation: Are we a step closer to achieving sustainability?, Chem. Rev., 116 (2016) 7159-7329. https://doi.org/10.1021/acs.chemrev.6b00075.

[40] B. Zhu, P. Xia, W. Ho, J. Yu, Isoelectric point and adsorption activity of porous g-C_3N_4, Appl. Surf. Sci., 344 (2015) 188-195. https://doi.org/10.1016/j.apsusc.2015.03.086.
[41] L. Zuccaro, J. Krieg, A. Desideri, K. Kern, K. Balasubramanian, Tuning the isoelectric point of graphene by electrochemical functionalization, Sci. Rep., 5 (2015) 11794. https://doi.org/10.1038/srep11794.
[42] L. Tian, F. Chen, Multiwfn: A multifunctional wavefunction analyzer, J. Comput. Chem., 33 (2012) 580-592. https://doi.org/10.1002/jcc.22885.
[43] S. Kraner, R. Scholz, F. Plasser, C. Koerner, K. Leo, Exciton size and binding energy limitations in one-dimensional organic materials, J. Phys. Chem., 143 (2015) 244905. https://doi.org/10.1063/1.4938527.
[44] S. Kraner, G. Prampolini, G. Cuniberti, Exciton binding energy in molecular triads, J. Phys. Chem. C, 121 (2017) 17088-17095. https://doi.org/10.1021/acs.jpcc.7b03923.
[45] X. Li, W. Bi, L. Zhang, S. Tao, W. Chu, Q. Zhang, Y. Luo, C. Wu, Y. Xie, Single-atom Pt as Co-catalyst for enhanced photocatalytic H_2 evolution, Adv. Mater., 28 (2016) 2427-2431. https://doi.org/10.1002/adma.201505281.
[46] A.V. Naumkin, A. Kraut-Vass, S.W. Gaarenstroom, C.J. Powell, NIST X-ray Photoelectron Spectroscopy Database, (2012). http://dx.doi.org/10.18434/T4T88K.
[47] V.W.-h. Lau, I. Moudrakovski, T. Botari, S. Weinberger, M.B. Mesch, V. Duppel, J. Senker, V. Blum, B.V. Lotsch, Rational design of carbon nitride photocatalysts by identification of cyanamide defects as catalytically relevant sites, Nat. Comm., 7 (2016) 12165. https://doi.org/10.1038/ncomms12165.
[48] J.-L. Bredas, Mind the gap!, Mater. Horiz., 1 (2014) 17-19. https://doi.org/10.1039/C3MH00098B.
[49] Y. Kofuji, S. Ohkita, Y. Shiraishi, H. Sakamoto, S. Tanaka, S. Ichikawa, T. Hirai, Graphitic carbon nitride doped with biphenyl diimide: Efficient photocatalyst for hydrogen peroxide production from water and molecular oxygen by sunlight, ACS Catal., 6 (2016) 7021-7029. https://doi.org/10.1021/acscatal.6b02367.

Part 4

Atomically dispersed antimony boosts oxygen reduction and water oxidation for efficient artificial photosynthesis of hydrogen peroxide

4.1 Introduction

Hydrogen peroxide (H_2O_2) is an important green oxidant[1] widely used in a variety of industries and a promising clean fuel for jet car and rockets[2-7] (60 wt.% H_2O_2 has an energy density of 3.0 MJ L^{-1}, higher than compressed H_2 gas at 35 MPa, 2.8 MJ L^{-1}). Currently, H_2O_2 is manufactured by the energy-consuming, waste-intensive, and indirect anthraquinone method[8, 9]. Photocatalytic H_2O_2 synthesis on semiconductor materials from water and oxygen has emerged as a safe, environmental-friendly and energy-saving process[10,11]. To achieve high selectivity and rate for H_2O_2 production, it is crucial to boost the $2e^-$ oxygen reduction reaction (ORR, eq. 1)[12] or the $2e^-$ water oxidation reaction (WOR, eq. 2)[13]. The light-driven $2e^-$ WOR pathway is difficult to be achieved because of the uphill thermodynamics (1.76 V vs. NHE), i.e. the as-synthesized H_2O_2 will decompose at this highly oxidative potential because H_2O_2 is an excellent hole scavenger[11,14]. On the contrary, the $2e^-$ ORR pathway has been realized for artificial photosynthesis of H_2O_2 in several particulate systems[12,15-22]. However, the highest apparent quantum yield (ΦAQY) for non-sacrificial H_2O_2 production (eq. 3) is still smaller than 8% (at λ = 420 nm)[15-23], much lower than the current record ΦAQY for overall water splitting (~30% at λ = 420 nm)[24]. To boost the photocatalytic activity for the non-sacrificial H_2O_2 production, both $2e^-$ ORR (eq. 2) and $4e^-$ WOR (eq. 4) should be promoted simultaneously. Unlike some other photocatalytic processes (e.g., overall water splitting and N_2 fixation)[24, 25], these redox reactions cannot be separately considered as irrelevant half reactions, since O_2 is not only a product in the $4e^-$ WOR (eq. 4), but also a reactant in the $2e^-$ ORR (eq. 1). If the in-*situ* generated O_2 from WOR (eq. 4) can be consumed rapidly by ORR, it will kinetically facilitate the WOR. Therefore, introducing highly active and selective sites for the $2e^-$ ORR in the photocatalytic system to consume the O_2 generated from the WOR shall offer a promising strategy for breaking the bottleneck of photocatalytic H_2O_2 synthesis.

$$O_2+2H^++2e^-\rightarrow H_2O_2 \quad (0.695\ \text{V vs. NHE}) \quad (1)$$
$$2H_2O\rightarrow H_2O_2+2H^++2e^- \quad (1.76\ \text{V vs. NHE}) \quad (2)$$
$$2H_2O+O_2\rightarrow 2H_2O_2 \quad (3)$$
$$2H_2O+4h^+\rightarrow O_2+4H^+ \quad (1.23\ \text{V vs. NHE}) \quad (4)$$
$$O_2+4H^++4e^-\rightarrow 2H_2O \quad (1.23\ \text{V vs. NHE}) \quad (5)$$

Manipulating metallic sites can change both the activity and selectivity of ORR[26].

The O_2 molecular adsorption on metal surface can be generally classified into three types (Figure 4-2a): Pauling-type (end-on), Griffiths-type (side-on), and Yeager-type (side-on)[26,27]. The end-on O_2 adsorption configuration is able to minimize the O-O bond breaking, leading to a suppressed $4e^-$ ORR (eq. 5), and thus, a highly selective $2e^-$ ORR. On metal particles, both end-on and side-on O_2 molecular adsorption exist, and thus the O-O bond splitting on the surface of metal particles can hardly be prevented[28,29]. Benefiting from the desirable features of single atom catalyst (SAC), the adsorption of O_2 molecules on atomically isolated sites is usually end-on type, which therefore could reduce the possibility of O-O bond breaking (Figure 4-2b)[30-33]. For instance, SACs with Pt^{2+} [34] and Co-N_4[35,36] centers could electrochemically reduce O_2 to H_2O_2 via a $2e^-$ ORR pathway with ultrahigh selectivity (>96 %). However, Pt^{2+} and Co-N_4 sites can hardly be coupled in the photocatalytic system due to their high charge recombination characteristics, which originate from the intermediate band formed by the half-filled d electrons. Constructing photocatalysts with atomically dispersed elements possessing the d^{10} electronic configuration can eliminate the formation of the intermediate band in the band structure, which shall be favorable for efficient charge separation and formation of reactive centers with high density of electrons/holes[37,38]. This implies that SACs with d^{10} electronic configuration would be ideal candidates for photocatalytic H_2O_2 synthesis via the $2e^-$ ORR.

Herein, we develop a Sb single atom photocatalyst (Sb-SAPC) for non-sacrificial photocatalytic H_2O_2 synthesis in a water and oxygen mixture under visible light irradiation, in which the oxidation state of Sb is regulated to +3 with a $4d^{10}5s^2$ electron configuration. Notably, a record-high apparent quantum efficiency of 17.6% at 420 nm and a solar-to-chemical conversion (SCC) efficiency of 0.61% are achieved on the as-developed photocatalyst. Combining experimental and theoretical investigations, it is found that the adsorption of O_2 on isolated Sb atomic sites is end-on type, which promotes formation of Sb-μ-peroxide (Sb-OOH), leading to an efficient $2e^-$ ORR pathway for H_2O_2 production. More importantly, the Sb sites also induce highly concentrated holes at the neighboring melem units, promoting the $4e^-$ WOR. The concept of using SAC to simultaneously boost

the reduction and oxidation reactions shall provide a design guide to develop more advanced photocatalytic systems for extensive applications.

4.2 Experimental details

4.2.1 Preparation of photocatalysts

Unless otherwise stated, the purities of all reagents for photocatalysts preparation and for photoelectrochemical measurements are above the analytical grade. The pristine PCN and PCN_Na15 were prepared according to the reported methods[18]. The Sb-SAPCs were prepared by a bottom-up method (Scheme 4-1) as follows: a certain amount of $NaSbF_6$ (HuNan HuaJing Powdery Material Co., LTD, 0.5 mmol, 1 mmol, 3 mmol, 5 mmol, 10 mmol, 15 mmol and 20 mmol) was dissolved in 30 mL ethanol under sonication for 60 min at 60 °C, followed by adding 4 g melamine (Wako Pure Chemical Industries, Ltd.). The solvent in the solution was removed by combination of rotatory evaporator and vacuum oven. The as-obtained white powder was transferred into a tube furnace. To ensure that oxygen was not present during thermal treatment, the tube furnace was firstly vacuumed to <1 Torr before switching on the N_2 gas flow. This process was repeated 3 times, and then 50 mL min^{-1} N_2 gas flow was maintained for 30 min before heat treatment. During the synthesis process (including heating and cooling), the system was pressurized by N_2 flow so that oxygen could hardly influence the synthesis. The temperature of the furnace was increased from 25 °C to 560 °C at a ramp rate of 2 °C min^{-1} in N_2 atmosphere then kept at 560 °C for 4 h (Scheme 4-1). After heat treatment, the furnace was cooled down naturally to 25 °C lasting for at least 8 h with continuous N_2 flowing. The as-prepared Sb-SAPC reached a quantity of 100 grams in one batch, which is very promising for scalable production (Figure 4-1).

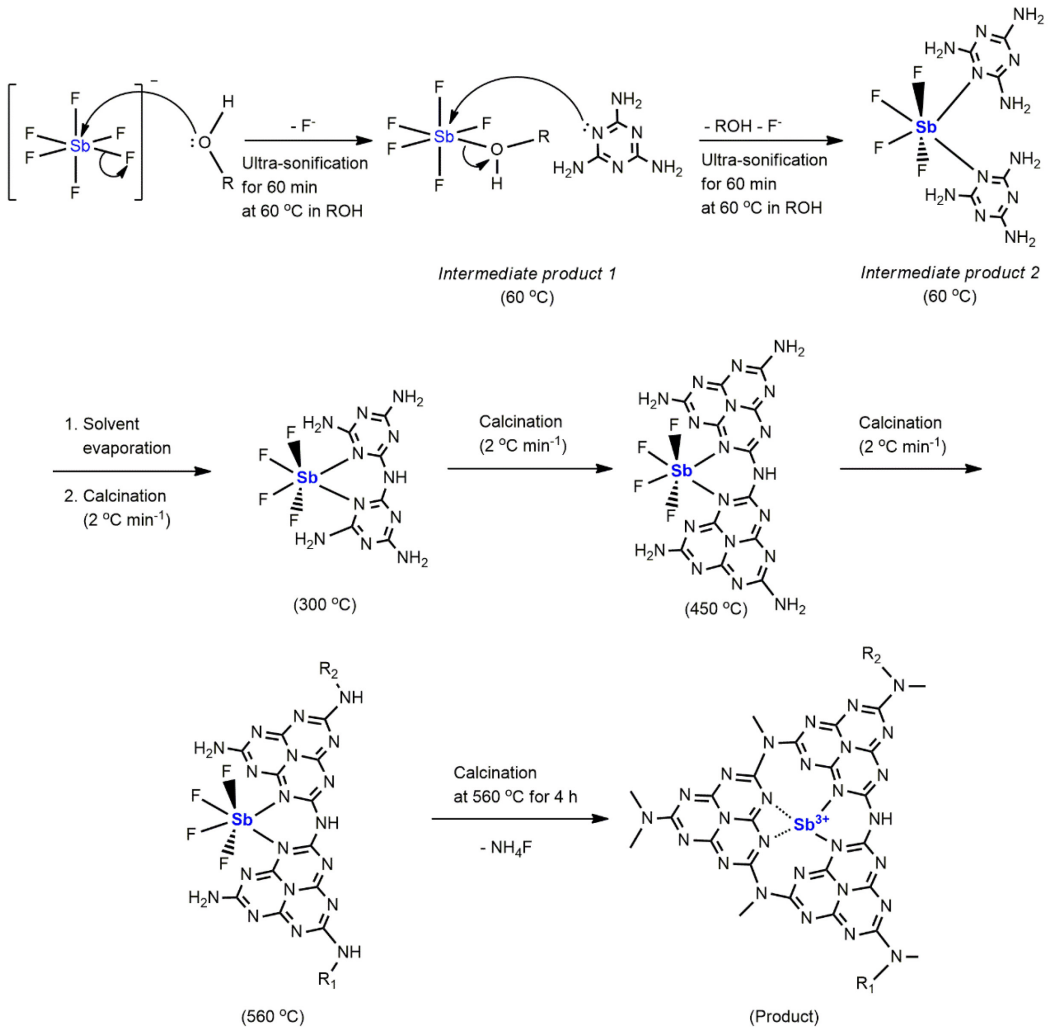

Scheme 4-1. The preparation procedure of the single Sb atom photocatalyst (Sb-SAPC). Dashed bonds in the product refers to the weak interaction between N and Sb atoms.

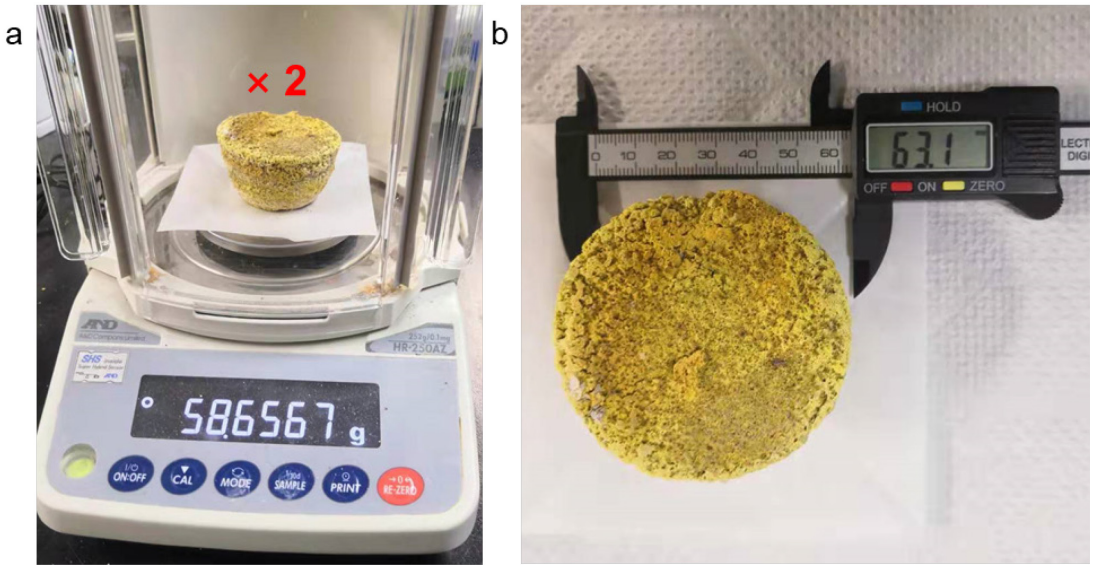

Figure 4-1. Digital photographs showing the as-prepared Sb-SAPC15 in one batch.

4.2.2 Photocatalytic reaction toward H_2O_2 production

100 mg of photocatalyst was added to 50 mL of deionized water in a borosilicate glass bottle (φ: 60 mm; capacity: 100 mL), and the bottle was sealed with a rubber septum cap. The catalyst was dispersed by ultrasonication for 15 min, and O_2 was bubbled through the solution for 30 min. The bottle was kept in a temperature-controlled air bath at 25 ± 0.5 °C with wind flow and was irradiated at λ > 420 nm using a 300 W Xe lamp (PXE-500, USHIO Inc.) under magnetic stirring. To study the WOR, 50 mg of photocatalyst was added into $NaIO_3$ (0.1 M, 50 mL) solution in a borosilicate glass bottle (φ: 60 mm; capacity: 100 mL). After completely removing O_2 from the reaction system, the bottle was irradiated by a 300 W Xenon Lamp. The light intensity of visible light and infrared-red light ($I_{>400}$) after passing a UV cut filter (λ > 400 nm) was firstly measured. Then, a glass filter with λ > 500 nm was used to replace the UV cut filter for measuring the light intensity ($I_{>500}$). The difference between $I_{>400}$ and $I_{>500}$ was used to calibrate the total light intensity. After a certain time interval, the gas was extracted from the bottle and examined by gas chromatography equipped with a TCD detector. To examine the H_2O_2 production from O_2 generated by WOR, a certain amount of photocatalyst (Sb-SAPC15: 200 mg, 100 mg and 50 mg; Pristine PCN: 200 mg) was added into 50 mL of $NaNO_3$ solution (pH = 7) with $AgNO_3$ (0.1 mM). 1.5 mL of solution was extracted every hour to acquire the time-dependent H_2O_2 production without the initial introduction of O_2. The amount of H_2O_2 in these experiments was determined by a colorimetric method using PACKTEST (WAK-H_2O_2, KYORITSU CHEMICAL-CHECK Lab., Corp.) equipped with a digital PACKTEST spectrometer (ED723, GL Sciences Inc.).

4.2.3 Apparent quantum efficiency analysis

The photocatalytic reaction was carried out in pure deionized water (30 mL) with photocatalyst (60 mg) with or without addition of ethanol as an electron donor in a borosilicate glass bottle. After ultrasonication and O_2 bubbling, the bottle was irradiated by an Xe lamp for 4 h with magnetic stirring. The incident light was monochromated by band-pass glass filters (Asahi Techno Glass Co.), where the full-width at half-maximum of the light is 11−16 nm. The number of photons that enter the reaction vessel was determined

by a 3684 optical power meter (HIOKI E.E. CORPORATION).

4.2.4 Determination of solar-to-chemical conversion efficiency

Solar-to-chemical conversion efficiency was determined by a PEC-L01 solar simulator (Peccell Technologies, Inc.). The photoreaction was performed in pure deionized water (100 mL) with photocatalyst (500 mg) under O_2 atmosphere (1 atm) in a borosilicate glass bottle. A UV cut filter (λ > 420 nm) was used to avoid decomposition of the formed H_2O_2 by absorbing UV light[12,15,22]. The irradiance of the solar simulator was adjusted to the AM1.5 global spectrum[12,15,22]. The solar-to-chemical conversion efficiency (η) was calculated by the following equation:

$$\eta(\%) = \frac{\Delta G_{H_2O_2} \times n_{H_2O_2}}{t_{ir} \times S_{ir} \times I_{AM}} \times 100\%.$$

where $\Delta G_{H_2O_2}$ is the free energy for H_2O_2 generation (117 kJ mol^{-1}). $n_{H_2O_2}$ is the amount of H_2O_2 generated, and t_{ir} is the irradiation time (s). The overall irradiation intensity (I_{AM}) of the AM1.5 global spectrum (300−2500 nm) is 1000 W m^{-2}, and the irradiation area (S_{ir}) is 3.14 × 10^{-4} m^2.

4.2.5 Instruments

High-resolution transmission electron microscopy (HRTEM), high-angle annular dark field scanning transmission electron microscopy (HAADF-STEM), selected area electron diffraction (SAED) and energy-dispersive X-ray spectroscopy (EDS) were performed on a Titan Cubed Themis G2 300 electron microscope (Field Electron and Ion Company, USA) with an accelerating voltage of 300 kV. Electron energy loss spectroscopy (EELS) was conducted using a Quantum ER/965 P detector. The crystalline phases were characterized by a powder X−ray diffraction (XRD) instrument (MiniFlex II, Rigaku Co.) with CuKα (λ = 1.5418 Å) radiation (cathode voltage: 30 kV, current: 15 mA). Absorption properties of the powder samples were determined using the diffuse reflection method on a UV/VIS/NIR spectrometer (UV-2600, Shimadzu Co.) attached to an integral sphere at room temperature. X−ray photoelectron spectroscopy (XPS) measurements were performed on a Kratos AXIS Nova spectrometer (Shimazu Co., Japan) with a monochromatic Al Kα X−ray source. The binding energy was calibrated by taking the carbon (C) 1s peak of adventitious carbon at 284.6 eV. Valence band X-ray photoelectron spectroscopy (VB-XPS)

was performed on an ESCALAB 250Xi (Thermo Scientific, USA). The equilibration of Fermi level of the instrument was performed by measuring the VB-XPS of Au metal basis as the reference. The Fermi level of the instrument was equilibrated at 4.5 eV. In this case, the numerical value of the binding energy in the calibrated VB-XPS spectrum is the same as the potential vs. standard hydrogen electrode. Electron spin resonance (ESR) signals of spin-trapped paramagnetic species with 5,5-diemthyl-1-pyrroline N-oxide (DMPO, methanol solution) were recorded with an A300-10/12 spectrometer. Photoluminescence spectroscopy was performed on a FP-8500 spectrofluorometer (JASCO Corporation, Japan). The temperature for the photoluminescence measurements was about 25 °C controlled by an air conditioner, which worked 24/7. Time-dependent photoluminescence spectroscopy was conducted on a FS5 fluorescence spectrometer (Edinburgh Instruments Ltd., UK). Raman spectra was performed on a Laser Microscopic Confocal Raman Spectrometer (Renishaw inVia, UK) at 785 nm. The pH value of the solution was measured by a pH meter (HORIBA pH meter D-51, HORIBA, Ltd.).

The X-ray absorption spectroscopy (XAS) for Sb K-edge was measured at beamline BL01C at the National Synchrotron Radiation Research Center (NSRRC, Hsinchu, Taiwan). The data analysis for the X-ray absorption spectroscopy using IFEFFIT was conducted by Demeter system.

4.2.6 Photoelectrochemical characterizations

Photoelectrochemical (PEC) characterizations were conducted on a conventional three-electrode potentiostat setup connected to an electrochemical analyzer (Model 604D, CH Instruments, Inc.). The fluorine-doped tin oxide (FTO) glass of 1 cm × 2 cm in size was covered with photocatalyst that was achieved by first mixing a catalyst (100 mg) with ethyl cellulose binder (10 mg) in ethanol (6 mL) for one hour and then depositing the final viscous mixture by a doctor blade method followed by drying at room temperature and further drying at 40 °C overnight in a vacuum oven. The area of the photoelectrode was controlled to be 1 cm^2. The PEC system consisted of an FTO glass covered by the photocatalyst, a coiled Pt wire and a saturated Ag/AgCl/KCl (saturated) electrode as the working, counter, and reference electrode, respectively. The photocurrent was collected at 0.8 V vs. SHE

(0.6 V vs. Ag/AgCl) in a phosphate buffer solution (PBS, pH = 7.4). The solution was saturated with O_2 by bubbling O_2 for 15 min (0.5 L min^{-1})[12,39]. Electrochemical impedance spectroscopy (EIS) analysis was performed at a DC voltage of -0.6 V vs. Ag/AgCl with an AC voltage amplitude of 5 mV in a frequency range from 100 kHz to 0.01 Hz. For the Mott-Schottky measurements, similar strategy was performed on FTO glass (1.5 cm × 3 cm) by the same doctor blade method. The area of the electrode for the Mott-Schottky measurements was controlled to be 0.50 cm^2. Mott-Schottky measurements were performed at a potential range from 0.2 V to -0.6 V *vs*. SHE, with an AC voltage amplitude of 5 mV, and in a frequency range from 25 Hz to 500 Hz. Each increase of potential is 0.05 V. The quiet time for each test is 2 s.

4.2.7 Isotopic experimental details

4.2.7.1 Isotopic experiment with $^{18}O_2$ and $H_2{}^{16}O$

Firstly, 60 mg of Sb-SAPC15 was dispersed in 30 ml of $H_2{}^{16}O$ via sonication for 15 min. Subsequently, 10 mL of $^{18}O_2$ gas (≥ 98% ^{18}O; TAIYO NIPPON SANSO Corporation) was injected to the suspension. Then, the system was completely sealed and irradiated by visible light. After a certain time interval (6 h, 24 h, and 72 h), 1 mL suspension was extracted and injected into a glass test tube filled with N_2 and 0.1 g $Fe_2(SO_4)_3$ dissolved in 1 mL H_2SO_4. After injection of suspension, the test tube was sealed and irradiated under UV light for 5 h. The gas (0.1 mL) in the test tube was extracted by gas chromatography syringe and injected into a Shimadzu GC-MS system (GCMS-QP2010).

4.2.7.2 Isotopic experiment with $H_2{}^{18}O$

20 mg of Sb-SAPC15 was dispersed in 10 g of $H_2{}^{18}O$ (≥ 98% ^{18}O; TAIYO NIPPON SANSO Corporation) containing 1 mM $AgNO_3$ under sonication for 15 min. Afterwards, N_2 was bubbled into the suspension for 2 h at a flow rate of 0.5 L min^{-1} to ensure complete removal of the dissolved oxygen ($^{16}O_2$) in the system[15]. Then, the system was completely sealed and irradiated by visible light. After a certain time interval (0.5 h, 1 h, 3 h, 5 h, 10 h and 24 h), 1 mL suspension was extracted and injected into a glass test tube filled with N_2 and 0.1 g $Fe_2(SO_4)_3$ dissolved in 1 mL H_2SO_4. After injection of suspension, the test tube was sealed and irradiated under UV light for 5 h. The gas (0.1 mL) in the test tube was

extracted by gas chromatography syringe and injected into a Shimadzu GC-MS system (GCMS-QP2010).

4.2.8 H_2O_2 degradation study

50 mL of deionized water in a borosilicate glass bottle (φ: 60 mm; capacity: 100 mL) without addition of catalyst was bubbled with O_2 for 30 min. Then, a certain amount of H_2O_2 was added into the bottle, and the concentration of H_2O_2 was manipulated to be 1×10^2 mg L^{-1}. Finally, the bottle was sealed with a rubber septum cap. To investigate the hole transfer to H_2O_2, the following experiment was performed: 50 mg of photocatalyst was added into 50 mL $NaIO_3$ (0.1 M) and H_2O_2 (0.01wt.%) solution in a borosilicate glass bottle (φ: 60 mm; capacity: 100 mL). The same solution without addition of photocatalyst was also measured as a control. Additionally, the same experiment was also conducted in 50 mL $NaIO_3$ (0.1 M) phosphate buffer solution (0.1 M, pH = 7.4). After completely removing O_2 from the reaction system, the bottle was irradiated by a 300 W Xenon lamp with a UV cut filter (light intensity: 30.3 W m^{-2} at 420-500 nm).

4.2.9 Calculation details

4.2.9.1 Details for TD-DFT calculations

Melem_3 and Melem_3 coordinated with Sb were constructed to represent the basic photocatalytic reaction sites on PCN and Sb-SAPC. The optimization and frequency combined with the vertical excitation properties were performed via time-dependent density functional theory (TD-DFT) in the Gaussian 09 program S2, which was carried out by utilizing wb97xd/6-311g(d) level of theory for C, N and H elements and SDD for Sb element. 3 monolayer cluster models were optimized to represent the major surface properties of CN sites in PCN, Na sites in PCN_Na15 and Sb sites in Sb-SAPC15[40,41]. The charges of monolayer cluster models were settled in consideration of the oxidation state of Sb and Na based on the experimental results as follows: 0 for Melem_3; +1 for Melem_Na1+; and +3 for Melem_3Sb3+. To give a comprehensive understanding of the relationships between the electronic configuration during excitation and the realistic experiment results. 50 excited states (ES) of these three cluster models have been used to simulate of UV absorption spectra[40]. Note that the absorption edge of simulated UV spectra is usually

large than that of experimental ones because of the following two reasons: (1) To simulate the charge-transfer properties of the model with high qualities, function of ω97xd, a function including large amount of Hartree–Fock exchange, were used. These exchange functions usually overestimate the excitation energies, as well as the simulated HOMO-LUMO gap[40-42]; (2) In the solid state, p-conjugated molecules adjacent to the one carrying a charge do strongly polarize, an effect that stabilizes the cationic and anionic states (each generally by about one eV in p-conjugated materials). In this case, the band gap is typically considerably smaller in energy than the molecular fundamental gap, as well as the optical gap[6]. Since the evitable system error cannot be eliminated, the possible simulated ES that contributed to H_2O_2 production (corresponding to the spectra from 420 nm – 470 nm) was confirmed by comparing the experimental spectra and simulated ones. Then, the transition density of electron/holes were considered at all these ES.

For analysis of the excitation and charge transfer properties, Multiwfn Ver. 3.6 (released on May 21, 2019)[43] was performed. Visualization of hole, electron and transition density was also performed by Multiwfn; functions of *IOp(9/40 = 3)* were set during the vertical excitation based on TD-DFT calculation. The ES that contributed to the were presented if the electrons were mostly accumulated at the heteroatoms (electron distribution >50%). The electron distributions at these ES were presented as heatmaps by combination of GaussView and Multiwfn[43-47]. The iso surface of LUMO orbitals were presented by setting the isovalue of 0.05.

4.2.9.2 Details for Free energy diagram

The cluster model is more likely to predict the ORR process based on our previous investigation[35]. The free energy diagram of Melem_3Sb3+ was calculated as follows:

The optimized structure of Melem_3Sb3+ was used as the initial structure for calculating the most stable adsorption configurations of *OOH, *O, and *OH. The ORR following the $2e^-$ and $4e^-$ pathway produces H_2O and H_2O_2, respectively. The associative $4e^-$ ORR is composed of four elementary steps (a, b, c, and d):

$$* + O_2(g) + H^+ + e^- \rightarrow *OOH \quad (a)$$

$$* OOH + H^+ + e^- \rightarrow O* + H_2O(l) \quad (b)$$

$$O^* + H^+ + e^- \rightarrow {}^*OH \quad (c)$$

$$^*OH + H^+ + e^- \rightarrow H_2O(l) + ^* \quad (d)$$

The $2e^-$ ORR comprises of two elementary steps (e and f):

$$^* + O_2(g) + H^+ + e^- \rightarrow {}^*OOH \quad (e)$$

$$^*OOH + H^+ + e^- \rightarrow H_2O_2(l) + ^* \quad (f)$$

The asterisk (*) denotes the active site of the catalyst.

The free energy for each reaction intermediate is defined as:

$$G = E_{DFT} + E_{ZPE} - TS + E_{sol} \quad (g)$$

where E_{DFT} is the electronic energy calculated by DFT, E_{ZPE} denotes the zero point energy estimated within the harmonic approximation, and TS is the entropy at 298.15 K (T = 298.15 K). The E_{ZPE} and TS of gas-phase H_2 and reaction intermediates are based on our previous work[11]. For the concerted proton-electron transfer, the free energy of a pair of proton and electron ($H^+ + e^-$) was calculated as a function of applied potential relative to RHE (U versus RHE), i.e., $\mu(H^+)+\mu(e^-) = 1/2\mu(H_2)-eU$, according to the computational hydrogen electrode (CHE) model proposed by Nørskov[48]. In addition, the solvent effect was reported to play an important role in ORR. In our calculations, the solvent corrections (E_{sol}) for *OOH and *OH are 0.45 eV in accordance with previous studies[49,50]. We used the energies of H_2O and H_2 molecules calculated by DFT together with experimental formation energy of H_2O (4.92 eV) to construct the free energy diagram. The free energies of O_2, *OOH, *O, and *OH at a given potential U relative to RHE are defined as:

$$\Delta G(O_2) = 4.92 - 4eU \quad (h)$$

$$\Delta G(OOH) = G(*OOH) + \frac{3G(H_2)}{2} - G(*) - 2G(H_2O) - 3eU \quad (i)$$

$$\Delta G(O) = G(*O) + G(H_2) - G(*) - G(H_2O) - 2eU \quad (j)$$

$$\Delta G(OH) = G(*OH) + \frac{G(H_2)}{2} - G(*) - G(H_2O) - eU \quad (k)$$

4.2.9.3 Details for simulations of charge transfer between layers near surface phase

All theoretical calculations were performed based on density functional theory (DFT), implemented in the Vienna ab initio simulation package (VASP) [51-52]. The electron exchange and correlation energy were treated within the generalized gradient approximation in the Perdew-Burke-Ernzerhof functional (GGA-PBE)[53,54]. The valence

orbitals were described by plane-wave basis sets with cutoff energies of 400 eV. For the simulation of Na and Sb incorporated in bulk phase of g-C_3N_4, a 1 × 1 × 2 supercell of pristine bulk g-C_3N_4 was adopted. And the k-points were sampled in a 3 × 3 × 2 Monkhorst-Pack grid. For the simulation of Na and Sb near the surface of g-C_3N_4, the k-point sampling was obtained from the Monkhorst-Pack scheme with a (2 × 2 × 1) mesh. The atomic coordinates are fully relaxed using the conjugate gradient method (CG)[55]. The convergence criteria for the electronic self-consistent iteration and force were set to 10^{-4} eV and 0.02 eV/Å, respectively. The vacuum gap was set as 15 Å. To quantitatively compare the degree of charge transfer, a Bader charge analysis has been carried out[56].

4.3 Results and discussion

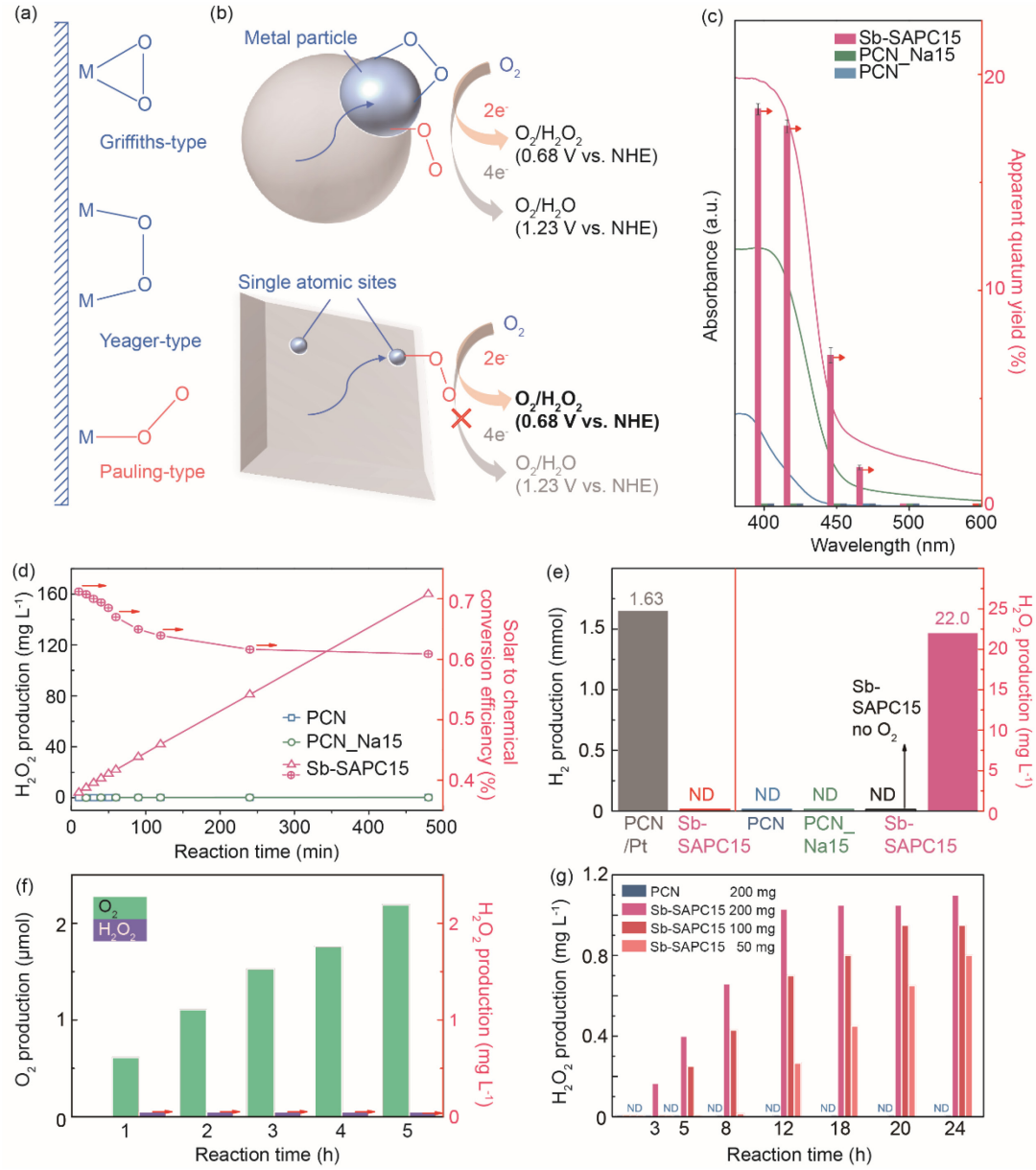

Figure 4-2. Photocatalytic performance of Sb-SAPC toward H_2O_2 production. a, Schematic structures of O_2 adsorption on metal surface. **b**, ORR on metal particle (top) and isolated atomic site (bottom). **c**, Action spectra of PCN, PCN_Na15 and Sb-SAPC15 toward H_2O_2 production in a phosphate buffer solution (pH = 7.4). Error bars represent the standard deviations of 3 replicate measurements. **d**, Solar-to-chemical conversion efficiency of PCN, PCN_Na15 and Sb-SAPC15 under AM 1.5 illumination in a phosphate buffer solution. **e**, Selectivity comparison of Sb-SAPC15 and pristine PCN for different photoreduction reactions. Left: comparison of hydrogen evolution activity of Sb-SAPC15 and PCN loaded with 1 wt.% Pt in a 10% (v/v) 2-propanol aqueous solution. Right: comparison of activity for photocatalytic H_2O_2 production on pristine PCN, PCN_Na15 and Sb-SAPC15 in a phosphate buffer solution with or without O_2. **f**, Amount of O_2 and H_2O_2 produced on Sb-SAPC15 in $NaIO_3$ (0.1 M, as the electron acceptor) solution. **g**, Photocatalytic H_2O_2 production with electron acceptor (0.1 mM Ag^+) under N_2 atmosphere.

Irradiation condition: λ > 420 nm (Xe lamp, light intensity at 420-500 nm: 30.3 W m^{-2}), at 298 K. NDs in Figure 4-2e and Figure 4-2g mean that H_2O_2 cannot be detected in the photocatalytic system.

4.3.1 Photocatalytic properties of Sb-SAPC for selective H_2O_2 production

4.3.1.1 Performance of Sb-SAPC for non-sacrificial H_2O_2 production

The photocatalytic performance of Sb-SAPC for H_2O_2 production was assessed in a water and oxygen mixture without presence of any sacrificial agents under visible light illumination. As shown in Figure 4-3, Sb-SAPC15 shows the highest H_2O_2 production rate (12.4 mg L^{-1} in 120 min) among the samples, which is about 248 times higher than pristine PCN (0.05 mg L^{-1} in 120 min).

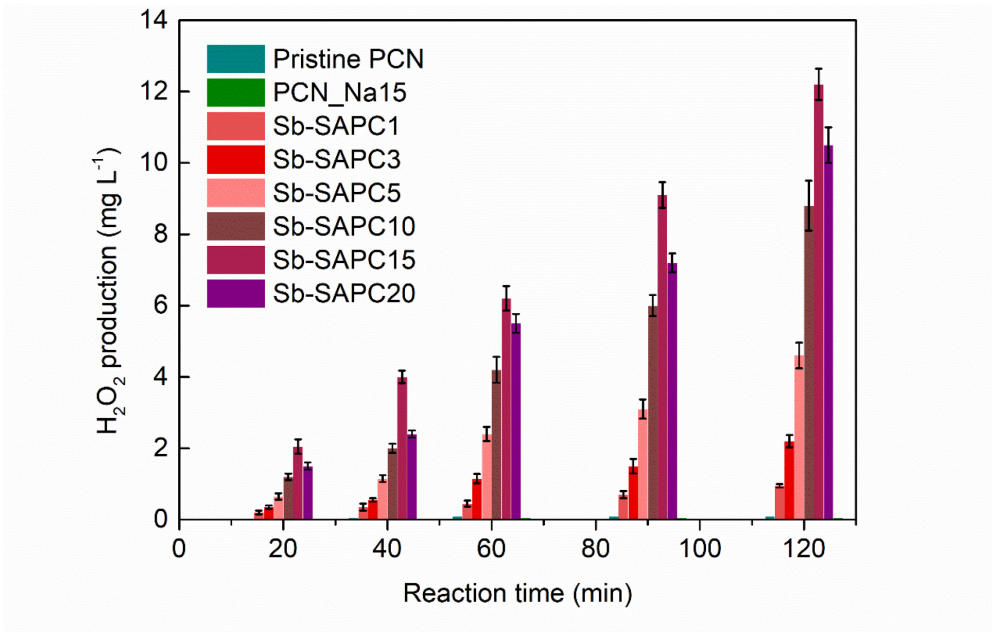

Figure 4-3. Comparison of activities of Sb-SAPCs and PCNs for photocatalytic H_2O_2 production (light source: Xe lamp, light intensity at 420−500 nm: 30.3 W m^{-2}; reaction medium: water at pH = 10.1 for Sb-SAPC15). Error bars represent the standard deviations of 3 replicate measurements.

It is noteworthy that the pH of the Sb-SAPC15 aqueous suspension (solvent is pure water) is 10.1 because addition of Sb-SAPC15 particles significantly accelerated self-ionization of water. The zeta potential of Sb-SAPC15 reached -30 mV in an acid solution, indicating that Sb-SAPC15 could be recognized as a solid-state Lewis base[22]. Addition of Lewis base into pure water could accelerate water self-ionization, thus leading to a significantly increased pH[22].

The surface area of Sb-SAPC15 (1.89 m^2 g^{-1}, Figure 4-4) is only about 1/7.78 of pristine PCN (14.7 m^2 g^{-1}), indicating that the activity per area enhancement induced by introducing Sb into PCN is increased by more than 1900 folds as compared to pristine PCN.

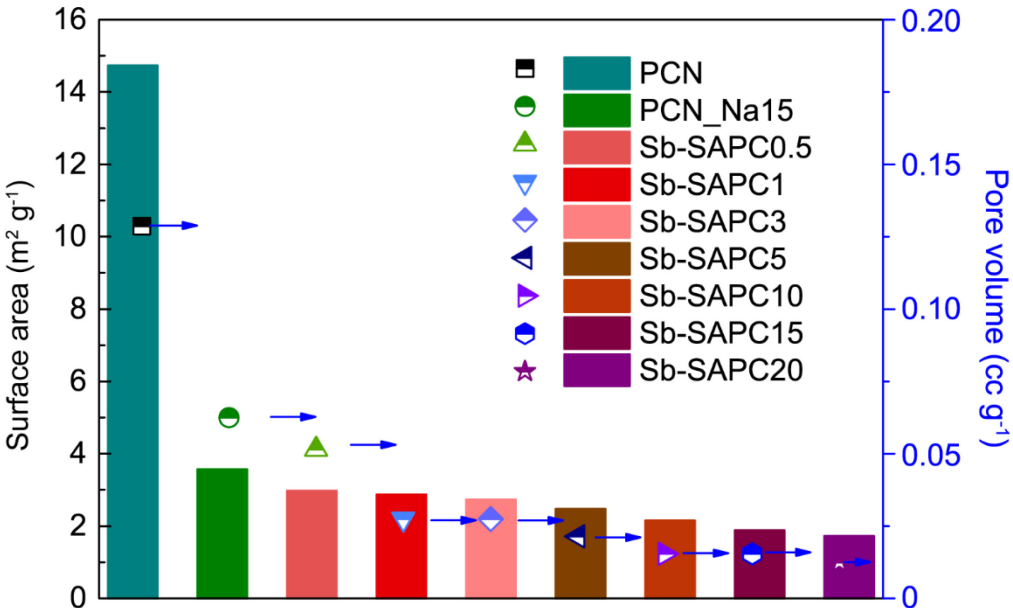

Figure 4-4. Specific surface area and average pole volume of PCN, PCN_Na15 and Sb-SAPCx.

After we optimized the reaction conditions (Figure 4-5)[18,22], the action spectra (Figure 4-2c) for H_2O_2 production were measured (The optimization of pH value of the solution and the ion species in this part is the same as the details in **2.3.2**). The best pH condition for non-sacrificial H_2O_2 production is 7, the same as the case of PCNBA samples. Additionally, phosphate buffer solution (PBS) is the best solution for H_2O_2 production. It is noteworthy that change in concentration of H_2O_2 with an electron acceptor versus time was plotted to investigate whether the holes transferred to H_2O_2 (Figure 4-6c). The concentration of H_2O_2 gradually decreased in 0.1 M $NaIO_3$ without Sb-SAPC since slight decomposition of H_2O_2 was unavoidable under visible light irradiation with high light intensity. After addition of Sb-SAPC15, the decomposition of H_2O_2 was accelerated, indicating that the transfer of photogenerated holes could decompose H_2O_2 in 0.1 M $NaIO_3$ solution. This phenomenon further confirmed that H_2O_2 could serve as a hole scavenger, which should be considered during the photocatalytic H_2O_2 production. However, addition

of the phosphate buffer solution could significantly suppress the decomposition of H_2O_2. These results indicate the crucial role of phosphate buffer solution, which is able to stabilize the produced H_2O_2 during the photocatalytic process.

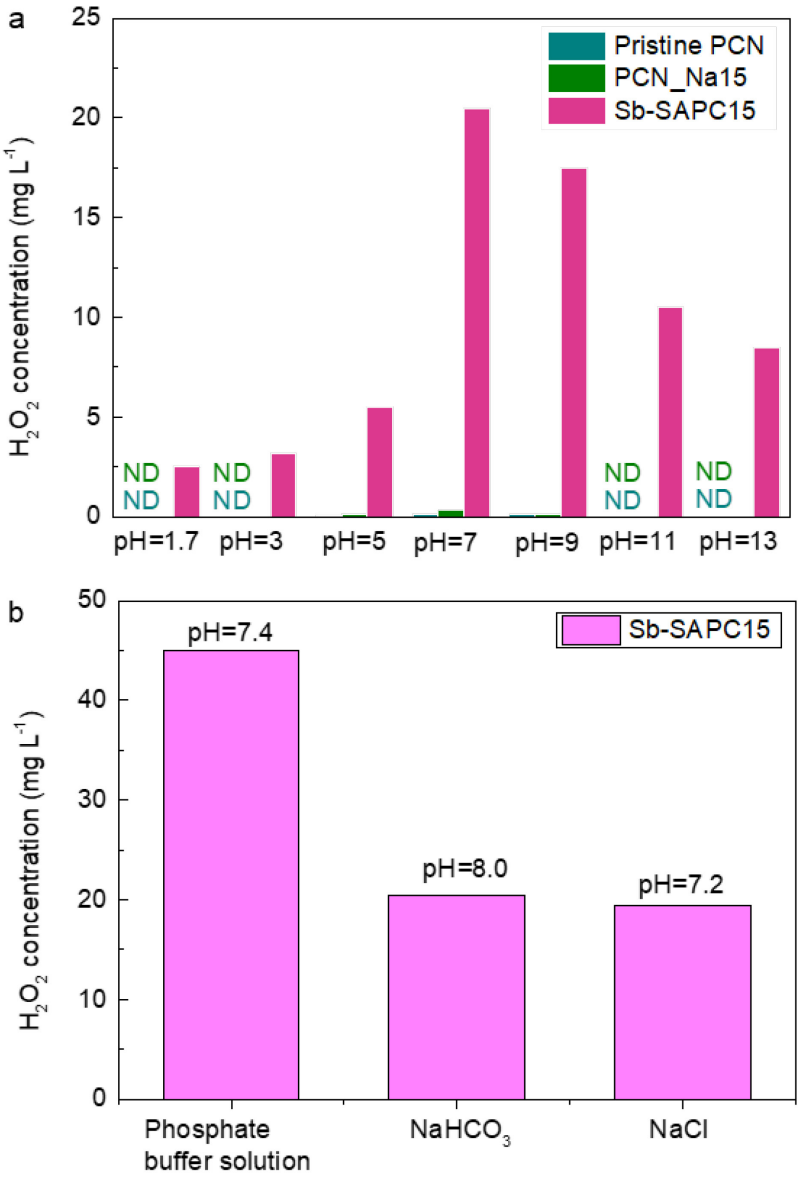

Figure 4-5. Optimization experiments for non-sacrificial photocatalytic H_2O_2 production. a, pH optimization. **b**, Solvent optimization. (light source: Xe lamp, light intensity at 420−500 nm: 30.3 W m^{-2}). The reaction time is 90 min.

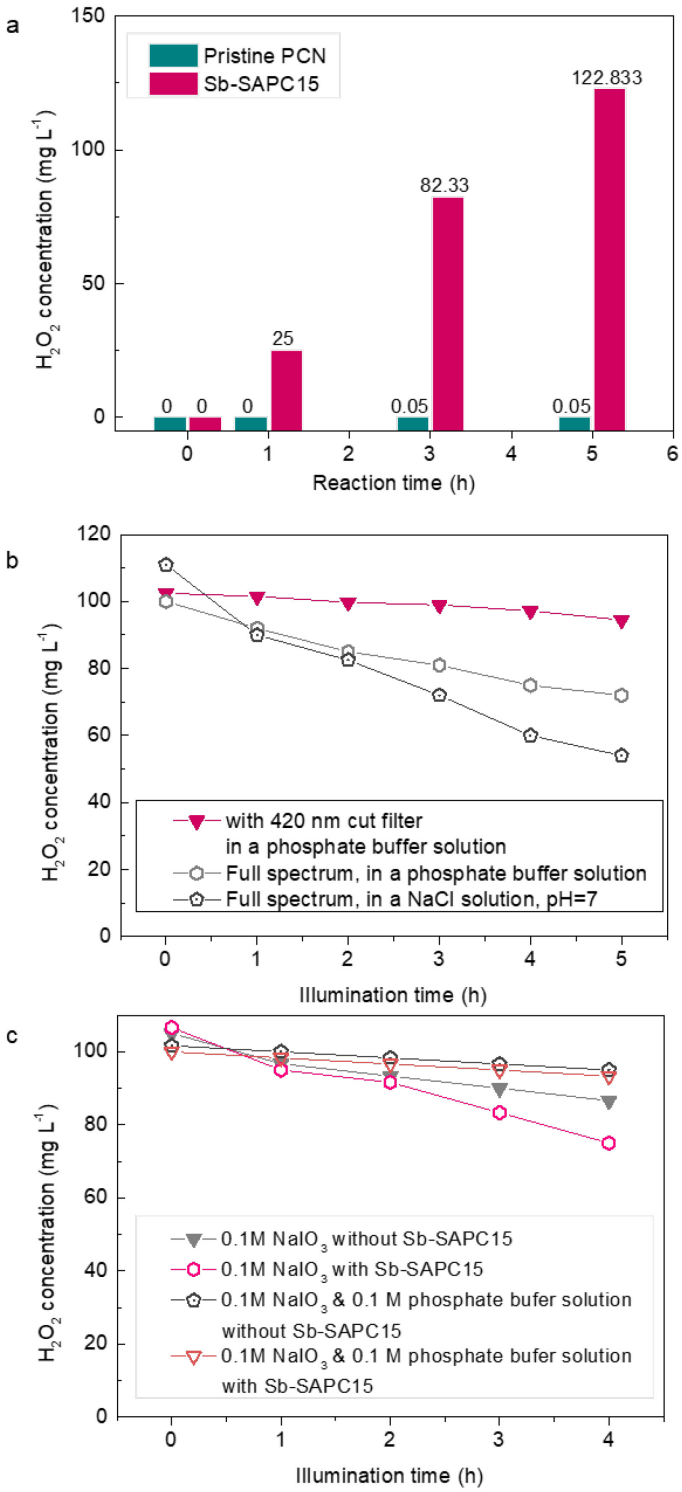

Figure 4-6. Long term activity for non-sacrificial photocatalytic H_2O_2 production. a, Long term photocatalytic H_2O_2 production using Sb-SAPC15 and pristine PCN as the photocatalyst. **b**, Optimization for light wavelength for H_2O_2 degradation study. **c**, Interactions between photogenerated holes and H_2O_2 in different kinds of solutions. The solution was irradiated by a 300 W Xenon Lamp with a UV cut filter (light intensity: 30.3 W m^{-2} at 420-500 nm).

The ΦAQY of Sb-SAPC15 at 420 nm is determined to be 17.6%, which is twice of the

most efficient photocatalyst (RF-resin, Table 4-1) for non-sacrificial H_2O_2 production[15].

Table 4-1. Activity comparison between Sb-SAPC15 and other reported photocatalysts and photoelectrodes for non-sacrificial H_2O_2 production.

Photocatalytic system	Concentration of photocatalyst	Irradiation condition	H_2O_2 yield	AQE/ SCC efficiency	Ref.
g-C_3N_4/PDIx	1.7 mg mL^{-1}	λ > 420 nm	50.6 μmol (48 h)	2.5% at 420 nm/ NA	[12]
g-C_3N_4/PDI/RGO	1.7 mg mL^{-1}	λ > 420 nm	38 μmol (2 h)	6.1% at 420 nm/ 0.2%	[39]
Graphene oxide	0.32 mg mL^{-1}	λ > 420 nm	1.4 μmol (6 h)	NA/ NA	[57]
Si/TiO_2-Au	------	λ = 365 nm	40 μmol (75 h)	NA/ NA	[58]
TiO_2-Pt	0.05 mg mL^{-1}	Full spectrum	5.096 μmol (1 h)	NA/ NA	[59]
g-C_3N_4/MTI	1.7 mg mL^{-1}	λ > 420 nm	27.5 μmol (24 h)	6.1% at 420 nm/ 0.18%	[60]
g-C_3N_4/PDI-BN-RGO	1.7 mg mL^{-1}	λ > 420 nm	34 μmol (24 h)	7.3% at 420 nm/ 0.28%	[61]
Resorcinol–formaldehyde resins	1.7 mg mL^{-1}	λ > 420 nm	99 μmol (24 h)	7.5% at 450 nm/ 0.5%	[15]
Sb-SAPC15	**2 mg mL^{-1}**	**λ > 420 nm**	**470.5 μmol (8 h)**	**17.6% at 420 nm/ 0.61%**	**This work**

The solar-to-chemical conversion efficiency of Sb-SAPC15 reaches as high as 0.61% (Figure 4-2d), comparable with the most efficient water splitting photocatalyst (~0.8%)[24]. Interestingly, the Sb-SAPC15 displays negligible photocatalytic activity for the hydrogen evolution reaction (Figure 4-2e, left). Furthermore, by comparing the photocatalytic products at two different reaction conditions (with and without O_2), the H_2O_2 is clearly shown to be produced via the $2e^-$ ORR (no H_2O_2 was detected in the photocatalytic system without O_2, Figure 4-2e, right). Besides activity, more than 95% of the initial activity (Sb-SAPC15) could be maintained after 5 consecutive photocatalytic runs indicating the good stability (Figure 4-7a). Reproducibilities of Sb-SAPC15 (5 different batches) are also excellent for AQY and SCC measurements (Figure 4-7b-c). The long-term stability and potential for scalable photocatalytic H_2O_2 production using the Sb-SAPC photocatalyst were demonstrated in a fixed bed reactor (Figure 4-8).

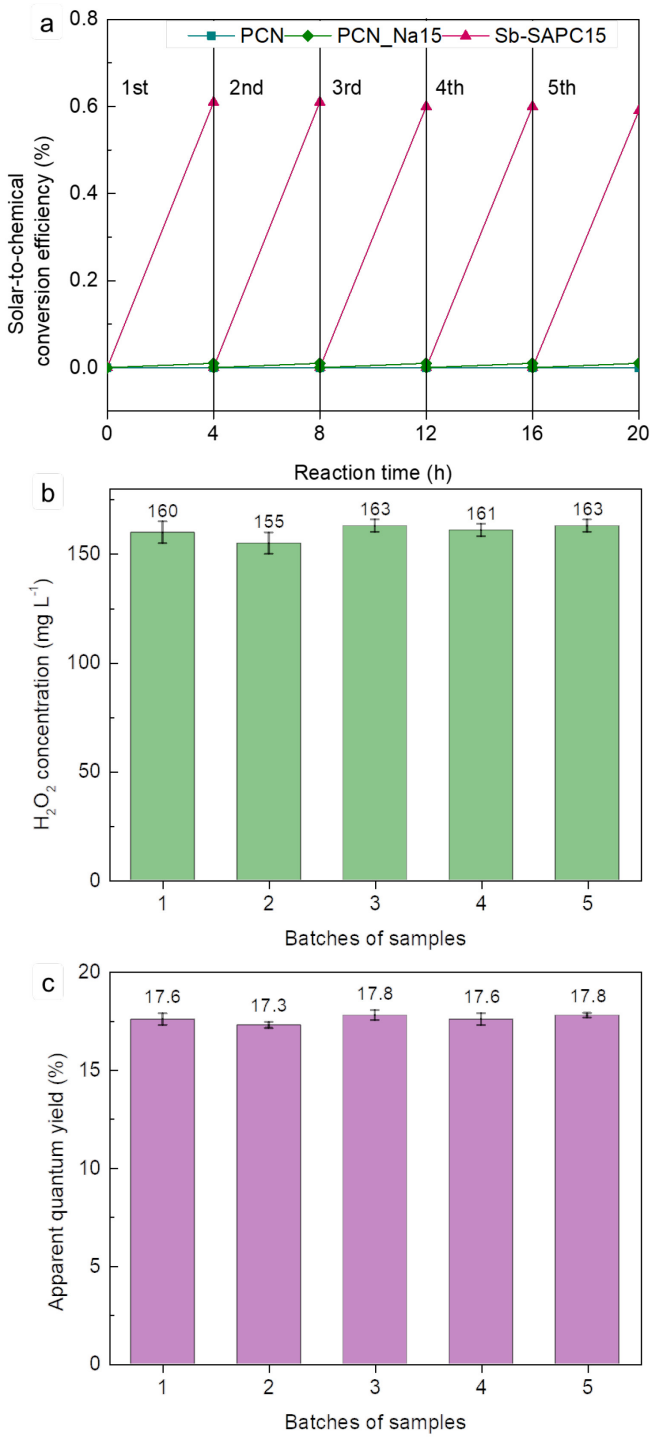

Figure 4-7. Repeatability and reproducibility of catalysts. a, Repeatability of the CN samples for photocatalytic production of H_2O_2. After each run, the catalyst was filtered and re-suspended in a fresh solution with pH adjusted to 7.4 by phosphate buffer solution. **b**, Reproducibility of photocatalytic H_2O_2 production for calculating solar-to-chemical conversion efficiency. **c**, Reproducibility for apparent quantum yield (λ = 420 nm). Light source: Xe lamp, light intensity at 420−500 nm: 30.3 W m^{-2}; reaction medium: phosphate buffer solution at pH = 7.4. Error bars represent the standard deviation of 3 replicate measurements.

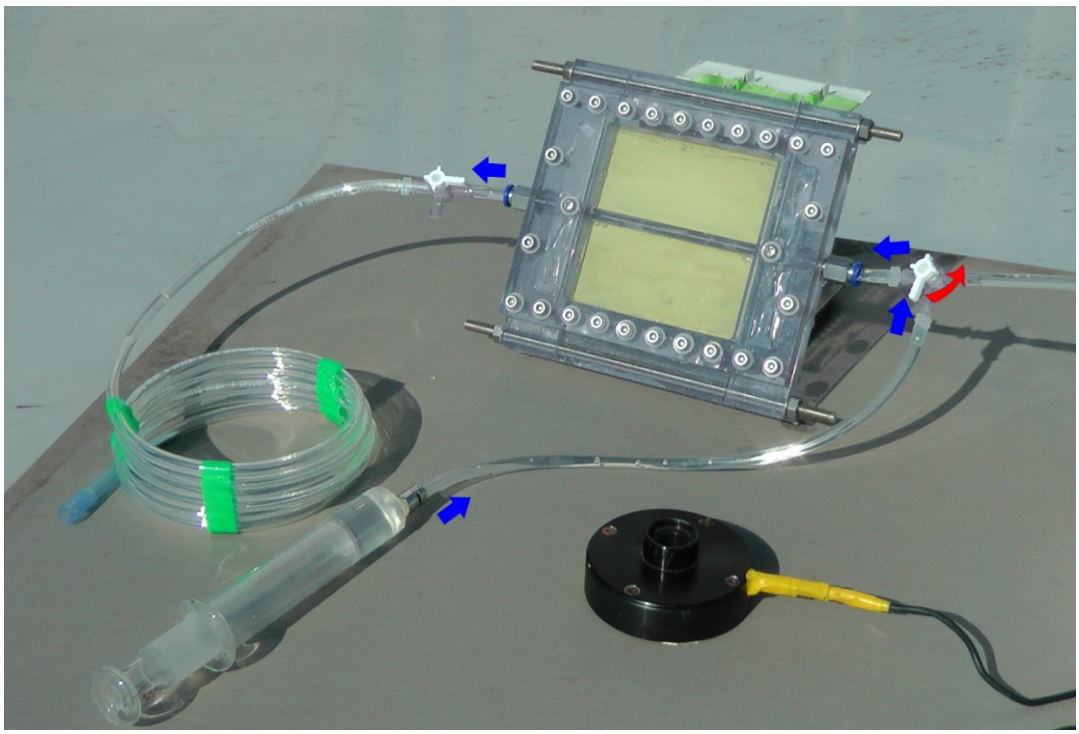

Figure 4-8. The practical experiment of photocatalytic H_2O_2 production using solar light. The blue arrow indicates the flow direction of aqueous solution. The red arrow tells the direction to open the valve.

4.3.1.1 Half-reactions for H_2O_2 production utilizing Sb-SAPC

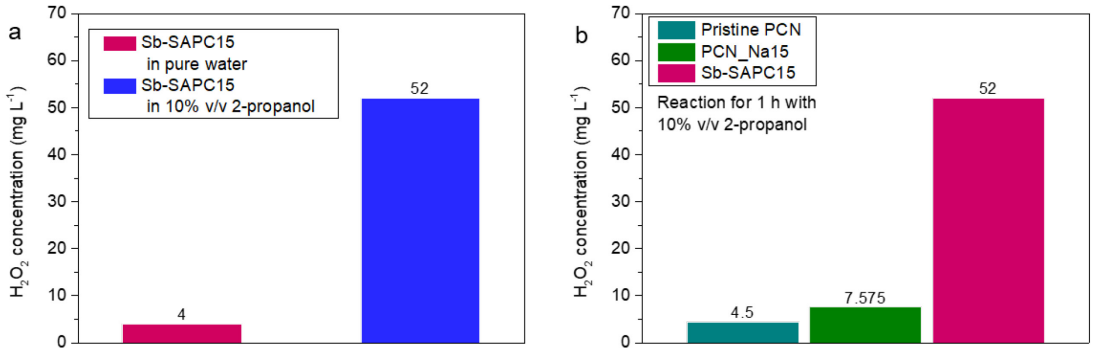

Figure 4-9. Half reaction with addition of an electron donor. a, Comparison of H_2O_2 formed in pure water and 10% (v/v) 2-propanol aqueous solution catalyzed by Sb-SAPC15. **b**, Comparison of H_2O_2 production in 10% (v/v) 2-propanol aqueous solution catalyzed by pristine PCN, PCN_Na15 and Sb-SAPC15. Reaction time: 60 min. Irradiation condition: $\lambda >$ 420 nm (Xe lamp, light intensity at 400−500 nm: 30.3 W m^{-2}), at 298 K.

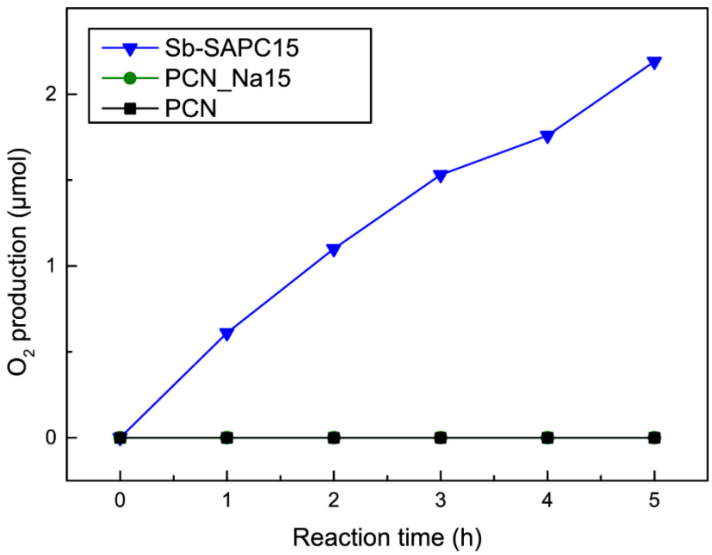

Figure 4-10. Comparison of oxygen evolution efficiency for PCN, PCN_Na15 and Sb-SAPC15 during the half reaction.

To study the overall reaction for photocatalytic H_2O_2 production, the half redox reactions on Sb-SAPC15 were separately investigated as follows: Sb-SAPC15 in a 2-propanol aqueous solution (2-propanol as an electron donor, 10% v/v) with saturated O_2 (Figure 4-9) and in a $NaIO_3$ aqueous solution ($NaIO_3$ as an electron acceptor) with N_2 (Figure 4-2f and Figure 4-10) respectively under visible light irradiation, which confirm that the H_2O_2 is indeed produced via the ORR on Sb-SAPC15.

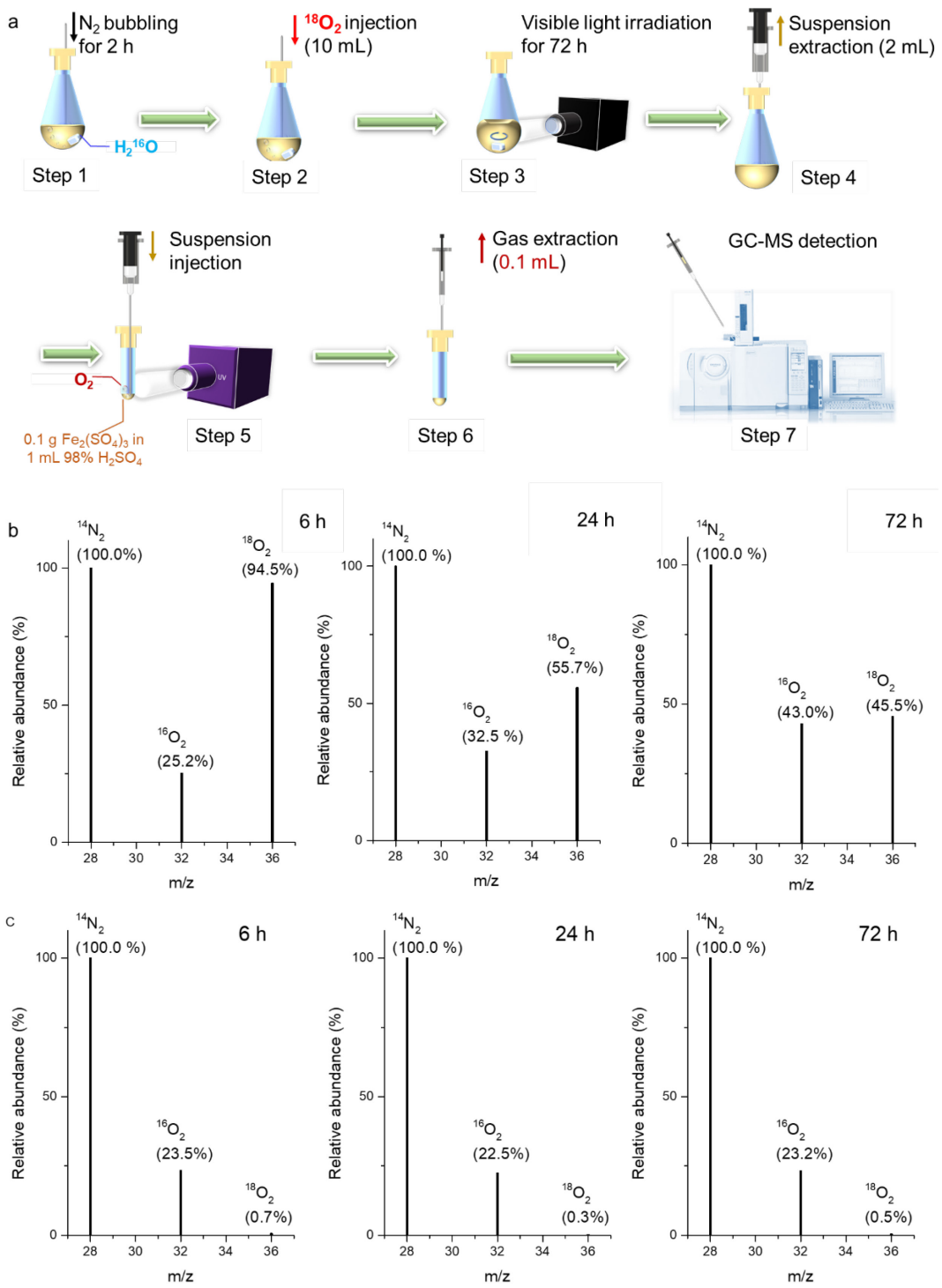

Figure 4-11. Isotopic experiments utilizing $^{18}O_2$. a, Schematic diagram showing the isotopic experimental procedure for H_2O_2 production with addition of $^{18}O_2$ as the electron acceptor. **b**, GC-MS spectra of the gas extracted from the Sb-SAPC15/Fe^{3+} system after the light illumination for 6 h, 24 h and 72 h in step 2. **c**, GC-MS spectra of the gas extracted from the same system without addition of Sb-SAPC15 at the reaction time point of 6 h, 24 h and 72 h in step 2. The reaction solution is pure $H_2{}^{16}O$ with injection of 10 mL $^{18}O_2$.

Isotope experiments[15] (Figure 4-11) were further performed to verify the $4e^-$ WOR

mechanism, in which Sb-SAPC15 in $H_2{}^{16}O$ and $^{18}O_2$ gas was irradiated for 6, 24 and 72 h. Fe^{3+} and high concentration H^+ were added into the reaction system to decompose H_2O_2 to release O_2, and the evolved gas was analyzed by gas chromatography-mass spectrometry. The gaseous product obtained after 6 h reaction exhibits a strong $^{18}O_2$ (m/z) peak (94.5%) and a weak $^{16}O_2$ (m/z) peak (25.2%), manifesting that $H_2{}^{18}O_2$ was produced by O_2 reduction at the initial stage of the reaction. The gaseous product obtained with increasing reaction time shows a decreased intensity of $^{18}O_2$ peak (24 h: 55.7%; 72 h: 45.5%) and an increased intensity of $^{16}O_2$ peak (24 h: 32.5%; 72 h: 45.5%), indicating that the oxygen generated by WOR gradually participated in the ORR process[15]. To identify whether the dissolved O_2 participated in the GC-MS detection, we have performed control experiment to ensure that the $^{18}O_2$ injected at the beginning of the experiment could be barely measured later. The details for the experiment are as follows: all experiments are the same as the experimental procedure except the addition of the photocatalyst. In this case, the H_2O_2 could hardly be formed, and only dissolved oxygen existed in the liquid phase[15]. As shown in step 3, the dissolved oxygen could be transferred to step 4 when liquid was extracted from the solution. The gas extracted from step 6 was also measured by GC-MS. As shown in the figure above, we could hardly detect the signal of $^{18}O_2$, indicating that the dissolved oxygen in the extracted solution (step 3) barely influenced the measurement. Note that the signal of $^{16}O_2$ is attributed to the small leakage of O_2 during the injection process.

To quantitatively reveal the relationship between the WOR and ORR, low-concentration electron acceptor (0.1 mM Ag^+) was added into the PCN and Sb-SAPC system in the absence of O_2. In this case, H_2O_2 can only be produced via the reduction of O_2 generated from water oxidation. PCN showed no photocatalytic activity in this condition, while Sb-SAPC gradually produced H_2O_2 in a certain time interval. After that, the H_2O_2 concentration kept constant ~1.0 mg L^{-1} no matter how much catalyst was used (Figure 4-2g). The quantitive relationship between the amount of added Ag^+ and H_2O_2 produced from WOR is discussed as follows. To calculate the H_2O_2 generated from the Sb-SAPC system, we made the following assumptions: (1) all added Ag^+ (4n mol) is consumed to provide

holes to generate the initial O_2 (n mol); (2) then, the Sb-SAPC reduces O_2 (n mol) to form H_2O_2 (n mol) and simultaneously oxidizes H_2O (n mol) to generate fresh O_2 (1/2n mol); (3) the O_2 generated in (2) keeps participating in the H_2O_2 production and WOR to generate O_2 (1/4n, 1/8n, 1/16n… mol) until all O_2 is completely consumed. As a result, the amount of H_2O_2 produced by the initially generated O_2 can be calculated as follows:

$$n_{H_2O_2} = \sum_{k=1}^{x} n_{O_2} r^{k-1} = \frac{n_{O_2}(1-r^x)}{1-r} \qquad \text{(I)}$$

where $n_{H_2O_2}$ is the generated amount of H_2O_2, n_{O_2} is the amount of generated O_2 by Ag^+, r is 1/2, *k* is number of reaction cycles for simultaneous H_2O_2 production and WOR. If the initial O_2 generated by Ag^+ (*k* = 1) was all consumed for H_2O_2 production (i.e., *k* equals to ∞), the total amount of H_2O_2 produced would be 2 times the amount of O_2 (*k* = 1) and 1/2 times the amount of added Ag^+. The constant concentration of H_2O_2 was measured to be 0.032 mM with addition of 200 mg catalyst, 64% of the ideal value (0.05 mM) calculated based on the initially added Ag^+ (0.1 mM). The 36% deficiency of H_2O_2 could be due to the reaction equilibrium of H_2O_2 production[28,30] and the dissolved O_2 in aqueous solution (O_2 solubility in pure water: 0.25 mM). Isotope experiment using $H_2{}^{18}O$ was also conducted to confirm that the H_2O_2 generated in the system is indeed derived from the O_2 produced by the $4e^-$ WOR process (Figure 4-12). The intensity of ${}^{18}O_2$ peak (m/z=36) gradually increases with increasing reaction time, indicating that $H_2{}^{18}O_2$ is originated from the ${}^{18}O_2$ generated by WOR.

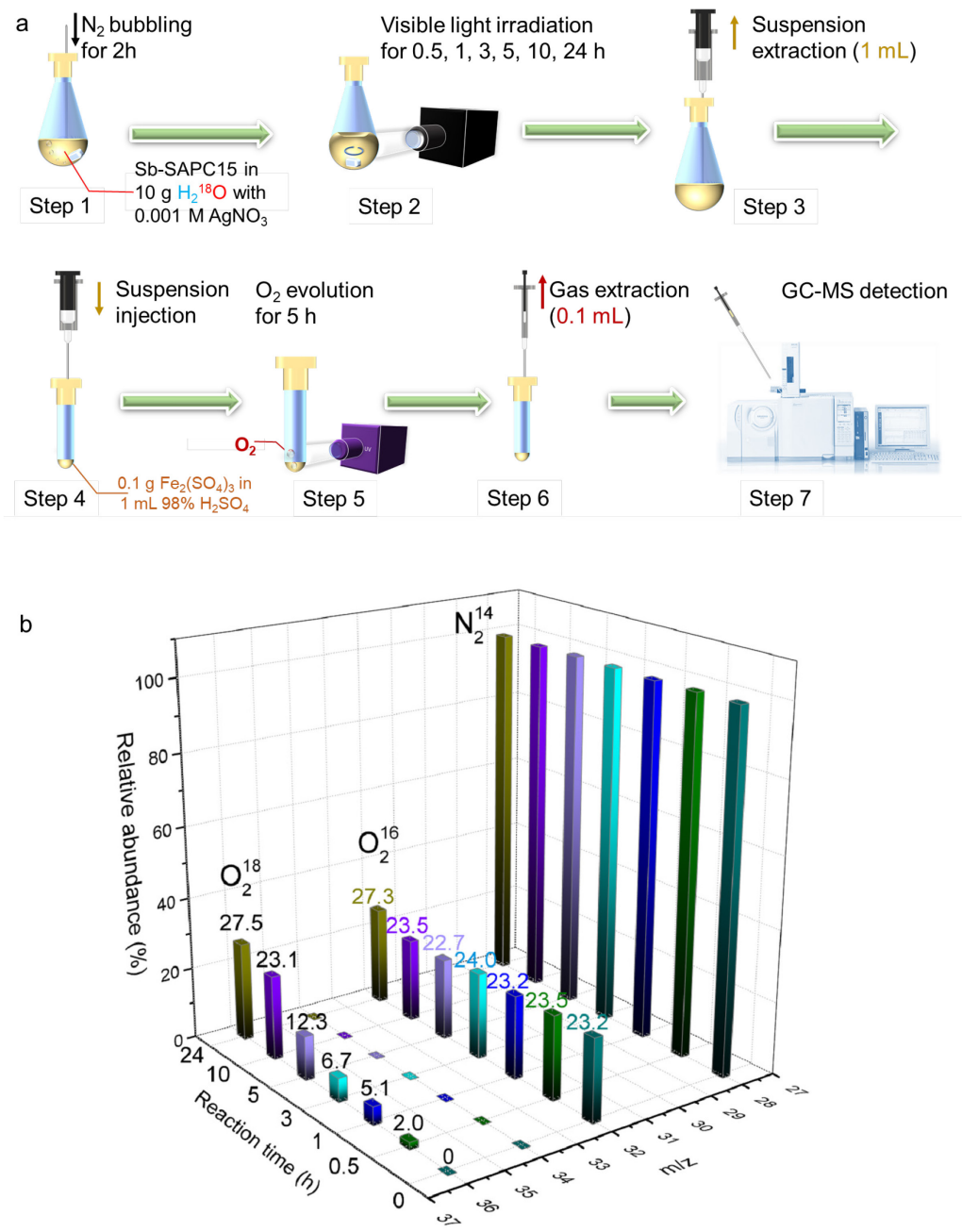

Figure 4-12. Isotopic experiments utilizing $H_2{}^{18}O$. a, Schematic diagram showing the isotopic experimental procedure for H_2O_2 production with addition of Ag^+ as the electron acceptor. **b**, GC-MS spectra of the gas extracted from the Sb-SAPC15/Fe^{3+} system after the Xenon lamp illumination of 0 h, 0.5 h, 1 h, 3 h, 5 h, 10 h and 24 h in step 2. The reaction solution is pure $H_2{}^{18}O$ with saturated ultrapure N_2. (Mass of the catalyst in step 1: 50 mg, Ag^+ concentration: 0.001M).

It is noteworthy that the signal of $^{16}O_2$ is attributed to the small leakage of O_2 during the injection process (step 7) since the signals of $^{16}O_2$ are almost the same (~23 %). Similar phenomenon could be also observed in the Figure 12c even no $^{16}O_2$ was injected in the

system. Although this system error existed, the increasing signal of $^{18}O_2$ with extended reaction time still revealed the water oxidation gradually happened with the addition of the electron acceptor. Therefore, the O_2 generated from WOR in Sb-SAPC system was rapidly consumed by the $2e^-$ ORR process to produce H_2O_2.

4.3.2 Characterization of Sb-SAPC

4.3.2.1 Synthesis process of Sb-SAPC

The synthesis of Sb-SAPC was first investigated to give a view of the structure of Sb-SAPC. Sb-ethoxide was formed after dissolving $NaSbF_6$ in ethanol. After addition of melamine, the lattice distance of the Sb-containing mixture was slightly increased. The formed Sb-containing compound can be assigned to the Sb-melamine, verified by X-ray diffraction (XRD, Figure 4-13a) and X-ray photoelectron spectroscopy (XPS, Figure 4-14 and 4-15). Typically, the chemical shift assigning to the Sb-O bond and Sb-N bond could be found, further confirming the synthesis process that is revealed in scheme 4-1. Then, thermal polymerization and removal of F element were performed by calcination at 560 °C for 4 hours (Figure 4-16).

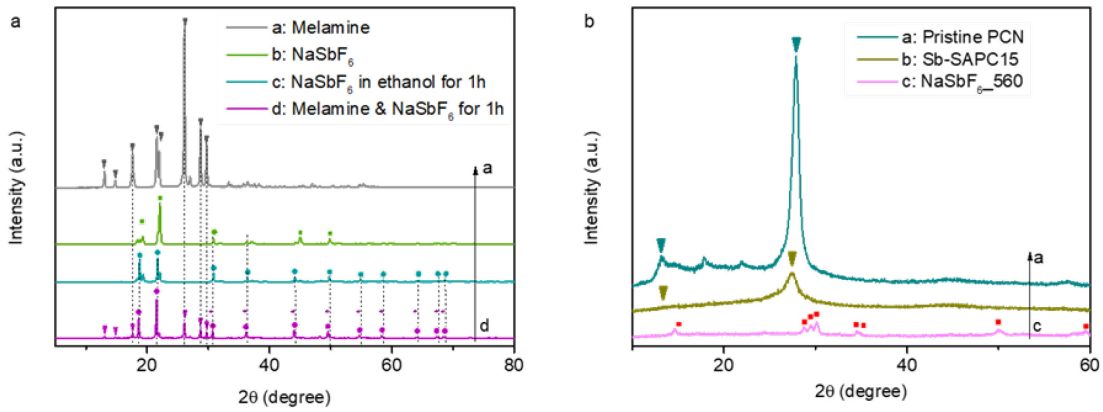

Figure 4-13. X-ray diffraction (XRD) patterns. a, XRD patterns of a: melamine; b: $NaSbF_6$; c: 3.881 g $NaSbF_6$ in ethanol with sonification for 1 hour (*Intermediate Product 1*); d: sample c mixed with 4 g of melamine in ethanol with 1 hour sonification (*Intermediate Product 2*). **b**, XRD patterns of pristine PCN, Sb-SAPC15 and $NaSbF_6$ prepared at 560 °C for 4 h ($NaSbF_6$_560).

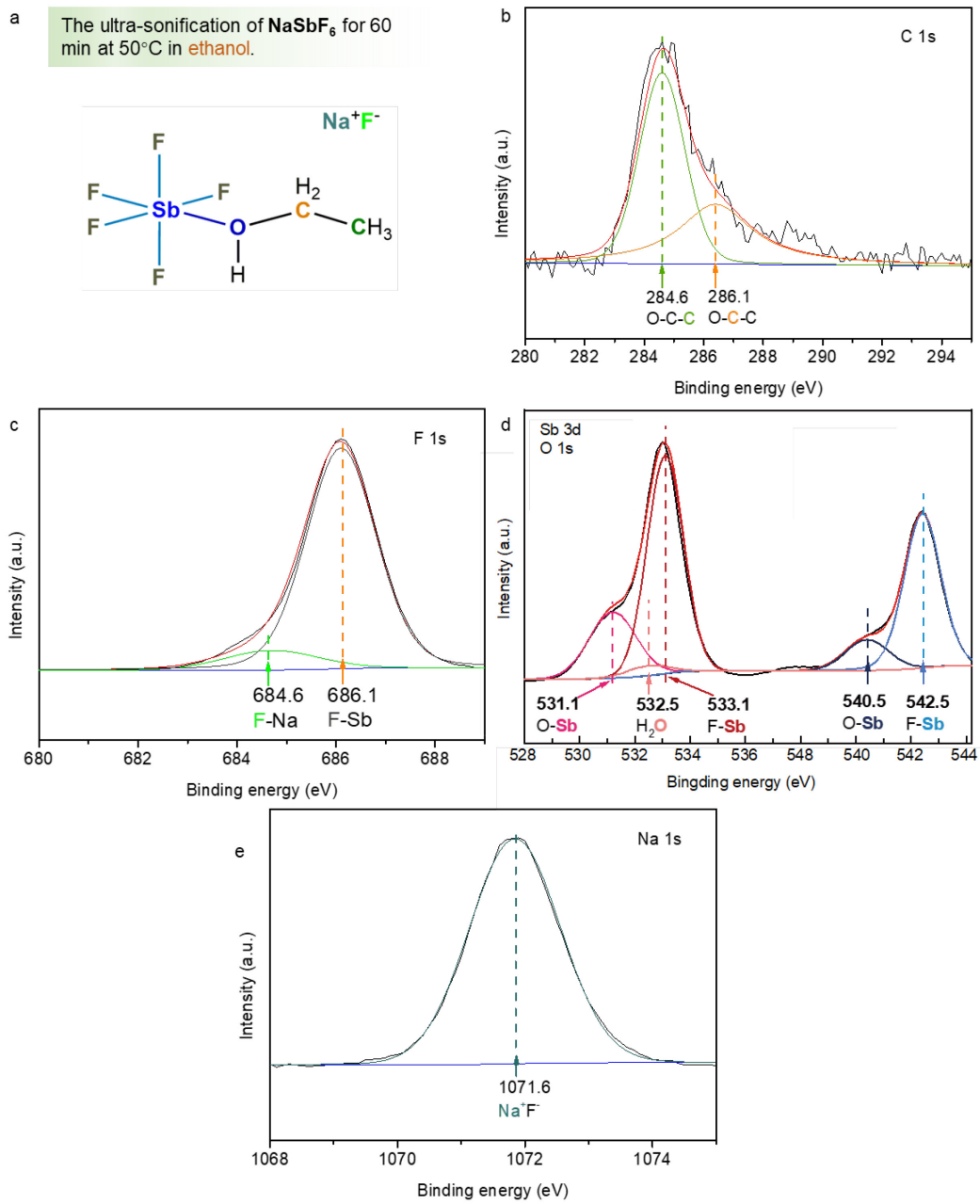

Figure 4-14. XPS spectra of 3.881 g $NaSbF_6$ in ethanol with sonification for 1 hour (*Intermediate Product 1*). a, Structure of *Intermediate Product 1*. **b-e**, High-resolution XPS spectra of C 1s (**b**), F 1s (**c**), O 1s (**d**) and Na 1s (**e**).

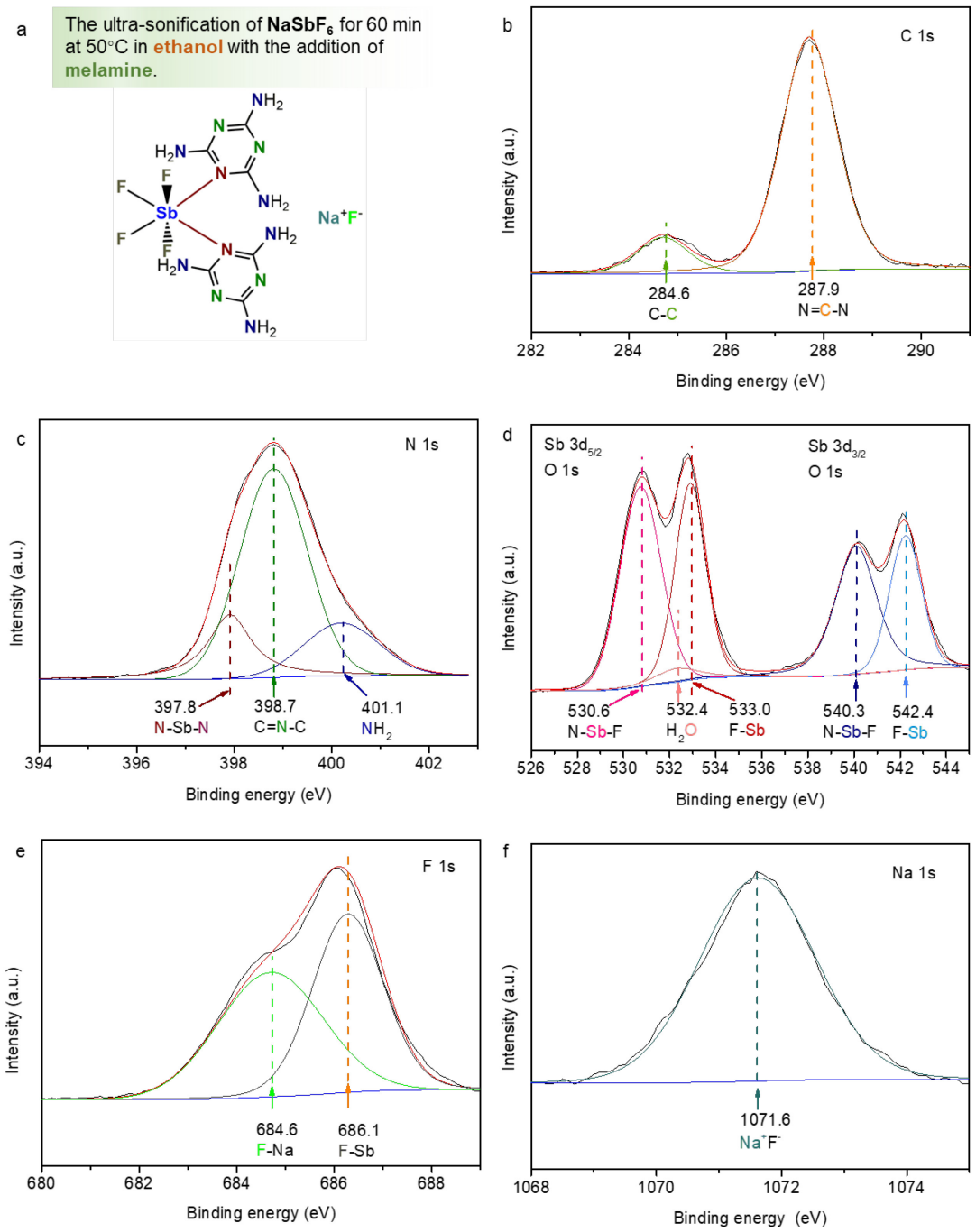

Figure 4-15. XPS spectra of 3.881 g $NaSbF_6$ in ethanol with sonification for 1 hour, followed by mixed with 4 g of melamine in ethanol with 1 hour sonification (*Intermediate Product 2*). a, Structure of *Intermediate Product 2*. **b-f**, High-resolution XPS spectra of C 1s (**b**), N 1s (**c**), O 1s (**d**), F 1s (**e**) and Na 1s (**f**).

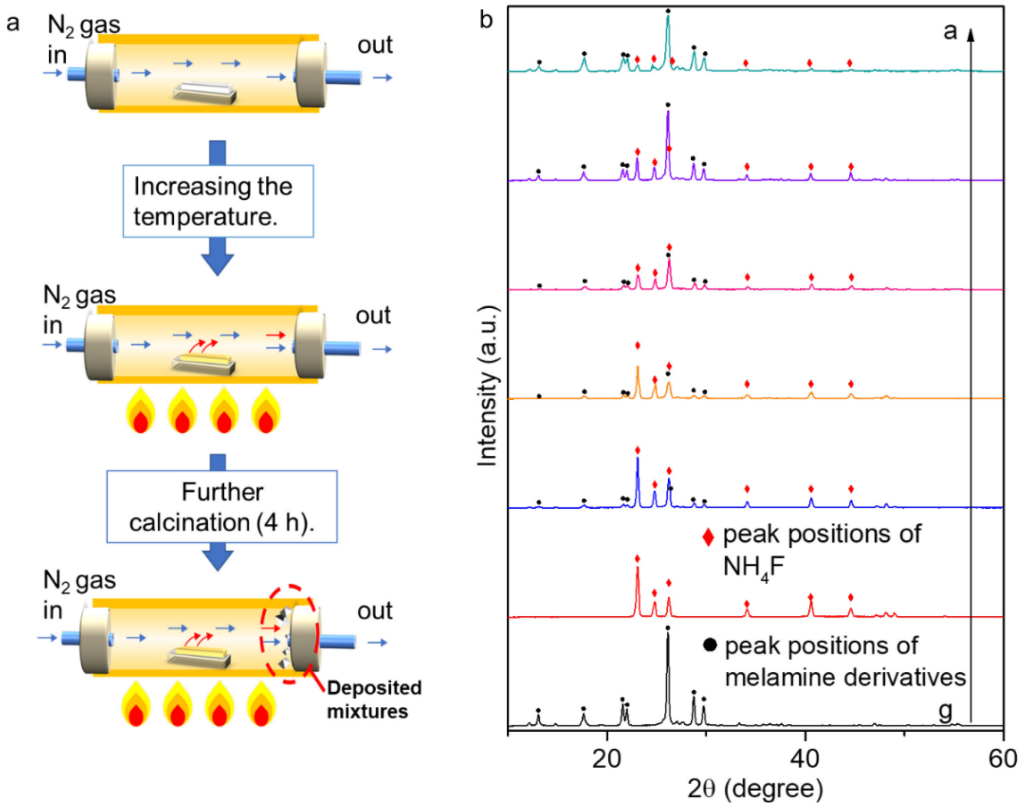

Figure 4-16. Characterization of the deposited mixture on the silicone plug of the tube furnace. a, A schematic diagram showing the deposition process during calcination. **b**, XRD patterns of the deposited mixture obtained during preparation of Sb-SAPC1 (pattern a), Sb-SAPC3 (pattern b), Sb-SAPC5 (pattern c), Sb-SAPC10 (pattern d), and Sb-SAPC15 (pattern e). XRD patterns of pure NH_4F (pattern h) and the deposited mixture during preparation of PCN (pattern g) are also included as references.

The calcination temperature was also investigated. Sb-SAPC5 (5 mmol of $NaSbF_6$ mixed with 4 g of melamine were used as the precursor) was prepared at 520 °C and 560 °C (named as Sb-SAPC5_520 and Sb-SAPC5_560), respectively. As shown in Figure 4-17a, the inner-panel diffraction of the (100) lattice completely disappears in Sb-SAPC5_520, and the inter-panel diffraction of PCN (002) lattice is also significantly decreased in Sb-SAPC5_560, while the crystalline structure of graphitic carbon nitride maintains. Additionally, the F element cannot be completely eliminated by heating at 520 °C, as shown in the XPS measurement (Figure 4-17b). These results imply that low calcination temperature cannot remove the F element in the PCN matrix, leading to an incomplete polymerization of the graphitic carbon nitride. Additionally, the Sb-SAPC5_520 shows much poorer photocatalytic activity toward H_2O_2 production, even worse than the pristine

PCN (Figure 4-17c). Therefore, Sb-SAPCs prepared at 560 °C were used for further photocatalytic investigation.

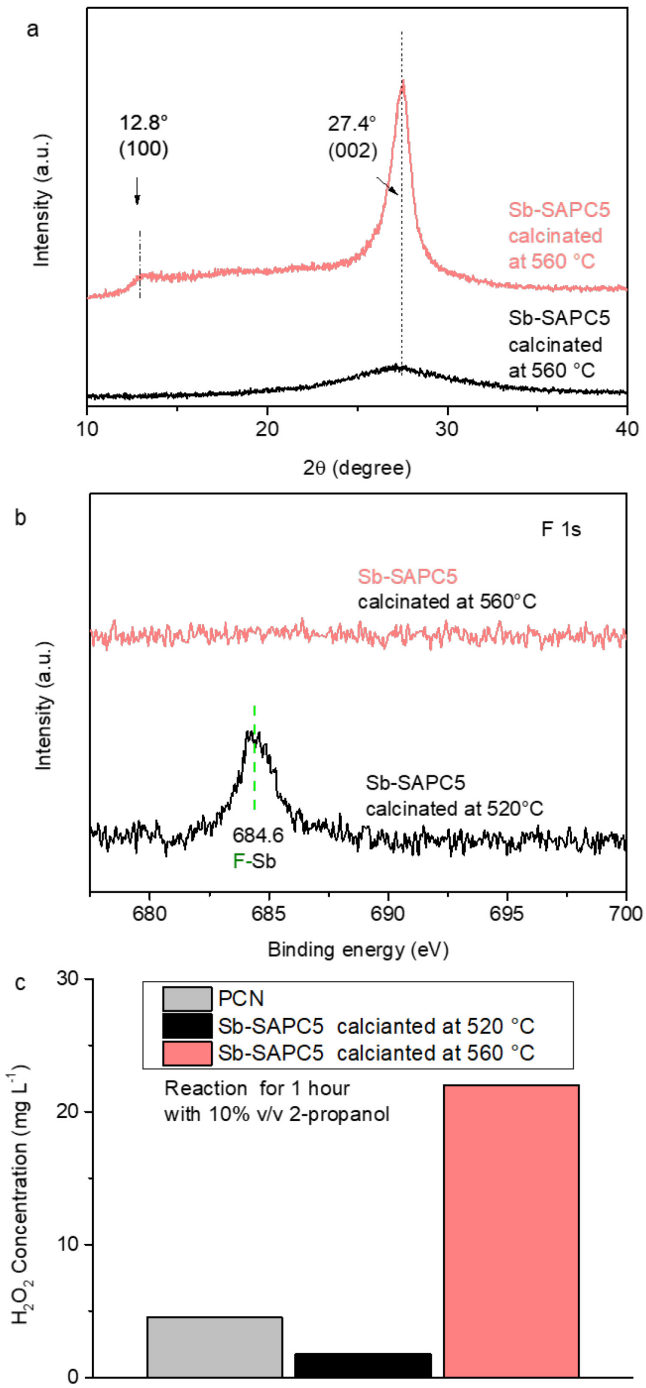

Figure 4-17. Comparison of Sb-SAPCs prepared at different temperatures. a-b XRD patterns (**a**) and high-resolution F 1s spectra (**b**) of Sb-SAPC5 prepared at 520 °C and 560 °C. **c**, Comparison of H_2O_2 formed in pure water and 10% (v/v) 2-propanol aqueous solution catalyzed by PCN and Sb-SAPC5 prepared at 520 °C and 560 °C. Reaction time: 60 min. Irradiation condition: λ > 420 nm (Xe lamp, light intensity at 400−500 nm: 30.3 W m^{-2}), at 298 K.

4.3.2.2 Characterization of as-prepared Sb-SAPC15

To understand the superb photocatalytic performance of Sb-SAPC for H_2O_2 production, the structural characteristics of the as-synthesized catalysts were carefully investigated. As revealed in the ζ-potential measurements, negative surface charges appeared on the as-prepared Sb-SAPCs to neutralize the positive charges induced by the incorporated Na and Sb cations (Figure 4-18).

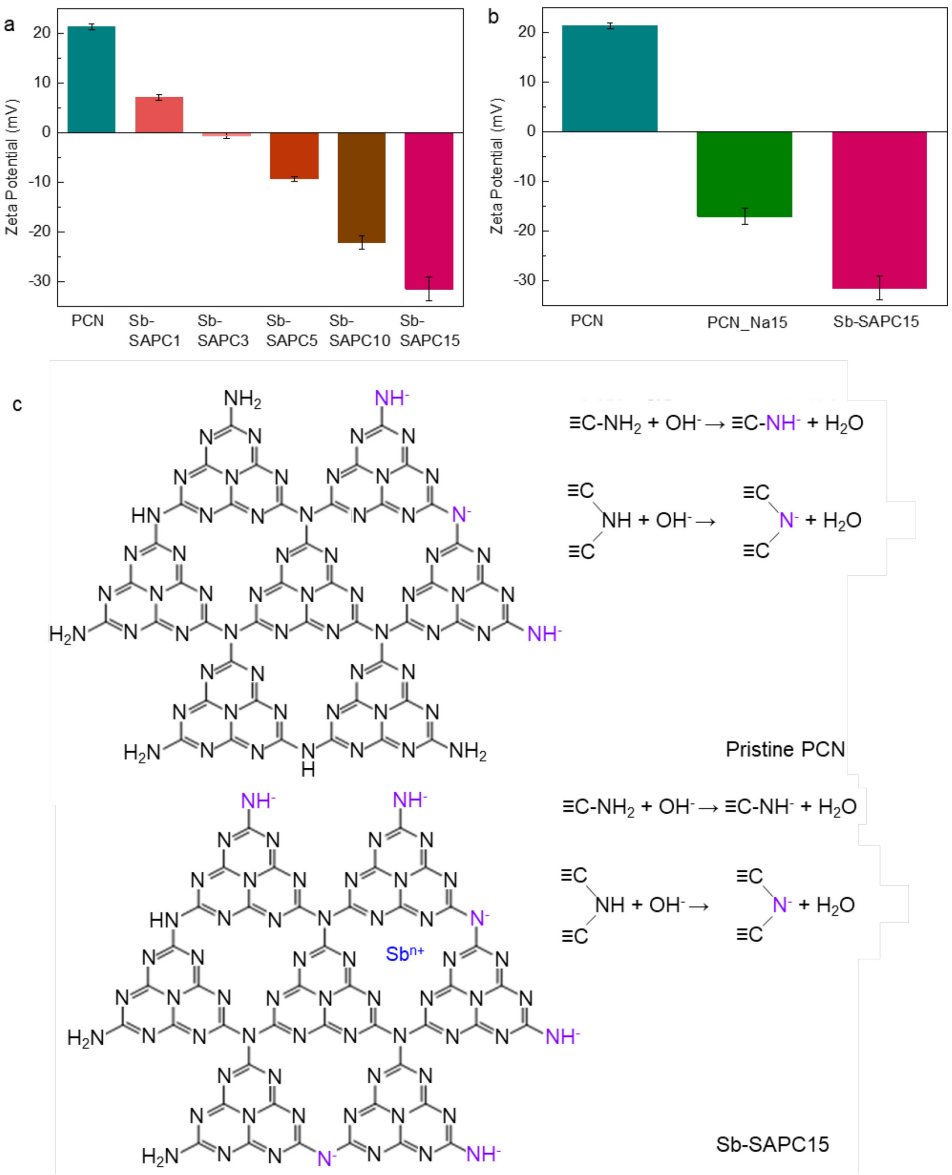

Figure 4-18. Surface charge of Sb-SAPCs and PCN samples at pH = 3. a, Zeta-potential of Sb-SAPCs with different Sb contents. **b**, Zeta-potential of PCN, PCN_Na15 and Sb-SAPC15. **c**, The possible mechanism of gradually increased surface negativity of Sb-SAPCs.

The crystalline structures of Sb-SAPCx show no obvious changes as compared to the pristine PCN, as evidenced in the XRD patterns and high-resolution transmission electron microscopy (HRTEM) images (Figure 4-19 and 4-20). XRD patterns of all Sb-SAPC samples show two characteristic peaks at about 27.6° and 13.1° (Figure 4-19), which can be ascribed to the interlayer stacking (002) and the inter planar structure packing (100) of tri-s-triazine units, respectively[31]. The slight shift in the diffraction angle of the (002) peak for Sb-SAPC15 can be attributed to the electrostatic repulsion between interlayers when positive ions are incorporated into the PCN matrix. The intensities of these two peaks gradually decrease when increasing the contents of precursors (Figure 4-20c), indicating that polymeric structure of melon/g-C_3N_4 could be slightly influenced by the foreign ions[32]. Although the long-range order of the (002) and (100) lattices significantly decreases, these two lattices can still be observed even when the content of ions reaches as high as 20 mmol. To further investigate whether the pristine structure is changed after the ion incorporation, high-resolution TEM measurements of the exfoliated Sb-SAPC were conducted (as shown in Figure 4-20). The (100) inter planar structure packing of the tri-s-triazine units can be readily observed, and the lattice distance is determined to be 6.81 Å, which is in accordance with the XRD results. Thus, the crystalline structure of melon can be well preserved in Sb-SAPC.

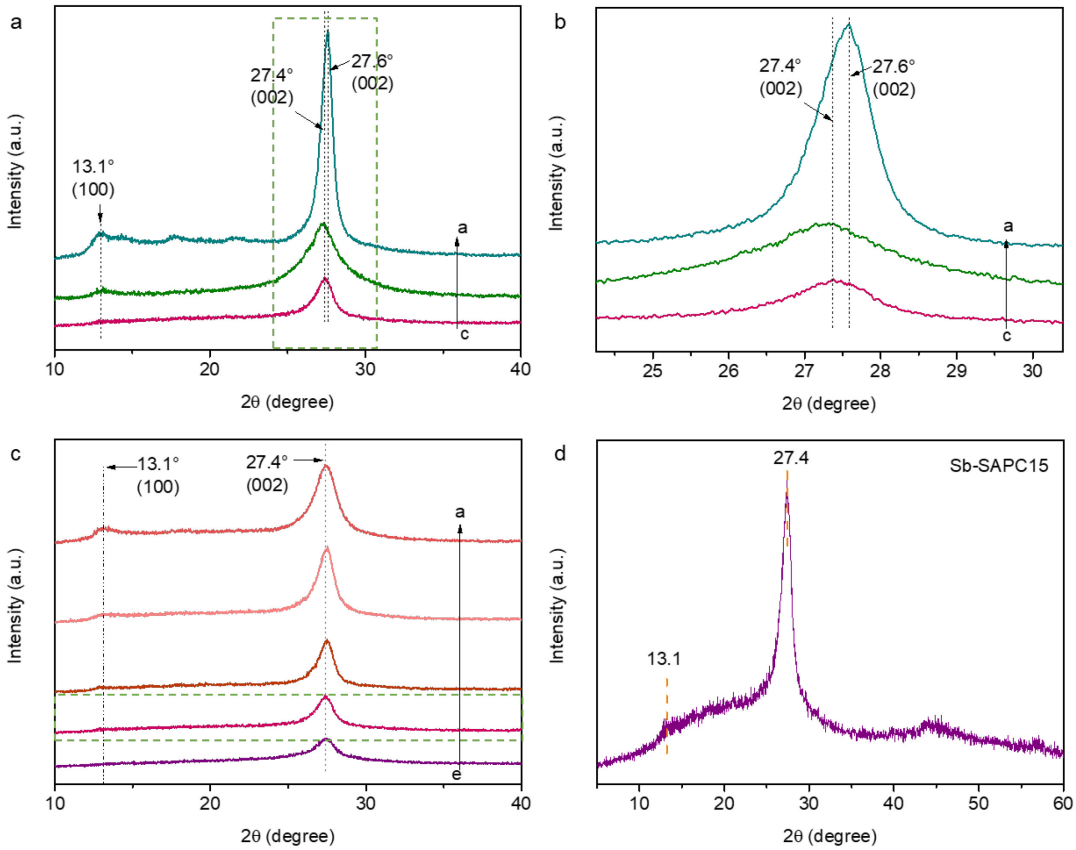

Figure 4-19. Crystallinity characterized by X-ray diffraction. a, XRD patterns of a: pristine PCN; b: PCN_Na15; and c: Sb-SAPC15. **b**, XRD patterns (high-resolution) of carbon nitride samples. **c**, XRD patterns of a: Sb-SAPC1; b: Sb-SAPC5; c: Sb-SAPC10; d: Sb-SAPC15; and e: Sb-SAPC20. **d**, XRD patterns (high-resolution) of Sb-SAPC15.

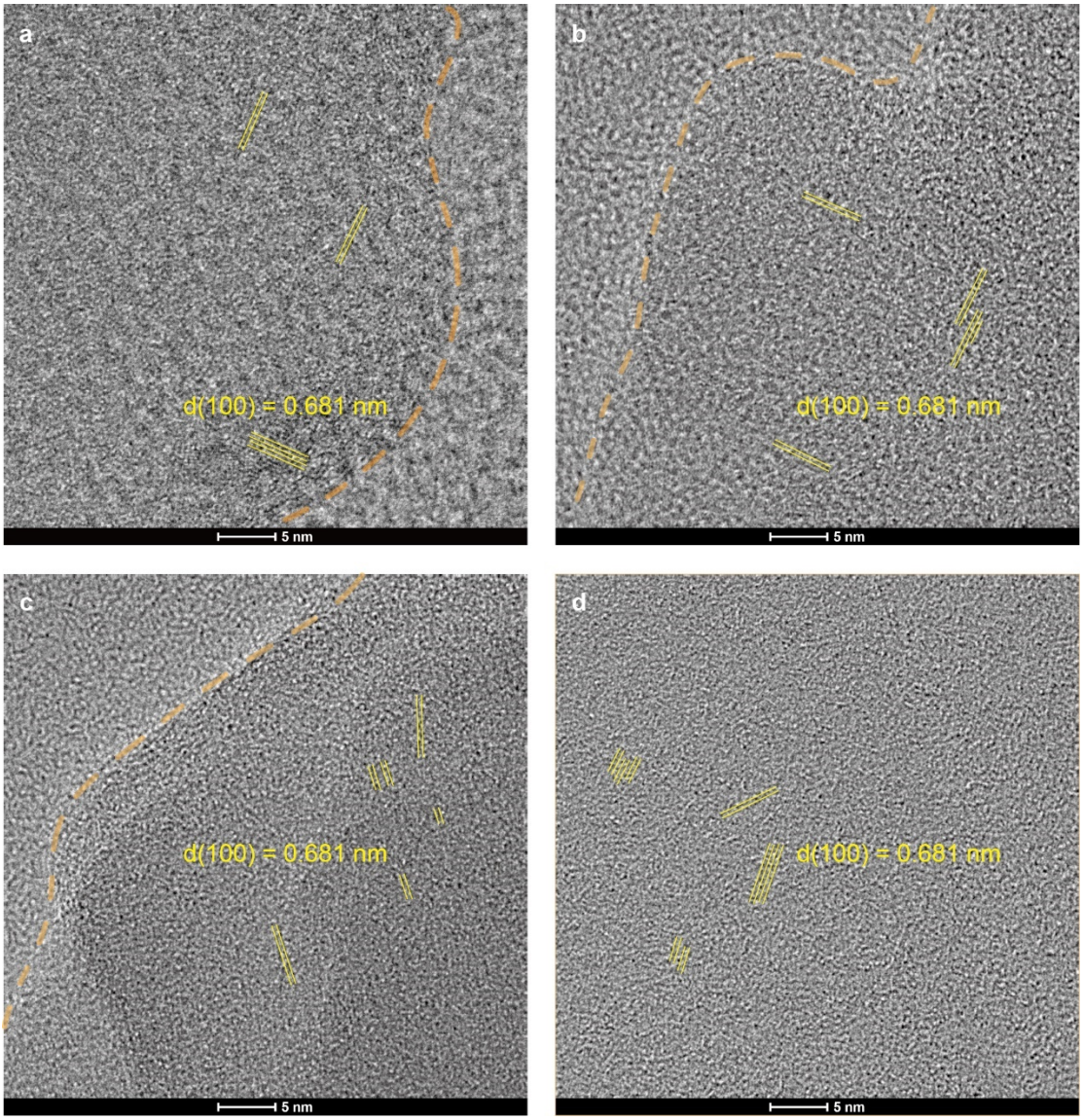

Figure 4-20. Crystallinity characterized by high-resolution transmission electron microscopy. a-d, HR-TEM images of Sb-SAPC1 (**a**), Sb-SAPC5 (**b**), Sb-SAPC10 (**c**) and Sb-SAPC15 (**d**). The yellow line indicates the lattice fringe of the (100) plane of g-C_3N_4.

As a powerful tool for visualizing individual heavy atoms, high-angle annular dark-field scanning transmission electron microscopy (HAADF-STEM) was used to further examine the morphology and elemental distribution (Figure 4-21). The Sb-SAPC15 is composed of aggregated two-dimensional nanosheets, on which Sb and Na elements are homogeneously distributed (Figure 4-22). For Sb-SAPC0.5, 1, 3, 5, 10 and 15, Figure 4-21a and Figure 4-23 show that the bright spots with high density are uniformly dispersed in the entire carbon nitride matrix. The electron energy loss spectroscopy (EELS) (Figure 2b and Figure 4-24) measurement reveals the bright spots corresponding to Sb atoms.

The size distribution as displayed in Figure 4-21a shows that 99.6% of Sb species are less than 0.2 nm, demonstrating that Sb exists exclusively as isolated single atoms[62]. The mass ratio of Sb species in Sb-SAPC15 (10.9 wt.%, Table 4-2) is considerably larger than that of the noble or transition metal single atom species in many reported SACs.

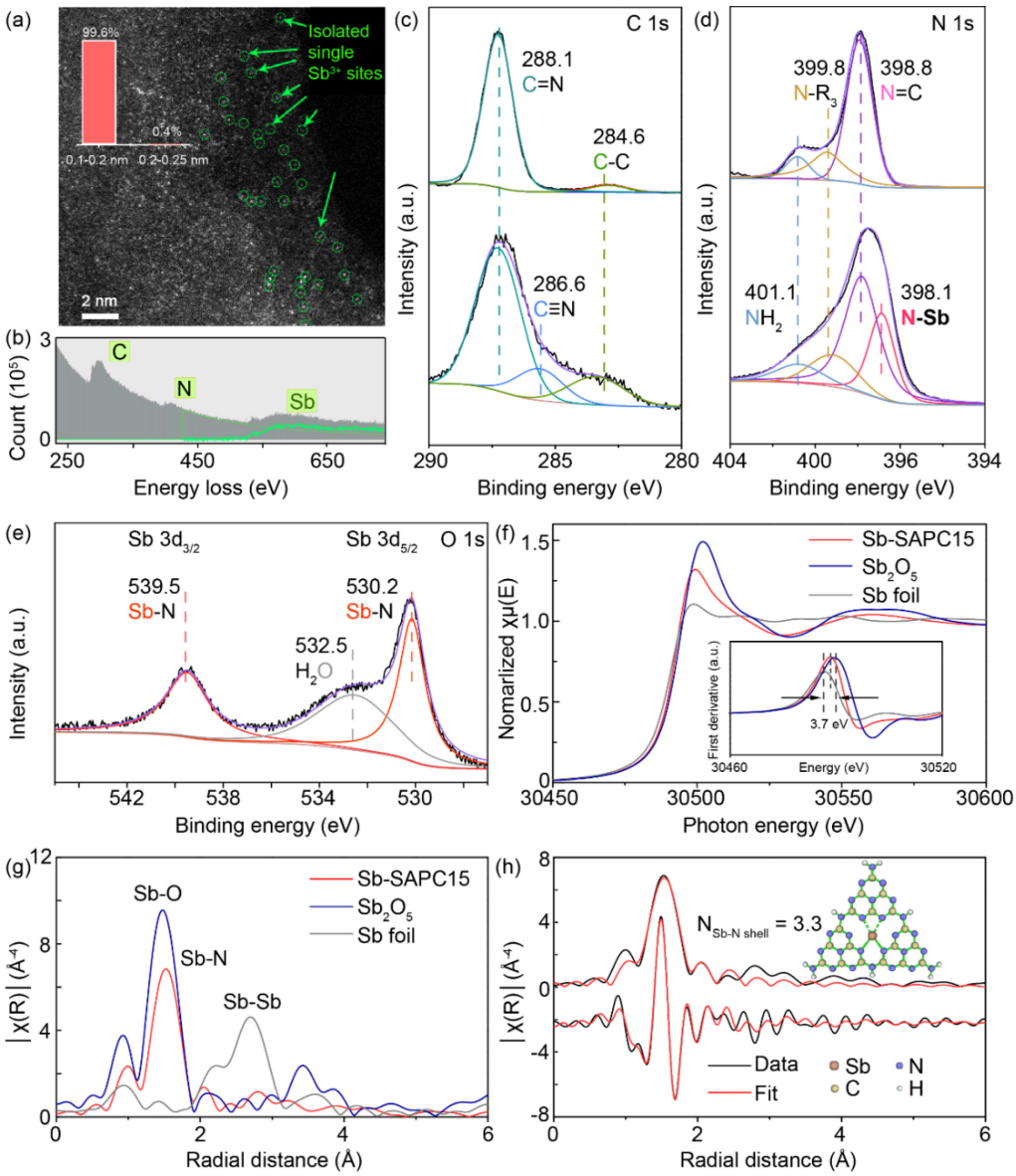

Figure 4-21. Characterization of Sb-SAPC. a, High-magnification HAADF-STEM image of Sb-SAPC15. Inset is the size distribution of the bright spots. **b**, EELS spectrum of Sb-SAPC15. **c-e**, High-resolution C 1s (**c**) and N 1s XPS spectra (**d**) of PCN and Sb-SAPC15 and Sb 3d XPS spectrum (**e**) of Sb-SAPC15. **f**,**g**, Sb-K edge XANES (**f**) and Fourier transform-extended X-ray absorption fine structure (FT-EXAFS) spectra (**g**) of the Sb foil, Sb_2O_5 and Sb-SAPC15. **h**, Fitting of the EXAFS data of the Sb-SAPC15 based on the model obtained from DFT optimization. Inserted figures: optimized molecular models based on DFT for EXAFS fitting.

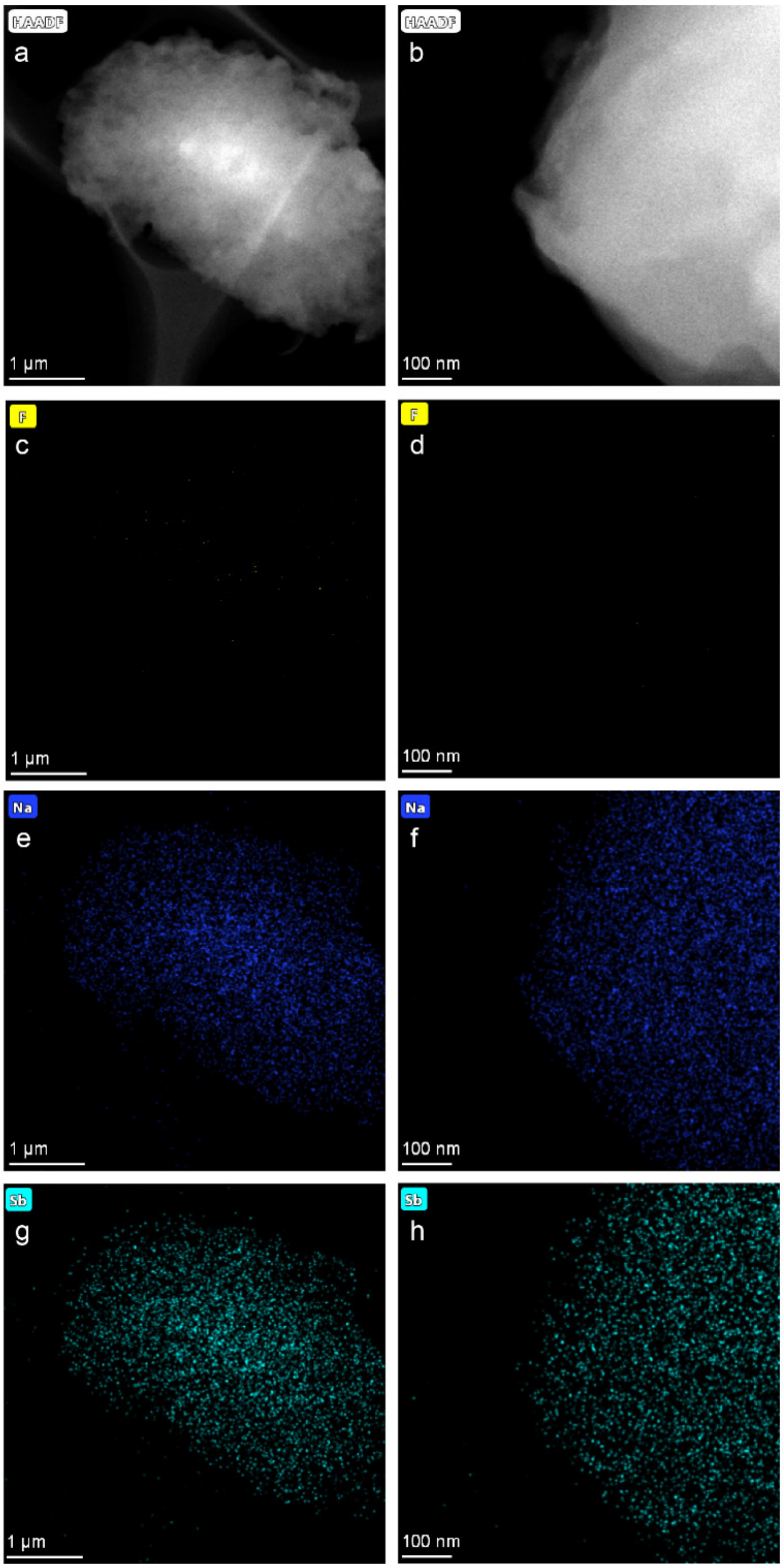

Figure 4-22. Elemental distribution in Sb-SAPC15. a-b, Low and high-magnification HAADF-STEM image of Sb-SAPC15. **c-h**, The corresponding EDS elemental mapping images of F (**c-d**), Na (**e-f**) and Sb (**g-h**) at low and high-magnification.

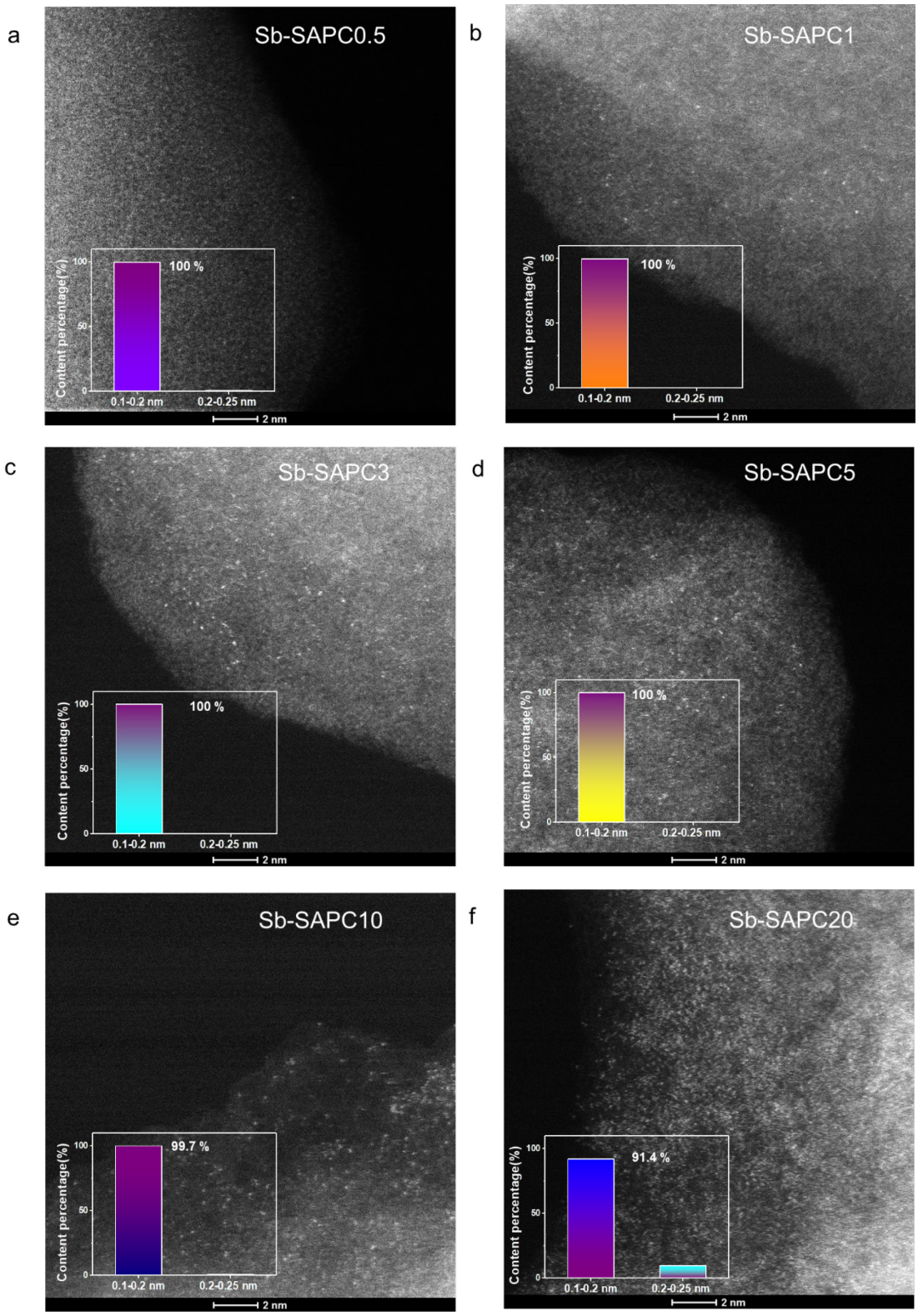

Figure 4-23. Characterization of isolated Sb species in SA-SAPCs with different Sb contents. a-f, HAADF-STEM images of Sb-SAPC0.5 (**a**), Sb-SAPC1 (**b**), Sb-SAPC3 (**c**), Sb-SAPC5 (**d**), Sb-SAPC10 (**e**) and Sb-SAPC20 (**f**). Inset shows the size distribution of the bright spots.

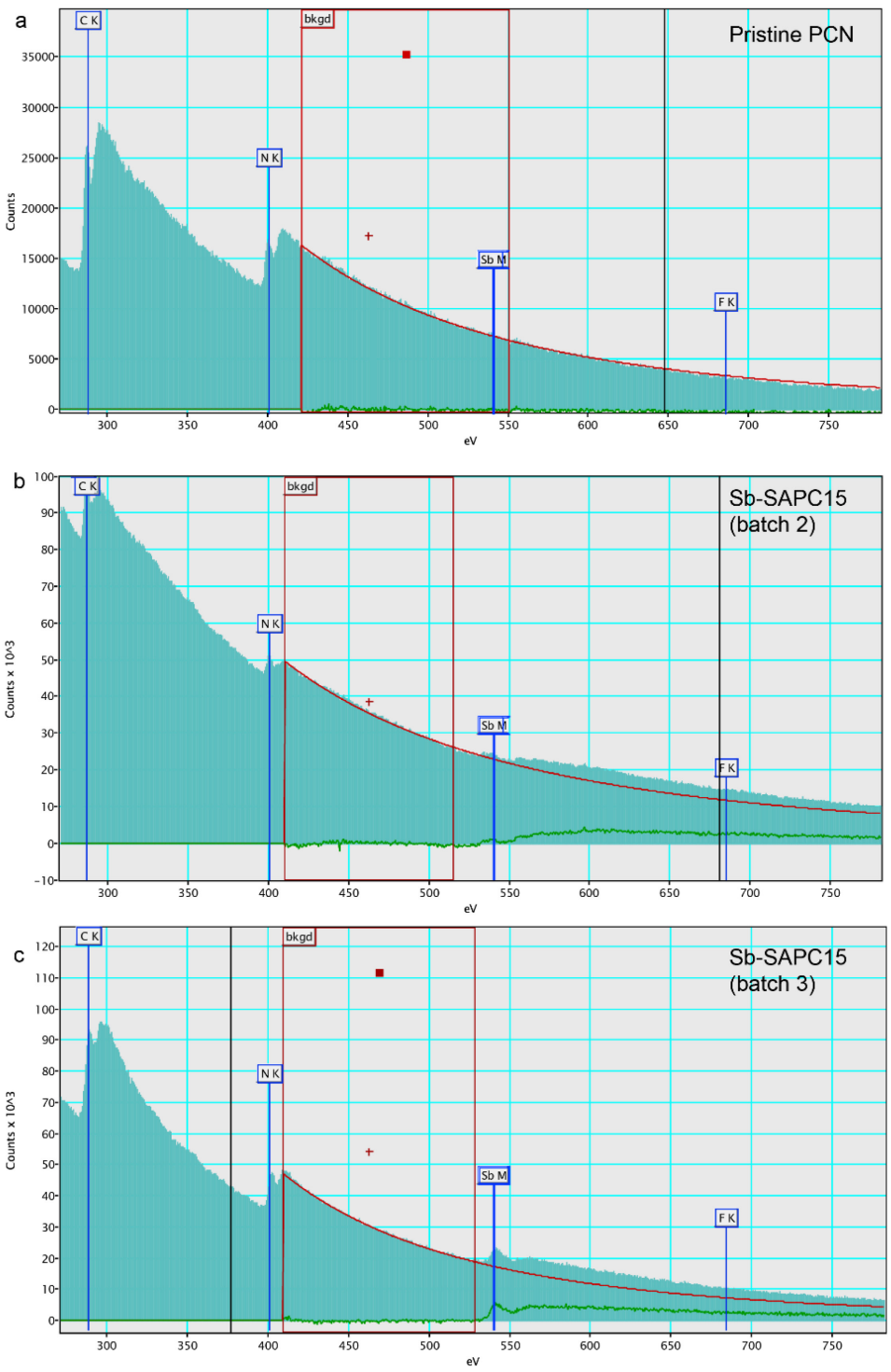

Figure 4-24. EELS spectrum of CN samples. a, pristine PCN. **b**, Sb-SAPC15 (batch 2). **c**, Sb-SAPC15 (batch 3).

Table 4-2. Mass percentage of Sb in Sb-SAPCx.

	Na mass percentage (%)	Substance amount of Na in 1 g catalyst (mmol)	Mass percentage of Sb (%)	Substance amount of Sb in 1 g catalyst (mmol)
PCN	0	0.00	0	0.00
PCN_Na15	2.00	0.87	0	0.00
Sb-SAPC0.5	0.08	0.03	0.63	0.05
Sb-SAPC1	0.16	0.07	0.96	0.08
Sb-SAPC3	0.44	0.19	2.28	0.19
Sb-SAPC5	0.72	0.31	4.31	0.36
Sb-SAPC10	1.18	0.51	7.85	0.65
Sb-SAPC15	1.51	0.66	10.88	0.90
PCN_Na15W*	2.01	0.87	0	0
Sb-SAPC15W*	1.50	0.65	10.85	0.89

* PCN_Na15W and Sb-SAPC15W indicate the samples washed by hot water (90 °C) for another 24 h.

Although we have tried to wash the as-prepared Sb-SAPC15 by hot water (90 °C) for extremely long time (24 hours) in order to remove the alkaline ions in the CN matrix[29]. However, the ICP result showed that the Na content kept almost constant after this treatment. The difficulty of removing Na in PCN by washing could be due to its existence nature. As revealed in the simulations based on DFT (both cluster model and periodic model), sodium tends to bond onto the matrix of g-C_3N_4. However, the introduction of Na into PCN only slightly enhanced its photocatalytic activity.

To investigate the interaction between the isolated Sb atoms and the PCN skeleton, FT-IR and XPS measurements were conducted. The spectrum of PCN, PCN_Na15 and Sb-SAPC15 show no obvious difference in the wavenumber range of 700-900 cm^{-1} and 1200-1600 cm^{-1} (Figure 4-25), indicating that the skeleton of PCN hardly changes before and after incorporation of Na and Sb ions (Table 4-3). All fluoride elements has been removed during the calcination process (Figure 24-25). In the high-resolution C 1s spectrum of pristine PCN (Figure 2c), the typical components at around 287.6 and 284.6 eV can be indexed as the C=N and adventitious carbon, respectively. It is important to note that a new nitrogen peak (N 1s) emerges at 398.1 eV in the spectrum of Sb-SAPC15 (Figure 4-21d), which can be assigned to the chemical bond of Sb-N. The binding energy

of Sb 3d for Sb-SAPC15 (Sb $3d_{3/2}$ at 539.5 eV and Sb $3d_{5/2}$ at 530.2 eV) is close to that for Sb_2O_3 (Sb $3d_{3/2}$ at 539.8 eV and Sb $3d_{5/2}$ at 530.5 eV)[63], indicating that the oxidation state of Sb in Sb-SAPC15 is close to +3 (Figure 2e).

FT-IR (Figure 4-25a) and XPS measurements also revealed the existence of -C≡N groups in both PCN_Na15 and Sb-SAPC15. The interrelationship between -C≡N groups and cations in carbon nitride matrix was investigated. As shown in Figure 4-25a, the absorption band around the wavenumber of 2180 cm^{-1} in the spectrum of PCN_Na15 is slightly stronger than that in the spectrum of Sb-SAPC15, manifesting the larger content of -C≡N groups in PCN_Na15. To investigate the influence of the cation content on the formation of -C≡N groups, ICP measurements were performed. As shown in Table 4-2, the Na amount in PCN_Na15 (0.87 mmol per gram) and Sb-SAPC15 (0.66 mmol per gram) are close, while PCN_Na15 contains no Sb species. Additionally, the ratios of the integration areas from the deconvoluted peaks at 288.1 and 286.5 eV are similar in the high-resolution XPS spectra of PCN_Na15 (0.268) and Sb-SAPC15 (0.228). These results indicate that the introduction of Sb sites into PCN has little influence on the formation of -C≡N groups, and the -C≡N group formation could be possibly due to the incorporation of alkaline metal ions[18,65]. These results are also in accordance with the proposed synthesis mechanism (Scheme 4-1) and the EXAFS fitting results.

Several studies have reported that the -C≡N is an electron-withdrawing group that may significantly enhance the charge separation, and thus improve the photocatalytic activity[18,65]. To clarify the influence of -C≡N groups and Sb species on charge separation and photocatalytic activity, a comprehensive investigation has to be carried out by comparing the photocatalytic performance of Sb-SAPC15 and PCN_Na15. As clarified in the previous paragraph, the Na ion content in Sb-SAPC15 is similar to that in PCN_Na15, giving a similar -C≡N content. But Sb-SAPC15 exhibits a much higher photocatalytic activity (Figure 4-9b), suggesting the crucial function of the Sb species for photocatalysis.

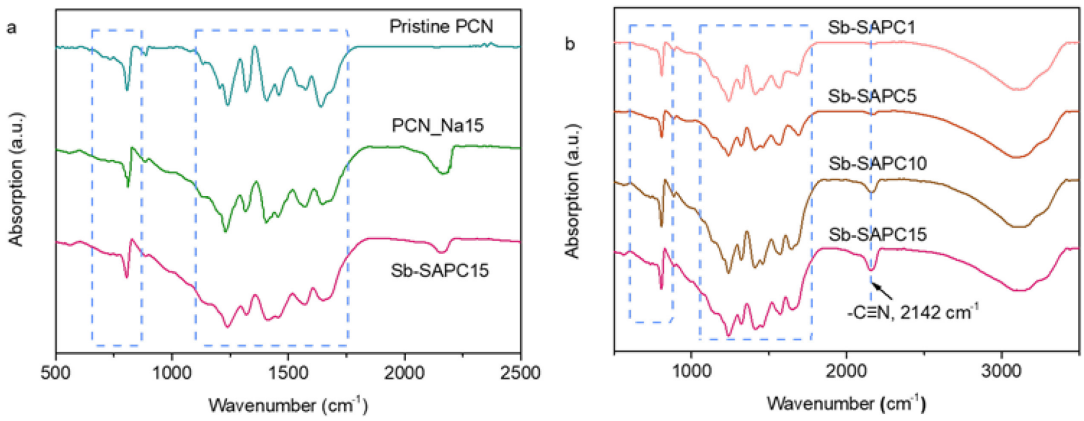

Figure 4-25. FT-IR spectra of PCN samples and Sb-SAPC. a, FT-IR spectra of pristine PCN, PCN_Na15, and Sb-SAPC15. **b**, FT-IR spectra of Sb-SAPC1, Sb-SAPC5, Sb-SAPC10 and Sb-SAPC15.

Table 4-3. Elemental analysis.

Sample name	N %	C %	H %	$Mass_C/Mass_N$
PCN	60.7	33.7	2.01	55.5%
PCN_Na15	57.5	33.1	1.70	57.5%
Sb-SAPC1	59.5	33.1	1.90	55.7%
Sb-SAPC5	56.8	31.7	1.78	55.8%
Sb-SAPC10	54.0	30.3	1.66	56.2%
Sb-SAPC15	49.6	28.5	1.61	57.5%
Sb-SAPC20	45.5	26.9	1.57	59.1%

The oxidation state of the Sb atoms in Sb-SAPC15 was further determined by the position of the absorption edge in the Sb K-edge X-ray absorption near edge structure (XANES) (Figure 4-21f). The absorption edge for Sb-SAPC15 is 2.2 eV higher than that for the Sb^0 foil, and 1.5 eV lower than that for $Sb^{+5}{}_2O_5$, suggesting around +3 valence state of the Sb atoms in Sb-SAPC15. FT-EXAFS spectrum (Figure 4-21g) obtained from k^3-weighted k-space (Figure 4-28) of Sb-SAPC15 shows only one peak at about 1.53 Å, and no Sb-Sb bond at 2.71 Å can be detected, implying that the Sb sites in Sb-SAPC15 are atomically dispersed. The coordination structure of the Sb atoms was estimated by fitting the EXAFS spectrum of Sb-SAPC15 using Artemis (version 0.9.25)[64] (Figure 4-21h, Table 4-4) based on the DFT optimization result of the carbon nitride cluster with single Sb sites (Melem_3Sb3+, Figure 4-29c). The best fitting result for the first shell shows that each Sb atom is coordinated with 3.3 N atoms in average and can be fitted well with the

optimized DFT model (Figure 4-29d), further indicating that the Sb species are atomically dispersed, consistent with the HAADF-STEM results (Figure 4-21a and Figure 4-23).

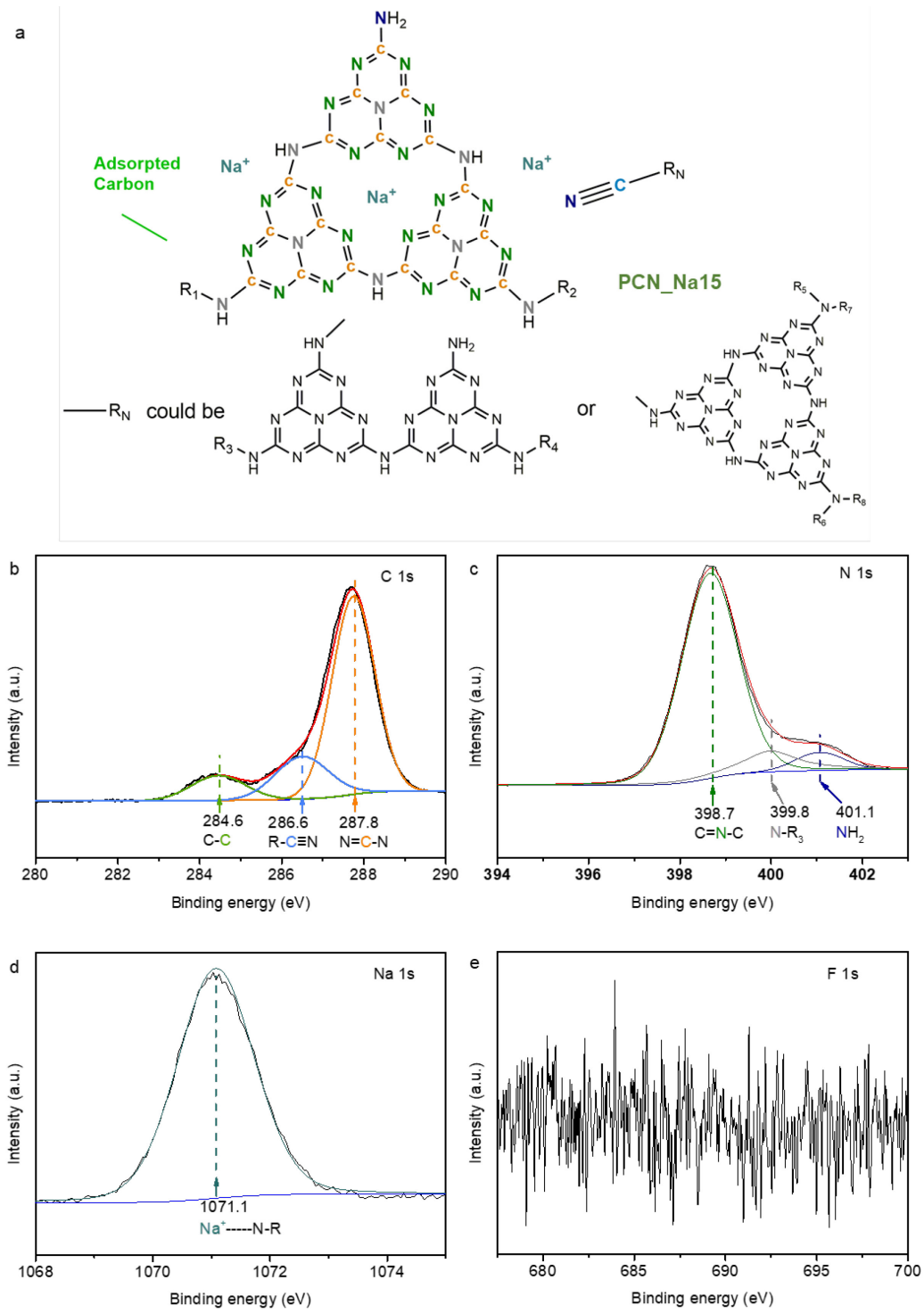

Figure 4-26. Surface chemical states of PCN_Na15. a, Schematic diagram showing the chemical states of elements in PCN_Na15. **b-e**, High-resolution XPS spectra of PCN_Na15: C 1s (**b**); N 1s (**c**); Na 1s (**d**); and F 1s (**e**).

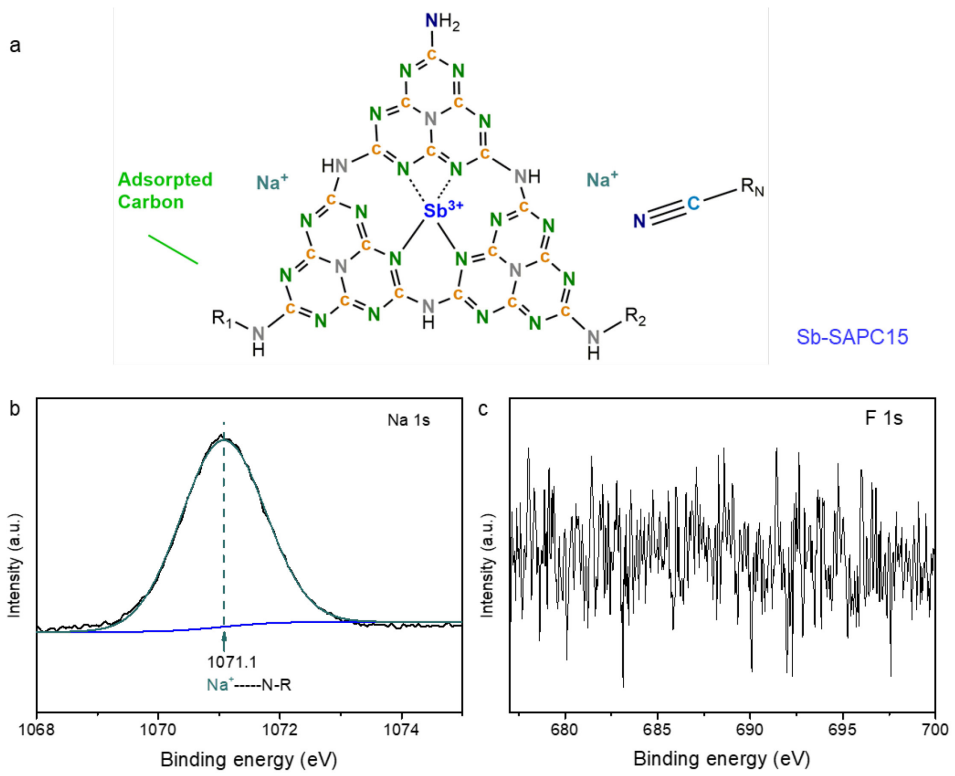

Figure 4-27. Surface chemical states of Sb-SAPC15. a, Schematic diagram showing the chemical states of elements in Sb-SAPC15. **b-c**, High-resolution XPS spectra of Sb-SAPC15: Na 1s (**b**) and F 1s (**c**).

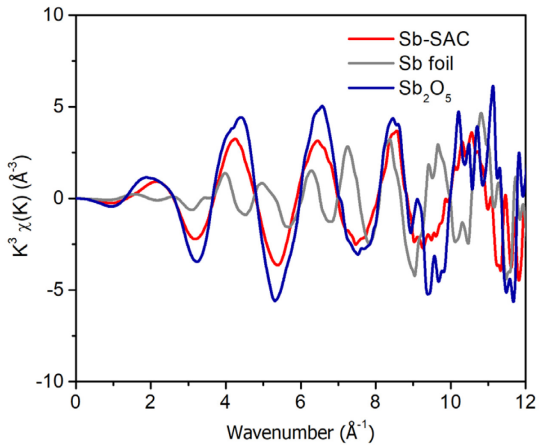

Figure 4-28. Extended X-ray absorption fine structure (EXAFS, k^3-weighted k-space) of Sb-SAPC.

Table 4-4. Fitting parameters of EXAFS data.

Sample	Shell	N	R/Å	ΔE	Debye-Waller factor σ^2 ($Å^2$)	R-factor
Sb_2O_5	Sb-O	4.2±0.20	1.96±0.007	7.85±1.04	0.003±0.001	0.02
Sb-SAPC	Sb-N	3.3±0.20	2.0±0.03	9.74±0.94	0.002±0.0009	0.018

Note: Shell: scattering pathway; N: coordination number; R: bond distance; ΔE: the inner potential correction. The obtained XAFS data was processed in Athena (version 0.9.25) for background, pre-edge line and post-edge line calibrations. The data range adopted for data fitting in k-space and R space are 3–11.5 $Å^{-1}$ and 1-3 Å, respectively.

As shown in Figure 4-29c & d, the sum of occupied π MOs at N12 and N40 strongly interacts with that at Sb54, thus two strong covalent bonds can be formed. Additionally, the sum of occupied π MOs at N27 and N28 also interacts with that at Sb54. The summed electronic intensity between N27 and Sb54 (as well as N28 and Sb54) is slightly weaker that that between N12 and Sb54 (as well as N40 and Sb54), indicating the slightly weaker interaction between N27 and Sb54 (Figure 4-29d). These results further manifest the best fitting result for the first shell that each Sb atom is coordinated with about 3.3 N atoms in average (Figure 4-21h).

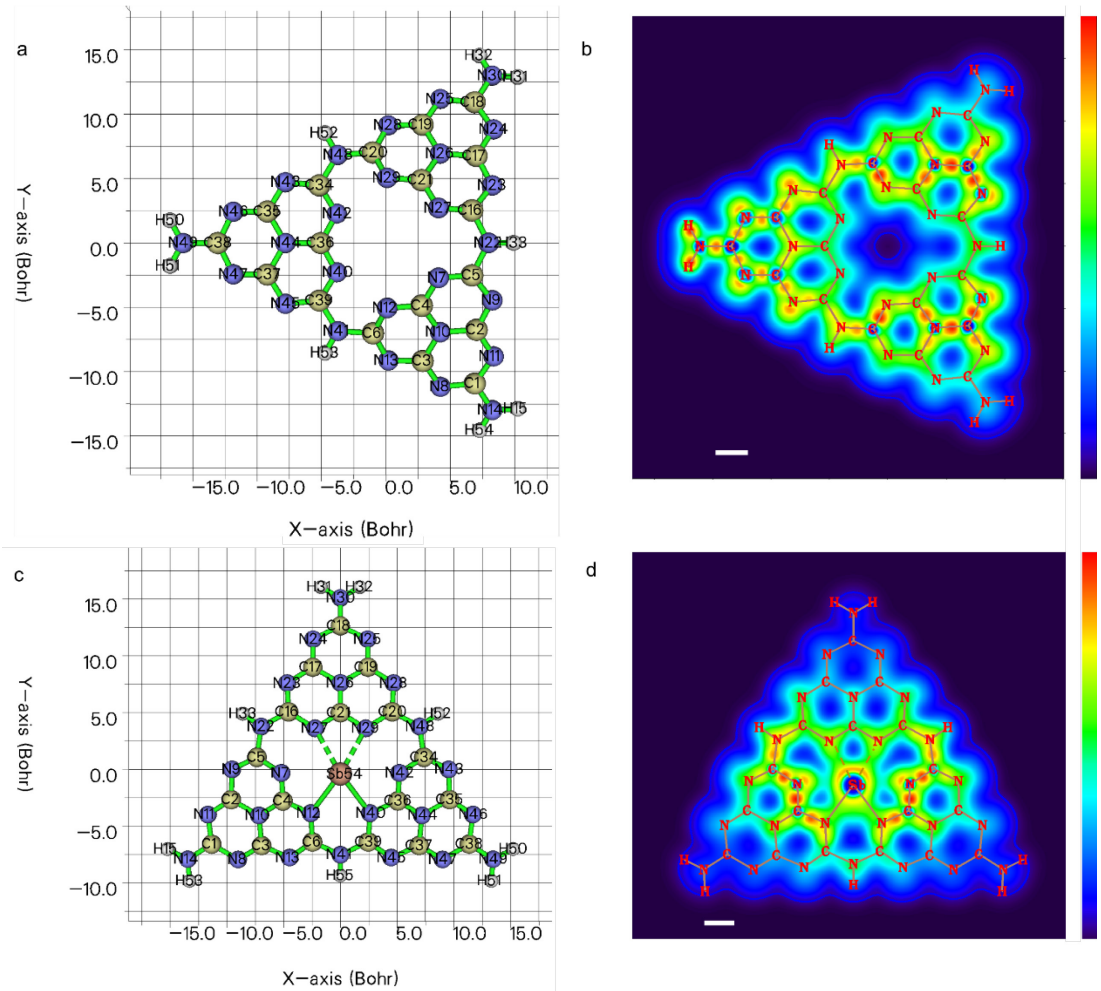

Figure 4-29. Optimized geometry configuration and localized orbital locator of cluster models. a, Optimized geometry configuration and atomic numbers of Melem_3 to represent pristine PCN. **b**, Localized orbital locator calculated based on π MOs of melem_3

(XY plane, Z = 0.45 Bohr). **c**, Optimized geometry configuration and atomic numbers of mlem_3Sb to represent Sb-SAPCs. **d**, Localized orbital locator calculated based on π MOs of melem_3Sb3+ (XY plane, Z = 1.2 Bohr). The dashed bonds refer to the weak interaction between N and Sb atoms. The scale bars in (**b**) and (**d**) are 5 Bohr. The maximum and minimum electronic density in (**b**) and (**d**) are 0.00 and 0.75.

It is noteworthy that post-characterizations of Sb-SAPC15 after continuous reaction for 5 days are almost the same as the fresh one (Figure 4-30), confirming the excellent stability of Sb-SAPC. The HAADF STEM image of Sb-SAPC15 after 5 days of photoreaction shows that the Sb sites remain atomically dispersed (Figure 4-30a). The UV-vis spectra show that the light absorption property of Sb-SAPC15 was hardly influenced by the continuous photoreaction (Figure 4-30b). The XRD pattern indicates that the crystallinity of Sb-SAPC15 hardly changed after 5 days of photoreaction. Note that both diffractions at 13.1° and 27.4° are clearly observable, indicating that the PCN structure in Sb-SAPC15 was well maintained after long-term photoreaction (Figure 4-30c). High-resolution N 1s, C 1s, O 1s and Sb 3d XPS spectra show that the chemical states of N, C, O and Sb on the surface of Sb-SAPC15 were hardly influenced by the long-time photoreaction (Figure 4-30d-f). The surface oxidation of CN and Sb were not observed. All of the above results demonstrate the excellent photocatalytic stability of Sb-SAPC15.

The maximum H_2O_2 concentration after 8 h of photocatalytic reaction is approximately 0.016 wt.% of H_2O_2. Thus to further investigate whether catalyst poisoning occurred on the surface of the catalyst, the photocatalytic activity was measured after soaking the as-prepared Sb-SAPC15 catalyst in different concentrations of H_2O_2 solution (ranging from 0.01 wt.% to 1 wt.%) for 8 h. The photocatalytic activity of Sb-SAPC15 showed no obvious decay after being soaked in different concentrations of H_2O_2 solution for 8 h. This result indicates insignificant catalyst poisoning during our photocatalytic H_2O_2 production process.

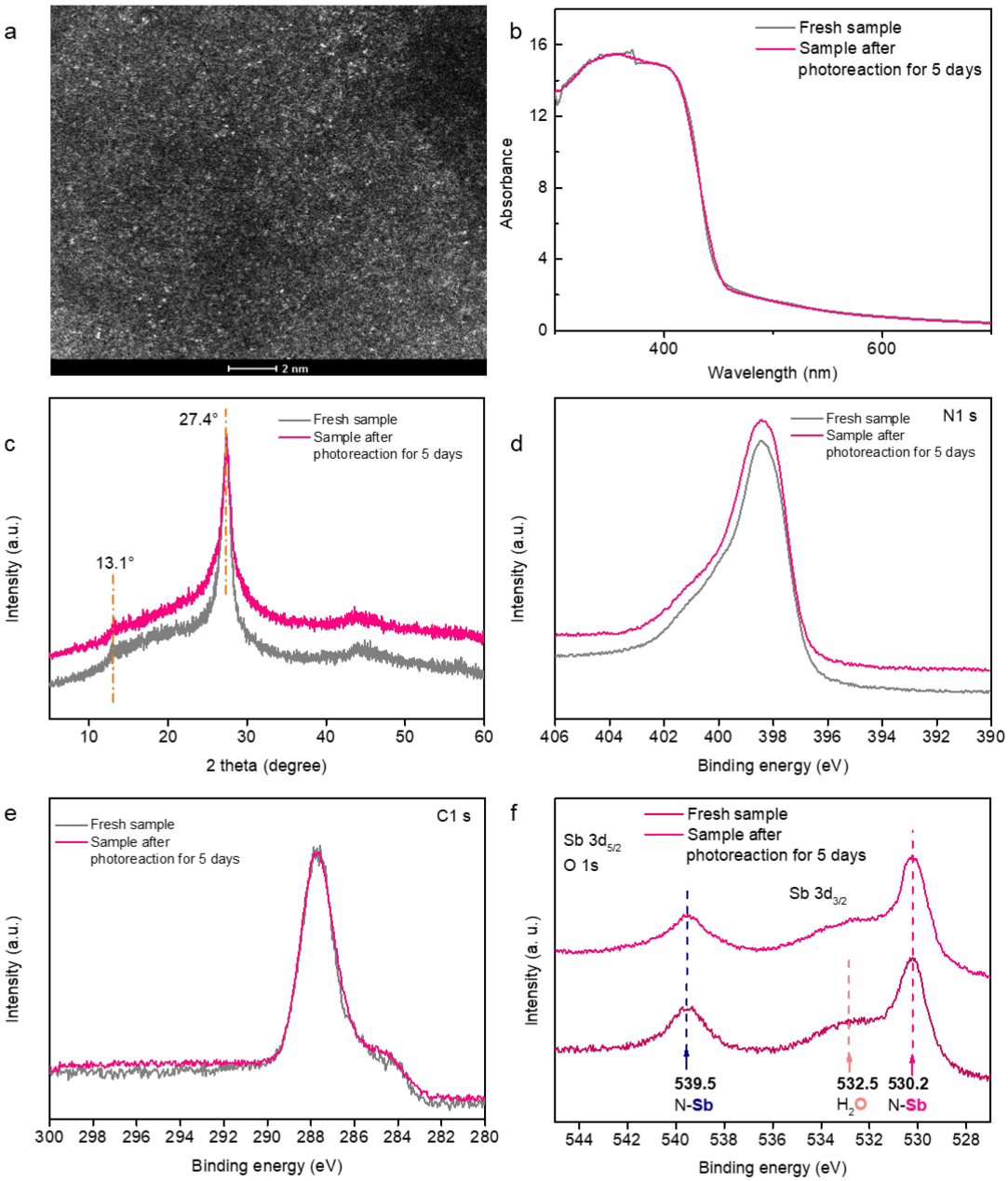

Figure 4-30. Post-characterization of Sb-SAPC15 after photocatalysis. a, HAADF STEM image of Sb-SAPC15 after 5 days of photoreaction. **b-f**, Comparison of as-prepared Sb-SAPC15 and Sb-SAPC15 after 5 days of photoreaction: (**b**) UV-vis spectra; (**c**) XRD pattern; (**d**) high resolution XPS N 1s spectra; (**e**) high resolution XPS C 1s spectra; and (**f**) high resolution XPS O 1s and Sb 3d XPS spectra. After every 8 h of reaction, the reaction solution was exchanged by fresh 0.1 M phosphate buffer solution saturated with O_2. Light intensity: 30.3 W m^{-2} at 420-500 nm.

4.3.3 Photochemical properties of Sb-SAPC and photocatalytic mechanism

4.3.3.1 Optical properties of Sb-SAPC

The optical properties and the band diagram of Sb-SAPC were investigated. The

introduction of Sb and Na species slightly narrowed the bandgap (2.77 eV for PCN and 2.63 eV for Sb-SAPC15) and significantly improved the light absorbance (Figure 1c and Figure 4-31a-b). Confirmed by valence-band XPS and Mott-Schottky measurements, the introduction of Na and/or Sb species slightly shifted the conduction band minimum (CBM) from ~-1.3 eV (vs. SHE) to ~-1.2 eV while rarely influencing the valence band maximum (~1.45 eV). As shown in the insert to Figure 4-31a, Sb-SAPC15 displays a deep yellow color, darker than the pale yellow color of pristine PCN and PCN_Na15. To determine the precise band positions of these samples, UV-vis spectroscopy, Mott-Schottky and valence band XPS measurements were conducted to obtain the bandgap width, CBM and VBM, respectively. As shown in Figure 4-31a-b, the light absorption (λ < 450 nm) of Sb-SAPC15 significantly enhances compared with that of PCN_Na15 and pristine PCN, possibly due to changes in electronic states resulted from Sb incorporation. Tauc plots of pristine PCN, PCN_Na15 and Sb-SAPC15 indicate that the bandgap almost keeps constant after introducing Sb and/or Na ions. VB-XPS results show that the VBM of PCN_Na15 and Sb-SAPC15 keep almost the same (~1.45 eV) to that of PCN (Figure 4-31c). Mott-Schottky plots reveal that the CBM slightly become more positive from pristine PCN to PCN_Na15 and to Sb-SAPC15 (Figure 4-31d-f). By summarizing these results for band positions, we draw the band position diagrams of these samples, as shown in Figure 4-31g.

The action spectra of Sb-SAPC15 (Figure 4-2c) also showed that the apparent quantum yield (ΦAQY) agrees well with the absorption spectrum (Figure 4-31a). The absorption in the wavelength larger than 500 nm of Sb-SAPC15 could not contribute to the production of H_2O_2. These results show that the VB-to-CB excitation of Sb-SAPC15 is responsible for the H_2O_2 production.

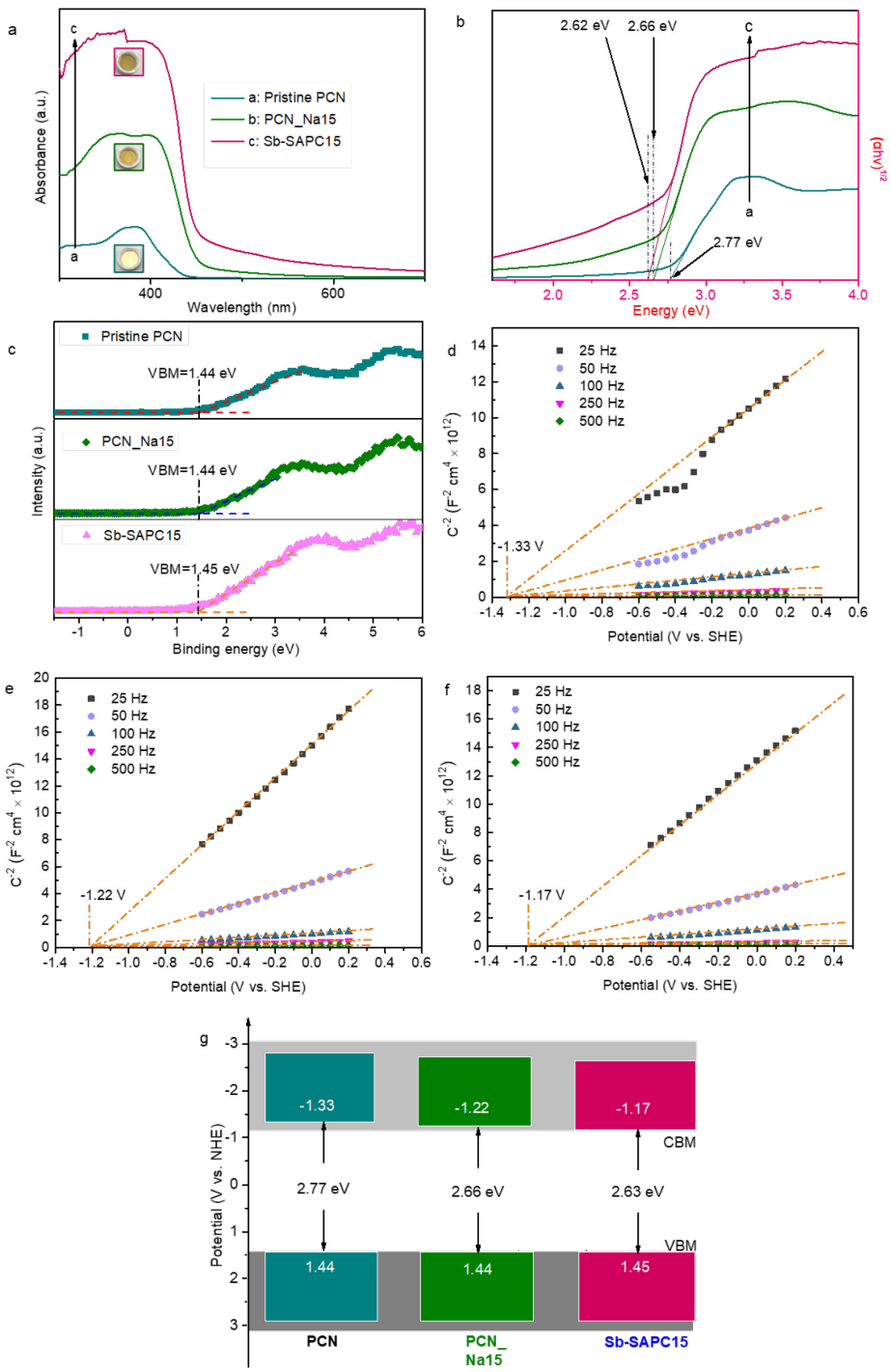

Figure 4-31. Characterization of the CBM and VBM. a, UV-vis diffuse reflection spectra of pristine PCN, PCN_Na15 and Sb-SAPC15. **b**, Tauc plot of pristine PCN, PCN_Na15 and Sb-SAPC15. **c**, Valence-band XPS spectra of pristine PCN, PCN_Na15 and Sb-SAPC15. **d-f**, Mott Schottky plots of (**d**) pristine PCN, (**e**) PCN_Na15 and (**f**) Sb-SAPC15. **g**, Band structure diagrams of PCN, PCN_Na15 and Sb-SAPC15. The Fermi level of the instrument (VB-XPS) is equilibrated at 4.5 eV utilizing Au metal basis as the reference. In this case, the numerical value of the binding energy in the calibrated VB-XPS spectrum is the same as the potential vs. standard hydrogen electrode.

4.3.3.2 Charge separation process of Sb-SAPC

The charge separation and recombination process were monitored by steady-state photoluminescence emission (PL) spectroscopy (Figure 4-32a)[65]. The radiative recombination of excited charge pairs was clearly observed in pristine PCN while the PL intensity was markedly reduced with addition of Sb and/or Na, indicating that the radiative recombination was greatly retarded after addition of Sb and/or Na species. This phenomenon is consistent with the highest photocatalytic activity of Sb-SAPC15. In addition, the onset of PL wavelength gradually red-shifted, which is also consistent with the narrowed bandgap. The facilitated charge migration in Sb-SAPC15 could be further verified by the enhanced photocurrent density (Figure 4-32b) and decreased electrochemical impedance in the Nyquist plots (Figure 4-32c). It is noteworthy that the significantly shortened life-time of PL (Figure 4-32d) could be attributed to the generated deeply trapped sites, which have been proved to facilitate the ORR process[65,66].

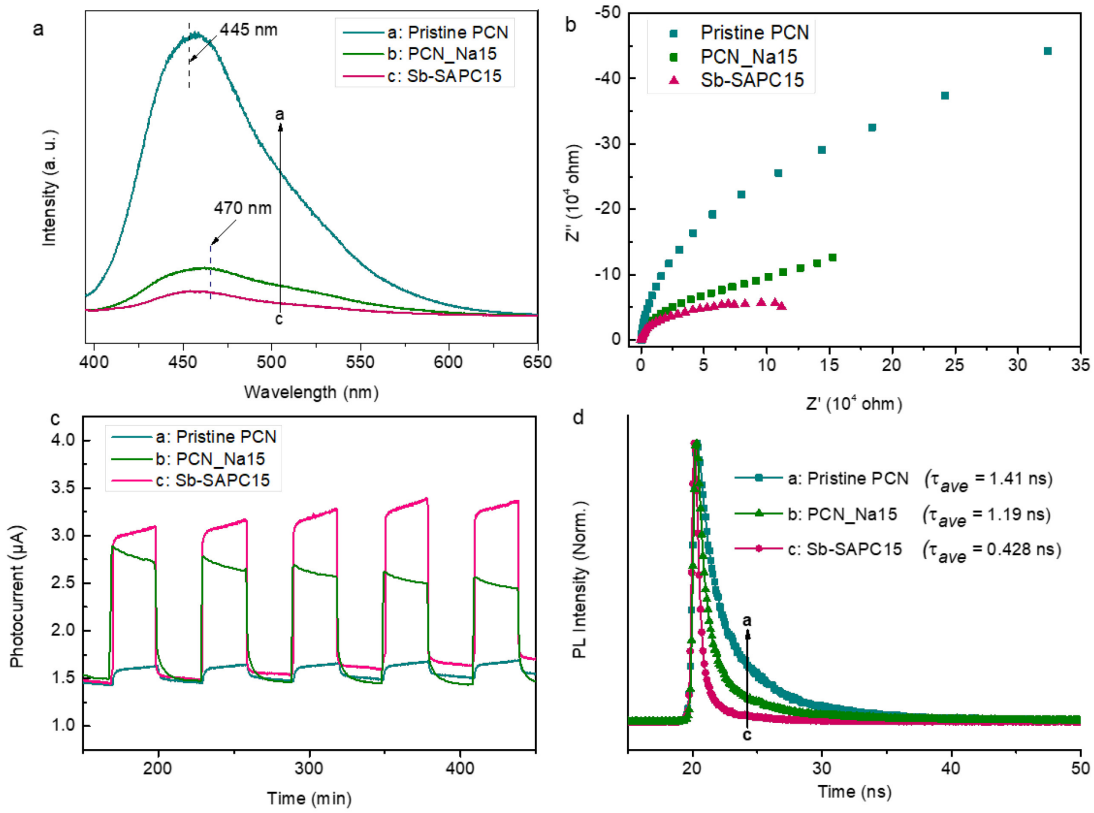

Figure 4-32. Evaluation of charge separation. a, Photoluminescence spectra of PCN, PCN_Na15 and Sb-SAPC15 at an excitation wavelength of 380 nm. **b**, Electrochemical impedance spectroscopy (EIS) spectra (Nyquist plots) of pristine PCN and Sb-SAPC15 in the frequency range from 100 kHz to 0.01 Hz at 0.6 V (vs. Ag/AgCl) under visible light

irradiation. **c**, Comparison of photocurrent response between pristine PCN and Sb-SAPC15 at -0.6 V (vs. Ag/AgCl) under visible light illumination. The light source used in the EIS and photocurrent measurement is a Xe lamp with a UV cut (λ > 420 nm) filter (light intensity at 420−500 nm: 30.3 W m^{-2}). **d**, Time-resolved photoluminescence spectra of pristine PCN, PCN_Na15 and Sb-SAPC15 recorded at 25 °C. The electrolyte used for the EIS and photocurrent measurement is 0.1 M phosphate buffer (pH = 7.4).

To further investigate whether the deeply trapped sites in Sb-SAPC15 could facilitate both ORR and OER, time-resolved infrared absorption (TR-IR) spectroscopy was performed to monitor the charge carrier dynamics in microsecond time-scale[65,67]. To probe the charge transfer dynamics from electron to O_2 and hole to H_2O, the decay kinetics of deeply trapped electrons (at 5000 cm^{-1}) of PCN, PCN_Na15 and Sb-SAPC15 were investigated (Figure 4-33a, Figure 4-34) and compared under N_2, O_2 and H_2O atmosphere (Figure 3-33b). The decay of the deeply trapped electrons at 5000 cm^{-1} on pristine PCN accelerated very slightly (Figure 4-33b) in O_2 as compared to that in N_2 (I_{O2}/I_{N2} = 0.83). The decay on PCN_Na15 showed a little acceleration in O_2 than that in N_2 (I_{O2}/I_{N2} = 0.66), indicating that introduction of Na could generate reactive sites for charge transfer of trapped electrons to O_2[65,67]. When Sb was introduced into the catalyst, we observed significant decay of the deeply trapped electrons on Sb-SAPC15 in O_2 as compared to that in N_2 (I_{O2}/I_{N2} = 0.46). This indicates that the reactant O_2 would preferentially react with the deeply trapped electrons that were induced by the Sb sites. In the case of holes, the decay on pristine PCN and PCN_Na15 changed very little in H_2O environment compared to that in N_2 (I_{H2O}/I_{N2} = 0.86 for PCN and I_{H2O}/I_{N2} = 1.09 for PCN_Na15), indicating that the photogenerated holes barely transferred to H_2O. On the contrary, the decay on Sb-SAPC15 was significantly retarded in H_2O as compared to that in N_2 (I_{H2O}/I_{N2} = 1.92), suggesting that the photogenerated holes could readily transfer to H_2O molecules: hole-consuming reaction by H_2O reduced the number of surviving holes in the catalyst and hence elongated the lifetime of electrons [67]. A clear signal of O_2 reduction to H_2O was detected by the ring disk, verifying O_2 generation on the Sb-SAPC surface via WOR.

Additionally, an isotopic experiment (Figure 4-35) to simulate the real system (without Ag^+ or $NaIO_3$) was conducted to verify the as-proposed mechanism of WOR by utilizing

$^{16}O_2$ (as an electron acceptor) and $H_2{}^{18}O$ (as an electron donor). As shown in Figure 4-35b, the signal of $^{18}O_2$ (m/z = 36) could be detected after photocatalytic reaction for 1 h, indicating that the oxygen evolution reaction indeed occurred in the real reaction system. It is important to note that this signal could not be detected in absence of Sb-SAPC15 or light irradiation, indicating that the photogenerated holes participated in the WOR to generate $^{18}O_2$. With increasing irradiation time, the signal of $^{18}O_2$ (m/z = 36) gradually increased (Figure 4-35c). Additionally, we also investigated the oxygen generation with addition of other electron acceptors (0.1 M Ag^+ or 0.1 M $NaIO_3$). The signal of $^{18}O_2$ (m/z = 36) significantly increased after addition of silver ion or $NaIO_3$ compared to the case with injection of 100 μL $^{16}O_2$ (Figure 4-35d), indicating that both of silver ion and $NaIO_3$ could serve as efficient sacrificial regent for oxygen evolution. To investigate whether the Ag^+ could directly produce oxygen or work as the sacrificial regent, we conducted a control experiment with Ag in solution. As shown in Supplementary Fig. 32e, the signal of $^{18}O_2$ (m/z = 36) could not be detected without the addition of photocatalyst, indicating that pure Ag^+ in the system could not produce O_2, which suggests that the Ag^+ just serves as a sacrificial regent for photocatalytic WOR.

As another effective method for monitoring the photocatalytic OER activity, photoelectrochemical current was recorded on a rotating ring disk electrode (RRDE)[23]. The highly active photo-generated holes for OER could also be confirmed by the boosted anodic polarization curves of RRDE modified by Sb-SAPC15 under visible light irradiation (Figure 4-36). A clear signal of O_2 reduction to H_2O was detected by the ring electrode (Figure 4-36c-d), verifying O_2 generation on the Sb-SAPC surface via photocatalytic WOR. As shown in Figure 4-36a, the disk current of the electrode modified by Sb-SAPC15 is significantly larger than that of the electrode modified by PCN or PCN_Na15, indicating that the rate of the oxidation reaction taking place on the surface of Sb-SAPC15 is faster than that on PCN and PCN_Na15 (Figure 4-36b). More importantly, clear signals of O_2 reduction to H_2O were detected by the ring electrode in both cases of Sb-SAPC15 with or without light irradiation, verifying O_2 generation on the Sb-SAPC15 surface via WOR (Figure 4-36c). Moreover, the ring current of the electrode modified by Sb-SAPC15 under

light irradiation is obviously larger than that in the dark condition, indicating that photo-induced holes indeed facilitated the WOR. Furthermore, the anodic current on the ring electrode under light irradiation appeared much earlier than that in the dark condition, which also manifested that the photogenerated holes participated in the OER (Figure 4-36d). Therefore, the highly active photo-generated holes boosted the OER via the WOR pathway in the Sb-SAPC15 system.

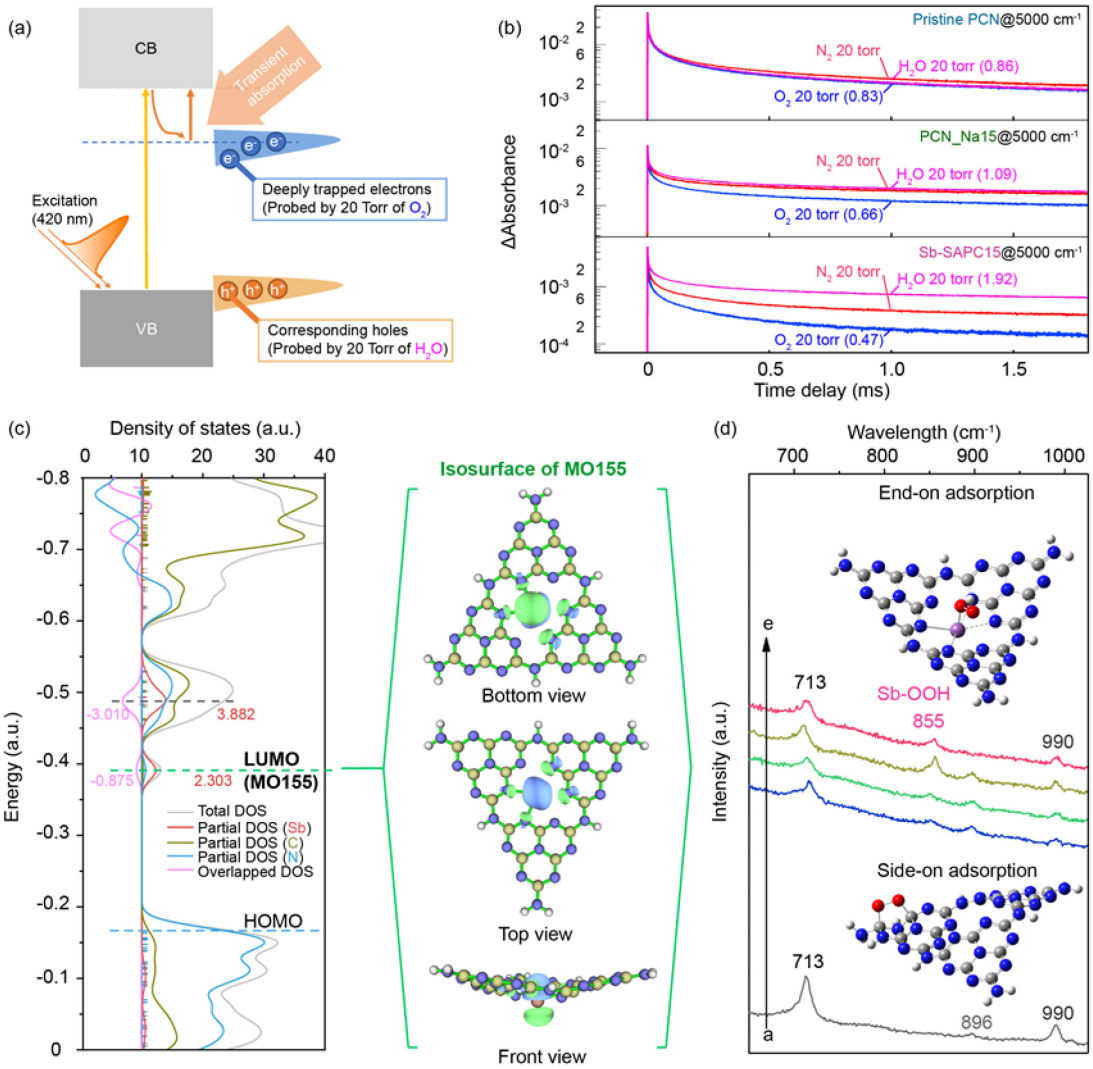

Figure 4-33. Excitation properties and OER/ORR reactivities of Melem_3Sb3+. a, The systematic diagram of transition absorption after excitation as the probe for OER/ORR (details for the pulsed light: 420 nm, 6 ns, 5 mJ and 0.2 Hz). **b**, The comparison of transient absorption decays among PCN, PCN_Na15 and Sb-SAPC15 at 5000 cm^{-1} under N_2, O_2 and H_2O atmosphere (20 Torr). The absorption intensities at the time point of 1 ms was used as the benchmark for investigating how deeply trapped electrons/holes interact with O_2/H_2O. **c**, Total density of states (TDOS), partial density of states (PDOS) and overlapped density of states (ODOS) of Melem_3Sb3+ conbined with the isosurface of LUMO (Isovalue is 0.05). **d**, Experimental Raman spectra recorded during photoreaction in an

ethanol aqueous solution with saturated oxygen. Spectrum a, b, c and d: PCN, Sb-SAPC1, Sb-SAPC5 and Sb-SAPC15 in 10% (v/v) 2-propanol aqueous solution. Spectrum e: Sb-SAPC15 in pure water.

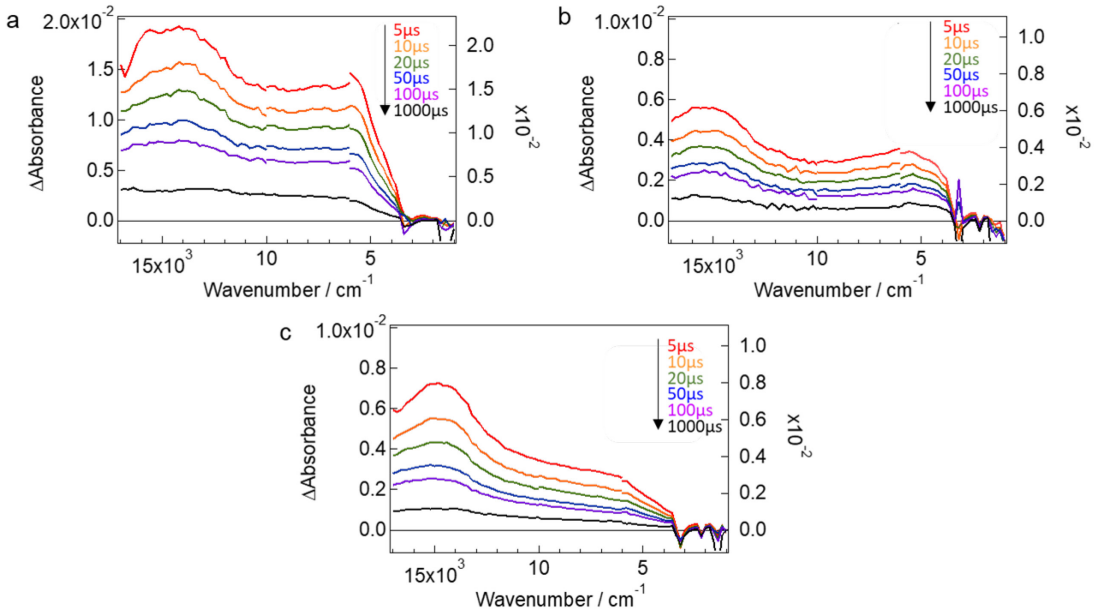

Figure 4-34. Transient infrared red (IR) absorption spectra. a-c, Transient IR absorption spectra for PCN (**a**), PCN_Na15 (**b**) and Sb-SAPC15 (**c**) evolved after 420 nm laser pulse excitation under vacuum (6 ns, 5 mJ, 5 Hz).

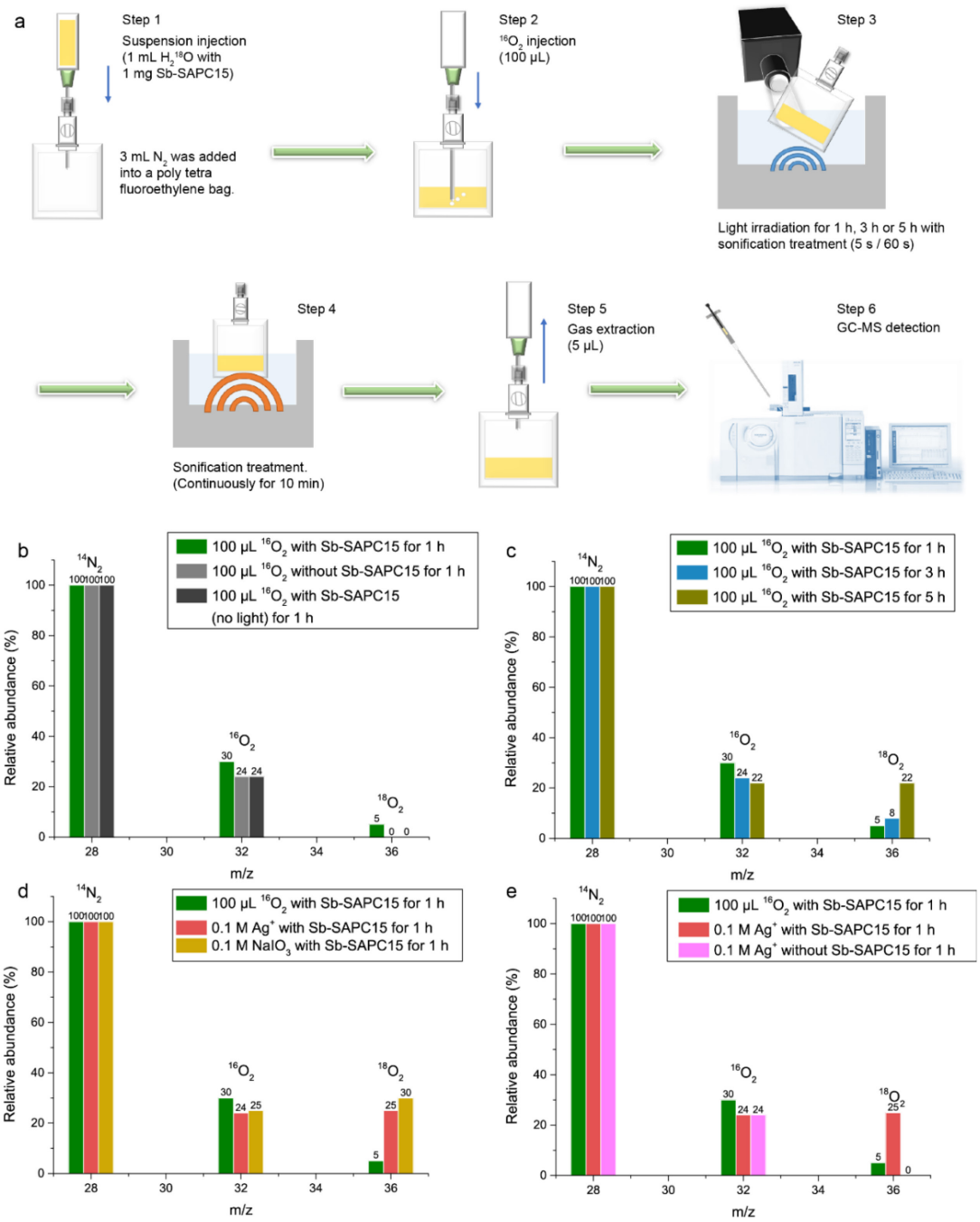

Figure 4-35. Isotopic experiment for the investigating of water oxidation mechanism. **a**, Schematic diagram showing the isotopic experiment for H_2O_2 production with addition of $^{16}O_2$ as the electron acceptor and $H_2{}^{18}O$ as the electron donor. **b**, GC-MS spectra of the gas extracted from the Sb-SAPC15 system with $^{16}O_2$ as the electron acceptor and $H_2{}^{18}O$ as the electron donor. Control experiments without addition of Sb-SAPC15 or without light irradiation were conducted for confirming the photo-induced oxygen generation reaction. **c**, GC-MS spectra of the gas extracted from the Sb-SAPC15 system after Xenon lamp illumination of 1 h, 3 h and 5 h in step 3. **d**, GC-MS spectra of the gas extracted from the Sb-SAPC15 system with different electron acceptors (100 μL O_2, 0.1 M Ag^+ or 0.1 M $NaIO_3$). **e**, GC-MS spectra of the gas extracted from the system with or without addition of Sb-SAPC in condition of adding different electron acceptors (100 μL O_2 or 0.1 M Ag^+).

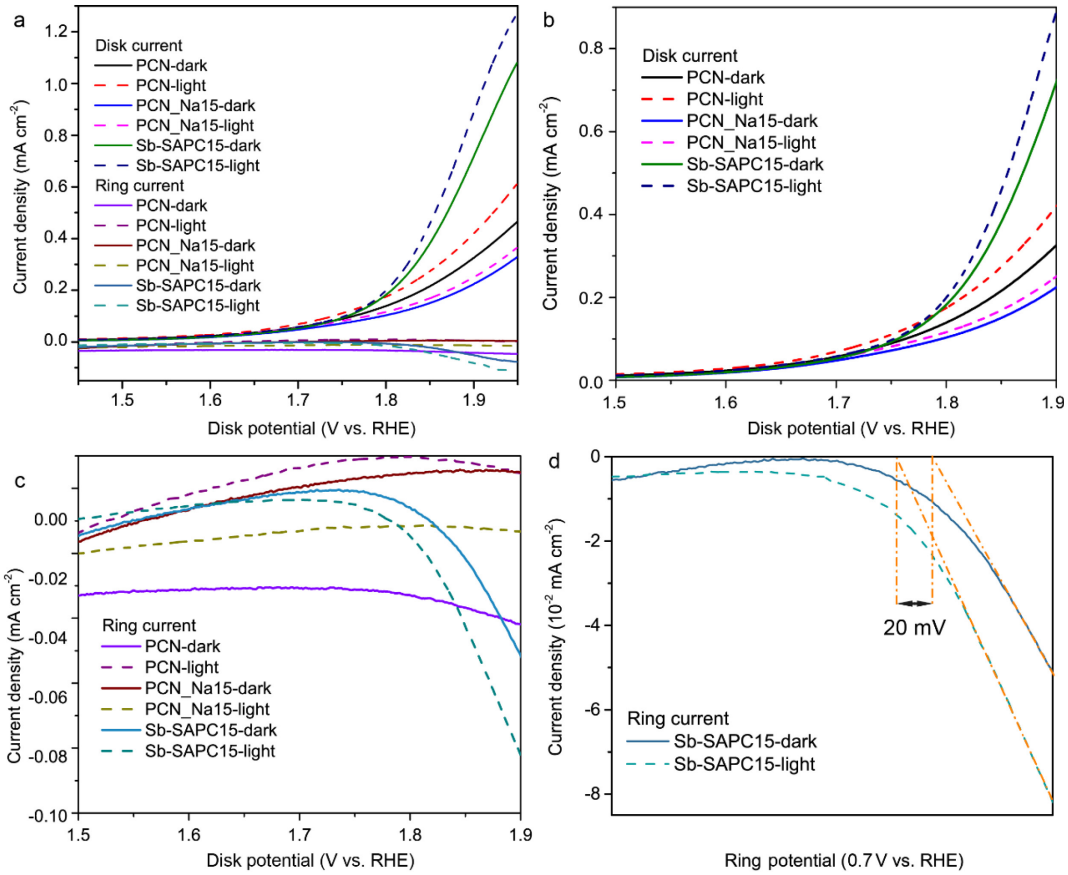

Figure 4-36. The anodic polarization curves of rotating ring disk electrode modified by PCN, PCN_Na15 and Sb-SAPC15 with or without light irradiation. a, Comparison of the anodic polarization curves of the rotating ring disk electrode PCN, PCN_Na15 and Sb-SAPC15 irradiated by light or in the dark condition. **b**, Anodic polarization curves of the rotating disk electrode PCN, PCN_Na15 and Sb-SAPC15 in dark condition or with light irradiation. **c**, Anodic polarization curves of the ring electrode PCN, PCN_Na15 and Sb-SAPC15 with light irradiation or in absence of light. **d**, Enlarged ring current of rotating ring disk electrode modified by Sb-SAPC15. The disk potential was shifted from 1.4 to 1.95 V (vs. RHE), and the potential of the ring was set at 0.7 V (vs. RHE). In this case, the signal of O_2 reduction to H_2O (0.7 V vs. RHE) could be immediately captured by the ring electrode if O_2 was generated by water oxidation reaction. Solution: 0.1 M KOH aqueous solution (pH = 12.9).

4.3.3.3 Simulated inter and inner layer charge transfer of Sb-SAPC.

The density functional theory (DFT) calculation also shows how the Sb and Na species promote the inner and inter layer charge transfer in Sb-SAPC (Figure 4-37 and 4-38). Four periodic models including graphitic carbon nitride (GCN), sodium incorporated graphitic carbon nitride (Na-GCN), antimony incorporated graphitic carbon nitride (Sb-GCN), and sodium and antimony co-incorporated graphitic carbon nitride (NaSb-GCN) were optimized, and the Bader charges of each layer in different models are presented in Figure 4-37[51-

56]. The Bader charge difference between each adjacent layers of pristine GCN is extremely small (|Δq| ~ 0.004 e), suggesting very weak adiabatic coupling between interlayers in GCN. The interlayer charge transfer could be difficult for GCN, which is in accordance to the poor charge separation and migration nature of pristine PCN. Both Na-GCN and Sb-GCN show relatively large number of electrons accumulated on the 2nd and 4th layer (~0.1 e of layer charge). As a result, the Na-GCN and Sb-GCN exhibit a high value of charge difference between the adjacent layers (|Δq| ~ 0.3 e), indicating that the adiabatic coupling has been significantly boosted by introducing Na or Sb. The co-presence of Na and Sb atoms makes the electron distribution more balanced between the layers (Figure 4-37l) [68,69]. In other words, when both Na and Sb are present in the carbon nitride structure, the Na-induced and Sb-induced electron density polarization can be counterbalanced, which lowers the |Δq| (~0.05 e) and at the same time the distance for adiabatic coupling is significantly increased (|Δq| between the 1st and 2nd layer and between the 3rd and 4th layer are significantly increased). This implies that the charge transfer between the interlayers in carbon nitride incorporated with Sb and Na atoms is more facilitated than that in pristine GCN, which may provide an explanation for the higher photocatalytic activities of PCN_Na15 and Sb-SAPC15 [68,69]. The deformation charge density near surface of NaSb-GCN reveals a clear pathway from Na to Sb. The Sb on the surface of GCN with weak interlayer bridging shows a larger number of electron accumulation on the first layer (–0.0395 e of layer charge) than the second layer (0.1345 e of layer charge) [68,69]. The co-presence of Sb and Na atoms induces anisotropic electron density distribution, forming an electron transfer channel from the 2nd layer to the 1st layer (Figure 4-38c). Note that a clear electron accumulation region and an electron depletion region respectively locate at the 1st and 2nd layer while the pristine CN layer (the 3rd layer) can hardly be polarized, indicating that the inner layer charge transfer is significantly improved with incorporation of Sb and Na species [68,69]. These results show that the electron transfer can be significantly promoted by the incorporation of Sb and Na species in GCN, which explains the higher photocatalytic activities of PCN_Na15 and Sb-SAPC15.

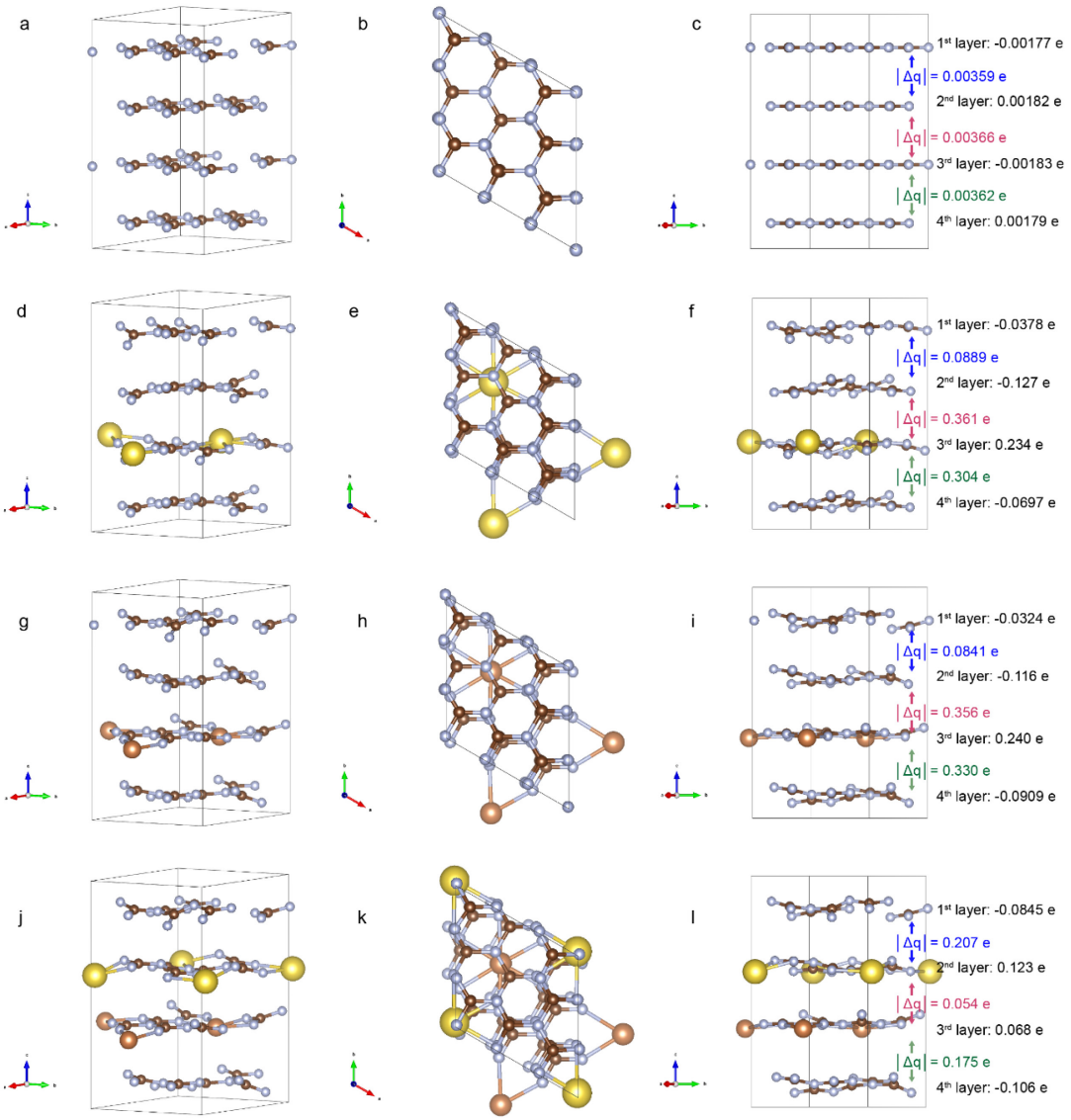

Figure 4-37. Bader Charge distribution analysis from density functional theory (DFT) calculations. a-l, Charge distribution of pristine GCN (**a-c**), Na-GCN (**d-f**), Sb-GCN (**g-i**), and NaSb-GCN (**j-l**). |Δq| represents the absolute value of the difference of the electron distribution between the layers.

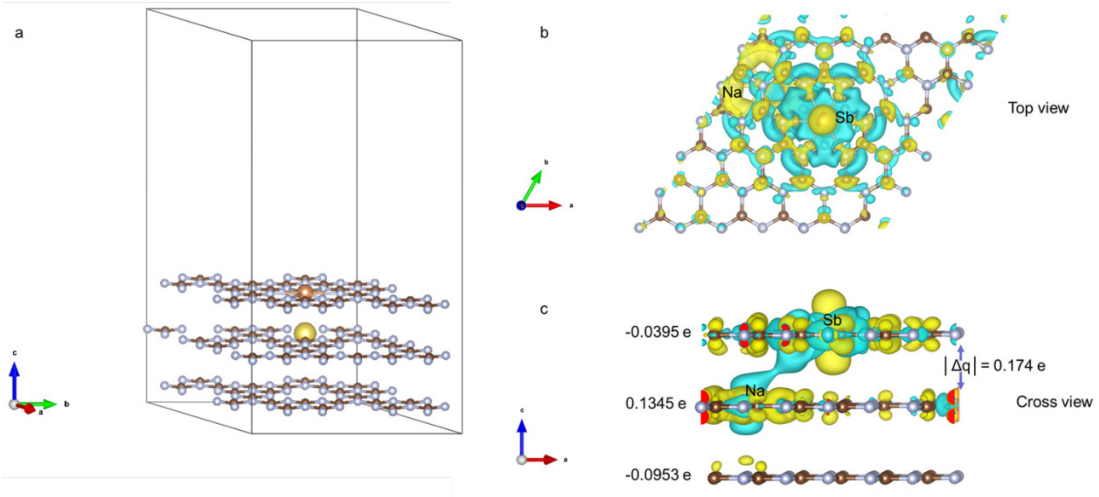

Figure 4-38. Charge distribution analysis near surface of NaSb-GCN from density functional theory (DFT) calculations. a, Optimized near surface crystal structure of NaSb-GCN. **b-c**, Enlarged top view (**b**) and cross view (**c**) of NaSb-GCN. lΔql represents the absolute value of the difference of electron distribution between the first and second layer. Yellow color represents electron accumulation and blue color represents electron depletion.

4.3.3.4 Simulation of the charge separation and charge transfer of H_2O_2

The excited properties of Sb-SAPC were further studied by Time Dependent DFT (TDDFT) to understand the correlation between structure and photocatalytic activity using a mono-layer cluster model[40,41]. The possible simulated excited states (ES) that contributed to photocatalytic H_2O_2 production (corresponding to the spectra from 420 nm to 470 nm) were confirmed by comparing the action spectra (Figure 4-2c) with the simulated ones (Figure 39a-c). Based on the action spectra and the photocatalytic H_2O_2 production activities, the ES1-16 of Melem_3, the ES 1-15 of Melem_3Na+ and the ES 1-26 of Melem_3Sb3+ are highlighted in the distribution heatmap of photogenerated electrons and holes (Figure 4-39d-i)[42]. On the one hand, most of electrons are accumulated at the Sb sites (ES 1-26, Table 4-5), a ligand-to-metal charge transfer from neighboring melem units to Sb, in Melem_3Sb3+ with high density (~20-80%), while most of states (ES 1-16 for Melem_3, Table 4-6; ES 1-15 for Melem_3Na+, Table 4-7) show averagely distributed electrons at the C sites (< 10%) in Melem_3 and Melem_3Na+[40-42]. Note that the photogenerated electrons and holes barely locate at the Na atoms, indicating that the coordinated Na species on the catalyst's surface could not serve as the

active sites for the photocatalytic reaction. The significantly improved separation of electron-hole pairs may effectively promote both photocatalytic ORR and WOR in Sb-SAPC15.

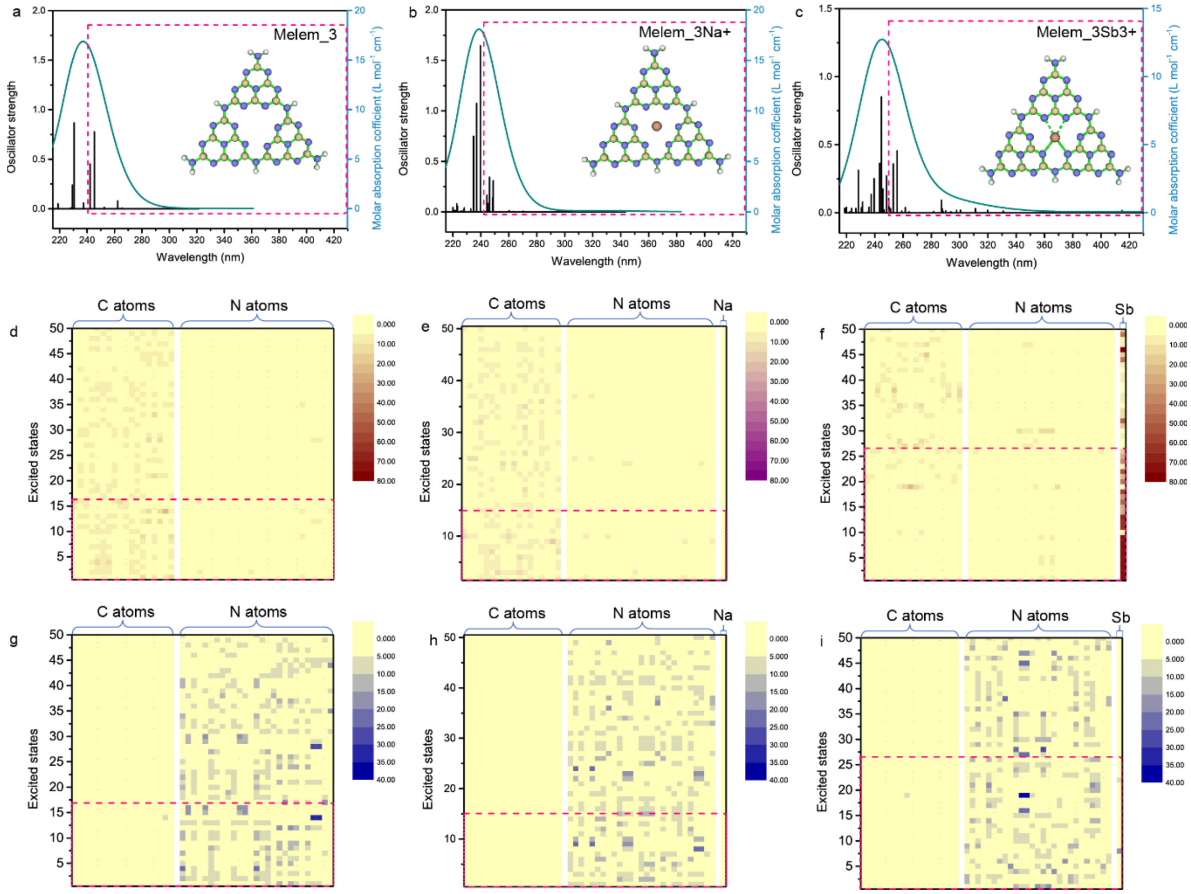

Figure 4-39. Simulated excitation properties of Melem_3, Melem_3Na+ and Melem_3Sb3+. a-c, TDDFT-calculated absorption spectra for (**a**) Melem_3, (**b**) Melem_3Na+ and (**c**) Melem_3Sb3+. **d-i**, The population of electron and hole distribution (vertical excitation at the excited states 1-50). (**d**) Electron distribution and (**g**) hole distribution for Melem_3. (**e**) Electron distribution and (**h**) hole distribution for Melem_3Na+. (**f**) Electron distribution and (**i**) hole distribution for Melem_3Sb3+. The magenta dash circles are the excited states that possibly participate in the photocatalytic H_2O_2 production.

Table 4-5. Excitation properties based on the wavefunctions of Melem_3.

	Molecule obtital contribution (Hole)			Molecule obtital contribution (Electron)				Molecule obtital contribution (Hole)			Molecule obtital contribution (Electron)		
	MO	151	14.071%	MO	154	68.397%		MO	138	16.530%	MO	154	51.954%
S0→S1	MO	152	27.839%	MO	155	14.459%	S0→S9	MO	143	22.826%	MO	155	17.193%
	MO	153	50.968%	MO	157	6.912%		MO	145	9.484%	MO	156	8.394%
	MO	151	28.569%	MO	154	18.080%		MO	137	19.313%	MO	154	29.615%
S0→S2	MO	152	15.441%	MO	155	62.993%	S0→S10	MO	138	11.299%	MO	155	37.942%
	MO	153	48.866%	MO	157	9.812%		MO	150	11.187%	MO	160	7.391%
	MO	151	37.218%	MO	154	37.462%		MO	151	36.625%	MO	154	33.124%
S0→S3	MO	152	37.269%	MO	155	37.027%	S0→S11	MO	152	15.992%	MO	155	14.635%
	MO	153	17.695%	MO	157	13.292%		MO	153	26.999%	MO	156	27.816%
	MO	150	47.527%	MO	154	20.177%		MO	151	3.065%	MO	155	34.473%
S0→S4	MO	151	8.132%	MO	155	57.173%	S0→S12	MO	152	34.192%	MO	156	33.596%
	MO	152	9.408%	MO	156	11.088%		MO	153	35.353%	MO	162	11.681%
	MO	146	16.036%	MO	154	39.300%		MO	151	26.303%	MO	154	23.953%
S0→S5	MO	149	15.260%	MO	155	32.108%	S0→S13	MO	152	7.807%	MO	155	18.083%
	MO	150	20.259%	MO	156	10.911%		MO	153	40.502%	MO	156	36.970%
	MO	146	7.248%	MO	154	44.219%		MO	138	22.850%	MO	154	44.924%
S0→S6	MO	148	33.220%	MO	155	23.903%	S0→S14	MO	141	33.109%	MO	157	12.639%
	MO	149	13.611%	MO	157	7.874%		MO	142	18.279%	MO	158	29.103%
	MO	136	13.136%	MO	154	37.571%		MO	140	22.905%	MO	154	16.970%
S0→S7	MO	143	6.749%	MO	155	28.780%	S0→S15	MO	142	26.607%	MO	155	33.323%
	MO	150	30.250%	MO	160	7.516%		MO	152	8.676%	MO	157	21.247%
	MO	136	13.859%	MO	154	40.885%		MO	140	33.930%	MO	155	33.086%
S0→S8	MO	137	17.967%	MO	155	29.284%	S0→S16	MO	141	24.611%	MO	157	28.433%
	MO	138	10.097%	MO	160	9.744%		MO	142	6.556%	MO	159	15.597%

Table 4-6. Excitation properties based on the wavefunctions of Melem_3Na+.

	Molecule obtital contribution (Hole)			Molecule obtital contribution (Electron)				Molecule obtital contribution (Hole)			Molecule obtital contribution (Electron)		
	MO	156	16.370%	MO	159	50.714%		MO	150	16.143%	MO	159	32.219%
S0→S1	MO	157	28.906%	MO	160	28.431%	S0→S9	MO	151	14.245%	MO	160	18.088%
	MO	158	47.236%	MO	165	9.882%		MO	152	23.079%	MO	162	16.494%
	MO	156	28.665%	MO	159	28.572%		MO	150	17.206%	MO	159	24.905%
S0→S2	MO	157	16.793%	MO	160	50.573%	S0→S10	MO	151	17.064%	MO	160	22.652%
	MO	158	47.059%	MO	165	9.935%		MO	152	15.489%	MO	165	17.995%
	MO	156	38.540%	MO	159	36.710%		MO	151	19.316%	MO	154	33.124%
S0→S3	MO	157	37.923%	MO	160	37.005%	S0→S11	MO	152	19.447%	MO	155	33.136%
	MO	158	16.787%	MO	165	13.014%		MO	153	8.630%	MO	156	14.383%
	MO	147	15.135%	MO	159	37.061%		MO	143	9.834%	MO	159	28.788%
S0→S4	MO	148	15.314%	MO	160	37.519%	S0→S12	MO	157	18.907%	MO	160	27.355%
	MO	151	8.723%	MO	161	13.147%		MO	158	10.371%	MO	161	18.108%
	MO	148	13.833%	MO	159	24.221%		MO	142	9.828%	MO	159	27.347%
S0→S5	MO	149	20.893%	MO	160	48.620%	S0→S13	MO	156	18.948%	MO	160	28.782%
	MO	152	12.584%	MO	161	10.043%		MO	158	10.349%	MO	161	18.116%
	MO	147	14.340%	MO	159	49.006%		MO	141	10.630%	MO	159	28.119%
S0→S6	MO	149	20.718%	MO	160	23.845%	S0→S14	MO	141	18.961%	MO	160	28.836%
	MO	152	12.348%	MO	161	10.014%		MO	142	16.524%	MO	161	16.263%
	MO	145	15.746%	MO	159	28.623%		MO	141	10.658%	MO	159	28.819%
S0→S7	MO	146	15.655%	MO	160	28.829%	S0→S15	MO	156	18.931%	MO	160	28.102%
	MO	158	15.053%	MO	162	10.142%		MO	158	16.474%	MO	161	16.249%
	MO	150	14.208%	MO	159	16.990%							
S0→S8	MO	151	15.924%	MO	160	33.282%							
	MO	152	23.405%	MO	162	16.511%							

Table 4-7. Excitation properties based on the wavefunctions of Melem_3Sb3+.

	Molecule obtital contribution (Hole)			Molecule obtital contribution (Electron)				Molecule obtital contribution (Hole)			Molecule obtital contribution (Electron)		
	MO	149	3.633%	MO	155	**99.112%**		MO	146	37.096%	MO	155	**40.942%**
S0→S1	MO	151	65.610%				S0→S14	MO	153	11.569%	MO	156	27.918%
	MO	154	19.339%					MO	154	11.569%	MO	157	10.666%
	MO	149	17.637%	MO	155	**98.594%**		MO	141	11.460%	MO	155	**37.232%**
S0→S2	MO	151	13.214%				S0→S15	MO	151	23.242%	MO	156	20.075%
	MO	154	50.549%					MO	154	12.858%	MO	157	27.434%
	MO	150	12.440%	MO	155	**98.773%**		MO	147	10.948%	MO	155	**64.773%**
S0→S3	MO	152	17.901%				S0→S16	MO	148	37.814%	MO	156	6.228%
	MO	153	54.845%					MO	151	13.782%	MO	157	17.977%
	MO	144	7.421%	MO	155	**99.225%**		MO	146	20.726%	MO	155	**44.139%**
S0→S4	MO	150	32.476%				S0→S17	MO	151	11.805%	MO	156	27.976%
	MO	153	36.790%					MO	153	11.062%	MO	157	10.670%
	MO	141	32.952%	MO	155	**98.441%**		MO	141	18.967%	MO	155	**77.536%**
S0→S5	MO	145	32.842%				S0→S18	MO	142	35.504%	MO	156	5.924%
	MO	154	22.604%					MO	147	20.012%	MO	157	4.105%
	MO	143	12.371%	MO	155	**98.625%**		MO	147	10.237%	MO	157	55.007%
S0→S6	MO	150	11.062%				S0→S19	MO	148	83.253%	MO	163	5.986%
	MO	152	61.864%								MO	164	20.416%
	MO	141	9.700%	MO	155	**95.897%**		MO	139	14.951%	MO	155	**49.783%**
S0→S7	MO	145	31.267%				S0→S20	MO	146	25.432%	MO	156	20.017%
	MO	149	34.516%					MO	147	23.178%	MO	157	6.417%
	MO	139	7.962%	MO	155	**97.100%**		MO	146	36.714%	MO	155	**21.729%**
S0→S8	MO	143	23.509%				S0→S21	MO	147	41.974%	MO	156	31.893%
	MO	144	49.833%					MO	148	4.249%	MO	157	14.042%
	MO	143	37.403%	MO	155	**98.014%**		MO	139	16.928%	MO	155	**64.457%**
S0→S9	MO	144	28.745%				S0→S22	MO	140	24.402%	MO	156	15.844%
	MO	150	14.566%					MO	146	21.073%	MO	157	5.920%
	MO	152	9.902%	MO	155	8.267%		MO	145	19.544%	MO	155	**29.565%**
S0→S10	MO	153	22.497%	MO	156	26.006%	S0→S23	MO	151	8.865%	MO	156	28.095%
	MO	154	42.826%	MO	157	43.742%		MO	152	16.424%	MO	157	11.023%
	MO	145	12.654%	MO	155	**86.894%**		MO	138	38.207%	MO	155	**47.750%**
S0→S11	MO	148	41.191%	MO	156	4.160%	S0→S24	MO	153	8.226%	MO	156	12.316%
	MO	149	16.773%	MO	157	2.632%		MO	154	8.707%	MO	157	17.450%
	MO	142	38.982%	MO	155	**84.579%**		MO	146	21.944%	MO	155	**19.032%**
S0→S12	MO	146	6.215%	MO	156	5.009%	S0→S25	MO	147	24.951%	MO	156	12.536%
	MO	147	43.746%	MO	162	2.747%		MO	148	15.529%	MO	157	27.791%
	MO	139	20.544%	MO	155	**87.222%**		MO	137	21.180%	MO	155	**22.031%**
S0→S13	MO	140	27.510%	MO	156	4.259%	S0→S26	MO	146	35.194%	MO	158	20.115%
	MO	146	19.057%	MO	157	2.552%		MO	147	22.580%	MO	165	14.447%

It is noteworthy that the absorption edge of simulated UV spectra as well as computed optical gaps are usually larger than the experimental band gaps because of the following two reasons: (1) To simulate the charge-transfer properties of the model with high qualities, function of ω97xd, a function including large amount of Hartree–Fock exchange, was used. These exchange functions usually overestimate the excitation energies, as well as the simulated HOMO-LUMO gap; (2) In the solid state, p-conjugated molecules adjacent to the one carrying a charge strongly polarize, an effect that stabilizes the cationic and anionic states (each generally by about one eV in p-conjugated materials). In this case, the band gap is typically considerably smaller in energy than the molecular fundamental gap, as well as the optical gap[6]. Since the system error cannot be eliminated, the possible simulated ES that contributed to H_2O_2 production (corresponding to the spectra from 420 nm – 470 nm) were confirmed by comparing the experimental spectra and simulated ones. Then, the transition density of electron/holes was considered at all these ES.

The influence of Sb single atoms on the photo-redox reactions was further studied by analyzing the contributions of MOs to holes and electrons from ES1 to ES26 of Melem_3Sb3+ (Table 4-5). Several MOs with energetic levels equal to or lower than HOMO all contribute to holes (ranging from 0% to ~60%), while almost of electrons are contributed by LUMO (MO155) in most of transitions. This observation implies that the electronic configuration of LUMO can almost represent the photogenerated electronic configuration. The result from partial DOS (PDOS) of Melem_3Sb3+ shows that a new molecular orbital (MO) mainly contributed by electrons from Sb forms the LUMO. It is important to note that this MO exhibits a slightly lower energetic level than the MO contributed by C and N, which is in accordance with the slightly shifted CBM of Sb-SAPC15. Combined with the simulated results of charge separation, iso-surface of LUMO of Melem_3Sb3+ reveals that most of the electrons (>75%) are concentrated at the single Sb sites with ideal electronic configuration for adsorption of electrophilic oxygen (Figure 4-33c).

To give representative data for the assessment of charge separation, the boundary effect of above small cluster models (i.e., Melem_3) confined the distance of possible separated charges. To give a comprehensive assessment of charge separation by TDDFT

simulation, we have accessed to a supercomputer, and built larger models to represent pristine PCN (Melem_6), sodium incorporated PCN (Melem_6Na+) and single atomic Sb incorporated PCN (Melem_6Sb3+) to simulate the properties of charge separation. The systematic diagram of Melem_3 and Melem_6 models are presented in Figure 4-40.

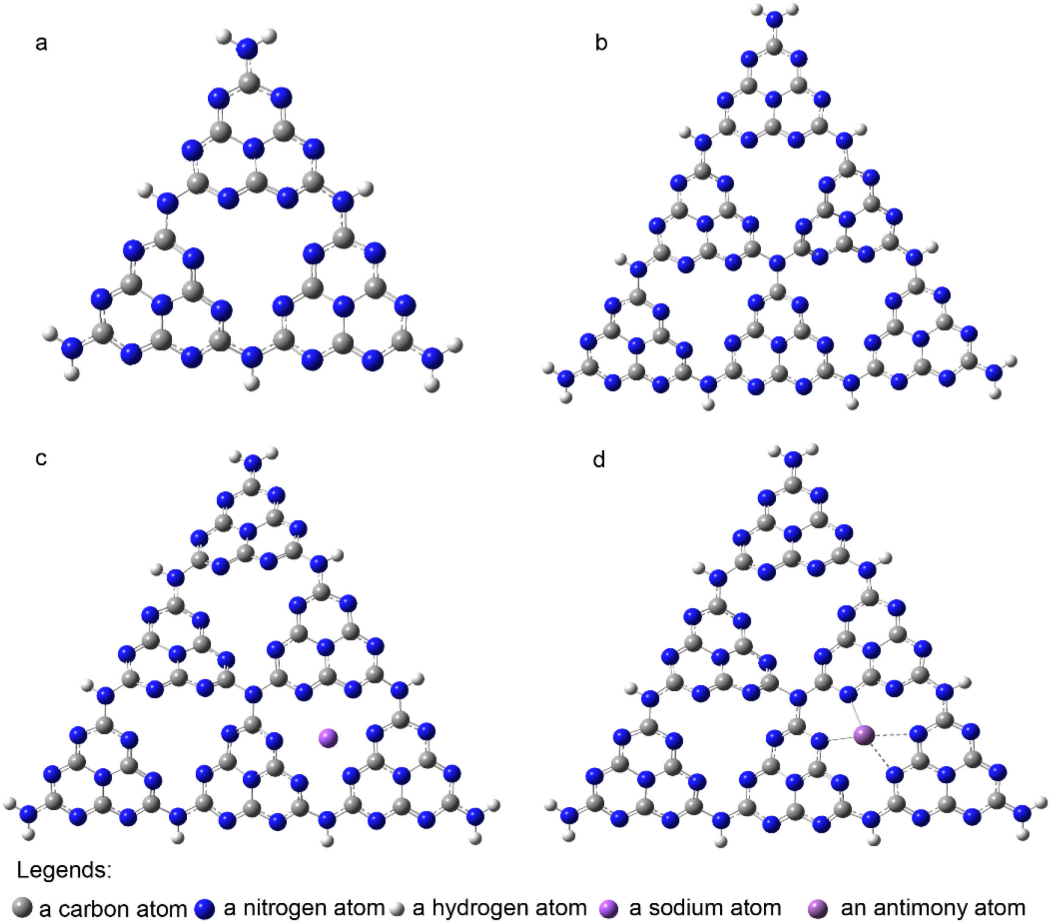

Figure 4-40. Cluster models for investigating charge separation properties. a, A cluster model for presenting Melem_3. **b**, Melem_6 for representing PCN. **c,** Melem_6Na+ for presenting sodium ion incorporated PCN. **d**, Melem_6Sb3+ for representing single atomic Sb incorporated PCN.

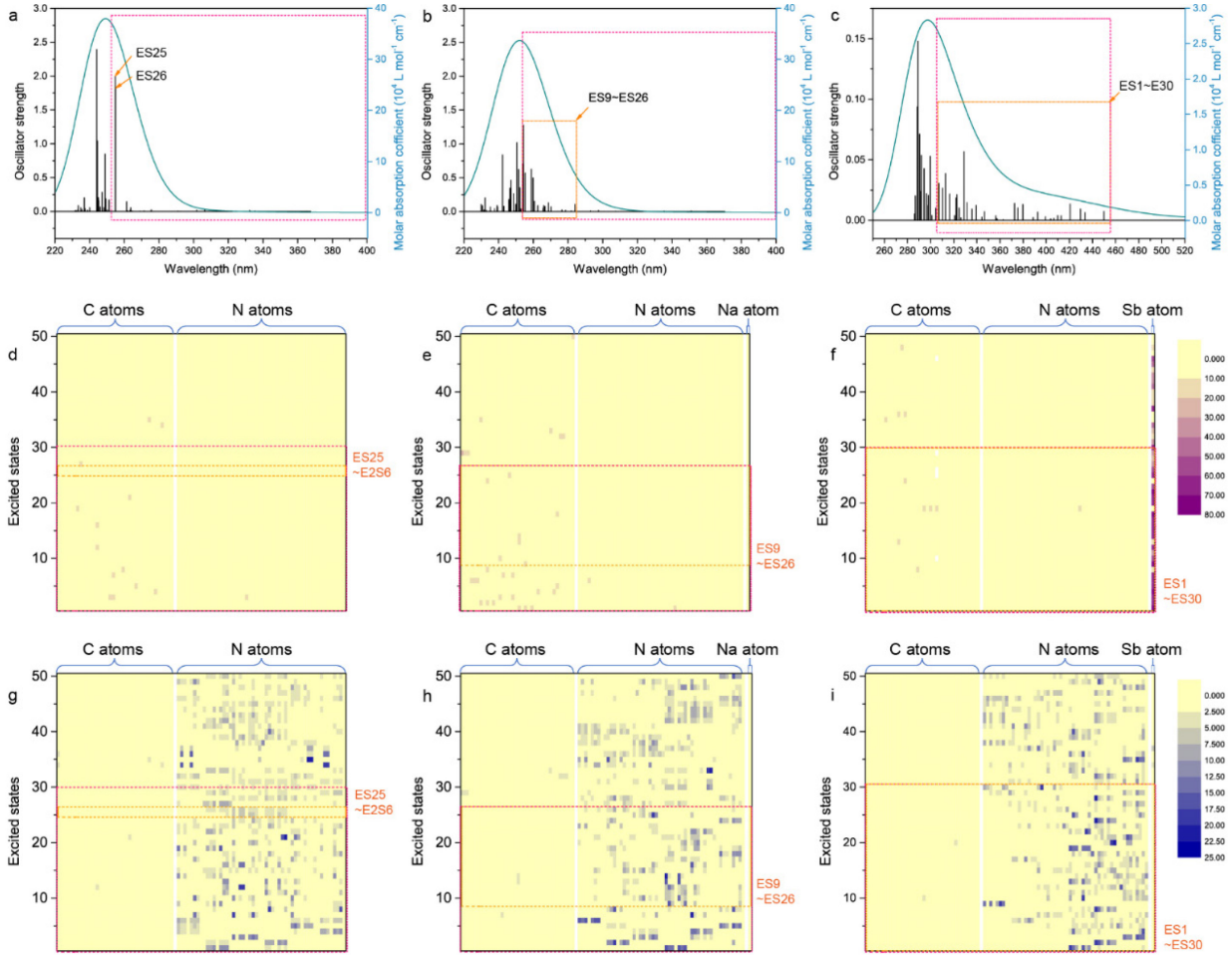

Figure 4-41. Simulated excitation properties of Melem_6, Melem_6Na+ and Melem_6Sb3+. a-c, TDDFT-calculated absorption spectra for (**a**) Melem_6, (**b**) Melem_6Na+ and (**c**) Melem_6Sb3+. **d-i**, The population of electron and hole distribution (vertical excitation at the excited states 1-50). (**d**) Electron distribution and (**g**) hole distribution for Melem_6. (**e**) Electron distribution and (**h**) hole distribution for Melem_6Na+. (**f**) Electron distribution and (**i**) hole distribution for Melem_6Sb3+. The magenta dash circles are the excited states that possibly participate in the photocatalytic H_2O_2 production. The orange dash circles represent the most important transitions that contribute the most for the spectra for photocatalytic H_2O_2 production.

Based on the action spectra and the photocatalytic H_2O_2 production activities, the ES 1-26 of Melem_6, the ES 1-26 of Melem_6Na+ and the ES 1-30 of Melem_6Sb3+ are highlighted in the distribution heatmap of photogenerated electrons and holes (Figure 4-41d-i). It is confirm that most of the electrons are accumulated at the Sb sites (ES 1-30, Melem_6Sb3+), a ligand-to-metal charge transfer from neighboring melem units to Sb, while most of the states (ES 1-26 for Melem_6 and Melem_6Na+) show averagely distributed electrons at the C sites. The photogenerated electrons and holes barely locate

at the Na atoms, indicating that the coordinated Na species on the catalyst's surface unlikely serve as the active sites for the photocatalytic reaction. The above results from Melem_6, Melem_6Na+ and Melem_6Sb3+ give almost the same electronic configurations as the results from Melem_3, Melem_3Na+ and Melem_3Sb3+.

To investigate the properties of charge separation in these three models, the most important transitions that can participate in the photocatalytic H_2O_2 production were figured out by checking the osillator strength of each transiton in the UV spectra (as shown in the orange dash circles; i. e., the transitions of ES25 and ES26 of Melem_6, ES9~ES26 of Melem_6Na+ and ES1~ES30 of Melem_6Sb3+). We then caluculated the distance between centroid of hole and electron (D index) in these transitions. This D index was defined followed by the Manual of the Multiwfn, which could reveal whether charge separation of photogenerated electron hole pair is efficient. The D index of the transitions of ES25 and ES26 of Melem_6, ES9~ES26 of Melem_6Na+ and ES1~ES30 of Melem_6Sb3+ are presented in Figure 4-42:

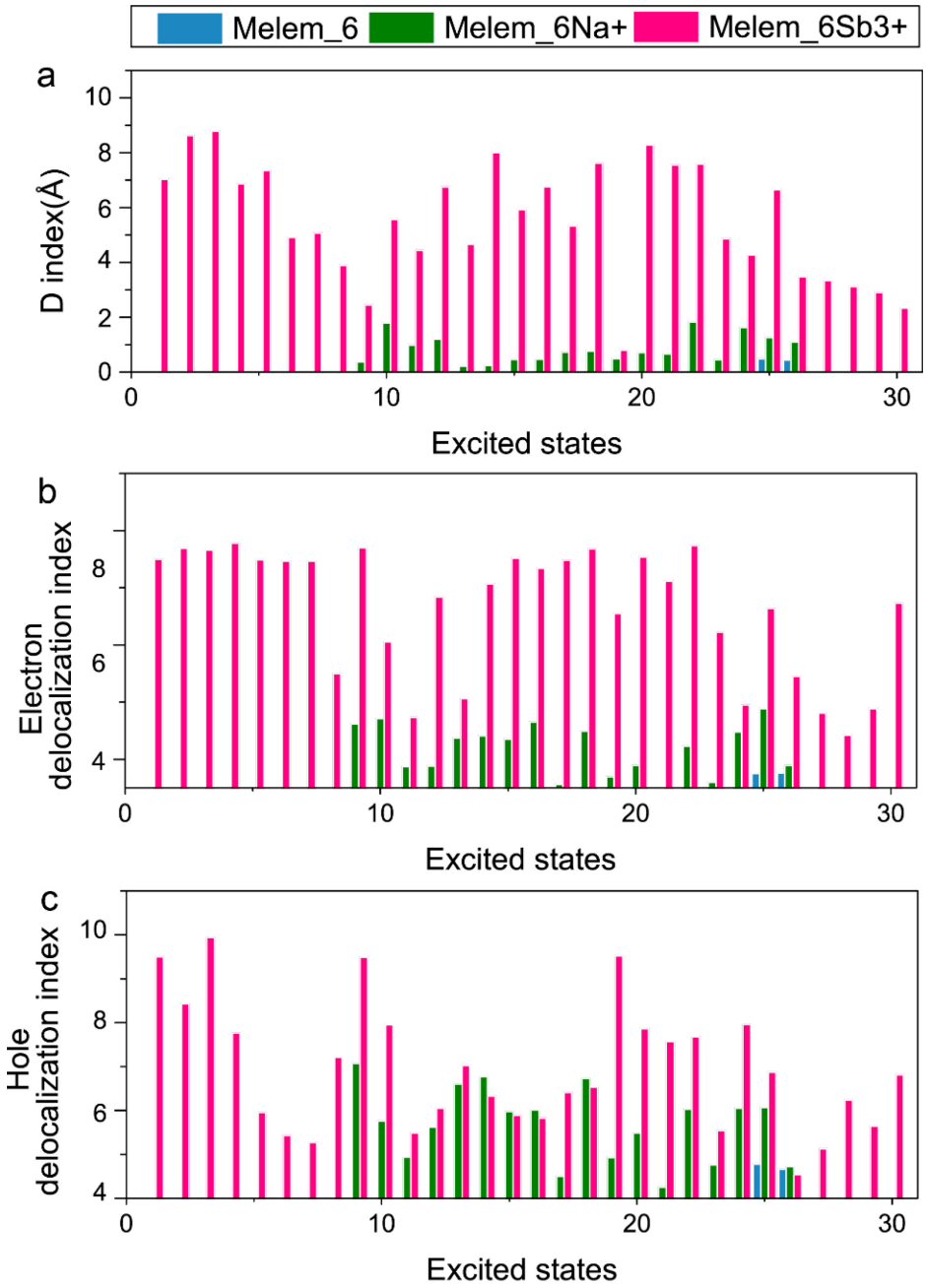

Figure 4-42. Simulated properties of Melem_6, Melem_6Na+ and Melem_6Sb3+ for charge separation and the localization of electrons and holes. a, D index of the transitions of ES25 and ES26 of Melem_6, ES9~ES26 of Melem_6Na+ and ES1~ES30 of Melem_6Sb3+. **b-c**, Delocalization index of (**b**) electrons and (**c**) holes for the transitions of ES25 and ES26 of Melem_6, ES9~ES26 of Melem_6Na+ and ES1~ES30 of Melem_6Sb3+.

As shown in Figure 4-42a**,** all of the D index of the transitions of Melem_6Sb3+ (ES1~ES30) are significantly larger than that of Melem_6 (ES25 and ES26) and Melem_6Na+ (ES9~ES26), indicating that the charge separation is significantly boosted

after the introduction of atomic antimony sites.

Additionally, another crucial property of photogenerated positive charge carriers (photogenerated holes or positive polarons) for facilitating WOR is their high localization levels. To simulate the localization level of photogenerated electrons and holes, we calculated the hole delocalization index (HDI) and electron delocalization index (EDI) as defined below:

$$HDI = 100 \times \sqrt{\int [\rho^{hole}(r)]^2 \, dr}$$

$$EDI = 100 \times \sqrt{\int [\rho^{ele}(r)]^2 \, dr}$$

ρ^{hole} and ρ^{ele} respectively indicate the distribution density of holes and electrons. It is found that the smaller the HDI (EDI) is, the larger the spatial delocalization of holes (electrons). HDI and EDI are useful in quantifying breadth of spatial distribution for electrons and holes. As shown in Supplementary Fig. 39b-c**,** the HDI and EDI of the transitions of Melem_6Sb3+ (ES1~ES30) are significantly larger than those of Melem_6 (ES25 and ES26) and Melem_6Na+ (ES9~ES26), indicating that both of the electrons and holes are highly concentrated after introduction of single atomic antimony sites.

In summary, based on the data from isotopic experiment in real experimental condition, the rotating ring disk electrode measurements under light irradiation as well as the TR-TAS spectra, we believe that the direct evidences for photocatalytic O_2 production via WOR have been throughtly given. The improved simulation results further confirmed that the introduction of atomically dispersed antimony sites significantly improved the charge separation and localized photogenerated holes (or positive polarons) at the N atoms in neigbouring melem units, which gave a theoretical explanation for the significantly improved WOR activity.

4.3.3.5 Oxygen reduction during the photocatalytic H_2O_2 production process.

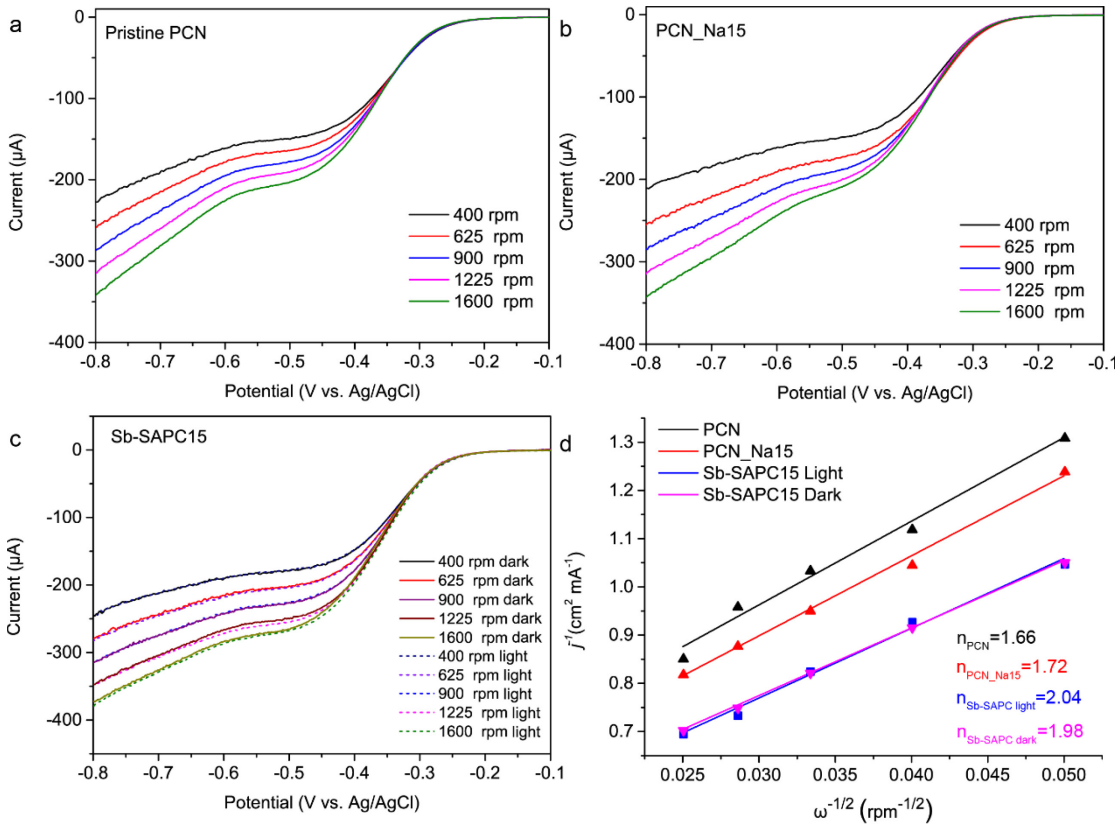

Figure 4-43. Investigation of electron transfer numbers. a-b, Linear sweep voltammetry (LSV) curves of pristine PCN (**a**) and Sb-SAPC15 (**b**) recorded on a rotating disk glassy carbon electrode in 0.1 M KOH saturated with O_2 in dark condition. **c**, Linear sweep voltammetry (LSV) curve of Sb-SAPC15 recorded on a rotating disk glassy carbon electrode in 0.1 M KOH saturated with O_2 under visible light illumination. **d**, Koutecky−Levich plots (at -0.6 V vs. Ag/AgCl).

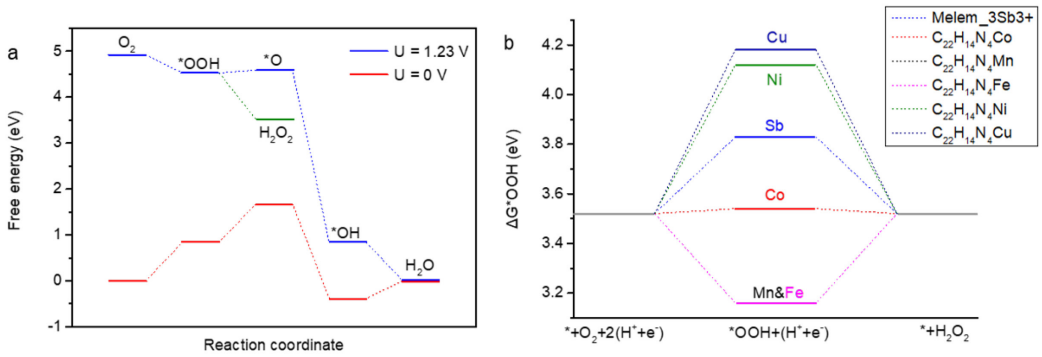

Figure 4-44. Energetic diagram for ORR. a, Calculated free energy diagrams at U = 0 (blue line) and U = 1.23 V (red line) vs. RHE for 2e$^-$ (green line) and 4e$^-$ ORR on Melem_3Sb3+. **b**, Comparison of ΔG_{*OOH} for the 2e$^-$ ORR on Sb-SAPC15 and $C_{40}H_{16}N_4M$, M = Mn, Fe, Co, Ni, and Cu at U = 0.7 V vs. RHE. The free energy diagram of $C_{40}H_{16}N_4M$ is adopted from our previous report[12].

To study the ORR mechanism on Sb-SAPC, rotating disk electrode (RDE) analysis was performed to investigate the number of electrons (n) transferred in the ORR process (Figure 4-43). The estimated “n” value is close to 2 for Sb-SAPC15 in both dark and light irradiation conditions. The preferred $2e^-$ ORR pathway on Sb-SAPC can be further supported by DFT calculation using the computational hydrogen electrode (CHE) method. As shown in Figure 4-44a, the calculated ΔG_{*OOH} is 4.53 eV (U = 0 V versus the reversible hydrogen electrode [RHE]), which is smaller than 4.59 eV of ΔG_{*O}, a crucial intermediate in $4e^-$ ORR[35]. The large energetic barrier toward forming *O would suppress the $4e^-$ ORR process. For a $2e^-$ ORR catalyst, the adsorption energy of *OOH should be larger than the thermoneutral value at the equilibrium potential (U = 0.7 V vs. RHE), corresponding to ΔG_{*OOH} of 3.52 eV. The calculated ΔG_{*OOH} is 3.83 eV (U = 0.7 V vs. RHE), suggesting that the ORR on single atom Sb may follow a $2e^-$ pathway (Figure 4-44b). It can be seen that the difference between *OH and *O is as high as 3.742 eV, indicating that a considerably large energetic barrier needs to be overcome for the $4e^-$ OER process. In this case, the Sb site should not function as an effective site to catalyze $4e^-$ OER.

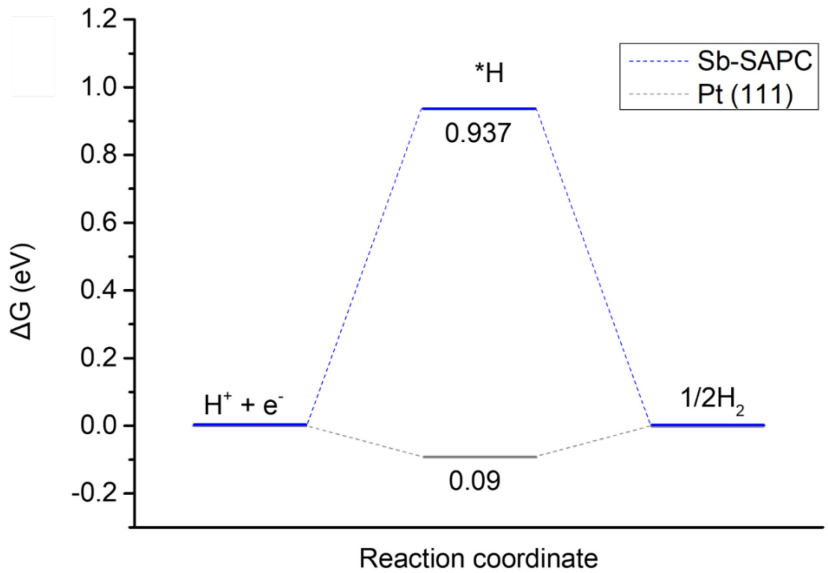

Figure 4-45. Interaction of hydrogen atoms and Sb sites and energetic diagram for HER. Comparison of ΔG_{*H} for HER on Melem_3Sb3+ and Pt (111).

It is noteworthy that the calculated ΔG_{*H} on Sb-SAPC15 is significantly larger (0.937 eV) than that on Pt (111) (Figure 4-45), suggesting that HER on Sb-SAPC15 is

energetically unfavorable, matching well with the experimental result (Figure 4-2e, left). These results also revealed that the interaction of hydrogen atoms and Sb sites is weak for the following reasons: (1) A typical Sb-H bonding exists in SbH_3. The oxidation number of Sb in SbH_3 is -3, whereas EXAFS fitting data shows that the chemical state of Sb sites in Sb-SAPC is close to +3. Thus, chemical bonding between Sb(+3) in Sb-SAPC and hydrogen is hardly believed. (2) The free energy diagram of Melem_3Sb3+*H is close to 1 eV, indicating that the adsorption of free H is quite hard on the Sb sites.

To identify the intermediate in the photocatalytic process, Raman spectroscopy measurements (Figure 4-33d) were performed under *operando* condition. For PCN, after reaction with 2-propanol as an electron donor under visible light irradiation, a new band appears at 896 cm^{-1}, which can be assigned to the C−O vibration and O−O stretching on the melem[12]. While for Sb-SAPCs, a new absorption band at 855 cm^{-1} increases with Sb content in the sample, which can be assigned to the O-O stretching mode of a Sb-OOH species with end-on adsorption configuration[69]. This relative chemical shift between O_2 end-on/side-on adsorption configuration has been also confirmed by our DFT calculations.

A function of ω97xd at 6-311g(d) level was used for optimization to investigate the most favorable adsorption site for O_2 on PCN. The initial and optimized configurations are summarized in Table 4-8. The calculation results show that the distance between O_2 and Melem_3 gradually increased during the optimization process. Therefore, the side-on adsorption of O_2 is not possible on site 2. On the contrary, O_2 can be adsorbed on site 1 of PCN with similar configuration to the previous literature. The distance between O_2 and the Melem unit is less than 1.5 Å. This bond length indicates that O_2 can be chemically adsorbed on site 1 with a typical side-on adsorption configuration.

To further understand the influence of O_2 adsorption configuration on the Raman spectrum, we calculated the Raman spectra of the optimized structure for Melem_3 and Melem_3Sb3+ after O_2 adsorption. The Raman spectra of Melem_3 and Melem_3Sb3+ before O_2 adsorption were also calculated for comparison (Figure 4-46). A new chemical shift appears at around 820 cm^{-1} (Figure 4-46b) after O_2 adsorption on Melem_3. Similarly,

a new chemical shift appears at around 780 cm^{-1} (Figure 4-46d) after O_2 adsorption on the Sb sites in Melem_3Sb3+. The relative position tendency of the changes in these newly observed chemical shifts are similar to the experimental results.

Table 4-8. Initial and optimized configuration for investigating the side-on adsorption of O_2 on PCN surface.

	Side-on adsorption of O_2 on Melem_3 (Site 1)		Side-on adsorption of O_2 on Melem_3 (Site 2)	
	Top view	Side view	Top view	Side view
Before optimization	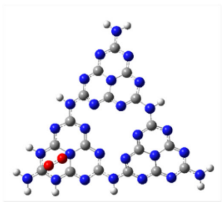	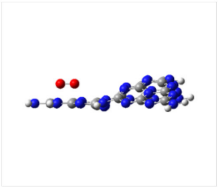	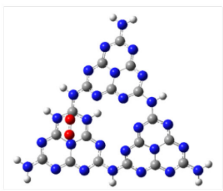	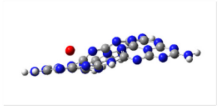
After optimization	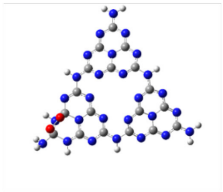	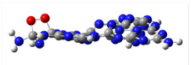	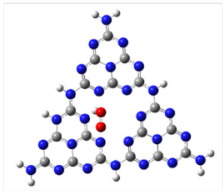	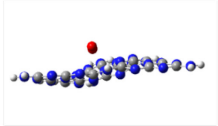

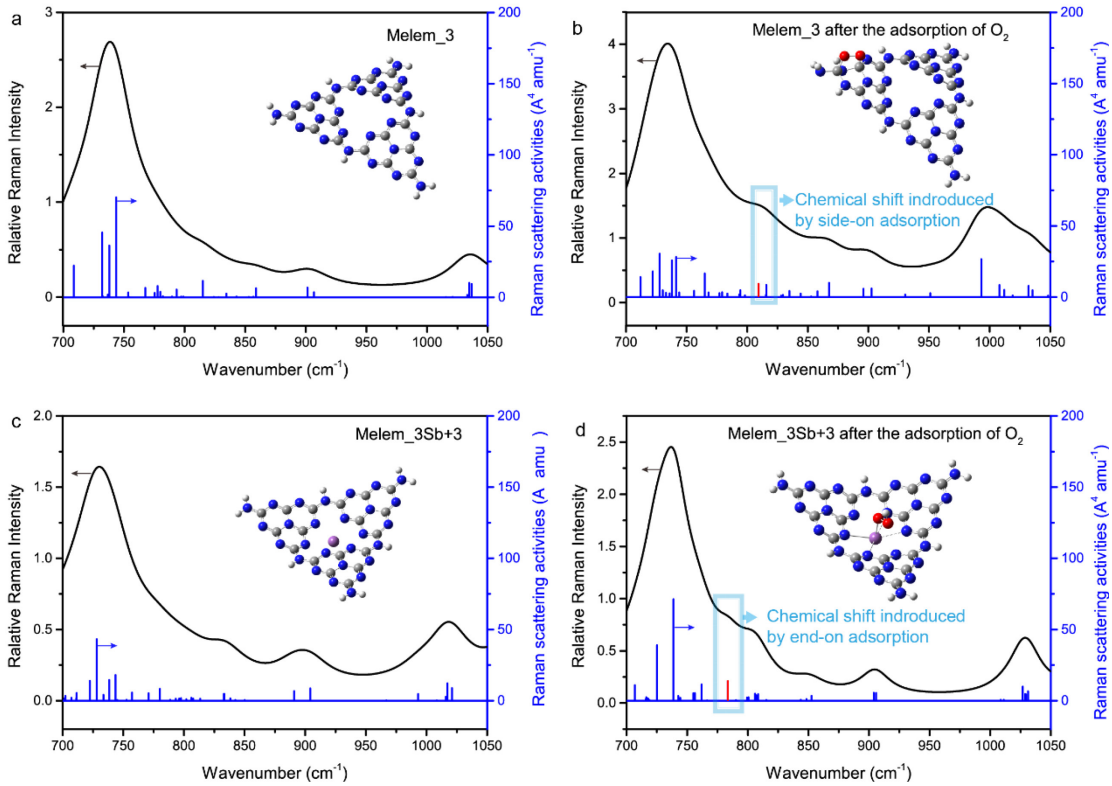

Figure 4-46. Calculated Raman shift by using the function of ω97xd at 6-311g(d) level. a-b, Simulated Raman spectra for (**a**) the tri-s-triazine unit and the units with (**b**) $^{16}O-^{16}O$

side-on species. **c-d**, Simulated Raman spectra for (**c**) the Sb-sites and the units with (**d**) $^{16}O-^{16}O$ end-on species Calculations were performed at the DFT level with the ω97xd/6-311g(**d**) basis set. The white, gray, blue, red, and purple spheres represent H, C, N, O and Sb atoms.

It is noteworthy that Sb-OOH exists even without addition of electron donor, implying that formation of Sb-OOH, rather than the side-on configuration, dominates in the photocatalytic process on Sb-SAPCs. The end-on adsorption shall significantly suppress the $4e^-$ ORR, leading to a high selectivity of the $2e^-$ process[28,29]. Additionally, electron spin resonance (ESR) signal of DMPO-O_2^- could be hardly observed in the Sb-SAPC system (Figure 4-47). Since O_2^- is an important intermediate in the stepwise $1e^-$ pathway (eq. 6) during formation of 1-4 endoperoxide, the invisible signal of DMPO-O_2^- in the Sb-SAPC system demonstrates rapid reduction of O_2 on Sb-SAPC to generate H_2O_2 via a $2e^-$ ORR pathway[20,22,70].

$$O_2+H^++e^-\rightarrow\bullet OOH\ (-0.046\ V\ vs.\ NHE) \quad (6)$$

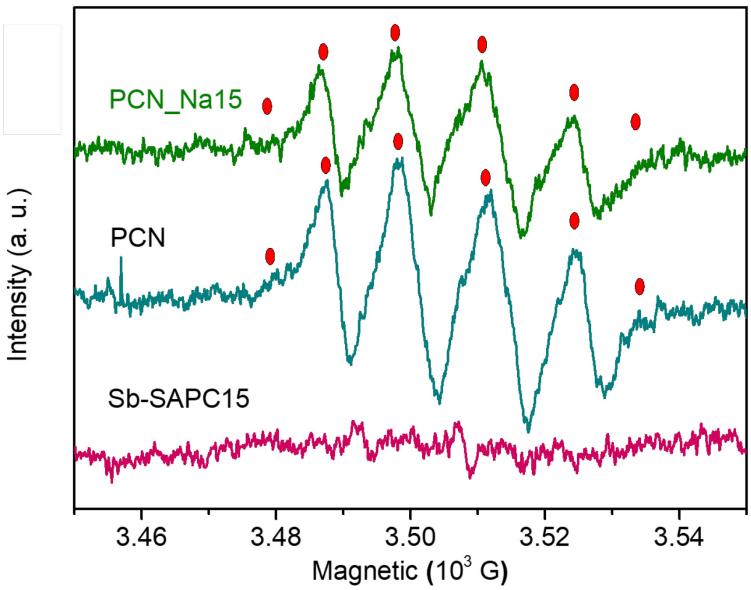

Figure 4-47. ESR spectra of PCN, PCN_Na15 and Sb-SAPC15 recorded in methanol solution using 5,5-diemthyl-1-pyrroline N-oxide as a radical trapper.

Based on the above characterizations and analyses, the reaction mechanism (Figure 4-48) of Sb-SAPC for photocatalytic H_2O_2 production is proposed as follows: 1. Efficient charge separation occurred on Sb-SAPC under visible light irradiation, generating

photoexcited electrons and holes for ORR and WOR, respectively. 2. Water molecules were oxidized to evolve O_2 by photogenerated holes localized at the N atoms next to the single Sb atoms. 3. The O_2 dissolved in water and generated from the WOR both participated in the ORR process to produce H_2O_2. It is worth noting that the efficient charge separation, ideal single atomic sites for end-on type O_2 adsorption and close spatial distribution of active sites boost both the $2e^-$ ORR and $4e^-$ WOR for efficient H_2O_2 production.

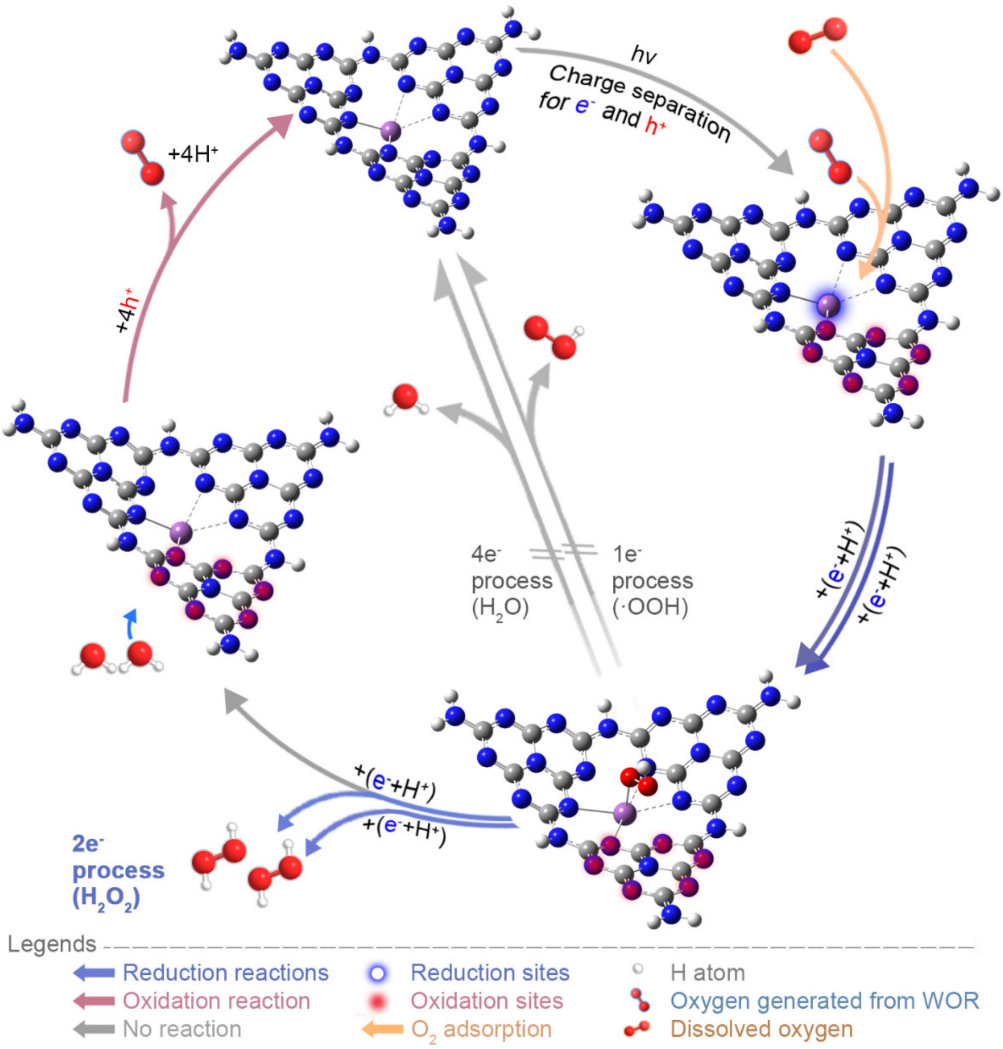

Figure 4-48. Mechanism of photocatalytic H_2O_2 production (The gray, bule, red and magenta spheres refer to carbon, nitrogen, oxygen and Sb atoms).

4.4 Conclusions

In summary, we have reported a well-defined, highly active, selective, and photochemically robust single Sb atom photocatalyst for non-sacrificial H_2O_2 production in

a water and oxygen mixture under visible light irradiation. The single Sb sites are able to accumulate electrons, which act as the photo-reduction sites for O_2 via a $2e^-$ ORR pathway. Simultaneously, the accumulated holes at the N atoms of the melem units neighboring to the Sb sites accelerate the water oxidation kinetics. The collaborative effect between the single atom sites and the support shall open up a new direction for designing various single atom catalysts for a variety of photocatalytic reactions in energy conversion and environmental remediation.

Reference

[1] K.P. Bryliakov, Catalytic asymmetric oxygenations with the environmentally benign oxidants H_2O_2 and O_2, Chem. Rev. 117 (2017) 11406-11459. https://doi.org/10.1021/acs.chemrev.7b00167.

[2] S.A.M. Shaegh, N.-T. Nguyen, S.M.M. Ehteshamiab, S.H. Chan, A membraneless hydrogen peroxide fuel cell using Prussian Blue as cathode material, Energy Environ. Sci. 5, 8225-8228 (2012). https://doi.org/10.1039/C2EE21806B.

[3] H.B. Gray, Powering the planet with solar fuel, Nat. Chem. 1 (2009) 7-7. https://doi.org/10.1038/nchem.141.

[4] D. Kim, K.K. Sakimoto, D. Hong, P. Yang, Artificial photosynthesis for sustainable fuel and chemical production, Angew. Chem. Int. Ed. 54 (2015) 3259-3266. https://doi.org/10.1002/anie.201409116.

[5] C. Xia, Y. Xia, P. Zhu, L. Fan, H. Wang, Direct electrosynthesis of pure aqueous H_2O_2 solutions up to 20% by weight using a solid electrolyte, Science 366 (2019) 226-231. https://doi.org/10.1126/science.aay1844.

[6] J.K. Edwards, E. Ntainjua N, A.F. Carley, A.A. Herzing, C.J. Kiely, G.J. Hutchings, Direct synthesis of H_2O_2 from H_2 and O_2 over gold, palladium, and gold-palladium catalysts supported on acid-pretreated TiO_2, Angew. Chem. Int. Ed. 48 (2009) 8512–8515. https://doi.org/10.1002/anie.200904115.

[7] S.J. Freakley, Q. He, J.H. Harrhy, L. Lu, D.A. Crole, D.J. Morgan, E.N. Ntainjua, J.K. Edwards, A.F. Carley, A.Y. Borisevich, C.J. Kiely, G.J. Hutchings, Palladium-tin catalysts for the direct synthesis of H_2O_2 with high selectivity, Science 351 (2016) 965-968. https://doi.org/10.1126/science.aad5705.

[8] S. Yang, A. Verdaguer-Casadevall, L. Arnarson, L. Silvioli, V. Čolić, R. Frydendal, J. Rossmeisl, I. Chorkendorff, I.E.L. Stephens, Toward the decentralized electrochemical production of H_2O_2: A focus on the catalysis, ACS Catal. 8 (2018) 4064-4081. https://doi.org/10.1021/acscatal.8b00217.

[9] Y. Yi, L. Wang, G. Li, H. Guo, A review on research progress in the direct synthesis of hydrogen peroxide from hydrogen and oxygen: Noble-metal catalytic method, fuel-cell method and plasma method, Catal. Sci. Technol. 6 (2016) 1593-1610. https://doi.org/10.1039/C5CY01567G.

[10] H. Hou, X. Zeng, X. Zhang, Production of hydrogen peroxide through photocatalytic process: A critical review of recent advances, Angew. Chem. Int. Ed., (2019)

https://doi.org/10.1002/anie.201911609.
[11] X. Shi, S. Siahrostami, G. Li, Y. Zhang, P. Chakthranont, F. Studt, T.F. Jaramillo, X. Zheng, J.K. Nørskov, Understanding activity trends in electrochemical water oxidation to form hydrogen peroxide, Nat. Commun. 8 (2017) 701. https://doi.org/10.1038/s41467-017-00585-6.
[12] Y. Shiraishi, S. Kanazawa, Y. Kofuji, H. Sakamoto, S. Ichikawa, S. Tanaka, T. Hirai, Sunlight-driven hydrogen peroxide production from water and molecular oxygen by metal-free photocatalysts, Angew. Chem. 126 (2014) 13672-13677. https://doi.org/10.1002/anie.201407938.
[13] K. Fuku, K. Sayama, Efficient oxidative hydrogen peroxide production and accumulation in photoelectrochemical water splitting using a tungsten trioxide/bismuth vanadate photoanode, Chem. Commun. 52 (2016) 5406-5409. https://doi.org/10.1039/C6CC01605G.
[14] J. H. Baek, T. M. Gill, H. Abroshan, S. Park, X. Shi, J. Norskov, H. S. Jung, S. Siahrostami, X. Zheng, Selective and efficient Gd-doped $BiVO_4$ photoanode for two-electron water oxidation to H_2O_2, ACS Energy Lett. 4 (2019) 720-728. https://pubs.acs.org/doi/10.1021/acsenergylett.9b00277.
[15] Y. Shiraishi, T. Takii, T. Hagi, S. Mori, Y. Kofuji, Y. Kitagawa, S. Tanaka, S. Ichikawa, T. Hirai, Resorcinol–formaldehyde resins as metal-free semiconductor photocatalysts for solar-to-hydrogen peroxide energy conversion, Nat. Mater. 18 (2019) 985-993. https://doi.org/10.1038/s41563-019-0398-0.
[16] W. Fan, B. Zhang, X. Wang, W. Ma, D. Li, Z. Wang, M. Dupuis, J. Shi, S. Liao, C. Li, Efficient hydrogen peroxide synthesis by metal-free polyterthiophene via photoelectrocatalytic dioxygen reduction, Energy Environ. Sci. 13 (2020) 238-245 . https://doi.org/10.1039/c9ee02247c.
[17] H. Kim, Y. Choi, S. Hu, W. Choi, J.-H. Kim, Photocatalytic hydrogen peroxide production by anthraquinone-augmented polymeric carbon nitride, Appl. Catal. B-Environ. 229 (2018) 121-129. https://doi.org/10.1016/j.apcatb.2018.01.060.
[18] G.-H. Moon, M. Fujitsuka, S. Kim, T. Majima, X. Wang, W. Choi, Eco-friendly photochemical production of H_2O_2 through O_2 reduction over carbon nitride frameworks incorporated with multiple heteroelements, ACS Catal. 7 (2017) 2886-2895. https://doi.org/10.1021/acscatal.6b03334.
[19] C. Chu, Q. Zhu, Z. Pan, S. Gupta, D. Huang, Y. Du, S. Weon, Y. Wu, C. Muhich, E. Stavitskid, K. Domen, J.-H. Kim, Spatially separating redox centers on 2D carbon nitride with cobalt single atom for photocatalytic H_2O_2 production, PNAS 117 (2020) 6376-6382. https://www.pnas.org/content/117/12/6376.
[20] Z. Wei, M. Liu, Z. Zhang, W. Yao, H. Tan, Y. Zhu, Efficient visible-light-driven selective oxygen reduction to hydrogen peroxide by oxygen-enriched graphitic carbon nitride polymer, Energy Environ. Sci. 11 (2018) 2581-2589. https://doi.org/10.1039/c8ee01316k.
[21] N. Kaynan, B.A. Berke, O. Hazut, R. Yerushalmi, Sustainable photocatalytic production of hydrogen peroxide from water and molecular oxygen, J. Mater. Chem. A 2 (2014) 13822−13826. https://doi.org/10.1039/c4ta03004d.
[22] Z. Teng, W. Cai, S. Liu, C. Wang, Q. Zhang, C. Su, T. Ohno, Bandgap engineering of

polymetric carbon nitride copolymerized by 2,5,8-triamino-tri-s-triazine (melem) and barbituric acid for efficient nonsacrificial photocatalytic H_2O_2 production. Appl. Catal. B 271 (2020) 118917. https://doi.org/10.1016/j.apcatb.2020.118917.

[23] X. Zeng, Y. Liu, Y. Kang, Q. Li, Y. Xia, Y. Zhu, H. Hou, M.H. Uddin, T.R. Gengenbach, D. Xia, C. Sun, D.T. Maccarthy, A. Deletic, J. Yu, X. Zhang, Simultaneously tuning charge separation and oxygen reduction pathway on graphitic carbon nitride by polyethylenimine for boosted photocatalytic hydrogen peroxide production, ACS Catal. 10 (2020) 3697–3706. https://doi.org/10.1021/acscatal.9b05247.

[24] Q. Wang, K. Domen, Particulate photocatalysts for light-driven water splitting: Mechanisms, challenges, and design strategies, Chem. Rev. 120 (2020) 919-985. https://doi.org/10.1021/acs.chemrev.9b00201.

[25] H. Hirakawa, M. Hashimoto, Y. Shiraishi, T. Hirai, Photocatalytic conversion of nitrogen to ammonia with water on surface oxygen vacancies of titanium dioxide photocatalytic conversion of nitrogen to ammonia with water on surface oxygen vacancies of titanium dioxide, J. Am. Chem. Soc. 139 (2017) 10929-10936. https://doi.org/10.1021/jacs.7b06634.

[26] A. Kulkarni, S. Siahrostami, A. Patel, J.K. Nørskov, Understanding catalytic activity trends in the oxygen reduction reaction, Chem. Rev. 118 (2018) 2302-2312. https://doi.org/10.1021/acs.chemrev.7b00488.

[27] E. Watanabe, H. Ushiyama, K. Yamashita, Theoretical studies on the mechanism of oxygen reduction reaction on clean and O-substituted Ta_3N_5(100) surfaces. Catal. Sci. Technol. 5 (2015) 2769-2776. https://doi.org/10.1039/C5CY00088B.

[28] C.H. Choi, H.C. Kwon, S. Yook, H. Shin, H. Kim, M. Choi, Hydrogen peroxide synthesis via enhanced two-electron oxygen reduction pathway on carbon-coated Pt surface. J. Phys. Chem. C 118 (2014) 30063-30070. https://doi.org/10.1021/jp5113894.

[29] C. Chu, D. Huang, Q. Zhu, E. Stavitski, J.A. Spies, Z. Pan, J. Mao, H.L. Xin, C.A. Schmuttenmaer, S. Hu, J.-H. Kim, Electronic tuning of metal nanoparticles for highly efficient photocatalytic hydrogen peroxide production. ACS Catal. 9 (2019) 626−631. https://doi.org/10.1021/acscatal.8b03738.

[30] M.L. Pegis, C.F. Wise, D.J. Martin, J.M. Mayer, Oxygen reduction by homogeneous molecular catalysts and electrocatalysts. Chem. Rev. 118 (2018) 2340-2391. https://doi.org/10.1021/acs.chemrev.7b00542.

[31] S. Yang, J. Kim, Y.J. Tak, A. Soon, H. Lee, Single-atom catalyst of platinum supported on titanium nitride for selective electrochemical reactions. Angew. Chem. Int. Ed. 55 (2016) 2058-2062. https://doi.org/10.1002/anie.201509241.

[32] M.M. Montemore, M.A. van Spronsen, R.J. Madix,; C.M. Friend, O_2 activation by metal surfaces: Implications for bonding and reactivity on heterogeneous catalysts. Chem. Rev. 118 (2018) 2816-2862. https://doi.org/10.1021/acs.chemrev.7b00217.

[33] A. Wang, J. Li, T. Zhang, Heterogeneous single-atom catalysis, Nat. Rev. Chem. 2 (2018) 65–81. https://doi.org/10.1038/s41570-018-0010-1.

[34] R. Shen ,W. Chen ,Q. Peng, S. Lu, L. Zheng, X. Cao, Y. Wang, W. Zhu, J. Zhang, Z. Zhuang, C. Chen, D. Wang, Y. Li, High-concentration single atomic Pt sites on hollow CuSx for selective O_2 reduction to H_2O_2 in acid solution, Chem 5 (2019) 2099–2110. https://doi.org/10.1016/j.chempr.2019.04.024.

[35] J. Gao, H. Yang, X. Huang, S.-F. Hung, W. Cai, C. Jia, S. Miao, H.Chen, X. Yang, Y. Huang, T. Zhang, B. Liu, Enabling direct H_2O_2 production in acidic media through rational design of transition metal single atom catalyst, Chem 6 (2020) 1-17. https://doi.org/10.1016/j.chempr.2019.12.008.

[36] E. Jung, H. Shin, B.-H. Lee, V. Efremov, S. Lee, H.S. Lee, J. Kim, W.H. Antink, S. Park, K.-S. Lee, S.-P. Cho, J.S. Yoo, Y.-E. Sung, T. Hyeon, Atomic-level tuning of Co-C-N catalyst for high performance electrochemical H_2O_2 production, Nat. Mater. 19 (2020) 436–442. https://doi.org/10.1038/s41563-019-0571-5.

[37] Y. Nosaka, A. Nosaka, Introduction to Photocatalysis: From Basic Science to Applications (2016). ISBN: 978-1-78262-320-5.

[38] Y. Inoue, Photocatalytic water splitting by RuO_2-loaded metal oxides and nitrides with d^0- and d^{10} -related electronic configurations, Energy Environ. Sci. 2 (2009) 364-386. https://doi.org/10.1039/b816677n.

[39] Y. Kofuji, Y. Isobe, Y. Shiraishi, H. Sakamoto, S. Tanaka, S. Ichikawa, T. Hirai, Carbon nitride–aromatic diimide–graphene nanohybrids: Metal-free photocatalysts for solar-to-hydrogen peroxide energy conversion with 0.2% efficiency, J. Am. Chem. Soc. 138 (2016) 10019-10025. https://doi.org/10.1021/jacs.6b05806.

[40] K.K. Ghuman, L.B. Hoch, P. Szymanski, J.Y.Y. Loh, N.P. Kherani, M.A. El-Sayed, G.A. Ozin, C.V. Singh, Photoexcited surface frustrated Lewis pairs for heterogeneous photocatalytic CO_2 reduction, J. Am. Chem. Soc. 138 (2016) 1206-1214. https://doi.org/10.1021/jacs.5b10179.

[41] N. Govind, K. Lopata, R. Rousseau, A. Andersen, and K. Kowalski, Visible light absorption of N-doped TiO_2 rutile using (LR/RT)-TDDFT and active space EOMCCSD calculations. J. Phys. Chem. Lett. 2 (2011) 2696-2701. https:doi.org/10.1021/jz201118r.

[42] J.-L. Bredas, Mind the gap! Mater. Horiz., 1 (2014) 17-19. https://doi.org/10.1039/C3MH00098B.

[43] T. Lu, F. Chen, Multiwfn: A multifunctional wavefunction analyzer, J. Comput. Chem. 33 (2012) 580-592. https://doi.org/10.1002/jcc.22885.

[44] T.L. Bahers, C. Adamo, I. Ciofini, A qualitative index of spatial extent in charge-transfer excitations, J. Chem. Theory Comput. 7 (2011) 2498-2506. https://doi.org/10.1021/ct200308m.

[45] S. Kraner, R. Scholz, F. Plasser, C. Koerner, K. Leo, Exciton size and binding energy limitations in one-dimensional organic materials, J. Chem. Phys. 143 (2015) 244905. https://doi.org/10.1063/1.4938527.

[46] S. Kraner, O. Prampolini, G. Cuniberti, Exciton binding energy in molecular triads, J. Phys. Chem. C 121 (2017) 17088-17095. https://doi.org/10.1021/acs.jpcc.7b03923.

[47] D. Kislitsyn, C. Gervasi, T. Allen, P. B. Palomaki, J. Hackley, R. Maruyama, G. Nazin, Spatial mapping of sub-bandgap states induced by local nonstoichiometry in individual lead sulfide nanocrystals, J. Phys. Chem. Lett. 5 (2014) 3701-3707. https://doi.org/10.1021/jz5019465.

[48] J.K. Nørskov, J. Rossmeisl, A. Logadottir, L. Lindqvist, J.R. Kitchin, T. Bligaard, H. Jo´nsson, Origin of the overpotential for oxygen reduction at a fuel-cell cathode. J. Phys. Chem. B 108 (2004) 17886-17892. https://doi.org/10.1021/jp047349j.

[49] F. Calle-Vallejo, J.I. Martı´nez, J. Rossmeisl, Density functional studies of functionalized graphitic materials with late transition metals for oxygen reduction reactions. Phys. Chem. Chem. Phys. 13 (2011) 15639–15643. https://doi.org/10.1039/C1CP21228A.
[50] H. Xu, D. Cheng, D. Cao, X.C. Zeng, A universal principle for a rational design of single-atom electrocatalysts. Nat. Catal. 1 (2018) 339–348. https://doi.org /10.1038/s41929-018-0063-z.
[51] G. Kresse, J. Furthmüller, Efficient iterative schemes for ab initio total-energy calculations using a plane-wave basis set, J. Phys. Rev. B 54 (1996) 11169–11186. https://doi.org/10.1103/PhysRevB.54.11169.
[52] G. Kresse, J. Furthmüller, Efficiency of ab-initio total energy calculations for metals and semiconductors using a plane-wave basis set. J. Comput. Mater. Sci. 6 (1996) 15–50. https://doi.org/10.1016/0927-0256(96)00008-0.
[53] J. P. Perdew, K. Burke and M. Ernzerhof, Generalized gradient approximation made simple, Phys. Rev. Lett. 77 (1996) 3865-3868. https://doi.org/10.1103/PhysRevLett.77.3865.
[54] P. E. Blöchl, Projector augmented-wave method, Phys. Rev. B 50 (1994) 17953-17979. https://doi.org/10.1103/PhysRevB.50.17953.
[55] W. Press, B. Flannery, S. Teukolsky, W.Vetterling, Numerical recipes, Cambridge University Press, New York (1986).
[56] E. Sanville, S.D. Kenny, R. Smith, G. Henkelman, Improved grid based algorithm for Bader charge allocation. J. Comput. Chem. 28 (2001) 899–908. https://doi.org/10.1002/jcc.20575.
[57] W.-C. Hou, Y.-S. W., Photocatalytic generation of H_2O_2 by graphene oxide in organic electron donor-free condition under sunlight, ACS Sustainable Chem. Eng. 5 (2017) 2994−3001. https://doi.org/10.1021/acssuschemeng.6b02635.
[58] N. Kaynan, B.A. Berke, O. Hazut, R. Yerushalmi, Sustainable photocatalytic production of hydrogen peroxide from water and molecular oxygen, J. Mater. Chem. A 2 (2014) 13822–13826. https://doi.org/10.1039/c4ta03004d.
[59] L. Wang, S. Cao, K. Guo, Z. Wu, Z. Ma, L. Piao, Simultaneous hydrogen and peroxide production by photocatalytic water splitting, Chin. J. Catal. 40 (2019) 470-475. https://doi.org/10.1016/S1872-2067(19)63412-1.
[60] Y. Kofuji, S. Ohkita, Y. Shiraishi, H. Sakamoto, S. Ichikawa, S. Tanaka, T. Hirai, Mellitic triimide-doped carbon nitride as sunlight-driven photocatalysts for hydrogen peroxide production, ACS Sustainable Chem. Eng. 5 (2017) 6478-6485. https://doi.org/10.1021/ acssuschemeng.7b00575.
[61] Y. Kofuji, Y. Isobe, Y. Shiraishi, H. Sakamoto, S. Ichikawa, S. Tanaka, T. Hirai, Hydrogen peroxide production on a carbon nitride-boron nitride-reduced graphene oxide hybrid photocatalyst under visible light, ChemCatChem 10 (2018) 2070-2077. https://doi.org/10.1002/cctc.201701683.
[62] X. Li, W. Bi, L. Zhang, S. Tao, W. Chu, Q. Zhang, Y. Luo, C. Wu, Y. Xie, Single-atom Pt as co-catalyst for enhanced photocatalytic H_2 evolution, Adv. Mater. 28 (2016) 2427–2431. https://doi.org/10.1002/adma.201505281.
[63] A.V. Naumkin, A. Kraut-Vass, S.W. Gaarenstroom, C.J. Powell, NIST X-ray

photoelectron spectroscopy database. http://dx.doi.org/10.18434/T4T88K.
[64] B. Ravel, M. Newville, ATHENA, ARTEMIS, HEPHAESTUS: data analysis for X-ray absorption spectroscopy using IFEFFIT, J. Synchrotron Radiat. 12 (2005) 537–541. https://doi.org/10.1107/S0909049505012719.
[65] P. Zhang, Y. Tong, Y. Liu, J. J. M. Vequizo, H. Sun, C. Yang, A. Yamakata, F. Fan, W. Lin, X. Wang, W. Choi, Heteroatom dopants promote two-electron O_2 reduction for photocatalytic production of H_2O_2 on polymeric carbon nitride, Angew. Chem. Int. Ed., 59 (2020) 16209-16217. https://doi.org/10.1002/anie.202006747.
[66] G.-h. Moon, M. Fujitsuka, S. Kim, T. Majima, X. Wang, W. Choi, Eco-Friendly photochemical production of H_2O_2 through O_2 reduction over carbon nitride frameworks incorporated with multiple heteroelements, ACS Catal. 7 (2017) 2886-2895. https://doi.org/acscatal.6b03334.
[67] A. Yamakata, T. Ishibashi, H. Onishi, Water- and oxygen-induced decay kinetics of photogenerated electrons in TiO_2 and Pt/TiO_2: A time-resolved infrared absorption study, J. Phys. Chem. B 105 (2001) 7258-7262. https://doi.org/10.1021/jp010802w.
[68] P. Zhang, D. Sun, A. Cho, S. Weon, S. Lee, J. Lee, J. W. Han, D-P. Kim, W. Choi, Modified carbon nitride nanozyme as bifunctional glucose oxidase-peroxidase for metal-free bioinspired cascade photocatalysis, Nat. Commun. 10 (2019) 940. https://doi.org/10.1038/s41467-019-08731-y.
[69] R. Jones, D. Summerville, F. Basolo, Synthetic oxygen carriers related to biological systems, Chem. Rev. 79 (1979) 139-179. https://doi.org/10.1021/cr60318a002.
[70] S. Li, G. Dong, R. Hailili, L. Yang, Y. Li, F. Wang, Y. Zeng, C. Wang, Effective photocatalytic H_2O_2 production under visible light irradiation at g-C_3N_4 modulated by carbon vacancies, Appl. Catal. B 190 (2016) 26–35. https://doi.org/10.1016/j.apcatb.2016.03.004.

Part 5

Conclusion and outlook

5.1 Conclusion

This dissertation focus on the functionalization strategies of polymetric carbon nitride for achieving highly efficient non-sacrificial H_2O_2 production.

First of all, to efficient boost the ORR reaction catalyzed by melem units, the band positions of polymetric carbon nitride can be rationally designed by using melem and barbituric acid as precursors. The C=O groups incorporated in the PCN matrix formed a positive valence band with sufficient potential (1.85 eV vs. SHE) for overcoming the large overpotential of water oxidation (c.a.>0.8 V). The light absorption edge also expanded from 450 to 550 nm, indicating the promoted light harvesting. With the further loading of $Na_2CoP_2O_7$ as an OER co-catalyst, the PCNBAs showed a record-high apparent quantum yield of 8.0% and a SCC of 0.30% for photocatalytic H_2O_2 production with only H_2O and O_2. The co-polymerization of BA and melem, as well as the loading of $Na_2CoP_2O_7$ significantly improved the charge separation. Analysis by DFT calculation combined with DOS showed that the positive shift of the band position is due to the O 2p states introduced by the co-polymerization of BA units. Co-polymerization of oxygen-rich motifs has been proven for the first time to be an effective approach for developing catalytic systems for enhanced H_2O_2 production in the aspect of electronic energy level.

Then, to explore the 2e- ORR sites beyond the melem, a series of metal ion-incorporated single-atom photocatalyst (M-SAPCs) was prepared by isolating TM metal (Fe, Co, Ni) and main-group (In, Sn) sites with pyridinic N atoms in PCN skeleton. The chemical state of atomically dispersed Fe is between (II) and (III), and the chemical states of Co, Ni, In and Sn species catalyst is close (II), (II), (III) and (IV), respectively. The simulation results revealed that the metal ions isolated by non-defected Melem_3 units are consistent with the practically prepared M-SAPC in terms of band structures and electronic configurations. E_{abX}, transition density distribution of elections and holes, D index and E_{Coulmb} revealed that the incorporation of atomically dispersed main-group metals (In (III) and Sn (IV)) significantly improved the charge separation efficiency. Additionally, the iso-surface of the dominant MO (electrons) in the models of Melem_3In3+ and Melem_3Sn4+ showed an ideal electronic configuration for the adsorption of electrophilic oxygen,

indicating that the ORR reduction could be accelerated by In and Sn sites. Furthermore, the experimental charge separation properties of M-SAPCs showed good accordance with the computed charge transfer profile of Melem_3M. The correlations among activity and experimental and theoretical charge separation properties also showed the rationalities of the proposed model for estimating charge separation properties. Our work provides not only a theoretical guideline based on the validated electronic configuration and excitation properties but also a blueprint for the design of single-atom photocatalyst with a high charge separation profile at atomic levels. Combined with the traditional simulation strategies such as CHE models and transition states, a precise benchmark for predicting both activity and selectivity might be established for many artificial photo-synthesis systems in a very near future.

Based on the primary guideline obtained from the TDDFT results in the previous section, we develop a Sb single atom photocatalyst for non-sacrificial photocatalytic H_2O_2 synthesis in a water and oxygen mixture under visible light irradiation, in which the oxidation state of Sb is regulated to +3 with a $4d^{10}5s^2$ electron configuration. Notably, a record-high apparent quantum efficiency of 17.6% at 420 nm and a solar-to-chemical conversion (SCC) efficiency of 0.61% are achieved on the as-developed photocatalyst. Combining experimental and theoretical investigations, it is found that the adsorption of O_2 on isolated Sb atomic sites is end-on type, which promotes formation of Sb-*μ*-peroxide (Sb-OOH), leading to an efficient $2e^-$ ORR pathway for H_2O_2 production. More importantly, the Sb sites also induce highly concentrated holes at the neighboring melem units, promoting the $4e^-$ WOR. The collaborative effect between the single atom sites and the support shall open up a new direction for designing various single atom catalysts for a variety of photocatalytic reactions in energy conversion and environmental remediation.

5.2 Outlook

The absorption edge of the functionalized PCN reported in this dissertation can hardly extended to >550 nm with decent AQY for H_2O_2 production. In this case, further narrowing the band gap is still of great importance. It is worth noting that the narrowing the bandgap could reduce the thermodynamic driving force, leading to weakened capability for reduction

reactions and oxidation reactions. In this case, reducing the over potential for $2e^-$ ORR and oxidation reactions on PCN surface is of great importance. Additionally, the overall activity of PCN based materials for non-sacrificial H_2O_2 production still suffers from their poor activities for water oxidation reaction. Seeking efficient strategies for improving the WOR activity is still of great importance.

Research achievements

Research articles

1. **Zhenyuan Teng**, Qitao Zhang, Hongbin Yang, Kosaku Kato, Wenjuan Yang, Ying-Rui Lu, Sixiao Liu, Chengyin Wang, Akira Yamakata, Chenliang Su, Bin Liu, Teruhisa Ohno. Atomically dispersed antimony boosts oxygen reduction and water oxidation for efficient artificial photosynthesis of hydrogen peroxide, ***Nature Catalysis***, 2nd Revision submitted.

2. Anyun Meng, **Zhenyuan Teng**, Qitao Zhang, Chenliang Su, Intrinsic defects in polymeric carbon nitride for photocatalysis applications. ***Chem Asian J.***, 2020, 15. DOI:10.1002/asia.202000850.

3. **Zhenyuan Teng**, Wenan Cai, Wenwen Sim, Qitao Zhang, Chengyin Wang, Chenliang Su, Teruhisa Ohno. Photoexcited single metal atom catalysts for heterogeneous photocatalytic H_2O_2 production: Pragmatic guidelines for predicting charge separation, ***Appl Catal B-Environ***, 2020, 282, 119589.

4. Zhi Zheng, Naoya Murakami, Jingjing Liu, **Zhenyuan Teng**, Qitao Zhang, Yu Cao, Honghui Cheng, Teruhisa Ohno. Development of plasmonic photocatalyst by site‐selective loading of bimetallic nanoparticles of Au and Ag on titanium(IV) oxide, ***ChemCatChem***, 2020, 12, 3783- 3792.

5. **Zhenyuan Teng**, Wenan Cai, Sixiao Liu, Chengyin Wang, Qitao Zhang, Chenliang Su, Teruhisa Ohno. Bandgap engineering of polymetric carbon nitride copolymerized by 2,5,8-triamino-tri-s-triazine (melem) and barbituric acid for efficient nonsacrificial photocatalytic H_2O_2 production, ***Appl Catal B-Environ***, 2020, 271, 118917.

6. Meng Yuan, **Zhenyuan Teng**, Sicong Wang, Yanqi Xu, Pingjian Wu, Yanting Zhu, Chengyin Wang, Guoxiu Wang, Polymeric carbon nitride modified polyacrylonitrile fabrics with efficient self-cleaning and water disinfection under visible light, ***Chem. Eng.***, 2020, 391, 123506. (equal contribution)

7. Sicong Wang, **Zhenyuan Teng**, Yanqi Xu, Meng Yuan, Yunhao Zhong, Sixiao Liu,

Chengyin Wang, Guoxiu Wang, Teruhisa Ohno, Defect as the essential factor in engineering carbon-nitride-based visible-light-driven Z-scheme photocatalyst, ***Appl Catal B-Environ,*** 2020, 260, 118145. (equal contribution)

8. **Zhenyuan Teng**, Nailiang Yang, Hongying Lv, Sicong Wang, Maozhi Hu, Chengyin Wang, Dan Wang, Guoxiu Wang. Edge-functionalized g-C_3N_4 nanosheets as a highly efficient metal-free photocatalyst for safe drinking water, ***Chem***, 2019, 5, 664–680.

Academic Conference:

Conference Presentation

2020.12 [Atomically Dispersed Antimony Boosts Oxygen Reduction and Water Oxidation] 8th International Symposium on Applied Engineering and Sciences. Virtual Conference, ZOOM.

2020.11 [アンチモン単一原子光触媒の合成と過酸化水素生成機構] 第 39 回光がかかわる触媒化学シンポジウム, ZOOM.

2019.9 [Enhanced Co-catalytic Performance of Group V Elements for Photocatalytic H_2O_2 Production] 7th International Conference on Semiconductor Photochemistry. Milano Italy. *Poster prize.*

2019.6 [Enhanced Co-catalytic Performance of Group V Elements for Photocatalytic H_2O_2 Production] 第 38 回光がかかわる触媒化学シンポジウム，トヨタ産業技術記念館　名古屋.

Patent

1. 横野照尚、滕鎮遠、須崎友文，堤内出，仮屋伸子. 光触媒および光触媒を用いた過酸化水素の製造方法. 三菱ケミカル株式会社、国立大学法人九州工業大学 2019, ID: 19P00875. (申请中)

Acknowledgements

I would like to express my great gratitude to Prof. Ohno for all his help during my PhD project. I would like to thank other professors and staffs in Kyushu Institute of Technology for their guidance and help during two years. Additionally, I would like to sincerely thank to Mitsubishi Chemical Corporation, and JSPS Fellow Grant (DC2, 20J13064) for their generous financial support. This project is supported by Dr. Qitao Zhang, Dr. Wenjuan Yang, Dr. Chenliang Su of Shenzhen University, Dr. Hongbin Yang, Dr. Bin Liu of Nanyang University of Science and Technology, Dr. Ying-Rui Lu of the National Synchrotron Radiation Research Center, Dr. Chengyin Wang and Mr. Sixiao Liu of Yangzhou University. I highly appreciate their generous help. Thanks to the help from Prof. Akira Yamakata and Dr. Kosaku Kato for the TAS measurement. They opened a new vista for me to get a more comprehensive understanding for charge separation process. I would like to thank Dr. Huang Xiang of the Faculty of Physics, Southern University of Science and Technology for cooperating with the theoretical calculation, and Dr. Jian Nan of the Electron Microscopy Center of Shenzhen University for cooperating with the HRTEM measurement.

I would also thank Prof. Ming Zhang in Yangzhou University for his recommendation that gave me such a good opportunity studying in Prof. Ohno's group. I would like to thank other students (i. e., Wenan Cai, Chao Chen, Yu Cao) who helped me during my PhD project.

Finally, I would like to thank my parents for their guidance and support since I was born.